Multivalent Adsorption of Biological Nanoparticles on Functional Surfaces

Dissertation

for the award of the degree

Doktoringenieurin

(Dr.-Ing.)

by M.Eng. Wenjing Wang

Date of birth: 7. December 1983

in: Shandong, China

accepted by the Faculty of Process and Systems Engineering of the Otto-von-Guericke-University Magdeburg

Reviewer: Prof. Dr.-Ing. habil. Kai Sundmacher

Prof. Dr. Katharina Landfester

Prof. Manuel J.T. Carrondo

Submitted on: 07. Juli 2016

Graduation Colloquium on: 28. November 2016

Abstract

Multivalent adsorption is a valuable concept of the interactions between biological partners. The topic of this thesis is the modeling and experimental investigation of the multivalent adsorption between biological nanoparticles and a membrane surface. It is motivated by applying this type of multivalent adsorption to develop biological technologies. The targeting of therapeutic nanoparticles to the membrane surface and the membrane-based separation of biological particles can be two application fields. The aim is to develop suitable models identified from the pivotal experimental data for analyzing the adsorption kinetics as well as designing an affinity membrane adsorber. Accordingly, this thesis is basically divided into two parts, where Part I is the experimental design and Part II is the model identification. As guided by the methodology of process systems engineering, the chemical synthesis at the molecular level, the adsorption kinetics at the phase level, and the adsorption process at the unit level are all investigated in order to fundamentally understand how to successfully manipulate the multivalent adsorption.

The synthesis of the bionanoparticles is performed by coating nanoparticles with ligands with the help of a carbodiimide reaction that is also used for immobilizing receptors on the membrane surface. The results show that oriented attachments of ligands to the particles can be achieved by carefully handling the positions of the functional groups, which helps ligands to keep their biological activities. The synthesis procedures demonstrate that the ligand density of the bionanoparticle and the receptor density on the membrane surface can be varied when the amount ratio is changed. These variations at the molecular level are important to study the correlation of the adsorption kinetics with ligand density and receptor density at the phase level.

The adsorption kinetics is detected in the microfluidic channel using the surface plasmon resonance spectroscopy. The assembled ligand-particle entities with different ligand densities are measured under the conditions of different receptor densities. Considering the multivalence, a new multi-site kinetic model is proposed to describe the multivalent adsorption kinetics of particles on the micro-scale membrane surface. Due to the geometrical constrains, the influence of the mass transport on the analysis of the adsorption kinetics is evaluated by an analytical solution of the mass transport. This analytical solution is derived as the development of the boundary layer based on the classical boundary layer theory. By fitting the simulation curves to the experimental data, the newly developed multi-site kinetic model is identified. It elucidates that the multivalence plays a key role in the correlation of the adsorption kinetics with ligand density and receptor density. All the presented results related to the adsorption kinetics on a micro-scale surface are useful for studying the target applications.

The adsorption process of the assembled ligand-particle entities is measured in an affinity membrane adsorber using the liquid chromatography. Accordingly, the process model at the unit level is developed to describe this adsorption process. The adsorption kinetic model at the process unit level is derived on the basis of the multi-site kinetic model at the phase level. With regard to the breakthrough, the models are identified by

fitting the simulated curves to the experimental data. Besides, the dynamic binding capacity of the affinity membrane adsorber can be approximately estimated using the isotherm at the adsorption equilibrium state. With the frontal analysis of the adsorption breakthroughs under the influence of different parameters, the model simulations indicate that the decrease of processing time may increase the consumption of materials for the purpose of an optimal design. Particularly, the number of bonds, i.e., the multivalence, can serve as one type of input from the production process in the upstream processing to the capture process in the downstream processing. The established model framework here can be a model tool for analyzing and further designing the affinity membrane adsorber for the biological nanoparticles.

Zusammenfassung

Die Multivalente Adsorption ist ein sehr nützliches Konzept, um die Interaktionen zwischen biologischen Partnern zu beschreiben. Daher ist das Thema dieser Doktorarbeit die experimentelle Untersuchung und damit verbundene Modellierung der multivalenten Adsorption zwischen biologischen Nanopartikeln und einer Membranoberfläche. Die Motivation für diese Arbeit stammt aus der Anwendung dieser Art der multivalenten Adsorption für die Entwicklung biologischer Technologien. Zu den Anwendungsfeldern gehört zum einen die gezielte Bindung von therapeutischen Nanopartikeln an eine Membranoberfläche als auch die membranbasierte Trennung von biologischen Partikeln. Ziel dieser Arbeit ist es, passende Modelle aus den experimentellen Schlüsseldaten zu entwickeln, um damit dann zunächst die Adsorptionskinetik zu analysieren und anschließend einen Affinitäts-Membran-Adsorber zu entwerfen. Dementsprechend teilt sich diese Doktorarbeit grundsätzlich in zwei Teile: Teil I beinhaltet das Design der Experimente, Teil II die Identifikation der Modelle. Geleitet durch die Methodik der Systemverfahrenstechnik werden die chemische Synthese auf der molekularen Ebene, die Adsorptionskinetik auf der Phasenebene sowie der Adsorptionsprozess auf der Prozesseinheitsebene untersucht, um grundsätzlich zu verstehen, wie die multivalente Adsorption erfolgreich benutzt werden kann.

Die Synthese der Bionanopartikel geschieht mithilfe der Carbodiimide-Reaktion, bei der die Nanopartikel mit Liganden beschichtet werden. Diese Reaktion wird auch genutzt, um Rezeptoren an einer Membranoberfläche zu immobilisieren. Die Ergebnisse zeigen, dass ein gezieltes Koppeln der Liganden an die Partikel durch die Behandlung der Positionen der funktionalen Gruppen erreicht werden kann, welches den Liganden hilft, ihre Bioaktivitäten zu erhalten. Die Syntheseverfahren zeigen, dass die Ligandendichte auf den Bionanopartikeln und die Rezeptorendichte auf der Membranoberfläche geändert werden können, wenn das Verhältnis der Mengen verändert wird. Diese Änderungen auf der molekularen Ebene sind wichtig, um die Korrelation der Adsorptionskinetik mit der Ligandendichte und der Rezeptorendichte auf der Phasenebene studieren zu können.

Die Adsorptionskinetik wird im mikrofluidischen Kanal mittels Surface-Plasmon-Resonance gemessen. Die mit verschiedenen Ligandendichten synthetisierten Bionanopartikel werden unter Betrachtung von verschiedenen Rezeptorendichten vermessen. In Anbetracht der Multivalenz wird ein neues Multi-site-kinetisches Modell entwickelt, um die multivalente Adsorptionskinetik der Partikel auf der mikro-skaligen Membranoberfläche zu beschreiben. Aufgrund der geometrischen Bedingungen wird der Einfluss des Massentransportes auf die Analyse der Adsorptionskinetik durch eine analytische Lösung des Massentransportes beurteilt. Diese analytische Lösung wird auf der Grundlage der klassischen Grenzschichttheorie als die Entwicklung der Grenzschicht abgeleitet. Durch das Anpassen der simulierten Kurven an die experimentellen Daten wird das neu entwickelte Multi-site-kinetische Modell identifiziert. Es erklärt, dass die Multivalenz eine zentrale Rolle bei der Korrelation der Adsorptionskinetik mit der Ligandendichte und der Rezeptorendichte spielt. Alle dargestellten Ergebnisse in Bezug

auf die Adsorptionskinetik auf einer mikro-skaligen Oberfläche sind zur Erforschung von Anwendungen dieser gezielten Kopplung nützlich.

Der Adsorptionsprozess der synthetisierten Bionanopartikel wird in einem Affinitätsmembranadsorber mittels der Flüssigchromatographie gemessen. Um diesen Adsorptionsprozess zu beschreiben, wird entsprechend ein Prozessmodell auf der Einheitsebene entwickelt. Das Modell der Adsorptionskinetik auf der Prozesseinheitsebene wird bezugnehmend auf das Multi-site-kinetische Modell auf der Phasenebene abgeleitet. Mit Blick auf die Durchbruchskurve werden die Modelle durch das Anpassen der simulierten Kurven an die experimentellen Daten identifiziert. Außerdem kann die dynamische Bindungskapazität des Affinitätsmembranadsorbers durch die Isotherme im Adsorptionsgleichgewichtszustand annäherungsweise geschätzt werden. Bei der direkten Analyse der Durchbruchskurven der Adsorption unter dem Einfluss mehrerer Parameter deutet die Modellsimulation darauf hin, dass die Abnahme der Durchlaufzeit den Materialverbrauch zum Zwecke des optimalen Designs erhöhen kann. Insbesondere kann die Anzahl der Bindungen, i.e., die Multivalenz, als eine Art Eingang des Produktionsprozesses vom Upstream zum Trennungsprozess des Downstream dienen. Der hier aufgestellte Rahmen der Modellierung kann ein Werkzeug sein, um den Affinitätsmembranadsorber für biologische nano-skalige Partikel zu analysieren und weiterzuentwickeln.

Acknowledgement

My work in this thesis was conducted from September 2010 to April 2016 as scientific employee at the Max Planck Institute for Dynamics of Complex Technical Systems and Otto-von-Guericke University Magdeburg, Germany.

I would like to express my sincere gratitude to Prof. Dr.-Ing. Kai Sundmacher for the challenging and interesting topic, the inter-cultural trust and the scientific freedom. I am very grateful for his discussions and the demands on lectures, publications, conference contributions and student supervisions, which all lead me to enjoy a scientific education in Germany. In addition, special thanks is expressed to Prof. Katharina Landfester and Prof. Manuel J.T. Carrondo for taking the peer-review of this thesis.

In pursuance of my thesis I have benefited from contributions of many people. I would like to thank my collaboration group, the downstream processing team in the group of Bioprocess Engineering at Max Planck Institute for Dynamics of Complex Technical Systems, especially for providing purified influenza virus materials. With this, my special thankfulness is addressed to Dr. Michael Wolff for his open discussions and kind support in allowing me to develop my experimental skills within his team. I express my sincere appreciation to Dr. Andreas Voigt for his constructive encouragement, helpful information about scientific education in Magdeburg and serious revisions of my publications. I would like to further thank the laboratory staff, especially to Saskia Nickel for her jovial willingness to help me with the experiments.

I esteem the time I have shared with my colleagues in Magdeburg, especially thanking my colleagues from the group of Process Systems Engineering at Max Planck Institute as well as at Otto-von-Guericke University. Additionally, I express my sincere thanks to my friend, Corina Siewert, for her kindness and openness to help me at the end of this thesis.

Finally, I cherish my beloved parents in China to accept me abroad, and thus want to present this thesis as my life symbol to them.

Wenjing Wang Magdeburg, June 2016

Contents

Abstract ..... **I**
Zusammenfassung ..... **III**
Acknowledgement ..... **V**
List of symbols ..... **IX**
Chapter 1 Introduction **1**
1.1 Aim of this work 4
1.2 Thesis guide 5
Part I Experimental design for detecting multivalent adsorption **7**
Chapter 2 Synthesis of bionanoparticles **9**
2.1 Materials 10
2.2 Bioconjugation experiments by coating nanoparticles with ligands 10
2.3 Detection of synthetic bionanoparticle characteristics 14
2.4 Summary 16
Chapter 3 Detection of adsorption kinetics at a receptor surface **17**
3.1 Materials 18
3.2 Immobilization of receptors at the sensor surface 18
3.2.1 Immobilization of EEL 20
3.2.2 Immobilization of Protein A 20
3.3 Detection of bionanoparticle interaction by SPR 22
3.3.1 Detection of influenza virus particles 23
3.3.2 Detection of human IgG – coated bionanoparticles 29
3.4 Summary 35
Chapter 4 Detection of the adsorption process in an affinity membrane adsorber **37**
4.1. Materials 38
4.2. Immobilization of receptors in the membrane adsorber 38
4.3 Detection of adsorption chromatograms by Liquid Chromatography (LC) 39
4.3.1 Detection of dispersion effects 39
4.3.2 Detection of breakthrough curves of BioNPs through AMA 45
4.4 Summary 46

Part II Model identification from experimental data 47
Chapter 5 Development of adsorption kinetic model 49
5.1 The Multi-site kinetic model 50
5.2 Kinetic model framework based on SPR flow cell 54
5.2.1 Flow field 56
5.2.2 Mass balance equations 58
5.2.2.1 The distribution of the diffusional boundary layer 63
5.2.2.2 The analytical solution of the diffusional boundary layer 65
5.2.2.3 The analytical solutions for the multivalent adsorption 68
5.3 Parameter estimation 71
5.3.1 Adsorption of influenza virus particles 72
5.3.2 Adsorption of synthetic bionanoparticles 74
5.4 Evaluation of multivalent interaction 83
5.5 Summary 85
Chapter 6 Development of the adsorption process model 87
6.1 Adsorption process model of an affinity membrane adsorber 88
6.2 System dispersion model of the LC system 91
6.3 Parameter estimation 93
6.3.1 Volumetric parameters in the dispersion model 93
6.3.2 Kinetic parameters in the adsorption process model 94
6.4 Simulation of the adsorption process of AMA 95
6.5 Summary 99
Chapter 7 Summary, conclusion and outlook 101
7.1 Summary 101
7.2 Conclusion and outlook 102
Supplementary Information. Derivation of system equations in SPR flow domain. 105
List of Figures 131
List of Tables 135
References 137

List of symbols

Latin symbols

b	Bound/blocked sites
b	Ratio of convective time scale to desorption time scale
c	Concentration of the particle solution, mg/ml
d	Diameter of bionanoparticles
D	Diffusivity, m^2/s
Da	Damköhler number
f	Free sites
h	Height of the flow cell, 0.01 mm
k_a	Adsorption rate constant, M^{-1} S^{-1}
k_d	Desorption rate constant, S^{-1}
K_d	Desorption equilibrium constant
l	Length
m_{PR_n}	Amount of adsorbed bionanoparticles at the receptor surface
m	Ratio of maximum receptor capacity to feed particle concentration
n	The number of bonds, or multivalence
p	Probability
Pe	Peclet number
$[P]$	Particle concentration in the mobile phase
$[PR_n]$	Adsorbed bionanoparticle concentration at the receptor surface
Q	Flow rate
r	Adsorption rate
R_{BioNP}	Radius of bionanoparticles
Re	Reynolds number
R	Receptor density at the surface
R_n	Cluster concentration of available receptors at the membrane surface
S	Sum of squares
t	time, minute
T	Temperature

v	Velocity
$\overline{v_x}$	Averaged velocity
V	Volume
x	Axis x
X	Dimensionless axis x
y	Axis y
Y	Dimensionless axis y
z	Axial direction

Greek symbols

β	Vector of parameters
δ	Thickness of the boundary layer
Δ	Difference
ε	Void porosity
ζ	Axial axis in dimensionless form
η_{w}	Viscosity of pure water at 25 ^{o}C, 8.94 x 10^{-4} Pa·s
θ	Dimensionless concentration
Θ	Dimensionless quantity
κ	Boltzmann's constant, 1.38066 x 10^{-23} J/K
ν	Kinematic viscosity
ρ	Density of total mass
τ	Dimensionless time

Superscripts

max	Maximum
s	At the solid surface
$*$	Dimensionless form

Subscripts

a	Adsorption
D	Diffusional boundary layer
e	Entrance region

exp	Experimental data
i	Point or element
in	Inlet
j	Point or element
l	In the liquid phase or in the mobile phase
n	The number of bonds, or multivalence
out	Outlet
p	Probing area
P	Particle
r	Residence time
R_n	n number of receptors as a cluster
R	Receptor
s	At the solid surface or in the solid phase
x	Axis x
y	Axis y

Abbreviations

AMA	Affinity membrane adsorber
BC	Boundary condition
BioNP	Bionanoparticle
CSTR	Continuously stirred tank reactor
CV	Column volume
DAE	Differential algebraic equations
EDC	N-(3-Dimethylaminopropyl)-N'-ethylcarbodiimide hydrochloride
EEL	*Euonymus europaeus* lectin
Fc of IgG	Fragment, crystallizable
fc/Fc	Flow cell
HA	Hemagglutinin
HBS-EP+	HEPES-buffered saline
IC	Initial condition
IgG	Immunoglobulin G
LC	Liquid chromatography

mAU	Milli-absorbance units
MES	2-(N-Morpholino)ethanesulfonic acid monohydrate
MW	Molecular weight
MWCO	Molecular weight cutoff
NA	Neuraminidase
NHS	N-Hydroxysuccinimide
NP	Nanoparticle
PBS	Phosphate-buffered saline
PFR	Plug flow reactor
Rc	Reference cell
rpm	Revolutions per minute
RU	Response units
SPR	Surface plasmon resonance
UV-Vis	Ultraviolet–visible

Chapter 1

Introduction

Multivalent adsorption plays an essential role in many natural phenomena. For example, the multivalent virus-receptor complex can determine the infection of virus to cells (Siess et al. 1996). This is an important concept about the interaction and thus receives the increasing attentions from researchers in the biotechnology engineering fields (Fasting et al. 2012). In general, various partners performing the multivalent adsorption can act as pairs between ligands and receptors. Thanks to the flexibility of assembling ligand-receptor pairs, the concept of multivalent adsorption can trigger many valuable inspirations about the structures for investigating interactions between biological partners, such as protein and carbohydrate (Che et al. 2010, Handa et al. 2010), lectin and glycosides (Mouline et al. 2014, Ye et al. 2014), antibody and antigen (Barua et al. 2013, Matthaiou et al. 2014), multivalent ions and their applied targets (e.g., heavy metals (Fisher-Power et al. 2016), colloidal suspension (Philippe and Schaumann 2014, Reščič et al. 2014), DNA on like charged lipid surfaces (Pastré et al. 2006, Martín-Molina et al. 2014), or alginate on the zwitterionic surfaces (Mi et al. 2012)), and so on. In brief, the multivalent adsorption in each specific interaction can improve the corresponding biological functionality, for example, binding affinity (Bozza et al. 2012, Maric et al. 2015), inhibition potency (Elshan et al. 2015), enzyme activity (Adak et al. 2014, Wu and Algar 2015), potent antiviral effects (Bastian et al. 2015), pharmacokinetic profiles of antibodies (Xie et al. 2012), signal transduction regulation (Maiti et al. 2014), etc..

Among various interaction principles, affinity or avidity is a fundamental one in the biological field. Consequently, one can open up many new biological applications by manipulating the naturally existed affinity-based interacting partners. Under this topic, the current issues address mainly the following two aspects, including separation technologies (Hage et al. 2012, Hussain et al. 2013, Chen et al. 2016), and targeting strategies (Shokeen et al. 2011, Xu et al. 2012, Garcia-Vallejo et al. 2013).

The methods of assembling application-oriented structures, i.e., attaching ligands or receptors to different scaffolds, mainly rely on the chemical synthesis reactions (Bolley et al. 2013, Cai et al. 2014) or the bioconjugation chemistry (Sletten and Bertozzi 2009). Most of the assembled entities are obtained in a stochastic way in terms of the distribution of functional molecules (ligands or receptors) on the scaffolds (nanoparticles or surfaces). For example, a Poisson distribution of ligands among the ligand-particle entities has been reported (Olariu et al. 2013, van Dongen et al. 2014). If a relatively accurate localization of functional molecules on the scaffolds is required, one may need to perform a more delicate conjugation by possibly controlling all experimental factors, such as, ratio of material amount, size, geometry, cleanliness of materials, etc.. For example, a strategy using the ligand-attached peptide nucleic acids in conjunction with the complementary DNAs has been reported to control ligand location, spacing, and valence (Dix et al. 2014).

Beside, Schiavo etc. have pointed out that, in order to study the bond formation accurately, the special treatment concerning the clean and sterile conditions, and also the very high resolutions of the recording devices have to be strongly required (Lo Schiavo et al. 2012).

The engineered structures for the interacting partners can be divided into two main types according to the mobility of the scaffold in the solution, either a movable solute or a stable surface (at least in a relative stable situation compared to others). Here, the ligand is defined as one attached to the movable solute while the receptor is the other immobilized on the stable surface. The examples of the ligand-attached entities include the multimeric constructs in which multiple ligands are displayed on a polymer (such as the dextran polymer (Morimoto et al. 2014)), the pseudopeptides (Destouches et al. 2012), or various types of nanoparticles with their materials as gold (Sykora et al. 2010, Tavernaro et al. 2015), silicon (Gu et al. 2012), polymer (Xu et al. 2013), quantum dots (Dorokhin et al. 2010), lipid (Akhter et al. 2013), etc.. The receptor-immobilized surfaces are then reported according to the ligand-attached entities. For example, Paran etc. have conjugated a variety of hepatitis B virus surface proteins to polystyrene beads to measure the virus attachment (Paran et al. 2001). All are especially promoted by the intervening development of nano-pharmaceuticals, for instance, coating polymer particles with protein antigens for developing the multivalent oral vaccine (Phanse et al. 2014, Walke et al. 2015) or virus like particles (Effio and Hubbuch 2014).

The particle-based ligand entity is extensively applied as a biomimetic model to different biological processes (Mahon et al. 2012, Shemetov et al. 2012). The advantages using a spherical nanoparticle may include the structural similarity in comparison with the natural biological particles, the easy availability in various types of materials, the experimental operations, or the flexibility with regard to the assembling methods. Particularly, with a high aspect ratio of surface area to volume, the coating of the spherical particle can be created either with multiple copies of or with different types of functional molecules (Howard et al. 2014), i.e., ligands, which is also an important engineering approach to the bottom-up synthetic biology. For example, Olubummo etc. have reported the feasibility of the polymer-covered CdSe nanoparticles in addressing recognition of supramolecules in a membrane with mixed components (Olubummo et al. 2014). Crespo-Biel etc. have used ß-Cyclodextrin-modified gold nanoparticles for creating the layer-by-layer assembly (Crespo-Biel et al. 2005, Crespo-Biel et al. 2006).

As another interacting partner, the surface-based receptor entity can help the engineers to investigate the performing potentials of the ligand-particle entity. With the possibility of assembling the receptor-surface entity, a more efficient investigation can be performed in a way that the key elements out of the complex biological systems will be focused on. Thus, the effective assembling methods are important directions of current researches, especially about the cell biology. For example, Rädler etc. have manifested that metal-affinity ligand-receptor pairs can be used to dock and to tether the lipid membranes (Rädler et al. 2000). Zhang etc. have displayed that an immobilization strategy of using different receptors on one surface can improve the capture efficiency of cancer cells (Zhang et al. 2014). Furthermore, studies about the surface-based receptor entity are also important to develop the membrane technologies for the separation and purification of natural biological materials, e.g., small proteins (Chenette 2014) or virus particles (Opitz et

al. 2007, Kalbfuss-Zimmermann et al. 2014). Briefly, the surface-receptor technology has a broad application that ranges from the nano-scale science to unit level application-oriented research.

The influencing factors of the multivalent adsorption relate to the elements of the synthesized interactions. They can be the ligands, the receptors, the scaffolds, the assembling methods, the measuring systems, and so on. For instance, the receptor density can influence the selectivity of the binding (Martinez-Veracoechea and Frenkel 2011), the binding capacity of the surface (Shi et al. 2015), or hinder the binding due to the clustering effect resulted from the high density (Shi et al. 2007).

The experimental measurements of the multivalent adsorption are mostly performed in the microfluidic systems. Their corresponding setups are mainly established with the help of the following four technologies, including surface plasmon resonance spectroscopy (SPR) (Johnsson et al. 1991, de Mol and Fischer 2010, Nilsson et al. 2010, Tassa et al. 2010, Vicente et al. 2010), atomic force microscopy (AFM) (Ellis et al. 2004, Verbelen et al. 2008, Gutiérrez Sánchez et al. 2015, Troiano et al. 2015), chromatography (Opitz et al. 2007, Walkey et al. 2012, Nishimura et al. 2013), and some other lab-on-a-chip platforms (Holden and Cremer 2005, Wu et al. 2016). With regard to their different measurements, SPR detects adsorption kinetics and isotherm, AFM probes the binding force and molecular structure, and chromatography is useful for studying the separations. Particularly, due to the superior label-free detection, SPR is extensively used to evaluate the biological functionalities of the assembled entities. Also, it is very important for further developing new sensing methods (Ammari et al. 2016, Li et al. 2016, Sonato et al. 2016). With regard to the characterization of the assembled entities, the reported experimental methods include various types of microscopy for measuring surface structure and particle size (Sheng et al. 2013, Chen et al. 2016), the dynamic light scattering for detecting particle size distribution (Jurasin et al. 2016), the fluorescence-related labeling strategies for probing biological activities (Majonis et al. 2013), NMR or MS spectra for confirming functional groups (Yin et al. 2016), flow cytometry for ligand quantification (Ugozzoli et al. 2011), and so on.

In addition to the experimental investigations, the theoretical studies through the modelling approaches can provide more systematic analysis of the factors influencing the multivalent adsorption. Among the theoretical methods, one modelling approach is to build system equations based on the conservation laws and adsorption kinetic model. In particular, a proper kinetic model describing the multivalent adsorption kinetics is the key or difficult point and thus is issued by many researchers. Concerning the development of the adsorption kinetic model, the number of bonds formed between one single ligand-particle entity and surface receptors plays a key role in describing the multivalent mode. In this work a multi-site adsorption kinetic model will be proposed later (Wang et al. 2014, Wang et al. 2016). As another interesting example, Perelson has developed a sequence of step equations with regard to the increasing number of bonds but by neglecting the steric hindrance effects between neighbouring sites (Perelson 1981). In addition, Monte Carlo simulation is one possible candidate as a random approach in combination with the probability distribution (Amar 2006). For instance, Chen etc. have used Monte Carlo simulations to clarify the effects of ligand valence, ligand branching length, and structure of a flat polymer layer on the approaching accessibility of ligands to receptors (Chen and

Dormidontova 2005). Wang etc. have also used Monte Carlo simulation to analyse the targeting efficiency of ligand-particle entity to the mobile receptors on cell surface under the influence of multivalent ligands (Wang and Dormidontova 2011). Based on the Monte Carlo approach, Liu etc. have investigated the effects of particle size, shear flow and resistance on the multivalent binding, especially addressing the issue of shear-enhanced binding (Liu et al. 2011). Moreover, a combination between the experimental investigation and the modelling methods can be another applicable approach in addition to the aforementioned pure theoretical studies (Silpe et al. 2013).

In summary, the multivalent adsorption is the valuable concept for performing biological interaction according to various application aims. Thus, this work is motivated to develop the possible modeling approaches in combination with the experimental investigations for applying the multivalent adsorption. Here, the application example for the multivalent adsorption can be to design an affinity membrane adsorber for the purpose of improving the capture of the influenza virus particles in the downstream processing of vaccine production. In addition to the discovered knowledge about the multivalent interactions, this work can also serve as an example of how to quantitatively connect the experimental results from different devices in the biological laboratory in a modeling way. Concerning the modeling studies of the biological processes, the recent works only focus either on the upstream processing or on the downstream processing. As one motivation, it is worth to connect two parts within one modeling framework so that the feedbacks between each other can be analyzed more comprehensively.

1.1 Aim of this work

The concept of the multivalent adsorption for the biological applications is targeted in this work. The aim of this work is to develop a suitable model framework for describing the multivalent interaction, especially about the adsorption kinetics, on a micro-scale surface as well as in a microliter unit. On a micro-scale surface, the presented studies are useful for the targeting application, i.e., applying the assemble bionanoparticles to target the specific receptors on the membrane surface. In a microliter unit, the model approach has the purpose of the separation application, by which the adsorption process in the affinity membrane adsorber is simulated so that the capture of the biological nanoparticles, such as influenza virus particles, can be optimized.

As the mentioned popular example before, the structures illustrated in Fig. 1.1 will be focused on in this work. Fig. 1.1 illustrates the biological nanoparticles coated with ligands and the corresponding membrane surface immobilized with receptors. The interaction mechanism is the affinity or the avidity, which are differentiated in terms of the number of bonds formed between a single particle and some receptors on the membrane surface.

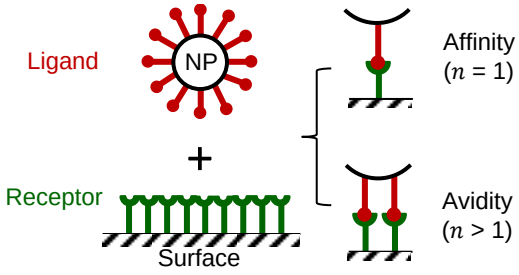

Figure 1.1: Illustration of multivalent interactions between two interacting partners. n is the number of bonds formed between ligands (in red color) of a single particle and receptors (in green color) on the membrane surface.

With the selected structures, the possible answers to the following questions will be provided in this work:

- How to assemble the ligand-particle entity and the receptor-membrane entity?
- How to characterize the ligand-particle entities?
- How to detect the multivalent adsorption on a microscale surface as well as in an adsorber unit?
- How to model the multivalent adsorption associated with different experimental systems, here including SPR system and liquid chromatography system?
- Is the number of bonds, i.e., the multivalence, very important to evaluate the adsorption? How big can this number be for different experimental conditions?
- How does the adsorption kinetics respond to the changes of the ligand density and the receptor density?
- How to mathematically analyze the adsorption behavior of biological particles through the affinity membrane adsorber, especially either increasing adsorption capacity or saving the breakthrough time?
- What can be a possible way to connect the modeling of the downstream processing with the upstream processing?

1.2 Thesis guide

Fig. 1.2 illustrates the content and structure of this thesis. The pyramid in the background elucidates the relationship among three main domains in this thesis. First, the basis is to assemble the interaction partners. This domain can be seen as the chemical synthesis at the molecular level. Second, the adsorption kinetics of the assembled partners is experimentally measured and theoretically modeled as well. This domain is conducted on a surface in the SPR-based microfluidic system, which can be seen as at the fluidic phase level. Finally, in the top of the pyramid, the adsorption process in an affinity membrane adsorber (AMA) is experimentally measured and theoretically modeled. This domain is located in the liquid chromatography field, which can then been seen as at the unit level. Besides, the adsorption kinetic model developed at the phase level is the base of that developed for the adsorption process at the unit level. In summary, this thesis is also an example for the multi-level study in the field of the process system engineering.

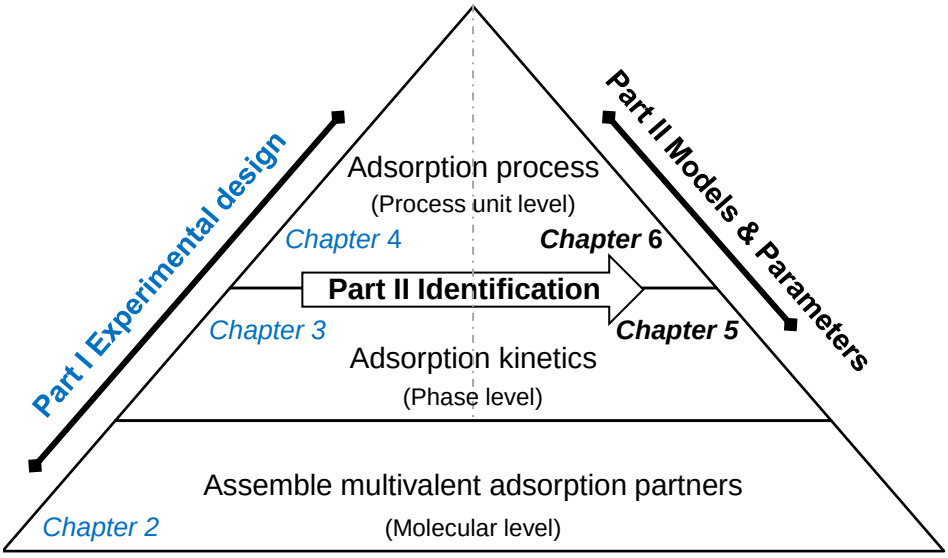

Figure 1.2: Thesis structure and its main contents.

Aimed at suitable model frameworks for the multivalent adsorption both at the phase level and at the unit level, the experimental data are accordingly required for the model identification. Thus, the experimental design is performed through the three domains in the pyramid. Unknown parameters in the models are estimated in the corresponding domains, including the adsorption kinetics at the phase level and the adsorption process at the unit level.

With the targeted application examples of the multivalent adsorption, both experimental investigations and model developments are addressed. Therefore, the thesis is divided into two main parts, as Part I is the experimental design for detecting the multivalent adsorption and Part II is the model identification from experimental data. Within the experiment Part I, according to the structure of the pyramid in Fig. 1.2, the chemical synthesis of the ligand-particle entity is first presented in Chapter 2, the detection of adsorption kinetics at a receptor surface is then depicted in Chapter 3, and finally the detection of the adsorption process in an affinity membrane adsorber is given. Within the model Part II, likewise, the development of adsorption kinetic model is first presented in Chapter 5 and then the development of adsorption process model is given in Chapter 6.

Last but not least, in addition to each specific summary in the respective chapter, summary, conclusion and outlook for the whole thesis are presented in Chapter 7.

Part I Experimental design for detecting multivalent adsorption

Chapter 2

Synthesis of bionanoparticles

In this chapter the preparation of synthetic bionanoparticles (BioNPs) is presented, including materials and experimental procedures. These BioNPs will be applied to the detection of multivalent adsorption kinetics at a receptor surface described in Chapter 3 and to the measurement of adsorption process in an affinity membrane adsorber described in Chapter 4. As connection of experimental design to model study, the useful characteristics of BioNP which are later parametrized into model equations are measured as well.

Fig. 2.1 illustrates that BioNP studied in this work is a type of spherical nanometer-sized particle with functional ligands existing on its surface. Surface proteins are called ligand and the inner particle is scaffold. Two examples of BioNP are studied here, including naturally-existed nanoparticles, such as influenza virus particles with surface proteins (hemagglutinin and neuraminidase), and synthetic nanoparticles, such as polystyrene nanoparticles coated with antibodies.

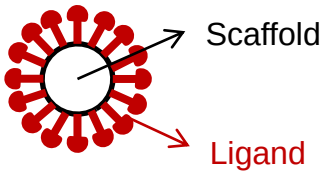

Figure 2.1: Sketch of bionanoparticle structure.

Thanks to our in-house collaboration group of Bioprocess Engineering, influenza A virus (Puerto Rico/8/34, H1N1) is available for some preliminary tests of its interactions with lectin immobilized membrane surface. However, we observe that it is difficult to repeat experimental results of influenza virus nanoparticles. This difficulty makes it complex to obtain the useful experimental data for identifying mathematical models. In addition, the in-house production of purified influenza virus materials in laboratory scale is not only amount-limiting but also time-consuming. In contrast, the alternative approach of

synthesizing bionanoparticles has advantages because enough materials for the synthesis are available in the market. As a result, there is no amount limitation to experiments and the repeatability can be appropriately tested. Another advantage of applying self-made BioNPs is that it is possible to change the ligand density on top of one single nanoparticle. This possibility is important to study the influence of ligand density on the avidity interaction. In fact, surface proteins of biological nanoparticles, among many other aspects, can be varied due to different cultivation batches of the upstream processing. These variations may result in ligand density changes and they are hard to be quantitatively analyzed. Hence, ligand density is an important researching aspect. By designing ligand density in the synthesis of nanoparticles, the influence of ligand density on the avidity interaction can be investigated systematically. Besides, in comparison to the biological complexity of practical systems, the synthetic system is easy to be controlled by allowing investigation focused on only ligand density. Moreover, it provides a simple example to study the correlation between upstream processing and downstream processing.

2.1 Materials

Polystyrene nanoparticles (NPs, 2.7 x 10^{13} particles/ml) with a diameter of 110 nm were purchased from Life Technologies, Thermo Fisher Scientific Inc.. MES (2-(N-Morpholino)ethanesulfonic acid monohydrate) is purchased from Carl Roth (Karlsruhe, Germany). Polyclonal human IgG, EDC (N-(3-Dimethylaminopropyl)-N'-ethylcarbodiimide hydrochloride), NHS (N-Hydroxysuccinimide), glycine, and all the other chemicals were purchased from Sigma-Aldrich Chemie GmbH, Germany. The dialysis membranes were purchased from Spectrum Labs (Frankfurt, Germany). Vivaspin 20 centrifugal concentrators with a molecular weight cutoff (MWCO) of 1000 KDa and syringe filters were purchased from Sartorius AG (Göttigen, Germany). All the buffers were prepared using Milli-Q water and finally filtrated using a filter with its pore size of 0.22 µm. All the glass accessories were autoclaved.

2.2 Bioconjugation experiments by coating nanoparticles with ligands

First of all, the purchased NP solution was adjusted to 10 mM MES, pH 6 by dialysis using MWCO 1,000 KDa membrane. Before dialysis, all dialysis accessories (including cylinders, closers of membrane tubes, magnetic stirrer, and floating Styrofoam) were sterilized by 70% ethanol under the sterilized bench overnight and then rinsed by 10 mM MES pH 6. Membrane tubes, each with a length of 6 cm, were soaked in the autoclaved Mili-Q water for at least 15 minutes at room temperature to remove the preservative agent (sodium azide). Before adding NP solution, membrane tubes were thoroughly rinsed five times by each 1 ml MES (10 mM, pH 6). 1 ml NP solution in each membrane tube were dialyzed against 1 L MES(10 mM, pH 6), three times (600 rpm, 2 hours, at room temperature for the first two times, and 350 rpm, overnight, at 4 ^{o}C for the third time). After

the third time, all NP solutions were collected in 15 ml falcon tube and stored at 4 ^{o}C for further use.

Figure 2.2 manifests a two-step reaction scheme (activation and coating) which was employed to synthesize the BioNPs. The synthesis is based on a carbodiimide reaction that causes the carboxyl groups covalently bind to the primary amine groups. The carbodiimide reaction is extensively used in the field of conjugation chemistries (Mahon et al. 2012). The surface of polystyrene nanoparticle was originally functionalized with carboxyl groups as purchased products. The N-terminal sides of human IgGs used as ligands are the primary amine groups. The experimental details of the synthesis were described in the following.

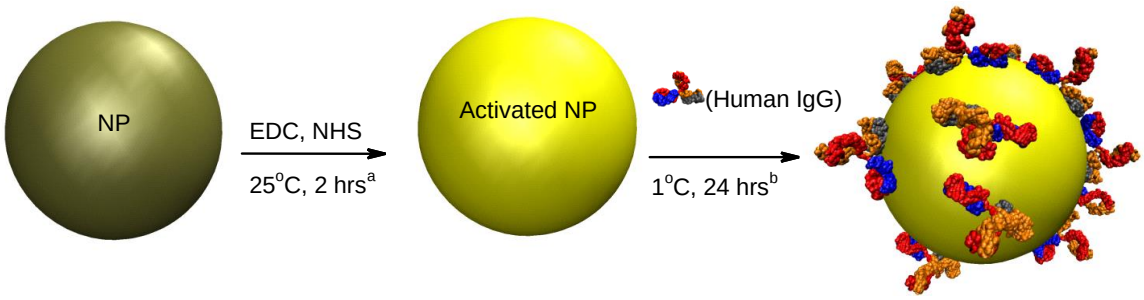

Figure 2.2: Synthesis scheme of human IgG coated BioNP via a carbodiimide reaction. [a] The activation step: NP denotes polystyrene nanoparticle. EDC is N-(3-Dimethylaminopropyl)-N'-ethylcarbodiimide hydrochloride and NHS is N-Hydroxysuccinimide. [b] The coating step: different molar amounts of human IgG were used to coat the activated nanoparticles.

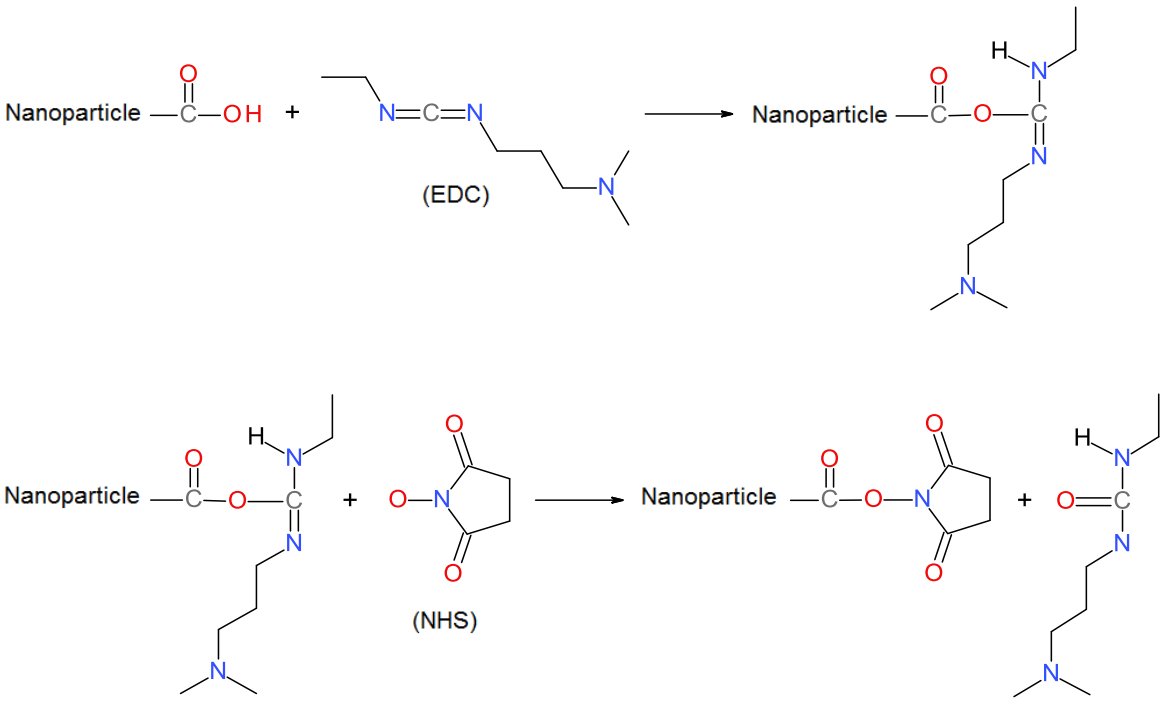

Figure 2.3: Reactions to activate the carboxyl groups of nanoparticles by EDC and NHS in the first step of synthesis scheme (see Figure 2.2).

The first step in Figure 2.2 was to activate the carboxyl groups at NP surface by EDC and NHS. The relevant reactions in this step are displayed in Figure 2.3. Finally, the carboxyl groups were activated into reactive succinimide esters.

The experimental procedures used are as follows. After a brief vortex, 1 ml NP solution were added into one centrifuge glass tube and diluted by 2.75 ml MES (10 mM, pH 6). After that, 1 ml EDC solution (1 M in water) and 0.25 ml NHS solution (1 M in water) which were mixed in advance were injected in a dropwise way to 3.75 ml NP solution in sonication bath. After the injection, the mixture with NPs was incubated for 2 hours at 25 ^{o}C in an inter-mixing mode, (30 seconds 600 rpm + 30 seconds pause, Thermomixer, Eppendorf). Then, the unreacted EDC and NHS were removed from the activated NPs by dialysis using MWCO 1,000 KDa membrane. Before dialysis, all dialysis accessories (including cylinders, closers of membrane tubes, magnetic stirrer, and floating Styrofoam) were sterilized by 70% ethanol under the sterilized bench overnight and then rinsed by PBS buffer (10 mM sodium phosphate, 150 mM NaCl, pH 7.4). Membrane tubes, each with a length of 6 cm, were soaked in the autoclaved Mili-Q water for at least 15 minutes at room temperature to remove the preservative agent (sodium azide). Before adding NP solution, membrane tubes were thoroughly rinsed five times by each with 1 ml PBS buffer (10 mM sodium phosphate, 150 mM NaCl, pH 7.4). Then 1 ml NP-EDC-NHS mixture were dialyzed against 1 L PBS buffer (10 mM sodium phosphate, 150 mM NaCl, pH 7.4). The dialysis buffer was changed three times (400 rpm, 2 hours, at room temperature for the first two times, and 350 rpm, overnight, at 4 ^{o}C for the third time). After the third time, all the activated NP solution was collected together in one 50 ml falcon tube for further use in the second step.

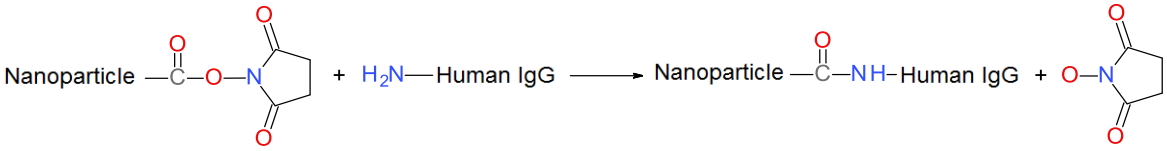

Figure 2.4: Reaction between activated nanoparticles and human IgG in the coating step of synthesis scheme (see Figure 2.2).

The second step in Figure 2.2 was to coat the activated NPs with human IgGs. The relevant reaction in this step is elucidated in Figure 2.4. The reactive succinimide esters reacted with the primary amine groups in the Fab fragments of human IgG (see protein structure in Figure 2.2). Then, ligands were covalently attached to nanoparticles by amide bonds. Moreover, this covalent attachment will not hinder the affinity interaction of human IgG with Protein A as the affinity site is in the Fc fragments. This is preferred by the experimental investigation of multivalent adsorption kinetics about the avidity interaction of human IgG coated BioNPs with Protein A immobilized membrane surface in the following Chapter 3.

The experimental procedures used are as follows. First, the purchased human IgG solution was adjusted to PBS buffer (10 mM sodium phosphate, 150 mM NaCl, pH 7.4) by dialysis using MWCO 20 KDa membrane. Before dialysis, all dialysis accessories

(including cylinders, closers of membrane tubes, magnetic stirrer, and floating Styrofoam) were sterilized by 70% ethanol under the sterilized bench overnight and then rinsed by 10 mM sodium phosphate, 150 mM NaCl, pH 7.4. Membrane tubes, each with a length of 7 cm, were soaked in the autoclaved Milli-Q water for at least 15 minutes at room temperature to remove the preservative agent (sodium azide). Before adding human IgG solution, membrane tubes were thoroughly rinsed five times by each with 1ml 10 mM sodium phosphate, 150 mM NaCl, pH 7.4. 0.5 ml human IgG solution were dialyzed against 500 ml 10 mM sodium phosphate, 150 mM NaCl, pH 7.4. The dialysis buffer was changed three times (400 rpm, 2 hours, at room temperature for the first two times, and 350 rpm, overnight, at 4 ^{o}C for the third time). After the third time, human IgG solutions were collected together in 15 ml falcon tube and stored at 4 ^{o}C for further use.

Table 2.1: Dilution volumes of human IgG solutions.

BioNP	4.8 mg / ml Human IgG, ml	PBS buffer, ml
0	0.14	3.86
1	0.28	3.72
2	0.70	3.30
3	0.98	3.02
4	0.28	3.72

Table 2.1 displays that different volumes of 4.8 mg / ml human IgG solution were diluted by the corresponding volumes of PBS buffer (10 mM sodium phosphate, 150 mM NaCl, pH 7.4) to give a final volume of 4 ml in each centrifuge glass tube. All the activated NP solutions produced in the first step were first set in sonication bath for 4 minutes. Then, in sonication bath, each one milliliter of this activated NP solution were drop-wise injected to each 4 ml human IgG solution as displayed in Table 2.1. After that, all samples were incubated for 24 hours at 1 ^{o}C in an inter-mixing mode (30 seconds 600 rpm + 30 seconds pause, Thermomixer, Eppendorf). In the end of the second step, the unreacted sites at NP surface were quenched by adding 556 µl 1 M glycine into each 5 ml sample. The solutions were then incubated for 2 hours at 25 ^{o}C in an inter-mixing mode (15 seconds 600 rpm + 30 seconds pause, Thermomixer, Eppendorf).

After activation and coating human IgG coated BioNPs were purifed. All the unreacted impurities were removed using Vivaspin 20 centrifugal concentrators and the centrifuge (Eppendorf Centrifuge 5702 RH). The concentrators were rinsed three times in advance with the solution sequence of 20 ml PBS buffer, 10 ml 70% ethanol, and 20 ml PBS buffer again. Each rinsing step was done following by the first filling of solution and then the centrifugation at 3000 rpm for 2 minutes at 4 ^{o}C. Then, 10 ml BioNP solution was added to one rinsed concentrator and centrifuged at 3000 rcf for 4 minutes at 4 ^{o}C. After the centrifugation, concentrated BioNP cake were taken out by re-dissolving BioNPs with 1 ml PBS buffer using pasteur pipette, and this taken step was repeated three times. The separated solutions without BioNPs in the bottom part of the concentrator tube were stored for further measuring the unreacted human IgG amounts. After a brief sonication, the BioNP solution was further filtrated by a two-step filtration by using syringe filters with two different pore sizes: 0.8 µm in the first step and 0.45 µm in the second step. The final BioNP samples were stored at 4 ^{o}C for further measurements within two weeks.

The distribution of human IgGs among nanoparticles was highly impacted by the mixing between ligands and nanoparticles.(van Dongen et al. 2014) An effective mixing can improve the available contact between human IgGs and nanoparticles in the coating step. Additionally, it is also helpful to avoid agglomerations and sedimentations of the nanoparticles as much as possible. Under experimental conditions of a normal biological laboratory, there were two points influencing the mixing strongly: sonication and adding sequences of the reactants. In order to achieve an effective mixing, these two important points were carefully investigated. According to observations, the instructive operations were described as following: in the first activating step of Figure 2.2 the mixture of EDC / NHS was injected into the nanoparticle solutions during the sonication; in the second coating step activated nanoparticle solutions were drop-wise injected into the human IgG solution during the sonication; and all reactions in the synthesis process were set under the intermittent moving modes (pause and rotation, alternately). The final concentration of BioNP solutions was estimated to be the magnitude of 10^6 particles/ml based on concentration measurements by IZON device.

2.3 Detection of synthetic bionanoparticle characteristics

Table 2.2 shows the characteristics of a single BioNP after the synthesis experiments in the last section. The here presented characteristics are required for the further model study in Chapter 5. Either the detection or calculation details concerning each of these characteristics are described in the following.

Number of human IgGs per BioNP represents the important parameter: ligand density. Concerning the ligand density, it is critical to understand the functionality of nanomaterials. Many efforts have been put in order to quantitatively estimate the ligand density per particle (Wei et al. 2012). Here, a common bulk sampling method was applied to give an average number of ligands per BioNP based on mass changes of ligand after synthesis experiments. The concentration of human IgG solutions was tested by UV – Vis measurements in Specord S600 device, Analytik Jena. Based on the tested concentrations, the total number of human IgGs attached to BioNPs in the second coating step of synthesis in Figure 2.2 can be calculated by subtracting the left unreacted amount after the coating step from the initial amount before the coating step. After that, this total number of human IgGs was divided by the total number of nanoparticles in the synthesis to finally result in the number of human IgGs per single BioNP in Table 2.2. At the same time, molecular weight (MW) of a single BioNP, can be calculated by adding the weight of a single NP to weights of human IgGs per BioNP.

Diameter of single BioNP, d, is measured by dynamic light scattering technology, Malvern Zetasizer Nano ZS device. For the experimental operation, one special notice was that BioNP solution after two minutes of sonication should be immediately put into the device for the detection. Interestingly, BioNP0, BioNP1, and BioNP4 appeared to be similar with regard to diameter according to the measurements. For BioNP1 and BioNP4, the same amount ratio between polystyrene nanoparticles and human IgGs in the coating

step was employed. The here measured diameter results demonstrate that the repeatability of the synthesis experiments is good. With the known diameter values, D, diffusivity, can be calculated by the Stokes-Einstein equation:

$$D = \kappa T/(6\pi R_{\mathrm{BioNP}}\eta_{\mathrm{w}}) \quad (2.1)$$

where κ is Boltzmann's constant, 1.38066 x 10^{-23} J/K; T is the temperature, 298 K; η_{w} is the viscosity of pure water at 25 ^{o}C, 8.94 x 10^{-4} Pa·s; R_{BioNP} is the BioNP radius.

Table 2.2: Characteristics of synthetic bionanoparticles (BioNP).

BioNP	Number of IgGs	d, nm	Layers	MW, x 10^8 Da	D, x 10^{-12} m^2/s
0	457	143.0	Mono-	5.112	3.414
1	934	140.0	Mono-	5.827	3.488
2	2319	308.0	Non-mono-	7.905	1.585
3	3264	365.5	Non-mono-	9.322	1.336
4	933	144.8	Mono-	5.826	3.372

The definition of mono- or non-mono- layer here was made according to the analysis of both BioNP diameter and number of human IgGs per BioNP. One human IgG has the maximum longitudinal length of approximately 16.6 nm.(Pease et al. 2008) As the diameter of the un-coated nanoparticle is 110 nm, the diameter of BioNP having the monolayer of human IgGs can be assumed as about 143.2 nm. With comparison of this calculated diameter to BioNP diameters in Table 2.2, one can assume that BioNP0, BioNP1, and BioNP4 have the monolayer coating while BioNP2 and BioNP3 might have the multilayer. In addition to diameter analysis, the maximum number of human IgGs forming the monolayer coating outside one BioNP can be also calculated by comparing the occupation area. The top area of one human IgG is about 62 nm^2 (Pease et al. 2008). By dividing the surface area of one nanoparticle (3.8 X 10^4 nm^2) by the top area of human IgG, the maximum number of human IgGs with their two Fab fragments both attached to the particle surface is possibly 612. If only one arm of Fab fragments instead of both is attached to the nanoparticle, the maximum number can be double as 1224. In Table 2.2 it is clear that the number of human IgGs per BioNP0, BioNP1, and BioNP4 are all within this maximum number of human IgGs forming the monolayer while BioNP2 and BioNP3 are beyond this maximum value. With regard to the coated structures of BioNP2 and BioNP3, measurements performed by dynamic light scatting technology did not display a detectable polydispersity. Therefore, both BioNP2 and BioNP3 can be assumed to be spherical. The layers of these two BioNPs might be more than one because the activated groups, after the first activation step of the synthesis in Figure 2.2, might stretch outwards in a branch style. The coated structure with respect to the ligand layer of neither BioNP2 nor BioNP3 can be precisely defined without structure photos. However, both ligand densities should be still bigger than those of BioNP0, BioNP1 and BioNP4. Therefore, BioNP2 and BioNP3 need to be still displayed here and will be applied later for the study of adsorption kinetics together with the other three BioNPs in Chapter 3 and Chapter 5.

2.4 Summary

Spherical nanoparticle with its surface functionalized with multiple ligands is a type of versatile biological material. As one example, antibody-coated nanoparticle is synthesized in this chapter to verify the potential application from the perspective of biological engineering approaches. As tools, human IgG was chosen as ligand and polystyrene nanoparticle was scaffold. The results demonstrate that the biological activity of ligand can be maintained by designing the ligand attachment with a proper orientation. It also elucidates that ligand density can be controlled by changing the concentration of ligand solutions in the coating step. Furthermore, one may even engineer the number of coating layer, which relates to the size of final synthesized particle.

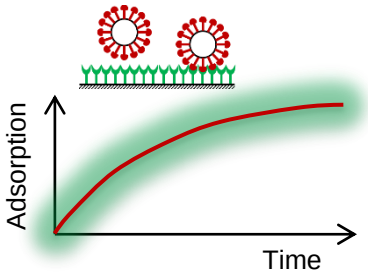

Chapter 3

Detection of adsorption kinetics at a receptor surface

In this chapter the experimental studies about multivalent interactions of BioNPs with surface receptors are presented. Two partners, BioNPs and surface receptors, are sketched in Fig. 3.1. Adsorption and desorption are measured by surface plasmon resonance spectroscopy (SPR) and recorded in sensorgrams. Two types of BioNP are used here: human IgG-coated nanoparticles as synthesized in Chapter 2 and influenza virus particles. Their receptors are Protein A and *Euonymus europaeus* lectin (EEL), respectively.

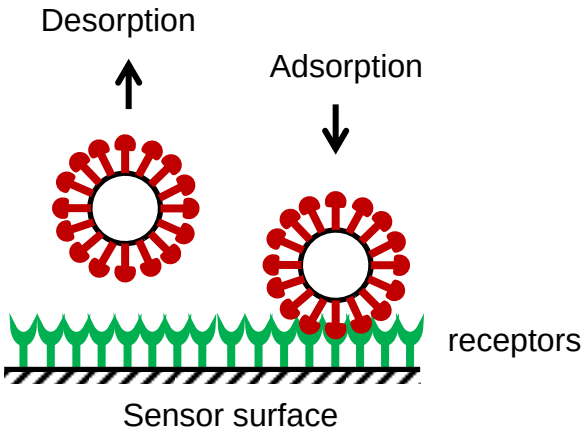

Figure 3.1: Sketch of two interacting partners. The red color stands for the ligand and the green color stands for the receptor.

First, the receptors are immobilized on the sensor surface, as described in Section 3.2. Following the immobilization, analyses of multivalent adsorption kinetics are described in Section 3.3. The adsorption kinetics of BioNPs can be influenced by particle concentration, receptor surface capacity, and ligand density. The influence of these three parameters will be discussed in this chapter. This chapter is aimed to display key experimental results together with reaction scheme and important experimental details. All of these are closely related to the modeling studies in chapter 5.

3.1 Materials

The purified material of Human influenza virus A/Puerto Rico/8/34 was provided by the in-house Group of Bioprocess Engineering, Max Planck Institute for Dynamics of Complex Technical Systems Magdeburg. Immobilization in Section 3.2 and detection in Section 3.3 were both performed by using BIAcore^{TM} 3000 device from GE Healthcare, Sweden. Sensor chip C1, amine coupling kit, 10 mM Acetate pH 5.0, and HBS-EP+ were purchased from GE Healthcare Bio-Sciences AB, Sweden. Streptavidin, EEL, and Protein A were purchased from Biozol, Germany. All the other chemicals were purchased from Sigma-Aldrich Chemie GmbH, Germany.

3.2 Immobilization of receptors at the sensor surface

The detected BioNPs here include influenza virus particles and synthetic nanoparticles. Accordingly, there were two types of receptors. One is the lectin, EEL, because of its affinity to the viral surface glycoproteins, hemagglutinin (HA) and neuraminidase (NA), which have a large amount of terminal α - galactose units. Optiz *et al.* have proved that it is possible to use EEL chromatography to purify several strains of Influenza A virus particles from MDCK cells.(Opitz et al. 2008) The EEL used in this study is biotinylated and has a high affinity to streptavidin. Thus, streptavidin is used as a linker for the attachement of EEL to sensor surface. Another receptor used in this study is Protein A because of its affinity to human IgG. Both streptavidin and Protein A contain primary amines. As a monolayer of carboxylate groups exist on the surface of sensor chip C1, streptavidin and Protein A are covalently attached to C1 surface via carbodiimide reaction (for reaction details, see Fig. 2.3 and Fig. 2.4).

Fig. 3.2 elucidates main reaction steps and a typical sensorgram of protein immobilization at the sensor chip C1 surface. Carbodiimide reaction is the one previously described in details in Chapter 2 but with slight modifications that at the end ethanolamine is used instead of glycine in order to block the left reactive succinimide esters. The final immobilized receptor capacity, i.e., maximum receptor density, was calculated on the basis of the relative difference of response signals between baseline point and end point (marked as crosses in Fig. 3.2). Here RU means the response unit and 1 RU = 10^{-10} g / cm^2.(handbook 2008) The protein immobilization described in Fig. 3.2 can be simply realized by usage of the standard amine coupling kit at 25 ^{o}C with the applied

concentration and volumes of materials shown in Table 3.1 (handbook 2008). Besides, the immobilization procedures are set using the provided software in BIAcore™ 3000 device.

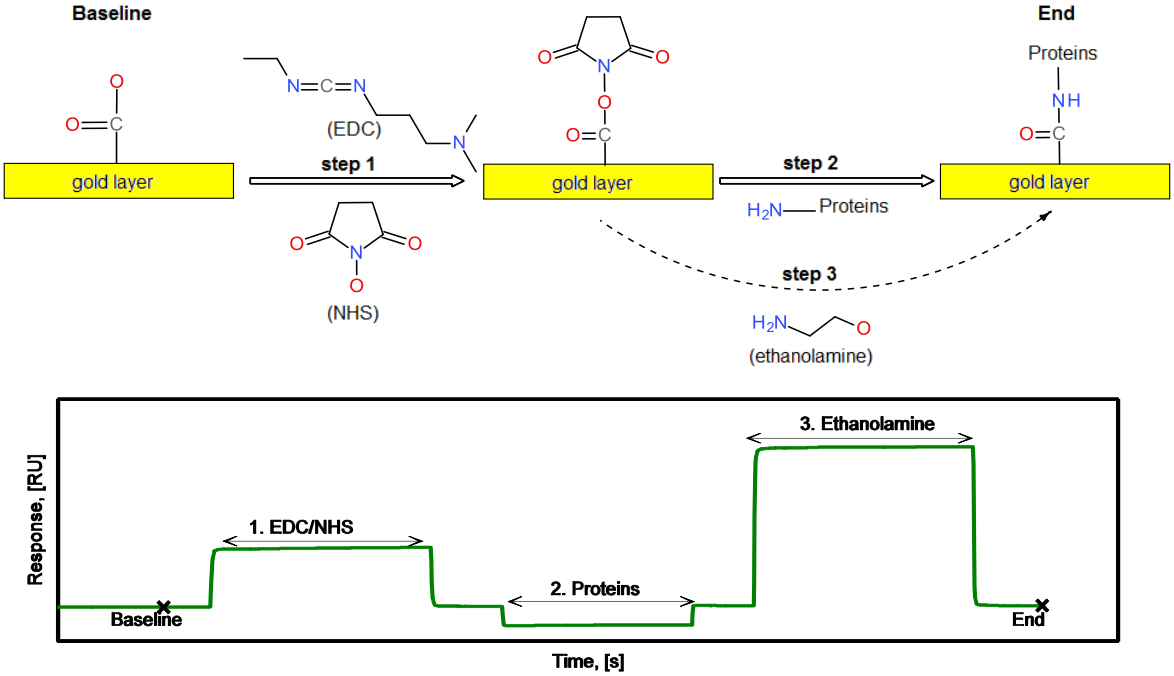

Figure 3.2: Cascade reaction (top) and typical sensorgram (down) of protein immobilization on sensor chip C1 surface (For the reaction details of carbodiimide reaction, see Fig. 2.3 and Fig. 2.4).

Table 3.1: Amount usage of materials in the carbodiimide reation.

Materials	Concentration, M	Volume, µl
EDC	0.4	115
NHS	0.1	115
Ethanolamine-HCl pH 8.5	1	75

Sensor chip C1 is chosen according its ability to form a monolayer of adsorbed BioNPs on top of a monolayer of carboxylic groups existing on the basis of the thin gold layer of C1 sensor chip, which is in accordance with a suggestion by BIAcore. This monolayer adsorption of BioNPs is preferred by the later model developments derived in Chapter 5. Besides, it has a relative low surface capacity that is suitable to analyze adsorption kinetics by SPR technology. Furthermore, the effective penetration depth of the evanescent wave in SPR technology is about 150 nm from the gold surface. As diameters of BioNPs are all larger than 100 nm, sensor chip C1 is suitable for BioNPs in this work because of its shortest matrix extension from gold surface. Finally, we have compared experimental performance of sensor chip C1 with another popular BIAcore chip, sensor chip SA. The sensorgrams display that binding equilibrium of influenza virus particles at EEL surface is easily reached on C1 chip but not on SA chip.

Surface structure of sensor chip allows single- or multi-channel detection in up to four flow cells (fc), namely fc 1, 2, 3, and 4 according to the BIAcore terminology. Among which

fcs 1 and 3 can be set as the on-line reference cells. The reference cells are used to quantify the non-specific binding without receptors. At the same time, another fc with receptors, a non-reference fc, is chosen to detect multivalent interactions between ligand-coated BioNPs and surface receptors. In such a way, a relative response can be produced by online subtraction of non-specific binding response. This relative response is assumed as experimental data for the specific multivalent interaction.

3.2.1 Immobilization of EEL

The surface of a new sensor chip C1 was washed twice by the freshly prepared buffer (0.1 M glycine-NaOH, pH 12 containing 0.3 % Triton X-100) for 1.5 minutes, at a flow rate of 20 µl / minute prior to receptor immobilization.

After the washing step, 100 µg / ml streptavidin in 10 mM Acetate, pH 5.0 was immobilized on all flow cells by amine coupling kit with HBS-EP+ running buffer for 16 minutes, at a flow rate of 12 µl / minute. The surface was stabilized for two hours under running buffer after streptavidin immobilization. The final amount of EEL immobilized on the sensor chip surface is required rather than the amount of immobilized streptavidin.

EEL immobilization followed streptavidin immobilization after the surface stabilization. The system was primed twice with the new running buffer, 10 mM HEPES (pH 7.5) containing 150 mM NaCl, 0.1 mM $CaCl_2$, and 0.01 mM $MnCl_2$. Then, 1 µg / ml EEL solution were injected only through the none-reference flow cells for 1 minute, at a flow rate of 50 µl / minute. The final result of EEL immobilization was 276.6 RU. By changing EEL solution concentration, another two immobilization surfaces with corresponding response units of 55 RU and 323.6 RU were produced. These three RUs are also defined as the surface capacity, R^{max}, in respect to model simulation later described in Chapter 5. In brief, $R^{max,1}$ = 55 RU, $R^{max,2}$ = 276.7 RU, and $R^{max,3}$ = 323.6 RU. Regarding to the immobilization results of surface EEL, an appropriate immobilization range needs to select because of the limited materials of influenza virus. Considering that a relatively low receptor density is superior in detecting the adsorption kinetics (Myszka 1997), the low density, $R^{max,1}$, is chosen for influenza virus. To be more comprehensive, another two relatively high densities, $R^{max,2}$ and $R^{max,3}$ are used to compare the influence of the receptor density on the adsorption kinetics.

Due to the biological complexity, the repeatability of the EEL immobilization amount between different sensor chips is low. Even the EEL immobilization amount among four flow cells within one chip is difficult to repeat. Alternatively, the repeatability of BioNP adsorption curves at one single surface was focused on rather than that of the receptor immobilization amount by experimental investigations.

3.2.2 Immobilization of Protein A

The first washing procedure of a new sensor chip C1 used in this section is as described in the last section. Running buffer used for the immobilization of Protein A is 10 mM sodium phosphate, pH 7.4, containing 150 mM NaCl, and 0.005 % Tween 20. Protein A was immobilized at the sensor surface using standard amine coupling kit provided by

Biacore. Main immobilization steps of Protein A are depicted in Fig. 3.2. Similar to EEL immobilization, a controlled flow cell without immobilizing Protein A was used as an on-line reference cell.

After the immobilization of Protein A, capacity of receptor surface, R^{max}, was determined by injecting free human IgG solutions. The equilibrium value of human IgG at Protein A surface was then defined as surface capacity, R^{max}. The binding equilibrium can be reached either by changing the concentrations of human IgG solutions or by changing the injection volume of human IgG solutions. Fig. 3.3 illustrates how to decide the equilibrium and to calculate values of surface capacity. Each equilibrium binding was repeated at least once. Surface capacity, R^{max}, for each surface was then calculated as average value of all end points (end response units), marked as crosses in Fig. 3.3. Four surface capacities are determined: $R^{max,a}$ = 53.4 RU, $R^{max,b}$ = 119.7 RU, $R^{max,c}$ = 9561 RU, and $R^{max,d}$ = 9884 RU.

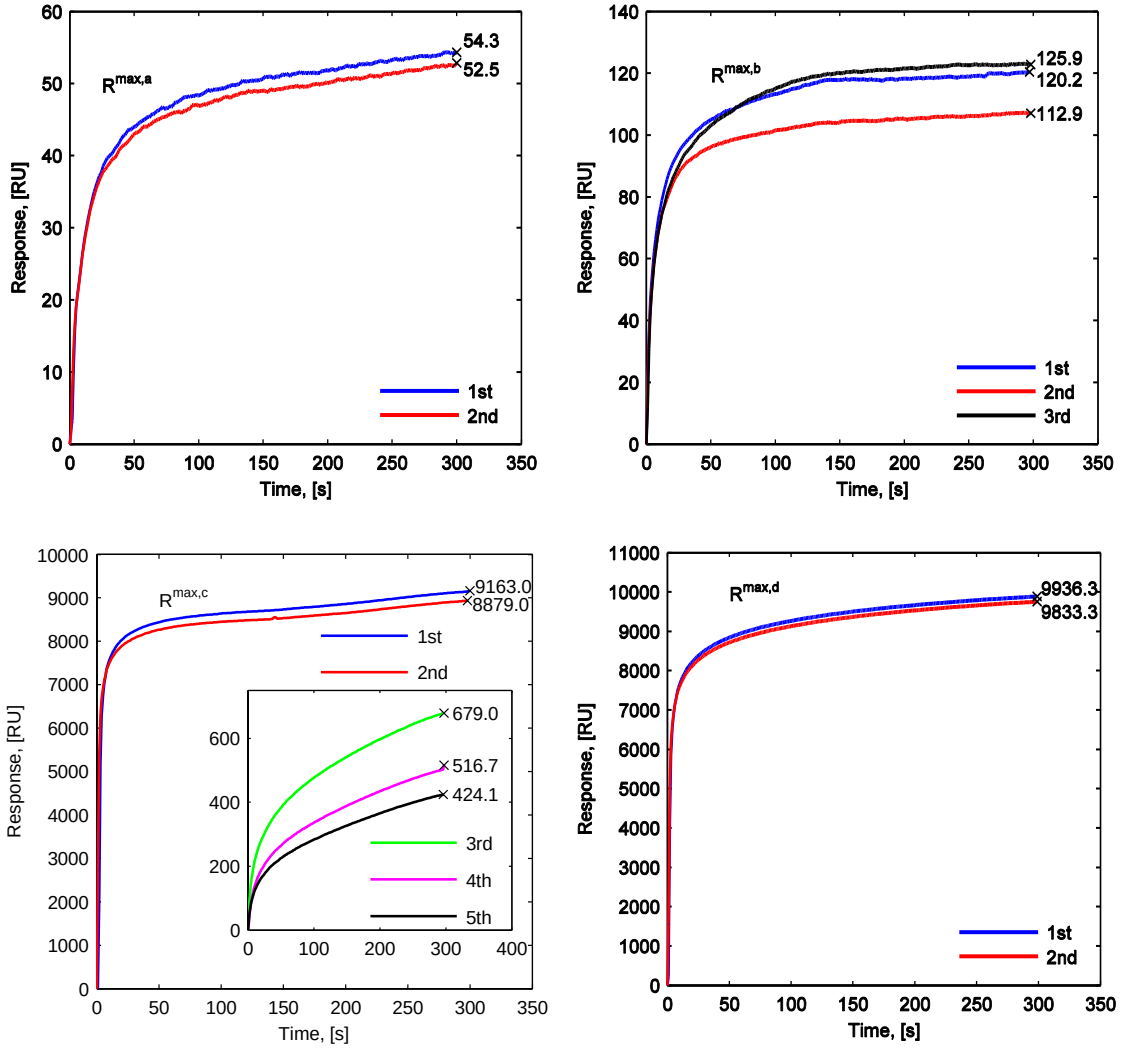

Figure 3.3: Determination of surface capacity of immobilized Protein A, R^{max}, by injection of free human IgG solutions.

Equilibrium was easier to reach with a lower amount of receptors immobilized at the sensor surface, as displayed in Fig. 3.3 that the slopes of curves near the ending period at $R^{max,a}$ and $R^{max,b}$ are lower than those at $R^{max,c}$ and $R^{max,d}$. Thus, For more accurate estimation of the binding capacity of sensor surface with higher amount of receptors, a repeated injection mode of free human IgG in solution without regeneration was employed. The results of such continuous injections is given at $R^{max,c}$. The inset of $R^{max,c}$ (Fig. 3.3) elucidates the three repeated injections of human IgG solutions starting from the ending point of the second injection (see the red line) without regenerations. Therefore, the increasing amount of human IgG following each injection is observed as a RU decrease in the inset. According to observations of curve growth, the horizontal plateau of equilibrium was difficult to reach. The reasons may include a slight protein-protein interaction between humn IgGs due to the high concentration of human IgG solution. Taking the above observation into consideration, the repeated injection was thus stopped after the fifth injection. The value of $R^{max,c}$ was then calculated in such a way that one average between the first two injections was added to the other average among the following three injections. The difference between the first two injections with regeneration in case of $R^{max,d}$ was much smaller than that in case of $R^{max,c}$, which is why this repeated injection mode, the inset of $R^{max,c}$, was not applied to $R^{max,d}$.

3.3 Detection of bionanoparticle interaction by SPR

SPR spectroscopy was applied to detect BioNPs, including natural entity, influenza virus particles, and synthetic entity, human IgG-coated nanoparticles. SPR has been extensively and successfully applied to detect avidity based multivalent interactions (Zhang and Mackenzie 2012, Choi et al. 2013, Reynolds et al. 2013, Silpe et al. 2013, Yu et al. 2013, Li et al. 2014, Varga et al. 2014). Fig. 3.4 illustrates the principle of detection of the interactions of BioNPs with surface receptors with SPR. Generally speaking, SPR technology is based on total internal reflection happening at the interface between glass layer and gold layer. The intensity of the reflected light can be changed due to BioNP interaction with surface receptors. For the details about the signal transformation between light angles and detected response unit (RU), one can refer to the work done by Stenberg (Liedberg et al. 1993). Furthermore, the unit transformation of detected RU into mass unit at the sensor surface can be found in the work performed by Fägerstam (Fägerstam et al. 1992).

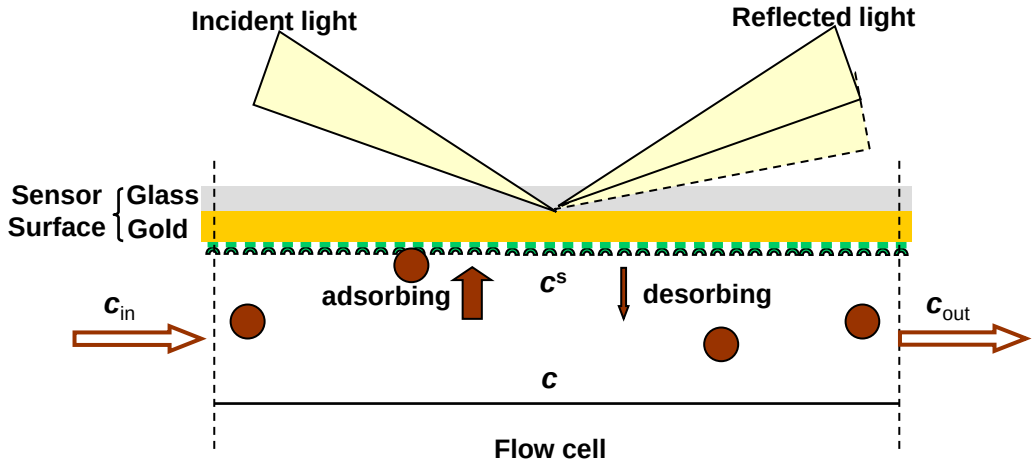

Figure 3.4: SPR detection principle.

Before detections of BioNP interactions with receptors on the surface, a calibration step is only performed to the new surface just after the immobilization of receptors. This step is used in order to minimize the difference between fresh receptor surface without any regeneration and used receptor surface after the regeneration since the receptor surface can be degraded due to non-ideal regenerations. For this purpose, a minor amount of BioNP solution is injected first to bind a small amount of BioNPs to the surface, and then, short time regeneration follows up in order to remove the adsorbed BioNPs. Besides, a blank injection is usually performed between two detections on the same surface for the purpose of analyzing the buffer influence on the binding signal. In this step, only the running buffer is injected through flow cells with flow rate and injection time the same as those used in the measurement step of BioNP interaction.

3.3.1 Detection of influenza virus particles

Fig. 3.5 illustrates four main experimental stages of the detection of influenza virus interactions with surface lectin, EEL: adsorption, desorption, elution, and regeneration. Adsorption and desorption are two critical parts and will be focused on in this section. During the entire detection, one single running buffer is used, 50 mM Tris, pH 7.4, containing 150 mM NaCl, 0.1 mM $CaCl_2$, 0.1 mM $MnCl_2$, and 0.005% tween 20. As previously mentioned in Section 3.2, two flow cells are used at the same time during the detection. As illustrated in Fig. 3.5, one is flow cell (pink curve, Fc) with immobilized receptors and the other is reference cell (blue curve, Rc) without immobilized receptors. The final response units are obtained by online subtracting the signals of Rc from the signals of Fc (black curve, Fc - Rc). Streptavidin-based sub-surface matrix introduced for the EEL immobilization depicted in Section 3.2.1 may interact with influenza virus particles, which would result in the non-specific binding. Therefore, Rc is then used in order to measure the signals caused by the non-specific binding.

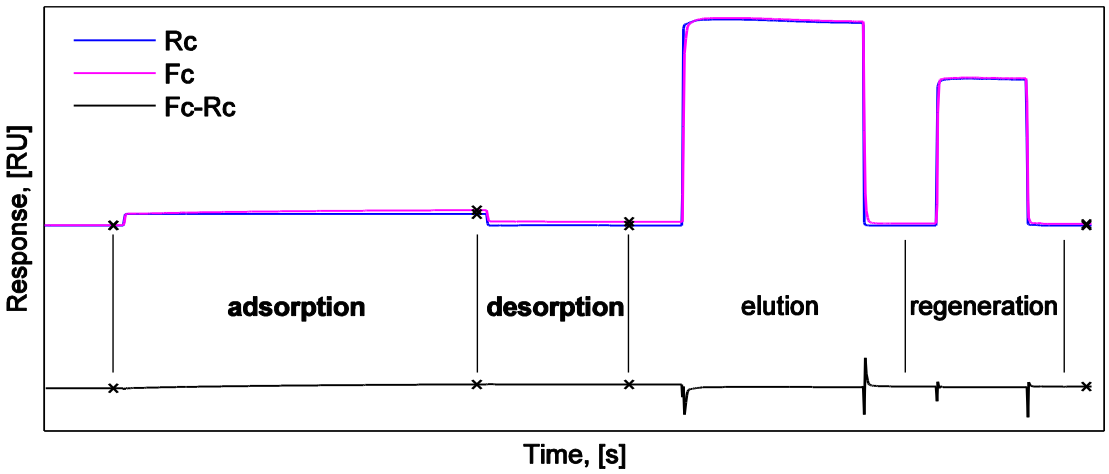

Figure 3.5: Main experimental stages of the detection of influenza virus particles and typical sensorgram monitored by SPR.

Furthermore, the systematic deviations take place easily under the circumstance of low surface capacity, especially at the receptor surface capacity, $R^{max,1}$ (55 RU shown in Section 3.2.1). The previously described step, blank injection, can be also employed in order to analyze the system deviations and to further delete the corresponding response units (Myszka 1999).

Before the injection of influenza virus solution, the stocks of purified influenza virus materials were diluted using the running buffer. Accordingly, five different inlet concentrations of influenza virus particles in the solution, $[P]_{in}$ as listed in Table 3.1, were prepared. After each dilution, influenza virus solution was then immediately injected through Fc and Rc at a flow rate of 50 µl / minute for 6.5 minutes. Each solution was injected three times in order to check the measurement repeatability of the interaction after the regeneration of the adsorbed surface. Fig. 3.6 illustrates the signals of adsorption and desorption recorded by the sensorgrams under the variations of inlet concentration $[P]_{in}$ and surface capacity R^{max} (as the values listed in Table 3.1). At the end of the adsorption, the two-minute desorption immediately followed up by only changing the influenza virus solution into the running buffer with all the other conditions kept constant.

Table 3.1: Inlet concentration of influenza virus solutions and receptor surface capacities.

	1	2	3	4	5
$[P]_{in}$, x 10^9 particles / ml	0.10	1.02	1.42	2.03	5.08
R^{max}, x 10^9 lectins / mm^{2}, [a]	0.24	1.19	1.39		

[a] Concentration in number unit was calculated based on RUs measured in section 3.2.1, molecular weight of EEL (1.4 x 10^5 g·mol^{-1}), and Avogadro constant (6.02 x 10^{23} mol^{-1}).

The elution stage and the regeneration stage in Fig. 3.5 were both performed at a flow rate of 30 µl / minute with the injection time of 6.5 minutes using two different buffers. Both buffers belong to 50 mM Tris buffer, pH 7.4, containing 0.1 mM $CaCl_2$, 0.1 mM $MnCl_2$, and

0.05% tween 20. However, the elution buffer additionally contains 150 mM Lactose and 150 mM NaCl while the regeneration buffer additionally contains 2 M NaCl. After the regeneration, Fc and Rc were rinsed immediately twice with the running buffer in order to remove some residual materials. All of these

By comparing three repeated experiments in Fig. 3.6 (a), the results display that three curves appear almost identical, which is also similar to the results in Fig. 3.6 (b) and (c). However, Fig. 3.6 (d) shows that the curve appear gradually decreasing as the experiment repeated, which is also similar to the results in Fig. 3.6 (e) and (f). The different appearance of curves in Fig. 3.6 (a)-(c) from those in Fig. 3.6 (d)-(f) implies that the BioNP interaction can be relatively easy to repeat when either a low surface capacity of receptors or a low inlet concentration of BioNPs is applied to the experimental measurements of the adsorption kinetics using SPR. Moreover, it indicates that the receptor surface capacity can be gradually degraded under the condition of strong interaction that is difficult to regenerate the adsorbed surface, especially at the high inlet concentration of BioNP (ref. Fig. 3.6 (d), (e) and (f)).

The final attached amount of influenza virus particles at the EEL-immobilized surface has a relationship with the inlet concentration, $[P]_{in}$, and the surface capacity, R^{max}. Fig. 3.6 (b) and (c) elucidate that, at the low surface capacity, $R^{max,1}$, the final response in RU increases when the inlet concentration increases from $[P]_{in,3}$ to $[P]_{in,5}$. Likewise, Fig. 3.6 (d), (e) and (f) display that, at the high surface capacity, $R^{max,2}$, the final response in RU increases when the inlet concentration increases from $[P]_{in,2}$, $[P]_{in,4}$, to $[P]_{in,5}$. Furthermore, Fig. 3.6 (c) and (f) illustrate that, when the inlet concentration ($[P]_{in,5}$) is kept constant, the final response in RU increases as well with the increase of surface capacity from $R^{max,1}$ to $R^{max,2}$. As a conclusion, the attached amount increases with the increase of either the inlet concentration or the surface capacity.

By comparison of the response signals of the desorption part with the adsorption part, Fig. 3.6 (a) displays that the signal decrease resulted from the desorption is so small that it can be almost negligible, which is also valid for all the other figures, i.e., Fig. 3.6 (d) to (f). This statement demonstrates that influenza virus particles have a strong avidity to EEL immobilized surface. Furthermore, parallel decreasing curves are observed in Fig. 3.6 (f), which means that, if the starting points of desorption curves in Fig. 3.6 (f) are put together, the desorption curve can be identical among the repeated experiments. This identical desorption result is also observed in the other five sub-figures, Fig. 3.6 (a) to (e). Therefore, unlike the adsorption, the desorption of influenza virus particles from the EEL-immobilized surface is not influenced by the experiment repeat.

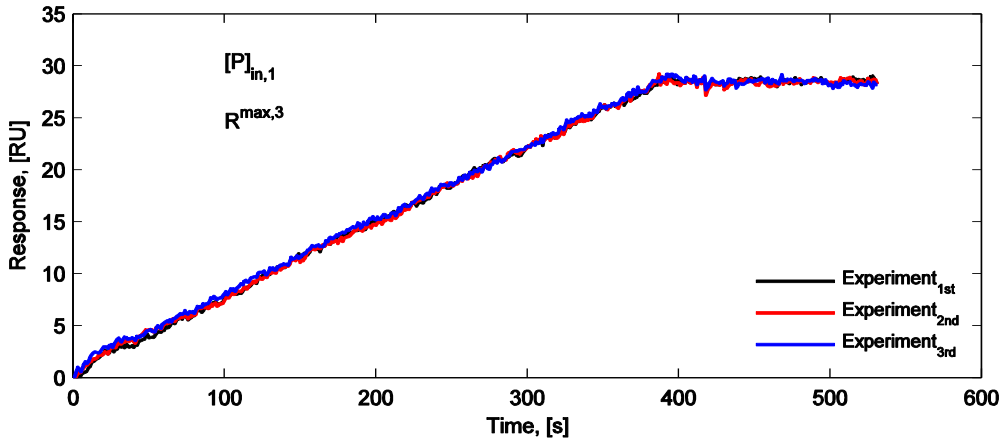

(a)

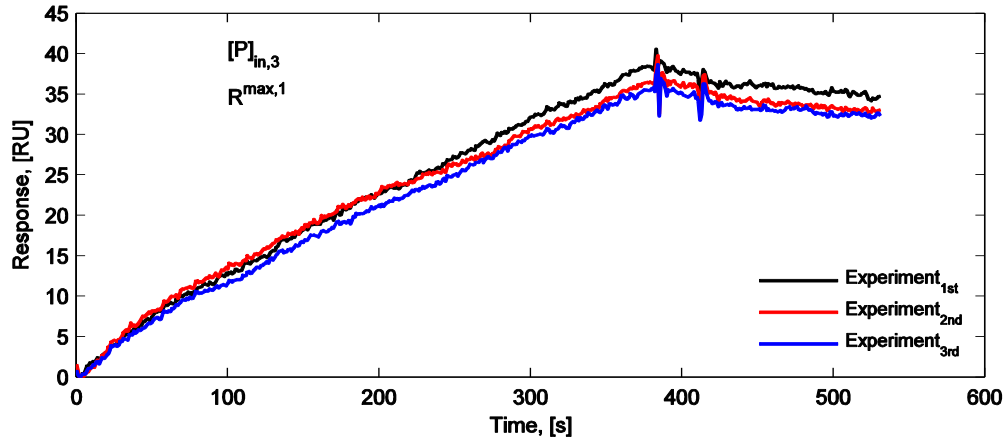

(b)

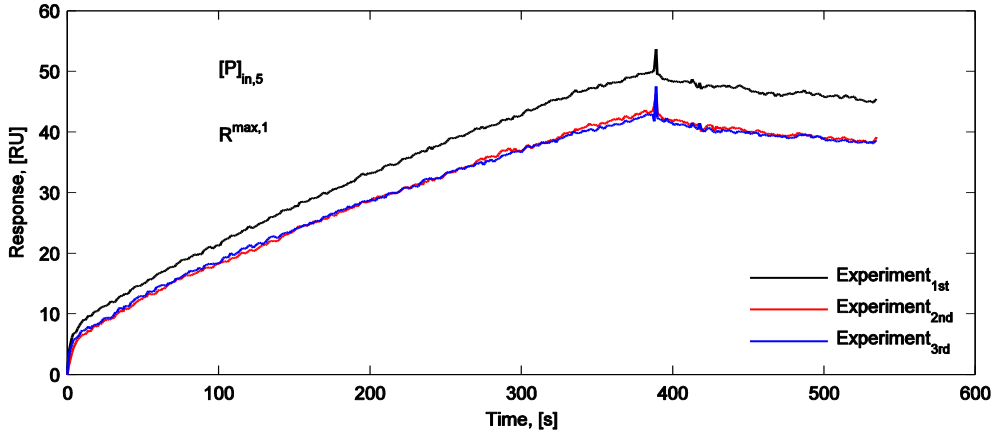

(c)

Figure 3.6: Adsorptions and desorptions of influenza virus particles at the lectin surface.

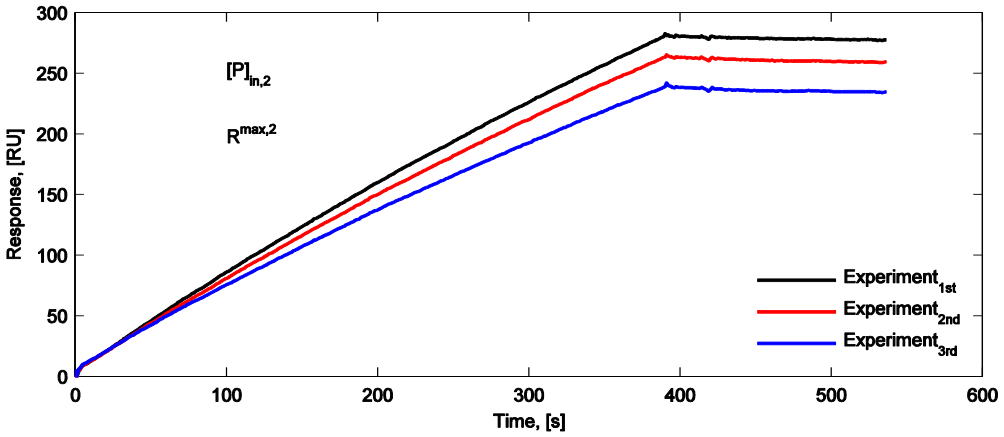

(d)

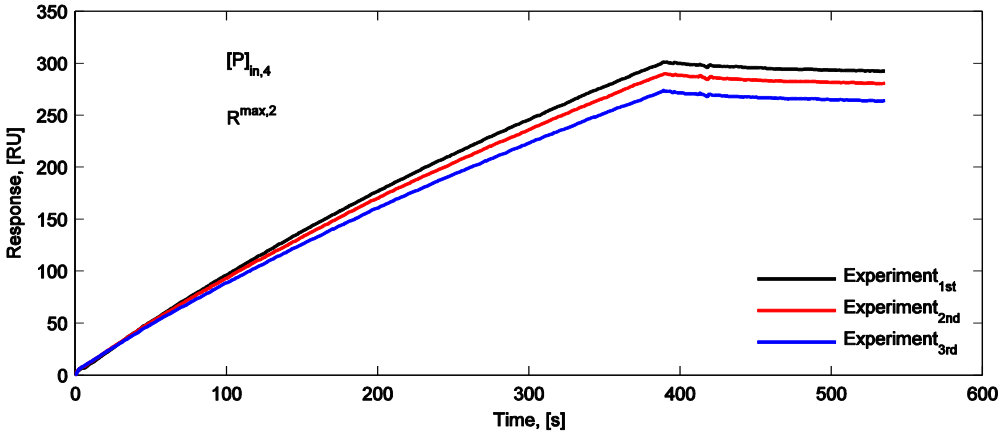

(e)

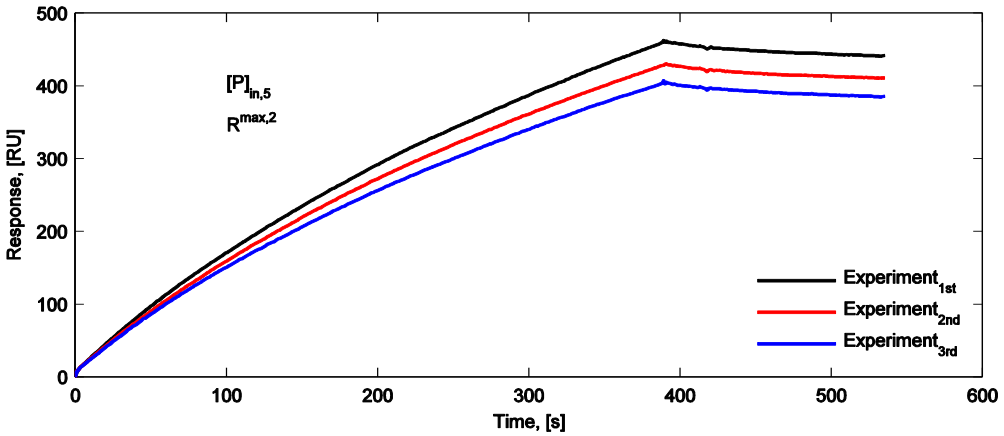

(f)

Figure 3.6: Adsorptions and desorptions of influenza virus particles at the lectin surface.

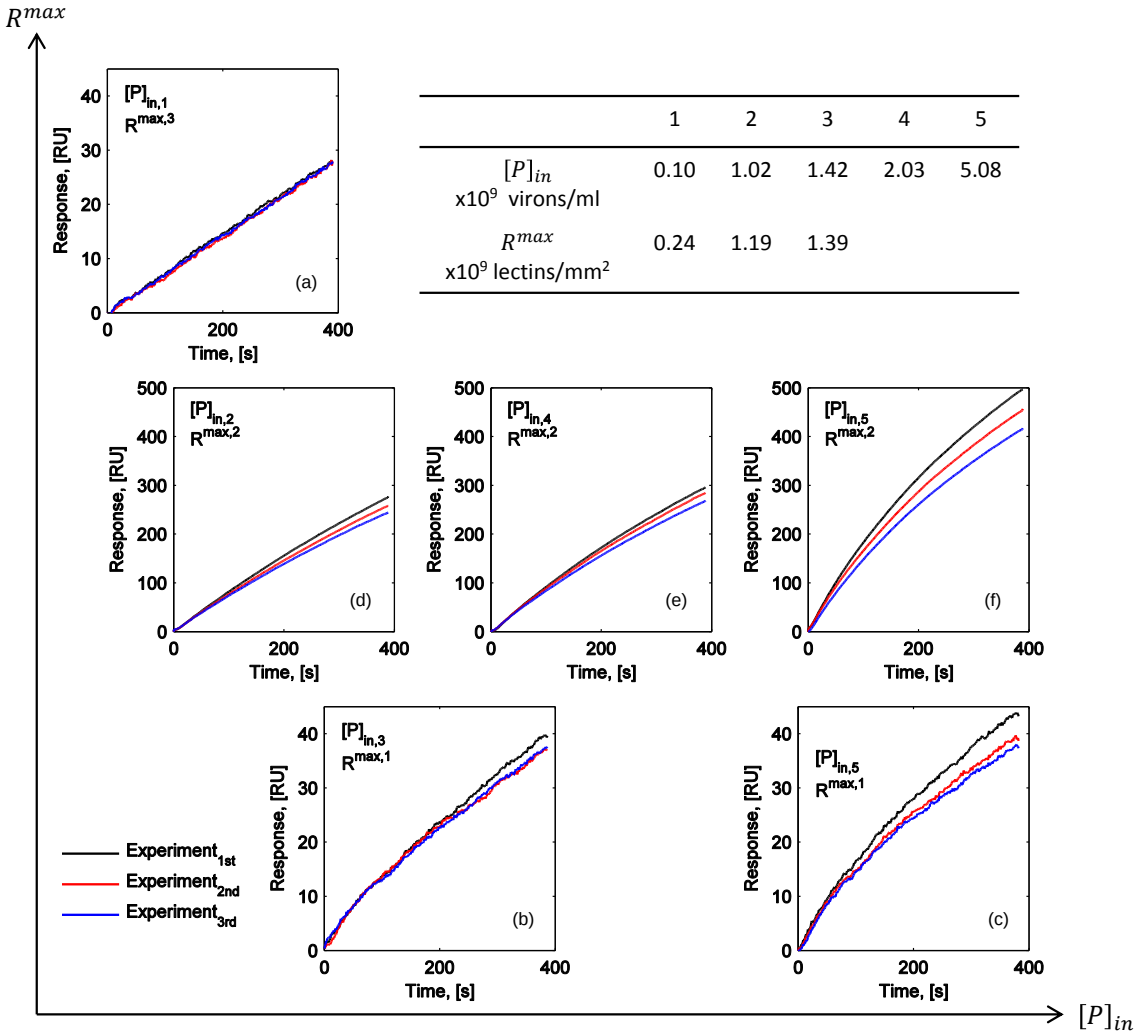

	1	2	3	4	5
$[P]_{in}$ x10^9 virons/ml	0.10	1.02	1.42	2.03	5.08
R^{max} x10^9 lectins/mm^2	0.24	1.19	1.39		

Figure 3.7: Comparison of influenza virus particles adsorption among different inlet concentrations and surface capacities.

In order to better understand both the influence of the inlet concentration and the influence of the surface capacity on the adsorption, the curves in the adsorption parts were further re-plotted in Fig. 3.7. From sub-plots (a), (b), and (c), it displays that, as long as one of these two factors is at a lower condition, the system signal noise becomes stronger. By comparing three plots under the condition of $R^{max,2}$ (ref. the middle panel in Fig. 3.7), one can see that the increase of adsorbed virus amount from $[P]_{in,4}$ to $[P]_{in,5}$ becomes stronger than that from $[P]_{in,2}$ to $[P]_{in,4}$. One fact is that the increase of inlet concentration is slightly different ($[P]_{in,5} \approx 2.5[P]_{in,4}$ where $[P]_{in,4} \approx 2[P]_{in,2}$). In particular, the increase of the adsorption amount with the increase of the inlet concentration is beyond a linear relationship. It indicates that a proper non-linear model will be required to describe the adsorption of BioNPs on the receptor surface. Furthermore, by globally comparing the distance between curves among all six figures, it seems that the systematic degradation due to the non-ideal regeneration of the adsorbed surface becomes stronger

as the inlet concentration increases. Another important observation is that the curvature of adsorption curve becomes bigger when the inlet concentration increases. On the contrary, this observation cannot be clearly obtained with regard to the surface capacity.

With regard to the influence of increasing the surface capacity, R^{max}, by comparing sub-plot (a) with sub-plot (b), although the inlet concentration decreases with an order of magnitude of nearly 3 ($[P]_{in,1} \approx 7 \times 10^{-2} * [P]_{in,3}$), RU responses between two plots are still in the same order of magnitude, because the surface capacity increases with nearly one order of magnitude ($R^{max,3} \approx 6R^{max,1}$). Additionally, by comparing sub-plot (d) with sub-plot (b), although $[P]_{in,2} \approx 7 \times 10^{-1} * [P]_{in,3}$, RU response in sub-plot (d) has one order of magnitude higher than that in sub-plot (b) because $R^{max,2} \approx 5R^{max,1}$. With these evidences, it is argued that R^{max} has a stronger influence on the adsorption than $[P]_{in}$.

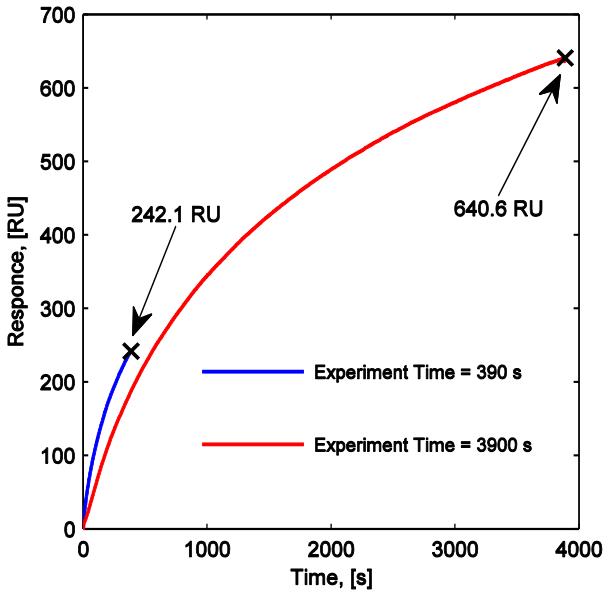

Figure 3.8: Comparison of influenza virus adsorption by changing the time.

The influence of time on the adsorption by keeping all the other experimental conditions constant is displayed in Fig. 3.8. In particular, although the experimental time was extended up to 10 times longer, one can see that the adsorption equilibrium was still not yet reached. Thus, the adsorption of influenza virus on the EEL-immobilized surface was slow. It implies that, in a micro-fluidic channel due to the geometry of the flow cell in BIACore device, the contribution of mass transport to the recorded response signals should be considered. Moreover, it is predictable that the adsorption is far away from the equilibrium status within the time of 6.5 minutes.

3.3.2 Detection of human IgG – coated bionanoparticles

Fig. 3.9 shows three main procedures for detecting the interactions of human IgG-coated nanoparticles at Protein A immobilized sensor surface: adsorption, desorption and

regeneration. In the same way as before, two flow cells were simultaneously applied to the sample solution. One had a sensor surface with Protein A immobilized (Fc) and the other had no Protein A (Rc). The final useful response was obtained by subtracting RUs in Rc from those in Fc. It can be seen that in the adsorption the sensor surface with Protein A gives out a clear increasing curve (see the pink curve in Figure 3.9) while the reference surface without Protein A gives a linear line (see the blue curve in Figure 3.9). It demonstrates that the established experimental system here is suitable to detect the multivalent interaction.

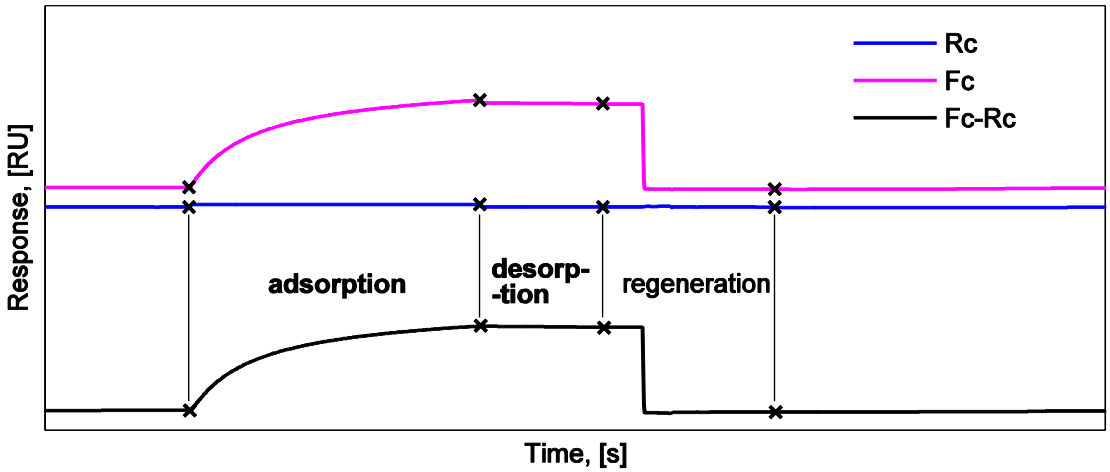

Figure 3.9: Main experimental stages in the detection of human IgG-coated nanoparticles and typical sensorgram monitored by SPR.

With regard to experimental conditions, the injection flow rate was 50 µl / minute and the injection time for adsorption part was 6.5 minutes. Running buffer here was 10 mM sodium phosphate, 150 mM NaCl, 0.005% tween 20, pH 7.4. The desorption was then performed by injecting running buffer through flow cells. After the desorption, the covered surfaces were regenerated by 0.1 M glycine pH 2 at a flow rate of 50 µl / min with a time of 30 seconds. After the regeneration, another blank injection using running buffer was followed at 50 µl / min, 6.5 minutes. Each experiment of bionanoparticle solution was repeated at least once.

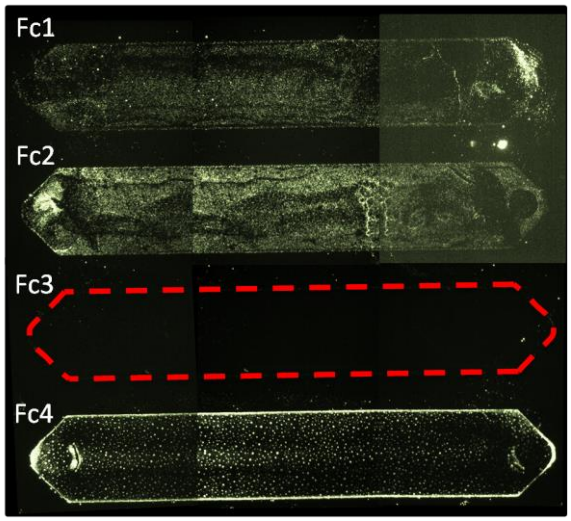

Figure 3.10: Microscopic pictures of human IgG-coated nanoparticles on each surface of four flow cells.

One advantage by using synthetic BioNPs is that the difference between surface with binding and surface without binding can be clearly identified with the help of fluorescence materials imbedded in polystyrene nanoparticles. As an example, Figure 3.10 shows one combined microscopic photo for an entire surface of one sensor chip. As mentioned already, one sensor chip has four flow cells, namely, Fc1, Fc2, Fc3, and Fc4. Here, Fc3 was the reference cell without Protein A immobilization while the other three was binding cells with Protein A immobilization. Therefore, after several repeated adsorptions the surface area of Fc3 is still black without luminescence under light condition and all the other three shows interesting distributions. Since this photo of the sensor was taken after the sensor was stored for about a week, it can only give a qualitatively estimation. The surface capacity of Fc2 is bigger than Fc1, and, thus, Fc2 seems more lighter than Fc1. Fc4 together with Fc3 have been injected for more than 10 runs. It is interesting to see that after the final regeneration, there are still lighted particles at the surface. This explains one reason for surface degradation due to inefficient regeneration.

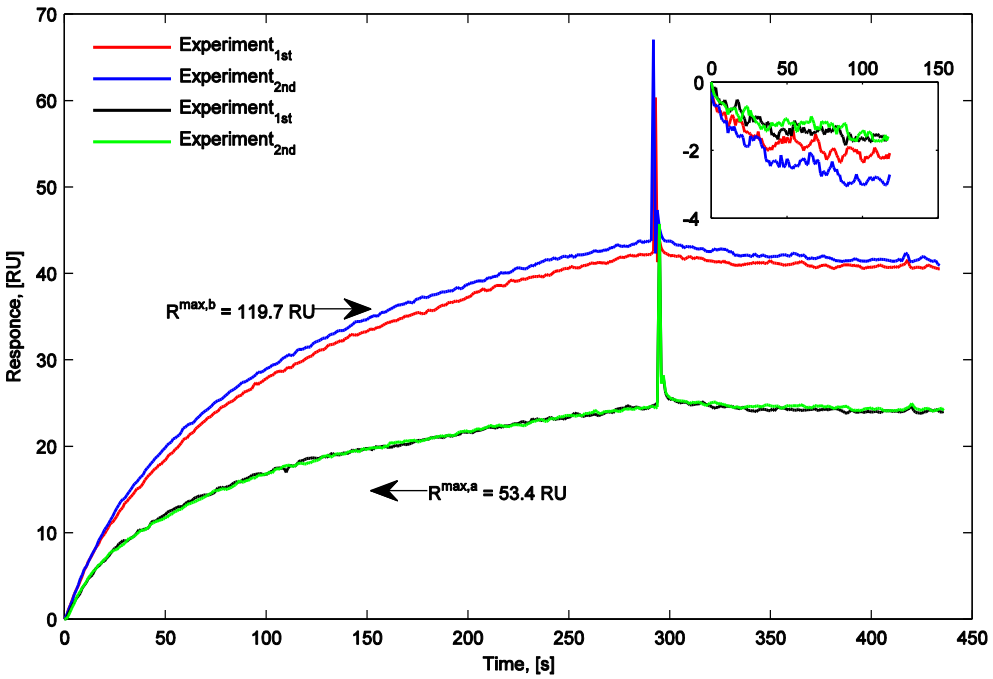

Figure 3.11: Comparison of adsorption and desorption of BioNP1 at two different surfaces $R^{max,a}$ and $R^{max,b}$. Curves in the inset are only desorption parts by putting starting points together.

Figure 3.11 shows the RU response of adsorption and desorption of BioNP1 (see Table 2.2) at two surfaces, $R^{max,a}$ and $R^{max,b}$. The adsorption curve increases with the increase of surface capacity from $R^{max,a}$ to $R^{max,b}$. With respect to the repeatability, similar to influenza virus adsorption, the curve of repeated experimental run descends when the surface capacity increase. One can see this descending by comparing the red curve in the second run with the blue curve in the first run at $R^{max,b}$. On the contrary, the repeatability at $R^{max,a}$ is good.

In order to better understand the desorption interaction, the desorption parts at two receptor surfaces ($R^{max,a}$ and $R^{max,b}$) were compared again as plotted in the inset of Fig. 3.11. On the contrary to the obvious differences of the adsorption curves between two receptor surfaces, the desorption appeared to behave nearly in the same way. Because the desorption curves were shown to stay closely to each other in comparison with the big distances between adsorption curves due to change of surface capacity. Besides, from the y-axis values, one can see that the decrease amount was very small to be almost negligible. It can be concluded that surface capacity has no influence on the desorption. It indicates that the avidity of human IgG-coated nanoparticles to Protein A immobilized surface is very strong.

So far, it seems that, by keeping the ligand density at the BioNP surface constant, the adsorption rate will change clearly with the increase of the receptor density but the desorption rate will respond nearly nothing to it. Especially the noise level of SPR detection can be comparable with the signal changes of multivalent desorption in the low range of receptor density (see $R^{max,a}$ and $R^{max,b}$ in the inset of Fig. 3.11). However, one may argue if these observations will be still obtainable at the high receptor density relative

to surfaces $R^{max,a}$ and $R^{max,b}$. Therefore, in order to enlarge the understanding horizon about the impact of the receptor density on the binding kinetics, in addition to the low surface capacities $R^{max,a}$ and $R^{max,b}$, the high surface capacities $R^{max,c}$ and $R^{max,d}$ were also applied in order to compare adsorption and desorption. Figure 3.12 shows interactions of BioNP4 at these two surfaces, respectively.

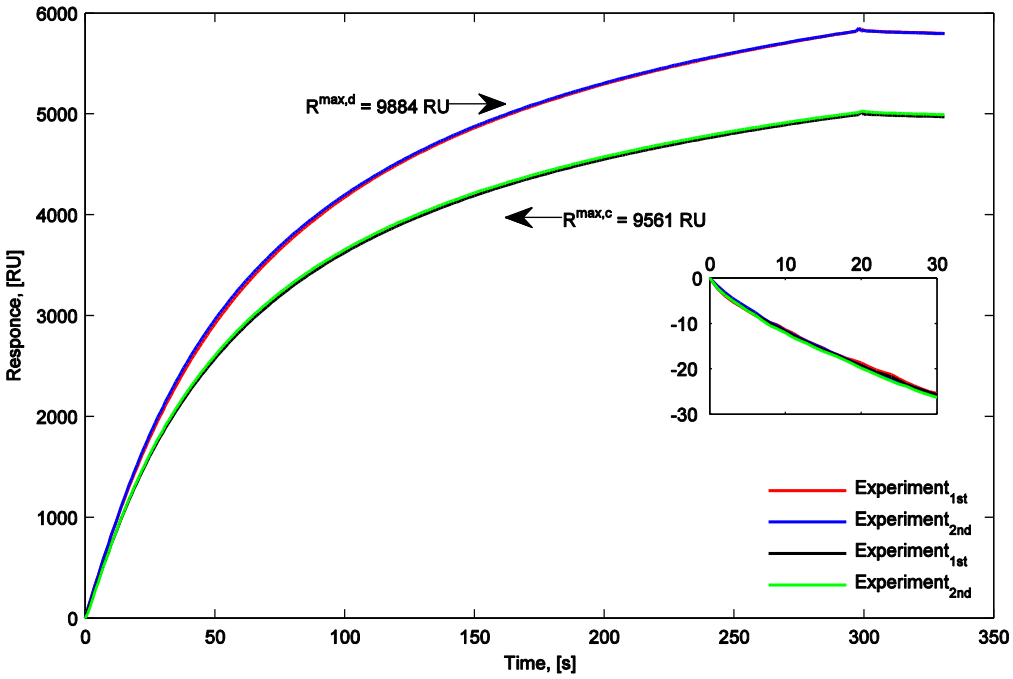

Figure 3.12: Comparison of adsorption and desorption of BioNP4 at two different surfaces $R^{max,c}$ and $R^{max,d}$. Curves in the inset are only desorption parts by putting starting points together.

Fig. 3.12 shows again that the RU response increases with the increase of surface capacity from $R^{max,c}$ to $R^{max,d}$. With regard to the repeatability, it is interesting to see that the repeated curves are very close to each other for both surfaces. This is different from the difference at $R^{max,b}$ surface in Figure 3.11. Besides, different from the bad repeatability in case of high surface capacity for detecting influenza virus particles as seen from sub-plot (a) to (f) in Figure 3.6, there is no apparent surface degradation for the synthesized interactions. It seems that the regeneration method here is sufficient enough to recover the bound surface receptors within certain ranges. From the here presented plots, the ranges may depend on the number of experimental runs and the number of receptors immobilized at the sensor surface. The better repeatability also indicates another advantage that the synthetic NPs, human IgG-coated particles, are more resistant to the harsh regeneration condition than the nature NPs, influenza virus particles.

Concerning the desorption of BioNP4 at the $R^{max,c}$ and $R^{max,d}$ surfaces, the inset of Figure 3.12 shows that the curves are almost identical for repeated experiments at both surfaces. Again, it demonstrates that surface capacity play a negligible role in the desorption. Besides, by comparing the y-axis values between Fig. 3.11 and Fig. 3.12, the

desorption amount at the high receptor density here was bigger than that at the low receptor density.

Combining BioNP1 at low surface capacity in Figure 3.11 and BioNP4 at high surface capacity in Figure 3.12, some further discussions can contribute to a more comprehensive understanding of the multivalent interactions. According to Table 2.2, BioNP1 and BioNP4 have the same characteristics. The signal noises appear to influence the RU signals at the low surface capacity whereas they seem to disappear at the high surface capacity. It seems that the repeatability of human IgG-coated BioNP is better at the high surface capacity than at the low surface capacity. The adsorbed amount in RU goes always up with the increase of surface capacity.

Another advantage by applying the synthesized BioNP is that ligand density on top of BioNP surface can be investigated, except for particle concentration and surface capacities. This helps to further study the functionality of nano-scale materials in many fields, e.g., smarting targeting (Mahon et al. 2012, Friedman et al. 2013, Zern et al. 2013), immune therapy (Gu et al. 2012, Hartwell et al. 2015), and etc. Figure 3.13 displays the interactions of BioNP1, BioNP2, and BioNP3 at the surface of $R^{max,b}$. Table 2.2 shows that the ligand density increases from BioNP1, BioNP2, and BioNP3. Concerning the RU signals in the adsorption period, they grow up with the increase of ligand density. Furthermore, the increase amount by increasing the ligand density from the mono-layer coating to the non-mono layer coating is bigger than by doing so within the non-mono layer coating. The evidence is to compare the distance difference among the black curves, red curves and blue curves. The repeatability is acceptable reasonably as the repeated experimental curves stay close to each other.

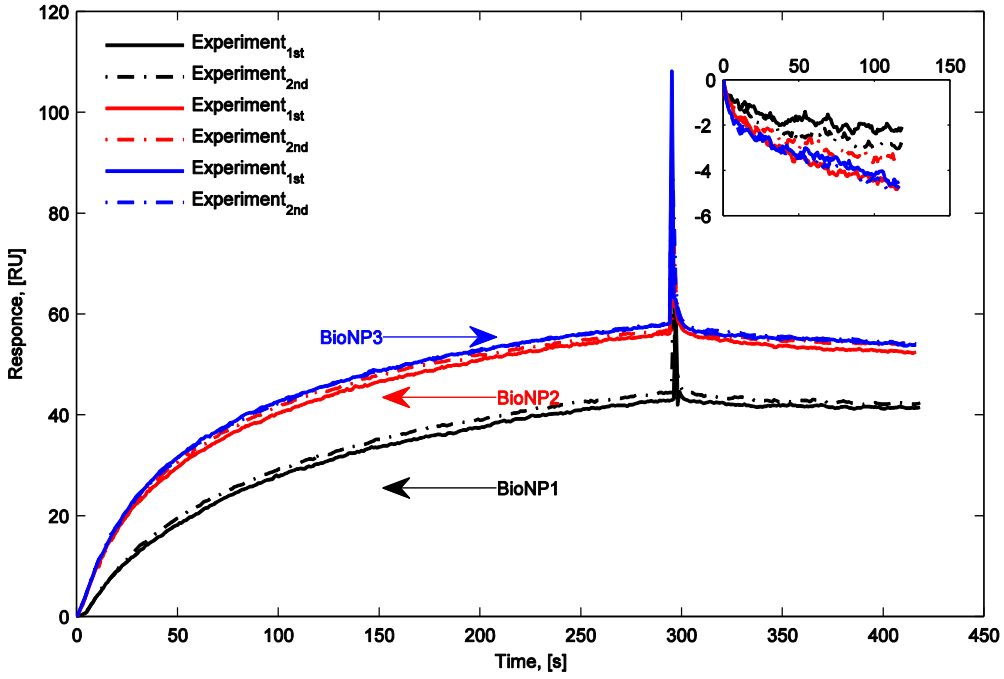

Figure 3.13: Comparison of adsorption and desorption of BioNP1, BioNP2, and BioNP3 at $R^{max,b}$ surface. Curves in the inset are only desorption parts by putting starting points together.

The desorption parts after the needle jumps at the end of adsorption injection seem to have the parallel lines. For a better comparison of desorption curves, the inset in Figure 3.13 displays the desorption parts of all these three BioNPs. It is interesting to see that their desorption curves were apparently analogous. Similar to the resistance of desorption to surface capacity, it appears that ligand density plays a tiny role in the desorption as well. It implies that the avidity resulted from the multiple bonds is so strong that the adsorbed particles will be difficult to desorb away from the surface receptors provided that no regeneration conditions are applied.

As a short summary by comparing the changing magnitude between adsorption and desorption from Fig. 3.11, Fig. 3.12 to Fig. 3.13, one can see that the desorption amount was at least two orders of magnitude smaller than the adsorption amount. It has been pointed out that the great kinetic advantages of the multivalent interaction compared to the monovalent interaction results from the slow desorption of the multiple ligands of the individual BioNP, e.g., the increased avidity of the multivalent binding thanks to the reduced desorption rate (Chittasupho 2012, Choi et al. 2013). Furthermore, the desorption amount did not respond to the density variation of either surface receptor or BioNP ligand while the adsorption amount was sensitive to both of them. It implies that, for the two interacting partners, after the steady establishment of one part, the bound BioNPs can resist the negative effects from the density uncertainty of the other part, which benefits from the multivalence. At least in the here presented range of bonds in hundreds the bound BioNPs keep stably staying at the functional place. Also, Silpe *et al.* suggest that, under the condition that the ligand density is sufficiently high, changes of the receptor density play a negligible role in the binding kinetics of dendrimer conjugate.(Silpe et al. 2013) The mentioned implication can be helpful to the nanomedicine development, especially for controlling the contacting time of the adsorbed functional materials at special cell surfaces. One preliminary condition for the multivalent interaction to possess the resistance advantage is that the number of bonds formed between one single BioNP and the surface receptors should reach an efficient number and it is a question to each particular interaction in biological systems.

3.4 Summary

The multivalent interaction can be experimentally established in this chapter based on SPR technology. EEL and Protein A, two types of receptors, were immobilized satisfactorily at the sensor surface with the help of amine coupling kit in Section 3.2. For EEL-immobilized surface, there were three surface capacities and for Protein A surface, there were four surface capacities. In such way, the influence of surface capacity on the adsorption kinetics can be studied. The results show that the signal noises appear in the detected RU curves at the low surface capacity. In case of influenza virus particles, the repeatability becomes better by decreasing the surface capacity. However, this result does not exist in case of human IgG-coated nanoparticles. Furthermore, the detection of influenza virus elucidates that surface capacity will influence the adsorption kinetics stronger than particle concentration. From the study of influenza virus concentration, it is learned that the curvature of adsorption curve will be increased with the increase of

particle concentration. But this increase of curvature is not clear by increasing the surface capacity.

Human IgG-coated nanoparticles synthesized in Chapter 2 were applied successfully to repeatedly detect multivalent interactions in Section 3.3.2. The results show that adsorption amount in RU increases by increasing either surface capacity or ligand density. Besides, it seems that the influence of surface capacity in the low range on the adsorption kinetics is stronger than that in the high range. This difference with respect to range may also be the same as for the ligand density because the RU signals were shown to increase bigger from BioNP1 to BioNP2 than those from BioNP2 to BioNP3. Contrary to adsorption, desorption appears not to respond to changes of either surface capacity or ligand density.

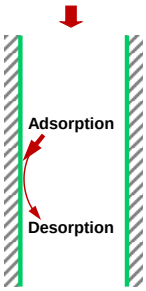

Chapter 4

Detection of the adsorption process in an affinity membrane adsorber

In this chapter the adsorption process of bionanoparticles (BioNP) through affinity membrane adsorbers is measured using liquid chromatography (LC). The applied BioNPs are prepared in Chapter 2. The affinity membrane adsorber (AMA) will be prepared in this chapter. Fig. 4.1 shows the two main components of the detected adsorption process, BioNPs and the affinity membrane adsorber.

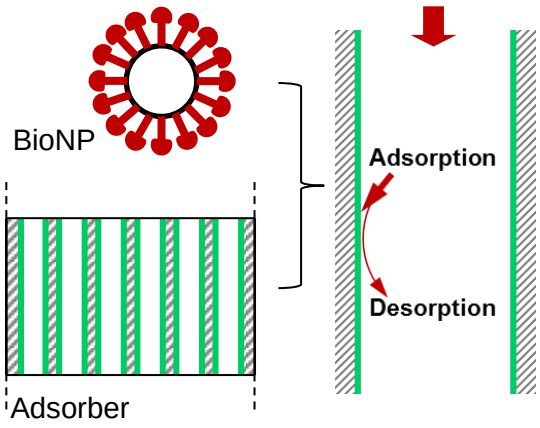

Figure 4.1: Sketch of two interacting partners. BioNP is the biological nanoparticle prepared in Chapter 2, where the red color denotes the ligand, human IgG. Adsorber is the affinity membrane adsorber (AMA) prepared in this chapter, where the green color denotes the receptor, Protein A.

In Fig. 4.1, the inner pore surface of the adsorber is immobilized with the receptors, Protein A, corresponding to the ligands, human IgG of BioNPs. On the inner pore surface of the adsorber, BioNPs will interact with the receptors, including adsorption and desorption. The interaction will be detected using the UV-Vis spectroscopy in the LC system (Äkta basic 100 system). In the following, the used materials will be introduced first, and then the preparation of AMA will be described. Finally, the prepared AMA will be detected with regard to the dispersion effect and the adsorption chromatogram of BioNPs.

The affinity membrane adsorber that is composed of porous membranes immobilized with functional receptors is superior to the bead-based chromatography in many aspects. For instance, Boi etc. have shown advantages of a type of membrane adsorbent for capturing human IgGs, including high binding capacity, good selectivity, high recoveries, high tolerance, and no ligand leakage.(Boi et al. 2011)

4.1. Materials

BioNP are prepared in Chapter 2. Sartobind MA75 C is used as the basic adsorber for the immobilization of Protein A, which was purchased from Sartorius Stedim Biotech GmbH, Goettingen. Protein A was purchased from Biozol, Germany. Amine coupling kit, including EDC, NHS, and ethanolamine hydrochloride-NaOH, was purchased from GE Healthcare Bio-Sciences AB, Sweden. All the other chemicals for preparing buffers were purchased from Sigma-Aldrich Chemie GmbH, Germany.

4.2. Immobilization of receptors in the membrane adsorber

The important technical data of the basic adsorber are: membrane diameter (25 mm), bed height (4.0 mm), bed volume (2.1 ml), porosity (0.8) and pore size (about 3 to 5 µm). The carboxylic groups existing at the inner pore surface of the basic adsorber, Sartobind MA75 C, are coupled to the primary amine groups of Protein A by the carbodiimide reaction, as the main reaction shown in Fig. 3.2, Chapter 3. Likewise, the three main steps in Fig. 3.2 were used to immobilize Protein A here. The first step is diluting 750 mg EDC and 115 mg NHS in 10 ml Milli-Q water and then letting the solution flow through the adsorber automatically drop-by-drop due to its gravity under 4 ^{o}C, overnight. The second step is diluting 5 mg Protein A in 10 ml buffer (10 mM sodium phosphate, 150 mM NaCl, pH 7.4) and then letting the solution flow through the activated adsorber in the same way as in the first step. The last step is blocking the unreacted sites by letting 3 ml 1 M ethanolamine hydrochloride – NaOH pH 8.5 flow through the adsorber automatically drop-by-drop due to its gravity under room condition. The immobilized amount of Protein A is roughly calculated as about 1.8 mg with the help of UV-Vis measurements, Tecan infinite 200Pro. For the further calculation of the receptor concentration per solid volume in the AMA, a 10% percentage of this amount was approximately taken. Finally, it is estimated that the concentration of immobilized receptors per solid volume in the AMA was about 0.1 mg/ml, which is also named as the receptor capacity of the AMA for the modeling

simulation later in Chapter 6. The calculation is based on the difference between the original amount of Protein A before immobilization and the amount of unreacted Protein A after immobilization.

4.3 Detection of adsorption chromatograms by Liquid Chromatography (LC)

Fig. 4.2 shows one typical chromatogram of BioNPs detected by the LC system (Äkta basic 100 system, GE Healthcare). BioNP4 prepared in Chapter 2 is detected here. Four main procedures are applied: loading BioNPs, washing away unbound BioNPs, eluting bound BioNPs, and re-equilibrating AMA. The injection speed is 1 ml/min and one column volume (CV) is 2 ml according to the technical data of the adsorber. The washing volume, the eluting volume, and the re-equilibrating volume are 5 CV, respectively.

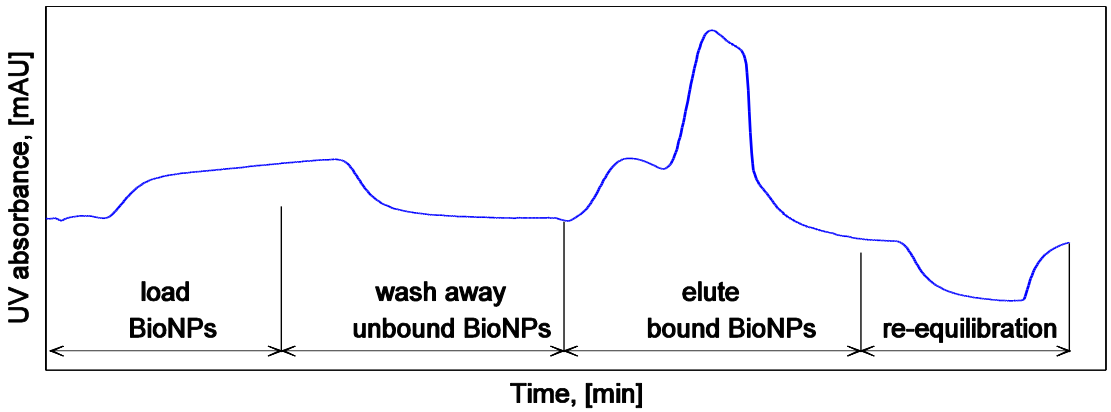

Figure 4.2: One typical detected chromatogram of BioNPs through AMA together with the main experimental procedures.

BioNP4 is prepared in the buffer, 10 mM sodium phosphate, 150 mM NaCl, pH 7.4. This buffer is also used as running buffer, washing buffer and re-equilibrating buffer in order to avoid changes while performing the chromatography. The elution buffer is 0.1 M glycine/HCl, pH 2.8. In Fig. 4.2, the UV absorbance in the loading step is increased due to the BioNPs. In the washing step, only the washing buffer without BioNPs is injected through AMA, and thus the UV absorbance decreases. In the following elution step, the elution buffer is injected which causes peaks showing the eluted BioNPs. After elution, the re-equilibrating buffer without BioNPs is applied, which results in the decrease of the UV absorbance again.

4.3.1 Detection of dispersion effects

Although there is no adsorption between particles and the adsorber due to the disappearance of ligands or receptors, the concentration distribution of particles inside the

adsorber can still spread along the adsorber axis. When there is no adsorption, the spreading of the particle breakthrough curve can result from the non-ideal flow patterns in the fluidic system, such as channeling, recycling, or forming stagnant regions. In particular, the volume of the here-prepared adsorber is relatively small (2 ml), and it is predictable that the influence of the non-idealities on the breakthrough can be strong enough to play a role in the detected adsorption signals of BioNPs to AMA. Therefore, a dispersion model needs to be developed in order to account for the effects of the axial spreading caused by non-ideal flow patterns, i.e., the dispersion effects, on the breakthrough behavior of the interacting BioNPs. To identify the proper dispersion model, the associated experimental data are obtained first in this section. Due to the limited volume of NP and BioNP materials, the pulse response experiment is performed. A short input with an injection of 500 μl sample is applied to all detections in the following figures.

The dispersion effects not only from the LC system (by setting the column by-pass) but also from the adsorber (by setting the column connected) are detected. For example, in the detection case of Fig. 4.3 the basic adsorber without immobilized receptors is connected to the LC system, while in case of Fig. 4.4 it is not connected to the system. The main purpose is to check the time difference of the breakthrough point because of the absence of the adsorber. This is important to the study of the residence time distribution, which will be discussed later in Chapter 6.

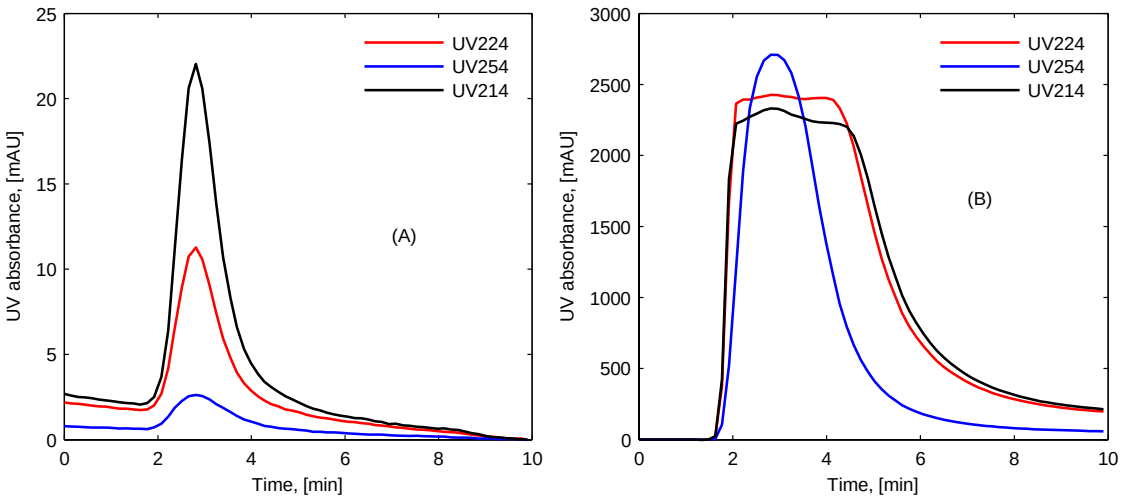

Figure 4.3: Breakthrough curves of NPs without ligands through the adsorber without receptors. (A) Concentration of the inlet NP solution is about 3.4 x 10^9 particles/ml and (B) Concentration of the inlet NP solution is about 3.4 x 10^{12} particles/ml.

Fig. 4.3 shows the breakthrough curves of nanoparticles (NPs) without attached ligands through the basic adsorber without immobilized receptors. Two different inlet concentrations of the NP solutions were detected, about 3.4 x 10^9 particles/ml in Fig. 4.3(A) and about 3.4 x 10^{12} particles/ml in Fig. 4.3(B). Three different wavelengths are used to measure the light absorbance of NPs. The results show that the wavelength influences the absorbance signals in the low range of inlet concentration (see three different peaks in Fig. 4.3(A)) while in the high range the signal peaks make no big

differences in the height (see Fig. 4.3(B)). However, one may still argue that in Fig. 4.3(B) the peak at the wavelength of 254 nm reaches a highest point whereas peaks at 224 nm and 214 nm have a kind of plateau. In comparison, there was no such difference in Fig. 4.3(A). It reflects that the light signals at the lower wavelength are more sensitive to the solution concentration. The signal peaks are higher in Fig. 4.3(B) because the inlet concentration is higher. In addition to the comparison of peak height, the width of the peaks is also influenced by the inlet concentration. The peaks in Fig. 4.3(B) appear wider (in a time lasting about 4 minutes) than those in Fig. 4.3(A) (about 2 minutes) because the NP solution measured in Fig. 4.3(B) has a higher inlet concentration than that in Fig. 4.3(A) under the condition of the same injected volume. It shows that more NP amount brings a longer lagging tail to the breakthrough curve. Furthermore, it seems that the inlet concentration has a negligible influence on the breakthrough of the NP solution. The breakthrough of NP in Fig. 4.3(A) and (B) started both at the time point around Minute 2, at least in the here presented concentration difference with an order of magnitude of three.

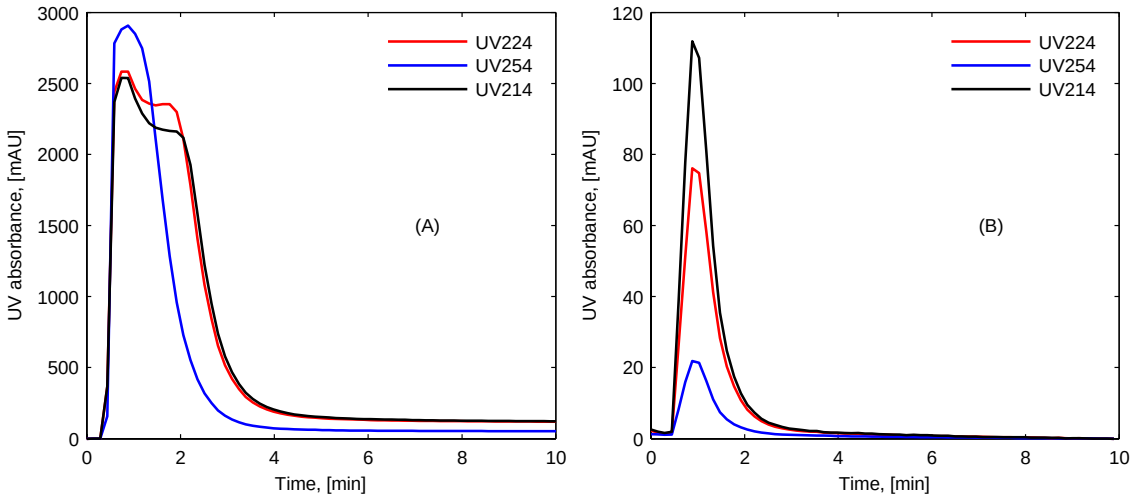

Figure 4.4: Breakthrough curves of particles in the LC system without adsorber. (A) The detected particles are NPs without ligands with the inlet concentration of 3.4 x 10^{12} particles/ml and (B) the detected particles are BioNPs with ligands with the inlet concentration of 2 x 10^{6} particles/ml.

Fig. 4.4 shows the influence of ligands on the breakthrough of particles in the LC system with the adsorber disconnected. The particles measured in Fig. 4.4(A) are not coated with ligands while those in Fig. 4.4(B) are BioNP coated with ligands. By comparing the time point when particles start breakthrough in both figures (around at minute of 0.5), the ligand-coating layer added to blank particles can have a negligible influence on the breakthrough point. One may argue this conclusion by noticing that in addition to the difference in ligand there is another difference in the inlet concentration between the two figures (see caption in Fig. 4.4). But the results in Fig. 4.3 show that the concentration has a negligible effect on the breakthrough point. It reflects that the size difference due to the coating layer (from 110 nm to 144.8 nm, see Table 2.2 in Chapter 2) is not big enough to influence the flow behavior of particles. The height and width of the

peaks in Fig. 4.4 change similarly to those in Fig. 4.3, which result from the difference of the inlet concentration. Therefore, the experimental data attained by using uncoated NP samples can be applied to study the dispersion model for BioNPs that are coated with ligands, which will be shown in Chapter 6.

So far, the ligand coating layer, the inlet concentration of particles, the absence of the basic adsorber, and the LC system have been detected with regard to the breakthrough curve. Another important factor, the receptor, is still waiting to be detected in order to check if the receptor immobilization to the basic adsorber will influence the breakthrough curve or not. Fig. 4.5 displays the breakthrough curves of uncoated NPs without ligands flowing through AMA with immobilized receptors. To improve a further comparison among Fig. 4.3, 4.4 and 4.5, the dimensionless plots are made in Fig. 4.6 and Fig. 4.7, respectively. It helps us to get rid of the dimensional influence from the detected experimental data and to compare the dispersion effects, i.e., the broadening of the breakthrough curves, under different conditions. For example, Fig. 4.5 shows that the peak in the repeated experiment has different height, although one wavelength of light was applied with all the other conditions kept constant. However, the dimensionless figures later (see Fig. 4.6(C) and Fig. 4.7(c)) illustrate that this height difference will disappear by transforming the experimental data to the dimensionless one. Fig. 4.5 manifests a breakthrough point at a time point closer to Minute 2 than that of Fig. 4.3(A), which means that the immobilization of the receptors can result in a delayed breakthrough point. It may be because the inner pore size of the basic adsorber becomes narrower due to the spatial occupation of immobilized receptors, which can hinder the flowing of particles through inner pores.

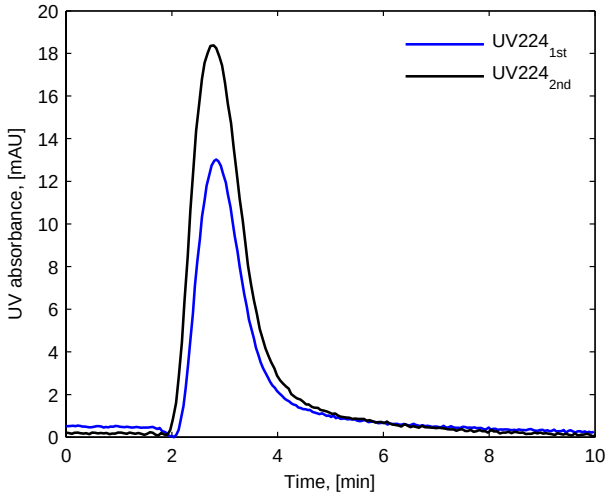

Figure 4.5: Breakthrough curves of NPs without ligands through AMA with receptors. The inlet concentration is about 3.4 x 10^9 particles/ml.

Before comparing the dimensionless plots for different breakthrough examples, their corresponding residence time of particles is first shown in Table 4.1. The presented

residence time is averaged based on three values for each experimental example and is calculated based on the following formula:

$$t_{residence} = \frac{\sum_i t_i \times c_i}{\sum_i c_i} \tag{4.1}$$

where c_i is the concentration of particle solution at time point t_i [min] and can be seen as the detected UV absorbance signal, [mAU].

The residence time results of Fig. 4.3(A) and 4.3(B) in Table 4.1 elucidate that a higher inlet concentration can increase the residence time of particles, which fits to the previous statement that the breakthrough curve will have a longer tail when the particle solution with a higher concentration is injected. The residence time of Fig. 4.4(A) is longer than that of Fig. 4.4(B), which is caused probably again by the higher inlet concentration (see caption in Fig. 4.4). The residence time of Fig. 4.5 (3.6 min) is a little longer than the residence time of Fig. 4.3(A) (2.9 min), which displays that the immobilization of the receptors can prolong the residence time of particles. When the adsorber was connected to the LC system, the residence time of Fig. 4.5 (3.6 min) is longer than the two cases of Fig. 4.4 (2.6 min and 1.2 min) where the adsorber was disconnected from the LC system. It is clear that the particles take some time to flow through the adsorber, which makes the residence time longer than that of the LC system alone.

Table 4.1. Residence time in average.

Experimental examples	Residence time, [min]
AMA without receptors & NPs without ligands: Fig. 4.3(A)	2.9
AMA without receptors & NPs without ligands: Fig. 4.3(B)	6.2
System without AMA & NPs without ligands: Fig. 4.4(A)	2.6
System without AMA & NPs with ligands: Fig. 4.4(B)	1.2
AMA with receptors & NPs without ligands: Fig.e 4.5	3.6

From the dimensional data in Fig. 4.3 and Fig. 4.7, the sensitivity of the light wavelength on measuring the breakthrough curves has been discussed. In addition to that, with the help of the dimensionless method, the further comparison among the breakthrough curves can get rid of the influence of units as illustrated in Fig. 4.6. The dimensionless methods here are to divide each UV absorbance point by the detected maximum absorbance value corresponding to each breakthrough curves in the y-axis and to divide the time point by the convection time scale in the x-axis. The convection time scale is calculated as (bed length, 0.4 cm) / (interstitial velocity, about 0.255 cm/min). One can find the associated information in Section 4.2.

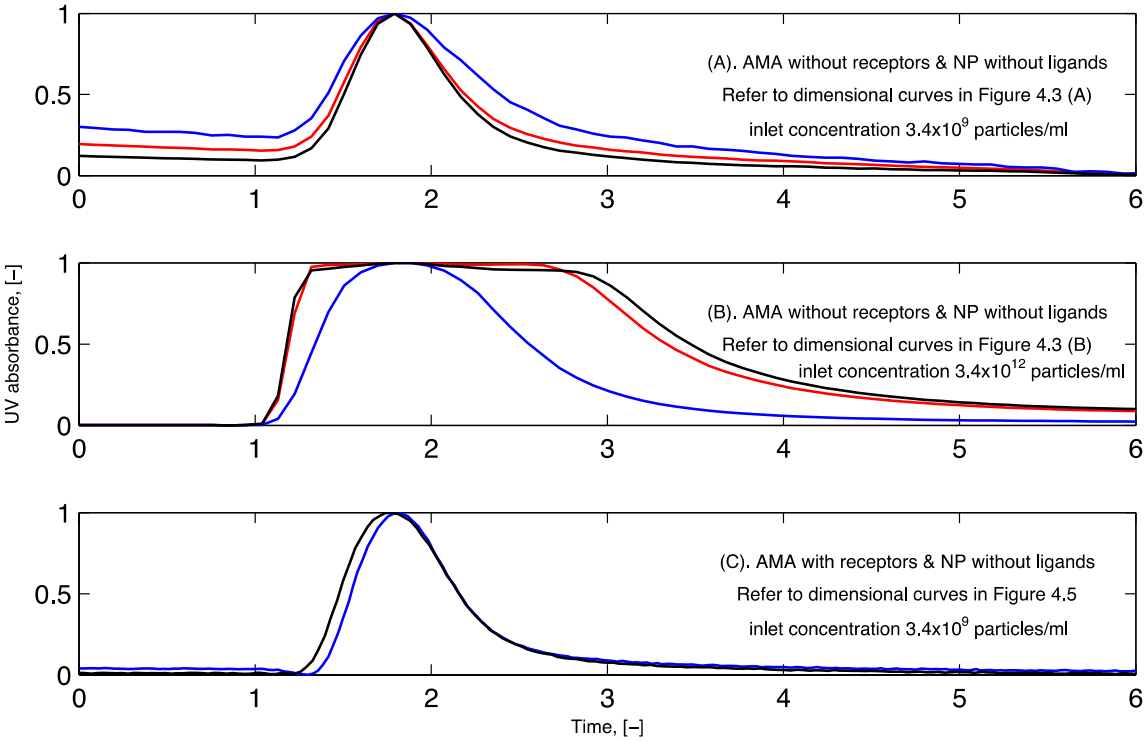

Figure 4.6: Comparison of the breakthrough curves influenced by the inlet concentration and the receptors.

It is much clearer now to compare the difference in the profiles of particle breakthrough made by the inlet concentration and the immobilization of receptors, such as the width of the peaks and the position of peaks. Fig. 4.6 illustrates that the positions of the highest points of three peaks are almost the same. However, their starting breakthrough points are different: Fig. 4.6(C) shows a delayed point compared to the other two, Fig. 4.6(A) and 4.6(B). It reflects that, in the here detected adsorber with a small volume of 2 ml, the immobilization of receptors can delay the breakthrough points but may not influence the time when the solution at the outlet reaches the highest concentration during the breakthrough. Besides, the width of three peaks in Fig. 4.6 fits well to the length of residence time as values listed in Table 4.1. The widest peak in Fig. 4.6(B) has the longest time of 6.2 min, and then the relatively narrower one in Fig. 4.6(C) has the decreased time of 3.6 min, and finally the narrowest one in Fig. 4.6(A) has the shortest time of 2.9 min.

In the same way, the dimensional data in Fig. 4.4 and Fig. 4.5 were plotted again in dimensionless form in Fig. 4.7. The purpose is here to improve the comparison of breakthrough curves under the influence of the ligand-coating layer and the absence of the adsorber.

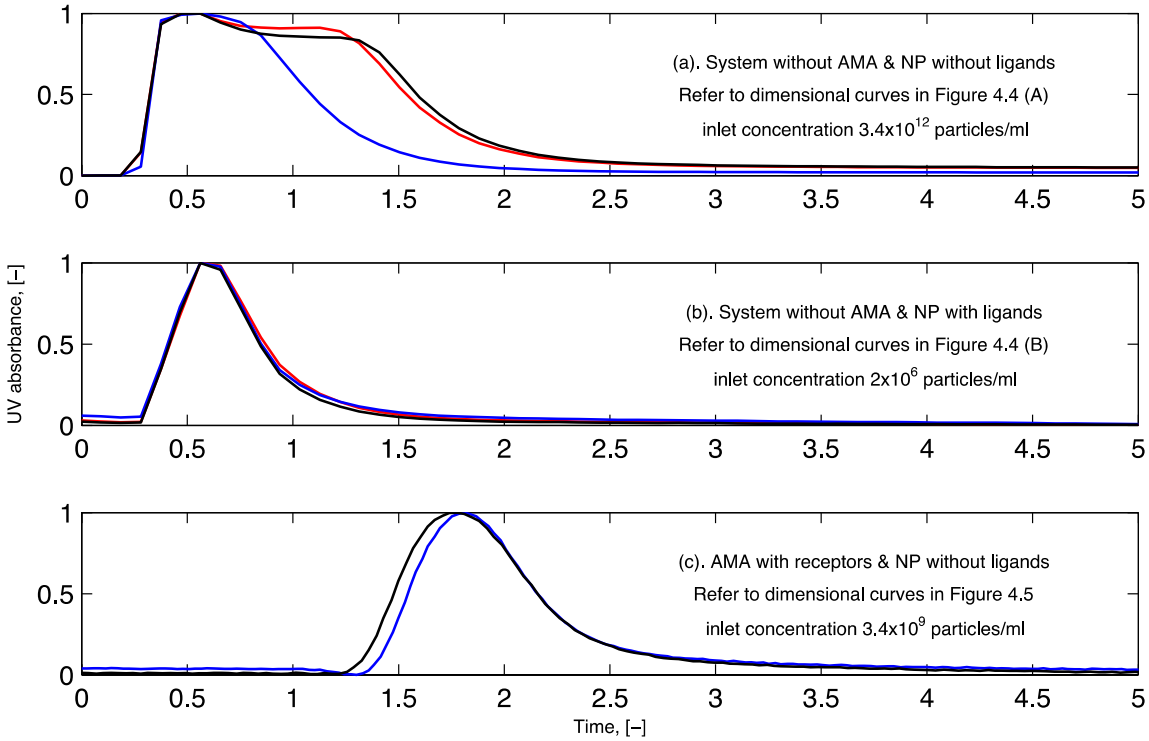

Figure 4.7: Comparison of the breakthrough curves influenced by the ligands or the AMA.

The curves in Fig. 4.7(a) and 4.7(b) show that there are no obvious differences both in the breakthrough points and in the time points related to the highest UV absorbance signals under the influence of the ligand-coating layer. However, the peak width becomes narrower in Fig. 4.7(b), which fits to the decreased residence time in Table 4.1. Due to the connection of AMA to the LC system, the breakthrough point and the highest point of the peak in Fig. 4.7(c) are both shifted later than the other two, Fig. 4.7(a) and (b). This is also true when one compares Fig. 4.7(a) to Fig. 4.6(B).

4.3.2 Detection of breakthrough curves of BioNPs through AMA

Fig. 4.8 displays the breakthrough profiles of BioNPs when their adsorption to receptors immobilized inside the AMA takes place. The curves illustrate that the experiments can be repeated. From Fig. 4.8(a), it seems that the curves in mAU units appear a bit different related to different light wavelengths. However, after the dimensionless manipulation, Fig. 4.9(b) shows that the profiles are almost the same. The experimental data in Fig. 4.9(b) will be used later in Chapter 6 in order to discriminate the proper adsorption model for the adsorption process of the chromatographic system. Here, it demonstrates that the prepared partners, BioNP4 in Chapter 2 and AMA in section 4.2 of this chapter, are applicable to measure the adsorption process of an adsorber unit in addition to the micro-scale surface in Chapter 3.

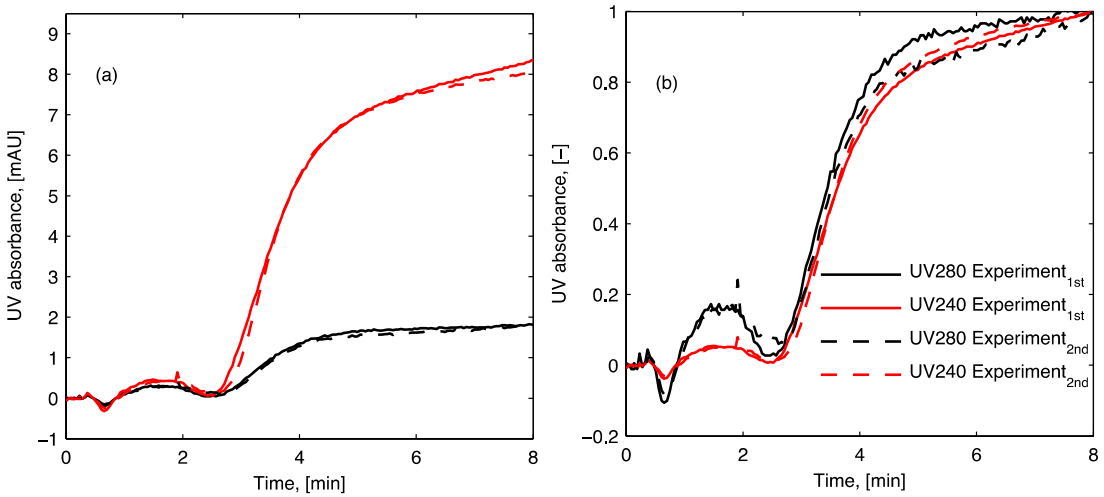

Figure 4.8: Breakthrough profiles of BioNPs through AMA. Figure (a) shows plots in dimensional units while Figure (b) shows the same data in dimensionless form.

4.4 Summary

In this chapter, the receptors, Protein A, are successfully immobilized to the basic adsorber for preparing the affinity membrane adsorber (AMA), which serves as an appropriate experimental model. Based on the self-prepared AMA and BioNP, the dispersion effects and the adsorption process are measured, which provides useful experimental data for further studying model simulations in Chapter 6. With regard to the dispersion detections, the following factors are investigated: the ligand coating layer, the inlet concentration of particles, the absence of the basic adsorber, the influence of the LC system, and the receptor immobilization to the basic adsorber.

Part II Model identification from experimental data

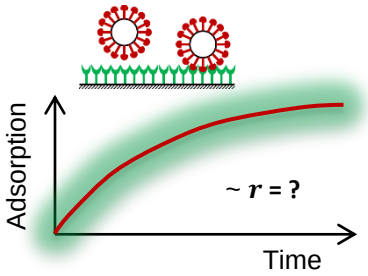

Chapter 5

Development of adsorption kinetic model

In this chapter, a multi-site kinetic model is developed to describe the multivalent adsorption kinetics between ligand-coated bionanoparticles (BioNP) and surface receptors. The corresponding experimental studies about the adsorption kinetics have been presented in Chapter 3. Fig. 5.1 highlights the key points that the work in this chapter is aimed to disclose the correlation between the binding kinetics and the number of bonds under the variations of ligand density and receptor density. As one of the important characteristics, the number of bonds formed between one-BioNP ligands and surface receptors plays a critical role in assessing the performance of multivalent interactions. The number of bonds is also named as the multivalence here.

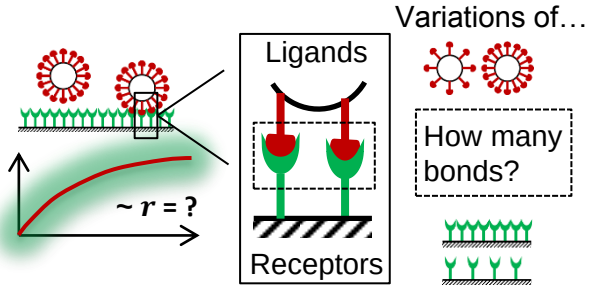

Figure 5.1: Highlights in the modeling study of adsorption kinetics.

One Protein A binds to two human IgGs(Yang et al. 2003). Hence, the established adsorption between human IgG-coated nanoparticles and Protein A-immobilized surface has the multivalent property. In order to better understand and to further develop a data

bank about multivalent design, the number of bonds is a very important parameter for the design, especially with regard to avidity, enhancement factor, cooperativity, or thermodynamics. At present, the bond design associated with various applications can be realized using versatile ligands through many smart coating methods for different nanomaterials. Most current works focus on a range of bond number within several up to tens of bonds, such as in the study of a dendrimer conjugate. However, in a relative high range of hundreds of bonds, there are only a few studies. The work in this chapter will illustrate the number of bonds not only in this high range but also beyond it.

5.1 The Multi-site kinetic model

Adsorption kinetic model of biological nanoparticles on their receptor surface is significant to understand biological functionalities, e.g., evaluating the chromatographic performance for particle separation. In terms of model identification, SPR detection can provide valuable experimental data to identify kinetic models appropriate for specific biological chromatographic systems. For example, Vicente has successfully used SPR spectroscopy as a scaled-down, pseudo-chromatographic tool for modeling protein binding under cyclic adsorption conditions.(Vicente et al. 2010) According to properties associated with various biological targets, there are many adsorption kinetic models developed to simulate the adsorption process. Among them, Langmuir adsorption model is the most popular one. Thanks to its basic assumption that one molecule binds to one molecule, many researches have benefited from its simplicity.(Shing Yi Suen and Etzel 1992, Kochan et al. 1996, Sridhar 1996, Sarfert and Etzel 1997, Tejeda-Mansir et al. 2003, Montesinos-Cisneros et al. 2007, Labanda et al. 2009, Dimartino et al. 2011, Patricia 2012) What is more, Langmuir mode has a broad applicability to develop kinetic model for various biological systems. A bi-Langmuir model has been derived to differentiate the specific and nonspecific adsorption.(Lisec et al. 2001, Boi et al. 2007) A steric hindrance model has been developed to include the blocking effect of adsorbed particles into Langmuir type adsorption.(Jin et al. 1994, Yang and Etzel 2003) A spreading model has been established to study the orientation or confirmation of adsorbed protein at the surface.(Lundstrom 1985, Yang and Etzel 2003) According to its broad applicability, the main principle of Langmuir model will be also introduced in this work in order to focus on the study of multivalence.

So far, multiple bonds formed between one single particle and its surface receptors, also namely multivalence, have not been quantitatively investigated from the aspect of adsorption kinetics. Multivalent adsorption kinetics is normally analyzed in a monovalent approach based on the Langmuir model.(Choi et al. 2013, Silpe et al. 2013, Yu et al. 2013, Li et al. 2014) However, it is often found out that simulated curves based on Langmuir model deviate from experimental data if the multivalence is disregarded, such as in the work by Kalinin et al.(Kalinin et al. 1995).

Essentially, a large number of ligands stretching outside one particle results in the multivalence of the binding. Therefore, the distribution of attached ligands among particles, especially among the synthesized ones, is important to formulate the adsorption kinetic model. So far, Mullen *et al.* have observed a skewed Poisson distribution in case of

the dendrimer-ligand conjugate.(Mullen et al. 2010). As another essential component, receptor distribution at the surface is also important to the formulation. For receptor distribution at the sensor surface, one can refer to the heterogeneity of the SPR surface.(Schuck and Zhao 2010) Reports on either ligand or receptor distribution are valuable to stochastically study the characteristics of two interacting partners in details. However, the model development here concentrates on the multivalence and tries to adopt the simplicity for the other factors as much as possible. The principle of Occam's razor is followed here and, thus, ligand distribution among BioNPs and receptor distribution at sensor surface are both assumed to be homogeneous.

Sequence of multiple bonds between ligands and receptors is another researched point in order to understand multivalent interaction mechanism. Three modes of binding sequence can be proposed as illustrated in Figure 5.2: all-or-none (a → d), zipper-like (a → b → c → d), or a mixed mode (a → c → d, or a → b → d). Sieben *et al.* have implied that both zipper-like and all-or-none events could exist when observing unbinding pathways of influenza virus.(Sieben et al. 2012) Following the simple rule again, all-or-none mode is applied in this work to formulate the kinetic model.

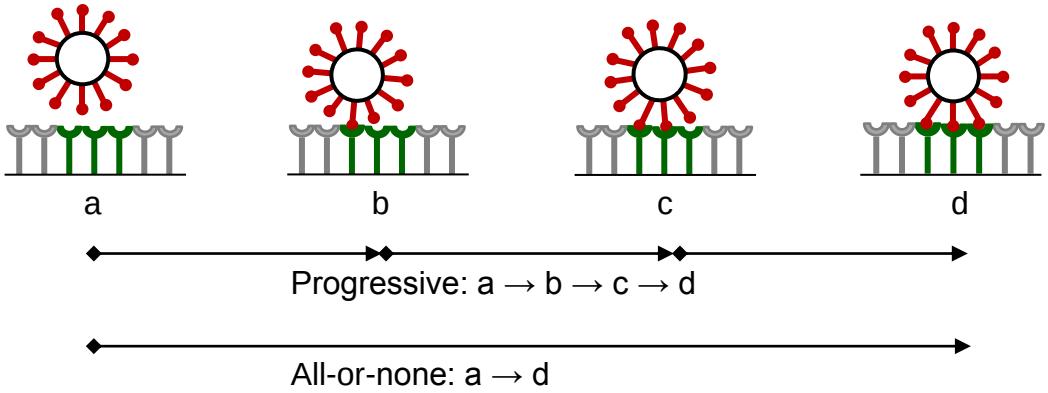

Figure 5.2: Modes of binding sequence between bionanoparticle ligands and surface receptors. As one example, the number of bonds between one-bionanoparticle ligands and surface receptors was n = 3.

As highlighted already in Figure 5.1, the number of bonds, n, is a key parameter to the development of adsorption kinetic model. Formed by two partners, this key parameter can be formulated into a concentration function of either BioNP ligands or surface receptors. With the comparison of their geometries, the 2D flat plan of receptor surface is simpler than the 3D sphere of BioNP. Therefore, the number of bonds is parametrized into the concentration function of surface receptors.

Figure 5.3 displays that a single BioNP binds to a corresponding cluster of receptors. The arrangement of receptors inside this cluster is assumed to be a linear lattice. Under this assumption, the function of cluster concentration in number unit can be then formulated by applying a conditional probability, first proposed by McGhee and von Hippel(Ken A. Dill et al. 2003). The steric hindrance effect due to the size of BioNP is also elucidated in Figure 5.3 as exemplified by unavailable sites in the dashed lines, which

exists in the neighborhood of adsorbed BioNPs. It implies that there are always unbound receptors between two neighboring BioNPs. For example, b3 bond and b1 bond in Fig. 5.3 are impossible to be next to each other, i.e., b3b1, in the given example of n = 3. This is realized in the formulation by excluding the b3b1 situation with the help of conditional probability.

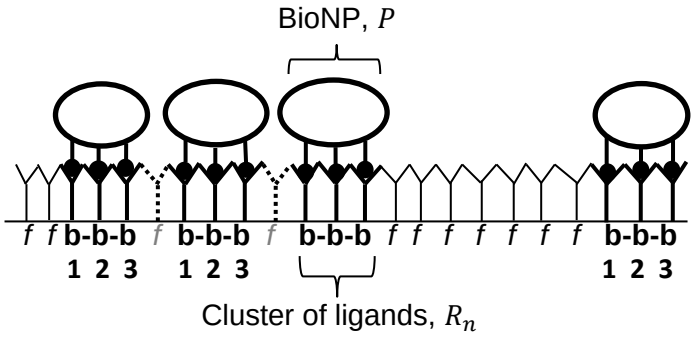

Figure 5.3: Illustration of multi-site binding between BioNPs and surface receptors in a linear lattice model. "**b**" stands for bound site, "*f*" stands for free site available for binding, and "*f*" under the dashed line stands for site unavailable for binding due to steric hindrance of adsorbed particles. "BioNP" stands for biological nanoparticle, P. As one example, the number of bonds between one-bionanoparticle ligands and surface receptors was again set as n = 3.

The concentration of available clusters of ligands for adsorption is

$$[R_n] = [R^{max}] \cdot p(f) \cdot p\left(f/f_{left}\right)^{n-1} \tag{5.1}$$

$p(f)$ is the probability of the free sites, f

$$p(f) = \frac{[R^{max}] - n[PR_n]}{[R^{max}]} \tag{5.2}$$

$p(f/f_{left})$ is the conditional probability that a site is free f given that its left site is also free f_{left}

$$p\left(f/f_{left}\right) = \frac{p\left(f_{left}f\right)}{p\left(f_{left}f\right) + p\left(f_{left}b_1\right)} \tag{5.3}$$

According to the rule of conditional probability, the term $p(f/f_{left})$ can be deduced into $p(f/f_{left}) = p(a\ site\ is\ f\ and\ its\ left\ site\ is\ f\ )/p(the\ left\ site\ is\ f)$. There are only two cases for the site to its left: either the site to its left is free, f, or it is blocked, b. As indicated in Fig. 5.3, for the free case, there are two types of combination: $f_{left}f$ and $f_{left}b_1$, and, for the blocked case, there are $(n+1)$ types: b_1b_2, b_2b_3,……, $b_{n-1}b_n$, b_nf, b_nb_1. However, b_nb_1 is impossible because of the blocking effect between neighboring particles. Thus, number of $\left(f_{left}f\right)$ = $[R^{max}]$ – number of $(f_{left}b_1 + b_1b_2 +$

$\cdots + b_{n-1}b_n + b_n f)$. Here, the counting order for the site is first the site itself and then its left site. Then, number of $(f_{left}b_1 + b_1b_2 + \cdots + b_{n-1}b_n + b_n f)$ = number of $(b_1b_2b_3 \cdots b_{n-1}b_n f)$ = $(n+1)[PR_n]$. Finally, Eq. (5.3) is given as

$$p(f/f_{left}) = \frac{[R^{max}] - (n+1)[PR_n]}{[R^{max}] - n[PR_n]} \tag{5.4}$$

From Eq. (5.1) to (5.4), the final function of cluster concentration, $[R_n]$, [receptors/mm^2], is

$$[R_n] = ([R^{max}] - n[PR_n]) \left(\frac{[R^{max}] - (n+1)[PR_n]}{[R^{max}] - n[PR_n]} \right)^{n-1} \tag{5.5}$$

where n is the number of the bonds, $[R^{max}]$ is the maximum number of surface receptors, [receptors/mm^2] which can be experimentally determined as surface capacity in Chapter 3, and $[PR_n]$ stands for the bionanoparticle concentration adsorbed at the receptor surface, [particles/mm^2].

According to experimental results discussed in Chapter 3, the here considered multivalent adsorption belongs to a strong type because of the high avidity of BioNPs to surface receptors. Besides, the adsorption within the injection time of SPR experiment is shown to be still close to the initial period and far away from the equilibrium. Moreover, the desorption amount is small enough to be neglected. Therefore, an irreversible and monolayer adsorption can be assumed.

Figure 5.3 illustrates that one BioNP corresponds to one cluster of receptors, which is again a type of one-to-one binding. This fits to the Langmuir-type adsorption category. Then, a formal stoichiometric expression for the adsorption of one BioNP particle at one cluster consisting of n ligands is given by

$$P + R_n \xrightarrow{r} PR_n \tag{5.6}$$

where P symbolizes particle concentration in the front vicinity adjacent to the adsorption surface; R_n symbolizes cluster concentration of available receptors at the membrane surface, ref. Eq. (5.1); r is the adsorption rate; PR_n symbolizes adsorbed particle concentration at receptor surface; and n is the number of receptor sites forming one cluster, i.e., the number of bonds.

According to all the aforementioned assumptions, the adsorption rate can be formulated as follows

$$r = k_a \cdot [P] \cdot [R_n] \tag{5.7}$$

where k_a is the adsorption rate constant; $[P](y = 0)$ is the concentration of bionanoparticles near the adsorbing surface, $y = 0$.

In order to solve the concentration function of bionanoparticles near the surface, $[P]$ (ref., Eq. (5.25)), mass balances will be derived in the next section 5.2. Here, for the benefit of a completed expression, only the final solution is first given: $[P](y=0) = [P]_{in} - \frac{2r}{3D}\delta_D$. With this solution, the combination of Eq. (5.7) with Eq. (5.5) yields the following multi-site adsorption rate expression

$$r = k_a\left([P]_{in} - \frac{2r}{3D}\delta_D\right)([R^{max}] - n[PR_n])\left(\frac{[R^{max}] - (n+1)[PR_n]}{[R^{max}] - n[PR_n]}\right)^{n-1} \tag{5.8}$$

When the number of bonds becomes $n = 1$, Eq. (5.8) can then be reduced to the classical Langmuir adsorption kinetic expression

$$r = k_a\left([P]_{in} - \frac{2r}{3D}\delta_D\right)([R^{max}] - [PR]) \tag{5.9}$$

Furthermore, the multi-site kinetic model in dimensionless formulation is given by

$$r^* = \frac{(1 - n\theta_{P,s})\left(\frac{1-(n+1)\theta_{P,s}}{1-n\theta_{P,s}}\right)^{n-1}}{\frac{1}{Da} + \frac{\delta_D^*}{3}(1 - n\theta_{P,s})\left(\frac{1-(n+1)\theta_{P,s}}{1-n\theta_{P,s}}\right)^{n-1}} \tag{5.10}$$

where Da stands for the Damköhler number, $Da = 2h[R^{max}]k_a/D$.

Accordingly, the dimensionless form of the single-site adsorption kinetics is

$$r^* = \frac{1-\theta_{P,s}}{\frac{1}{Da} + \frac{\delta_D^*}{3}(1-\theta_{P,s})} \tag{5.11}$$

The details of dimensionless formulation are given in Supplementary Information A.

5.2 Kinetic model framework based on SPR flow cell

During the formulation of the multi-site kinetic model in the last section, there is one term about particle concentration $[P]$ whose solution is obtained from the derivations of mass balances. It points to the mass transport effects on the SPR detected RU curves. One cannot simply take it for granted that the experimentally detected RU curves denote merely the adsorption kinetics. In particular, BioNPs detected here are relatively big in comparison with the normal proteins with their sizes of either several or tens of nanometers. Due to the big size of BioNP, which results in smaller diffusion coefficient of 10^{-12} m^2/s for BioNPs relative to 10^{-11} m^2/s for normal proteins, mass transport should partially influence the SPR data set. A general model to analyze mass transport together with adsorption kinetics should be established so that an estimation of adsorption rate constants can be improved. Consequently, not only the multi-site kinetic model but also

models for transport phenomena inside fluid flow will be established, and these models together form the here presented model framework.

Between the fluidic bulk and the receptor surface there should be mass transport of particles, including convection and diffusion. The transport mechanism rather than the inherent binding kinetics can be the main reason for producing the SPR experimental data at the receptor surface. Such kind of interaction is named as the transport-limited interaction. For example, Lok et al. have found that the adsorption data of two plasma proteins on a surface in a slit-like geometry similar to the microfluidic domain in Fig. 5.4 is possible to be analyzed with a mechanism considering only the mass transport effects by neglecting adsorption kinetics.(Lok et al. 1983) On the other hand, SPR detected curves can reflect the true adsorption kinetics without the mask from the mass transport by proper experimental design. Such kind of interaction is accordingly named as the kinetic-limited interaction. Then, the modeling work can exclude the mass transport mechanism and focus on a simple kinetic expression being one first-order ordinary differential equation. For example, Karlsson et al. have found that linear plots based on Langmuir kinetic equation can evaluate adsorption rate constants for monoclonal antibody-antigen interaction.(Karlsson et al. 1991) Also, Edwards has found that linear regression based on initial rate analysis is useful for determination of association rate constants by focusing on only the initial portion of the binding curve.(Edwards and Leatherbarrow 1997) These two aforementioned limited interactions are determined by comparing the magnitude of adsorption rate with the magnitude of mass transport rate. In such a way, the modeling complexity can be reduced. Efforts have been put in order to find a suitable limit coefficient to differentiate these two limited interactions. Glaser has first described quantitatively the transition between kinetic-limited interaction and transport-limited interaction by determining and thereby comparing two Onsager coefficients.(Glaser 1993) Based on this theory of Onsager coefficient, under certain conditions, it is possible to analytically analyze the influence of binding capacity (Karlsson et al. 1994) and also to analytically determine the protein concentration (Christensen 1997).

For an improved estimation of rate constants, it requires to go beyond just two values of the limited interactions but to model the mass transport influence together with the kinetic model, since the computational technology allows the addition of another one more equation beside the kinetic expression. Mysza et al. have proposed a two-compartment model, which includes one mass balance, in addition to Langmuir adsorption kinetic expression, for particles in the inner compartment adjacent to the binding surface with its height assumed constant.(Myszka et al. 1998) In the two-compartment model, the influence of mass transport from the outer compartment to the inner compartment was lumped into a coefficient, which corresponds to a type of film theory. However, it is interesting to see how the mass transport will be locally distributed along the flow direction. For this purpose, a disturbed model along with the length distance in the x-coordinate will be required. Therefore, the diffusional boundary layer theory is applied here to derive the distribution of BioNP concentrations in the liquid phase. Furthermore, it will elucidate the adsorbed BioNP distribution in the space domain in addition to the time domain.

Fig. 5.4 displays that the multivalent interactions take place inside a microfluidic domain of SPR channel, i.e. flow cell. With inlet concentration being step-input (lower part in Fig.

5.4), an output is generated to reflect the amount of BioNPs binding to the probing area on top of the flow cell while the solution flows continuously through the cell (*x*-direction, upper part in Fig. 5.4) at a constant flow rate.

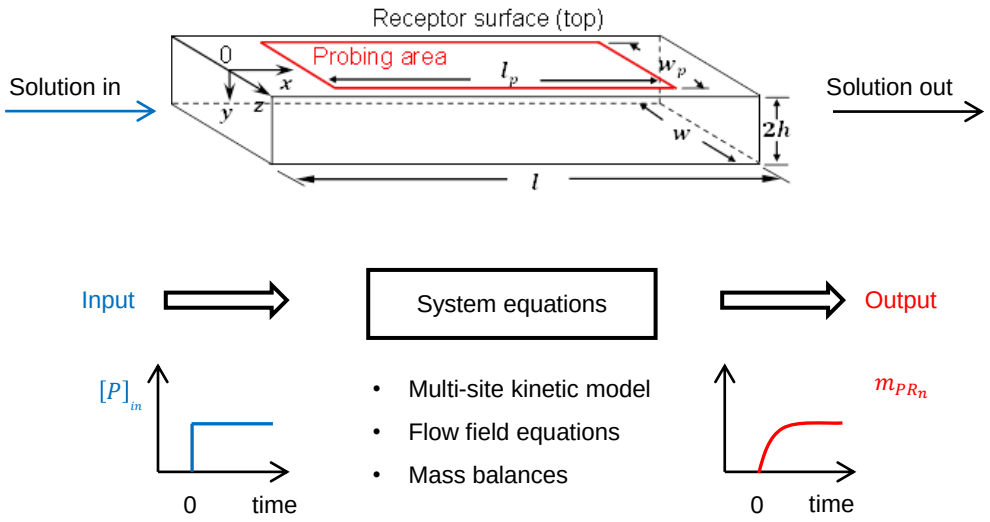

Figure 5.4: Sketch of the fluid domain (upper part) and elucidation of the input-output system behavior (bottom part). The geometrical parameters are l = 2 mm, w = 0.5 mm, h = 0.01 mm, l_p = 1.8 mm, and w_p = 0.2 mm. $[P]_{in}$ is the inlet concentration of the bionanoparticle solution. $m_{PR_n}(t)$ is the amount of adsorbed bionanoparticles at the receptor surface.

As shown in Fig. 5.4 (middle panel, lower part) the system equations of the model framework include the multi-site kinetic model in Section 5.1, the equations for the flow field derived from momentum balances, and the mass balances of BioNPs. Mass balances couple with momentum balances via the velocity field. Thus, in Section 5.2.1 the momentum balances will be first solved with the help of the classical velocity boundary layer theory, which gives finally an analytical expression for the velocity field in the fluid domain. Based on that, in Section 5.2.2 the mass balance of the BioNPs transported by the fluid flow can be formulated. This mass balance in the fluid phase is connected to the mass balance of BioNPs adsorbed at the receptor surface through the multivalent interactions. Finally, with the well-established model framework, the multi-site kinetic model developed in the last section will be identified from output data of SPR experiment (ref. Chapter 3).

5.2.1 Flow field

Following assumptions can be made in accordance with geometrical constraint of the SPR flow cell: (I) a quasi-2D flow by neglecting the model equations in the *z*-direction due to the large aspect ratio ($w/2h \gg 1$); (II) a steady and laminar flow with total mass density and viscosity constant; (III) the negligible force of gravity; (IV) the same velocity of bionanoparticles as that of the fluid; (V) an ideal plug flow for the feed profile with a given velocity: $v_x(x = 0, y) = \overline{v_x}$ ($\overline{v_x}$ is the average velocity) and $v_y(x, y) = 0$. Fig. 5.5 is plotted

according to the finally derived equations in this section to illustrate the velocity field distribution. As illustrated in Fig. 5.5 (a), the flow profiles are developing in the entrance region $(0 < x < l_e)$ until two boundary layers meet in the middle of the channel and then keep constant in the subsequent fully developed region $(x \geq l_e)$.

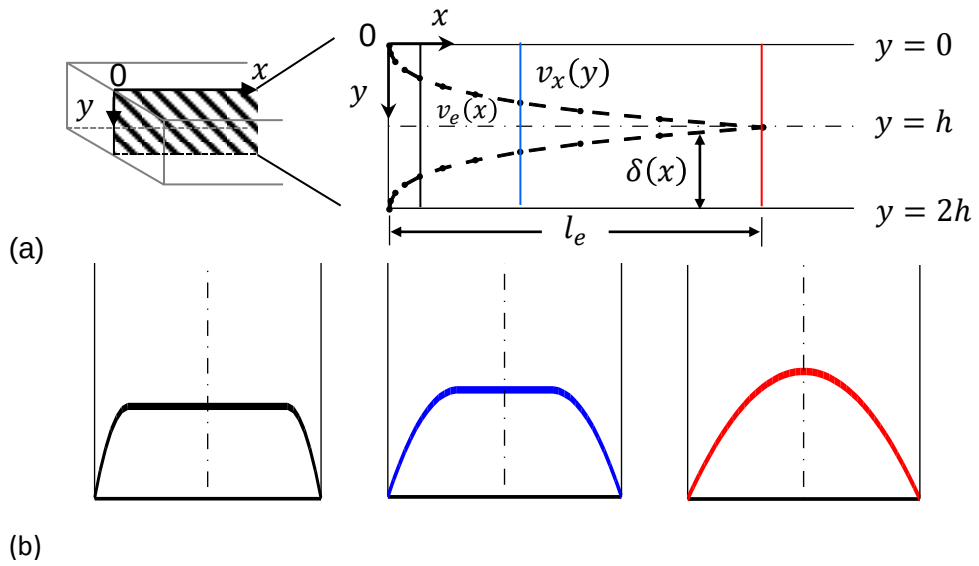

Figure 5.5: Entrance region of the velocity field in the SPR flow cell. In subfigure (a), $\delta(x)$ is the thickness of the velocity boundary layer. $v_x(y)$, Eq. (5.15), is the fluid velocity in the region of velocity boundary layer. $v_e(x)$, Eqs. (5.12), (5.13) and (5.14), is the fluid velocity in the region of potential flow between two velocity boundary layers. In subfigure (b), velocity profiles at three different positions are depicted as examples. l_e, Eq. (5.16), is the length of the entrance region.

Within the entrance region, the velocity profile is approximated by the following functions

$$\frac{v_x}{v_e} = 2\left(\frac{y}{\delta}\right) - \left(\frac{y}{\delta}\right)^2 \qquad \text{(boundary layer region, } 0 < y < \delta\text{)} \qquad (5.12)$$

$$\frac{v_x}{v_e} = 1 \qquad \text{(potential flow region, } \delta < y < h\text{)} \qquad (5.13)$$

$$v_e(x) = \frac{h}{h - \frac{1}{3}\delta(x)}\overline{v_x} \qquad (5.14)$$

with the velocity in the entrance region $v_e = v_e(x)$ and the thickness of the velocity boundary layer $\delta = \delta(x)$.

Based on these three profiles of velocity and the aforementioned assumptions, the 2D momentum balances along with the 2D total mass balance in the entire flow domain

illustrated in Fig. 5.4 (upper part) can be solved by means of the analysis of orders of magnitude and the integral method of von Kármán.(Bird et al. 2002) The derivations are supplied in the Supplementary Information A. Finally, in the fully developed velocity region displayed in Fig. 5.5 (a) $(x \geq l_e)$, the applied fluid flow equation sounds

$$v_x(y) = \frac{3}{2}\overline{v_x}\left(2\left(\frac{y}{h}\right) - \left(\frac{y}{h}\right)^2\right) \tag{5.15}$$

With the help of Eqs. (5.12) to (5.14), the development of flow profile in the flow direction is clarified. For instance, Fig. 5.4 (b) elucidates velocity profiles near the starting point, in the middle of the entrance region, and in the fully developed region (i.e., the ending point of the entrance region). One can see a symmetrical distribution of fluid flow divided by the plan at $y = h$ where there is the maximum velocity. The narrow microfluidic channel has an acceleration function similar to the nozzle, which increases the maximum velocity from the average velocity $\overline{v_x}$ to 1.5$\overline{v_x}$ (according to Eq. (5.15)).

Furthermore, the length of the entrance region can be analytically expressed

$$l_e \approx \frac{0.104h^2\overline{v_x}}{\nu} \tag{5.16}$$

where, ν is the kinematic viscosity. For the details of the derivation, one can refer to Supplementary Information A. The comparison of this entrance length with the entire length of the flow cell gives a ratio $l_e/l \approx 5 \times 10^{-4}$. This ratio clearly indicates that the entrance region is small enough to be neglected. Hence, the flow field for the SPR domain is dominated by a fully developed velocity profile, Eq. (5.15).

5.2.2 Mass balance equations

In this section the mass balances are derived on the basis of the boundary layer theory. The derivation begins with the classical mass balance of bionanoparticles in the fluid domain. Then, the reduction of mass balance equations using the analysis of the order of magnitude follows. Additionally, the BioNP concentration in the fluid is formulated in order to obtain the final solution to the thickness of the diffusional boundary layer. Here only displays the main equations, and the derivation details are provided in Supplementary Information A.

Based on the flow field distribution in Section 5.2.1, the 2D mass balance of bionanoparticles in the mobile phase is given by

$$\frac{\partial[P]}{\partial t} = -v_x(y)\frac{\partial[P]}{\partial x} + D\left(\frac{\partial^2[P]}{\partial x^2} + \frac{\partial^2[P]}{\partial y^2}\right) \tag{5.17}$$

where $[P]$ is the bionanoparticle concentration in the mobile phase, [particles/mm^3]. The diffusivity of bionanoparticles D is estimated from the Stokes–Einstein equation (see Eq.

(2.1) in Section 2.3). By introducing dimensionless variables: $\tau_a = t/t_a$, $X = x/l$, $Y = y/\delta_D$, $\theta_{P,l} = [P]/[P]_{in}$, $v_x^*(Y) = v_x/\overline{v_x}$, Eq. (5.17) can be reformulated as follows

$$\frac{t_r}{t_a}\frac{\partial\theta_{P,l}}{\partial\tau_a} = -v_x^*(Y)\frac{\partial\theta_{P,l}}{\partial X} + \frac{1}{Pe}\left(\frac{\partial^2\theta_{P,l}}{\partial X^2} + \left(\frac{l}{\delta_D}\right)^2\frac{\partial^2\theta_{P,l}}{\partial Y^2}\right) \tag{5.18}$$

where $Pe = l\overline{v_x}/D$ is the Peclet number and δ_D is the thickness of the diffusional boundary layer.

From Eq. (5.18) the x-direction diffusion term can be cancelled due to one fact $l/\delta_D \gg 1$. Physically speaking, the diffusional transport in y-direction dominates and the diffusion transport in the flow direction can be neglected. Furthermore, by comparing another time ratio between two important times Eq. (15) can be further reduced. One important time is the residence time of BioNP solution in the SPR channel t_r, which is $t_r = l/\overline{v_x}$ and about 0.024 s, the other is the characteristic adsorption time, t_a, which is in the range of hundreds of seconds estimated from the experimental observations in Chapter 3. Therefore, the ratio of these two time constants is $t_r/t_a \ll 1$. According to this very small time ratio, the accumulation term in Eq. (5.18) is not important comparing to the convective transport term and thus can be cancelled too. Since the time scale is adjusted to experimental time scale of t_a = 100 s, the mass balance in the mobile phase is then simplified as:

$$0 = -v_x^*\frac{\partial\theta_{P,l}}{\partial X} + \frac{1}{\mathrm{Pe}}\left(\frac{l}{\delta_D}\right)^2\frac{\partial^2\theta_{P,l}}{\partial Y^2} \tag{5.19}$$

Four boundary conditions (BC) are formulated in relation to the physical conditions. The velocity at the solid surface ($v_x\,(y=0) = 0$) has the non-slip condition, which results in BC1 from Eq. (5.19). The y-direction diffusion rate from the mobile phase to the receptor surface should equal to the adsorption rate at the receptor surface, which results in BC2. According to the boundary layer theory, at the edge of the diffusional boundary layer there is no difference for the particle concentration, which results in BC3 and BC4.

$$\text{BC1: } y = 0, D\left.\frac{\partial^2[P]}{\partial y^2}\right|_{y=0} = 0 \tag{5.20}$$

$$\text{BC2: } y = 0, D\left.\frac{\partial[P]}{\partial y}\right|_{y=0} = r \tag{5.21}$$

$$\text{BC3: } y = \delta_D(x), \left.\frac{\partial[P]}{\partial y}\right|_{y=\delta_D} = 0 \tag{5.22}$$

$$\text{BC4: } y = \delta_D(x), [P](t, x, y = \delta_D) = [P]_{in} \tag{5.23}$$

The bionanoparticle concentration profile in the diffusional boundary layer, $[P](t,x,y)$, can be approximated by a third-order polynomial profile

$$[P](t,x,y) = a + by + cy^2 + dy^3 \left(0 \le y \le \delta_D(x)\right) \tag{5.24}$$

where $a, b, c,$ and d are functions of x and t. Based on the boundary conditions BC1 to BC4, i.e., putting Eq. (5.24) into Eqs. (5.20) to (5.23), the following expression yields

$$\theta_{P,l} = \begin{cases} 1 + \left(Y - \dfrac{4}{3(\delta_D^*)^2}Y^3 - \dfrac{\delta_D^*}{3}\right)R, & \left(0 \le Y \le \dfrac{\delta_D^*}{2}\right) \\ 1, & \left(\dfrac{\delta_D^*}{2} \le Y \le 1\right) \end{cases} \tag{5.25}$$

Based on this analytical expression for BioNP concentration in the mobile phase, the governing equation for the mass balance in the mobile phase, Eq. (5.19), can be further integrated from $Y = 0$ to $Y = 1$ combining the flow field equation, Eq. (5.15). Finally, the expression for the diffusional boundary layer thickness is given by

$$(18(\delta_D^*)^2 - 5(\delta_D^*)^3)r^* \frac{d\delta_D^*}{dX} + 6(\delta_D^*)^3 \frac{\partial r^*}{\partial X} = 30\left(\frac{l}{h}\right)^2 \frac{r^*}{Pe} \tag{5.26}$$

with the dimensionless thickness of the diffusional boundary layer, $\delta_D^* = \delta_D/h$, and the dimensionless adsorption rate, $r^* = (2hr)/(D[P]_{in})$.

The classic mass balance of bionanoparticles at the receptor surface is given by $\partial[PR_n]/\partial t = r$. By introducing the dimensionless concentration of adsorbed BioNPs at the surface $\theta_{P,S} = [PR_n]/[R^{max}]$ and dimensionless time variable $\tau = t/\left(2h[R^{max}]/(D[P]_{in})\right)$, the governing equation becomes

$$\frac{\partial \theta_{P,S}}{\partial \tau} = r^* \tag{5.27}$$

It can be seen now that the two governing mass balances, Eqs. (5.26) and (5.27), is coupled by the adsorption rate. Accordingly, there are two initial conditions (IC)

$$\text{IC1: } \delta_D^*(X = 0) = 0 \tag{5.28}$$

$$\text{IC2: } \theta_{P,S}(\tau = 0, X) = 0 \tag{5.29}$$

As illustrated in Fig. 5.4 the experimental data were obtained within the probing area that is a certain proportion of the whole upper surface. Thus, the observed response should be expressed under the geometrical constraint, which includes the width and length of the probing area, w_p and l_p respectively. Finally, the amount of adsorbed particles, which corresponds to SPR detected RU signals, is given by

$$m_{PR_n}(t) = w_p \int_{\frac{l-l_p}{2}}^{\frac{l+l_p}{2}} [PR_n](t,x)\,dx \tag{5.30}$$

In addition to the multi-site kinetic model, Eq. (5.10), the other two parts of system equations have been clearly derived, flow field equation Eq. (5.15) and mass balances, Eq. (5.26) and Eq. (5.27). In summary, the model framework derived above contains two independent variables, τ and X, three dependent variables, $\theta_{P,s}$, δ_D^* and r^*, and four dimensionless parameters, namely (l/h), Pe, Da and n. Da and n are unknown parameters which will be estimated later from the adsorption experimental data. $\theta_{P,s}$, δ_D^* and r^* are aimed to be simulated.

Due to the coupled partial differential equation (5.26), the numerical solution is required for solving the model equations. The first step is to spatially discretize the mass balances in the x-direction of the flow domain into 100 equidistant elements, i.e. $\Delta X = 0.01$ for each element, using the backward difference scheme. Thereby, with the help of the chain rule $\frac{\partial r^*}{\partial X} = \frac{\partial r^*}{\partial \delta_D^*}\frac{d\delta_D^*}{dX}$, the following differential algebraic equations (DAE) are obtained

$$0 = 15\left(\frac{l}{h}\right)^2 \frac{r_1^*}{Pe} - \left(18\left(\delta_{D,1}^*\right)^2 r_1^* - 5\left(\delta_{D,1}^*\right)^3 r_1^* - 2\left(\delta_{D,1}^*\right)^3 (r_1^*)^2\right)\frac{\delta_{D,1}^*}{\Delta X} \tag{5.31}$$

$$0 = 30\left(\frac{l}{h}\right)^2 \frac{r_i^*}{\mathrm{Pe}} - \left(18\left(\delta_{D,i}^*\right)^2 r_i^* - 5\left(\delta_{D,i}^*\right)^3 r_i^* - 2\left(\delta_{D,i}^*\right)^3 (r_i^*)^2\right)\frac{\delta_{D,i}^* - \delta_{D,i-1}^*}{\Delta X}, \tag{5.32}$$

$$(2 \le i \le 100)$$

$$\frac{d\theta_{P,s,i}}{d\tau} = r_i^*, (1 \le i \le 100) \tag{5.33}$$

where i denotes the spatial elements.

Comparing the length of geometrical parameters l and l_p, one can see that the probing area covers the elements from i = 6 to i = 95. Correspondingly, using the dimensionless quantity $\Theta = m_{PR_n}/\left([R^{max}] l_p w_p\right)$, the SPR output function, Eq. (5.30), is given in the discretized form here

$$\Theta = \frac{l}{l_p}\sum_{i=6}^{95} \theta_{P,S,i}\,\Delta X \tag{5.34}$$

The dimensionless form of SPR experimental data [RU] were determined according to the following calibration formula

$$\Theta_{exp} = \frac{\mathrm{MW}_R * \mathrm{RU}}{\mathrm{MW}_{BioNP} * R^{max}} \tag{5.35}$$

MW_R is the molecular weight of one receptor. MW_{BioNP} is the molecular weight of a single particle (see Table 2.2 in Section 2.3). R^{max} is surface capacity given in Section 3.2.

The estimation of two unknown parameters, Da and n, were done by least squares fitting simulated curves, Eq. (5.34) to experimental time series of adsorption data, Eq. (5.35) based on the Gauß-Newton method. The applied sum of squares was defined as

$$S = \sum_{j=1}^{END_{exp}} \left(\Theta_{exp,j} - \Theta_j\right)^2 \tag{5.36}$$

where j denotes the time point. The value END_{exp} counts the total time points in a given time series of SPR data. The simulation of DAE, Eq. (5.31) to Eq. (5.35), and the parameter estimation were implemented via the ode15s solver in MATLAB 7.12.0 (R2011a).

All key equations in the model framework have been clarified so far and the corresponding derivation details are given in the Supplementary Information A. After the derivation, the next step is to validate the proposed model framework together with the multi-site kinetic model. In order to elucidate the validity of the multi-site kinetic model, the experimental data in Fig. 3.6 (e) in Section 3.3.1 was first taken as an example.

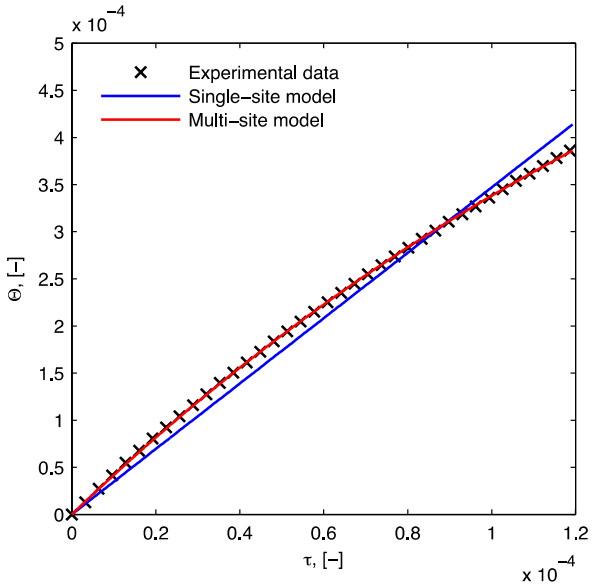

Figure 5.6: Comparison of simulated curves with experimental data. The experimental data were from Figure 3.6 (e) in Section 3.3.1. The multi-site model is Eq. (5.10) and the single-site model is Eq. (5.11).

Fig. 5.6 illustrates the comparison of experimental data obtained from the adsorption phase with the simulated data calculated by the model framework using two different adsorption kinetic models: the multi-site model, Eq. (5.10), and the single-site model, Eq. (5.11). In both cases optimal parameters have been estimated by least squares fitting. The deviation of the blue curve from the experimental data clearly reveals that the single-site model is not suitable for describing the multivalent binding of BioNPs on the receptor surface. However, the multi-site model fits the experimental profile very well by adding only one additional parameter, namely the number of adsorption sites forming a ligand cluster, n (see Fig. 5.3 in Section 5.1). Thus, the multi-site kinetic model will satisfy the accuracy of the model studies about multivalent adsorption.

5.2.2.1 The distribution of the diffusional boundary layer

As discussed in the beginning of Section 5.2, because of the mask of mass transport to multivalent adsorption kinetics, the model of the transport phenomena should be developed. One way to model transport phenomena is to use lumped parameters for estimating the transport influence.(Glaser 1993, Myszka et al. 1998, Goldstein et al. 1999) In such a way, it is quick to estimate rate constants from SPR data. However, it is lack of the knowledge about the transport dynamics in the flow direction and also about local correlation between mass transport and adsorption kinetics. Given these limitations, the transport equations of momentum and mass were formulated in a locally distributed way based on the classical boundary layer theory. Eq. (5.25) derived in Section 5.2.2 demonstrates that, for the microfluidic flow analyzed here under the appropriate assumptions, the BioNP concentration in the mobile phase is still in the entrance region of the diffusional boundary layer while the BioNP velocity is already in a fully developed field (see Eq. (5.15) in Section 5.2.1). For the fully developed region of mass transport, one can refer to solutions provided by the work from Gervais et al.(Gervais and Jensen 2006) The governing equation for the mass transport is finally deduced as the partial differential equation of the diffusional boundary layer thickness coupled with the adsorption rate, Eq. (5.26). From this equation, in addition to the adsorption rate, r, the diffusional boundary layer is also influenced by the following parameters: the geometrical constraint of the flow cell (l, h, w), the BioNP diffusivity (D), the flow rate (Q), and the inlet concentration ($[P]_{in}$).

Under experimental conditions of influenza virus nanoparticles as detected interactions illustrated in Fig. 3.6 (d), Fig. 5.7 illustrates the profiles of the corresponding diffusional boundary layer in the flow direction. Spatially speaking, the layer thickness increases in the flow direction. Dynamically speaking, the decreasing of diffusional boundary layer is clarified by comparing its longitudinal profiles at t_0 and at t_{end}. This decreasing size, i.e. the lateral distance between two profiles, is small enough to be negligible within the experimental time of around 100 seconds. The spatial increase of the layer thickness indicates the spatial decrease of the adsorption rate in X direction. The dynamic decreasing of the layer thickness is because the adsorption rate is decreasing due to the occupation of available receptors by the adsorbed BioNPs. Looking at the maximum thickness that is nearly 10% of the SPR channel height, one should thus consider the establishment of the diffusional boundary layer when evaluating the multivalent interactions at least for the here analyzed BioNPs in this dissertation.

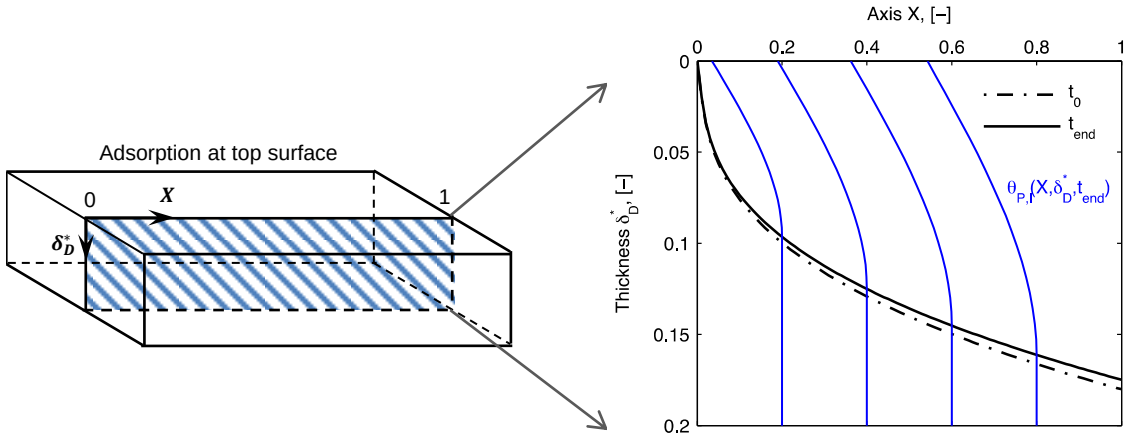

Figure 5.7: Profiles of the diffusional boundary layer thickness, δ_D^*, in X-direction at the beginning, t_0, and in the end, t_{end}, of the adsorption experiment. Concentration profiles, $\theta_{P,l}(X, \delta_D^*, t_{end})$, at four different X-positions (X = 0.2, 0.4, 0.6 and 0.8) are depicted in the blue lines according to Eq. (5.25). The calculation parameters are $[P]_{in,2}$ = 1.015 x 10^6 particles/µl, D = 3.76 x 10^{-12} m^2/s by Eq. (2.1) with the diameter assumed as 130 nm, and $[R^{max}]$ = 1.19 x 10^9 receptors/mm^2.

Additionally, the concentration profiles of the bionanoparticles in the end of adsorption experiment were also plotted in Fig. 5.7 in the selected X positions (X = 0.2, 0.4, 0.6, and 0.8) in order to elucidate the mass diffusion to the receptor surface in terms of concentration variations. Outside the boundary layer, the concentration of particles equals to one value, the inlet concentration. Inside the boundary layer, the particle concentration starts to decrease from the bulk towards the receptor surface. The plots show that the smaller the layer thickness becomes, the less the concentration decreases. For example, at the entrance point, there is no concentration decrease when the layer thickness is zero. It also implies that the X-related adsorption rate decreases in the flow direction and its maximum is at the entrance point.

Based on all parameters used in Fig. 5.7, Eq. (5.26) was used again to study the effect of the inlet concentration $[P]_{in}$ on the mass transport. For the purpose, the diffusional boundary layer at the outlet (X = 1) at three different inlet concentrations was plotted in Fig. 5.8. The results reveal that the layer thickness decreases by increasing the inlet concentration. However, it can be seen that, although the inlet concentration increased in fivefold, this decrease is still very slight. It seems that small changes around inlet concentration within certain window will not influence the thickness of the diffusional boundary layer. Besides, as discussed in Fig. 5.7, the time-related decrease of layer thickness is displayed here to be very small again.

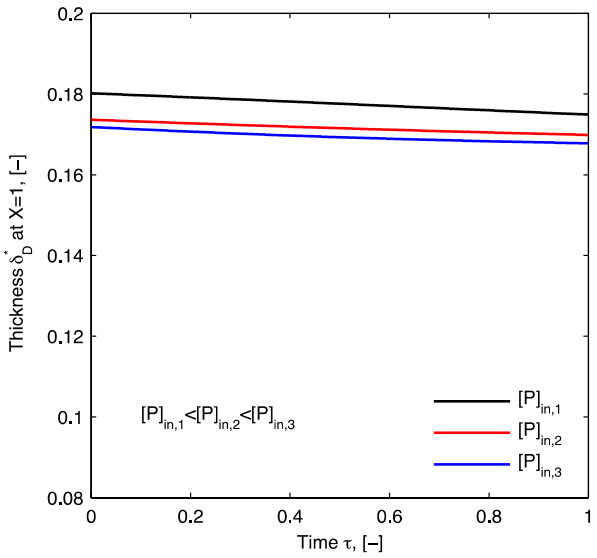

Figure 5.8: Dynamic profiles of diffusional boundary layer at the outlet (X = 1) by changing inlet concentrations: $[P]_{in,3} = 5[P]_{in,1}$, $[P]_{in,2} = 2.5[P]_{in,1}$.

5.2.2.2 The analytical solution of the diffusional boundary layer

As elucidated by both spatially dependent curves in Fig. 5.7 and time dependent curves in Fig. 5.8 the thickness of diffusional boundary layer decreased very slightly during the experimental period. Thus, it seems that the diffusional boundary layer is fully developed as long as the initial conditions are determined. It indicates that the time-related terms in Eq. (5.26) may be cancelled so that an approximate analytical solution can be derived from the exact numerical solution. Indeed, from the thickness displayed in Fig. 5.7, the terms containing $(\delta_D^*)^3$ in the Eq. (5.26) have an order of magnitude of at least 10^{-3}. The terms of $(\delta_D^*)^3$ can be neglected, which gives the following analytical solution

$$\delta_D^* = \sqrt[3]{5\left(\frac{l}{h}\right)^2 \frac{X}{Pe}} \tag{5.37}$$

With this analytical solution, the computation cost can be reduced to just several seconds for estimating the unknown parameters (D_a and n). Besides, this derivation accords fully with the order-of-magnitude estimation described in the work of Lok.(Lok et al. 1983) In order to verify the suitability of the analytical solution to approximate the numerical solution, Fig. 5.9 illustrates the diffusional boundary layers plotted through both solutions, Eq. (5.26) and Eq. (5.37), under the here considered experimental conditions when mass transport still influences adsorption rate. The insignificant deviation between two curves tells that the analytical solution, Eq. (5.37), is a good approximation to the numerical solution, Eq. (5.26), and thus can be used to estimate the diffusional boundary layer reasonably.

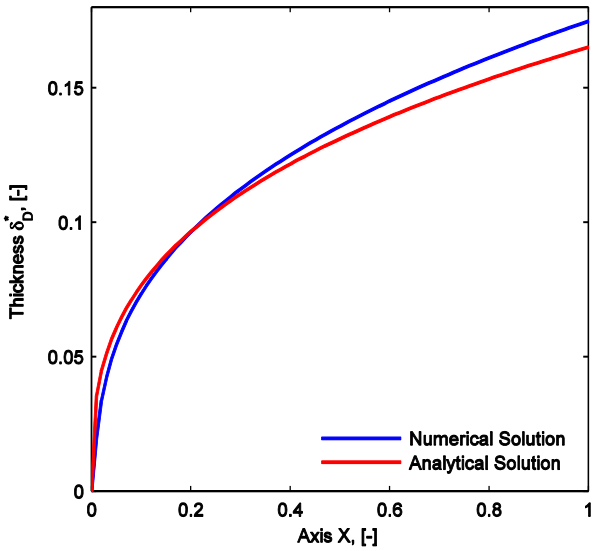

Figure 5.9: Comparison between the numerical solution, Eq. (5.26), and the analytical solution, Eq. (5.37). The parameters were taken the same as those used in Figure 5.7.

In addition to the good estimation of the analytical solution to the diffusional boundary layer in Fig. 5.9, its validity to estimate unknown parameters from the SPR experimental data is argued as well. For the purpose, two experiments from the adsorption detection of influenza virus particles were taken as estimation examples. The model framework with the numerical solution of the diffusional boundary layer (Eq. (5.26)) has been confirmed to successfully describe the multivalent adsorption of influenza virus particles from Fig. 5.6. Based on this confirmation, the parameters estimated using the numerical solutions will be the judgments for the parameters estimated by the model framework with the analytical solution of the diffusional boundary layer (Eq. (5.37)). Table 1 manifests the estimated parameters by changing only the solution for the diffusional boundary layer and keeping all the other equations in the model framework constant. With the comparison of values of estimated parameters in two experimental cases, they are very close to each other. So, it seems that the model framework with the analytical solution Eq. (5.37) is valid to estimate the parameters.

Table 5.1: Estimated parameters by the model framework using two solutions of the diffusional boundary layer from the SPR experimental data.

		Numerical	Analytical
n, -	$[P]_{in,2}$	413	388
	$[P]_{in,4}$	330	328
k_a, M^{-1} s^{-1}	$[P]_{in,2}$	3.20×10^6	2.96×10^6
	$[P]_{in,4}$	8.16×10^5	8.10×10^5

As an another validation, in addition to the comparison of the estimated parameters, the simulated curves are also compared with the experimental data in Fig. 5.10. The experimental data for $[P]_{in}$ and $[R^{max}]$ were taken from Fig. 3.6 (f), for $[P]_{in}/5$ and $[R^{max}]$

were from Fig. 3.6 (d), and for $[P]_{in}$ and $[R^{max}]/5$ were from Fig. 3.6 (c). The simulations were performed by the model framework with the analytical solution of δ_D^*, Eq. (5.37). The results demonstrate that the simulated curves fit to the experimental data very well.

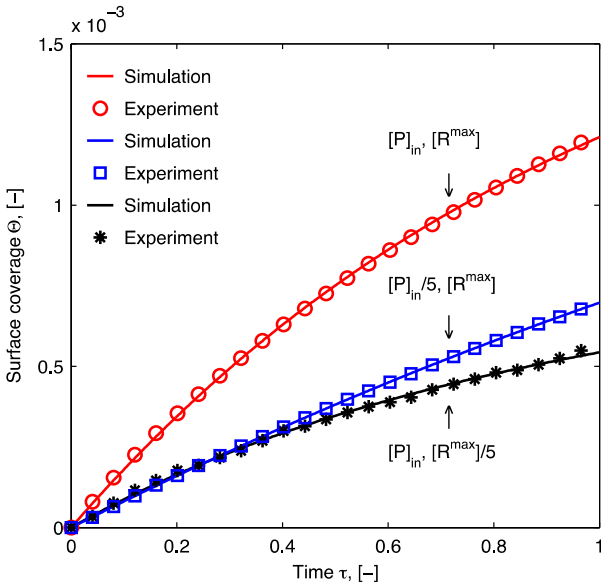

Figure 5.10: Comparison of the model simulated curves with the SPR experimental data. The simulation was done by the framework with the analytical solution of Eq. (5.37).

Moreover, with changes of the inlet concentration $[P]_{in}$ and surface capacity $[R^{max}]$, Fig. 5.10 illustrates their influence on the multivalent interaction. The ratio of the bionanoparticle concentration $[P]_{in}$ to receptor capacity $[R^{max}]$ was shown to play an important role in the multivalent adsorption. The deviation from the initial ratio (see 1:1 in red) to a 1:5 (in blue) or to a 5:1 (in black) results in different adsorption kinetics. Interestingly, with the same one-fifth decrease for both two interacting partners, the decrease of $[R^{max}]$ reduces the adsorbed amount more than the decrease of $[P]_{in}$. It may indicate that the surface receptor capacity influences the multivalent adsorption stronger than the inlet concentration of BioNPs. This indication relates to one common experimental experience that a higher surface capacity would enhance the role of the nonspecific interaction in the multivalent interaction. Therefore, it is wise to focus first on the design of receptor surface when the optimization of the multivalent interaction system is aimed.

In this section, the numerical solution was reduced as an analytical solution to simulate the diffusional boundary layer. This analytical solution was verified to be capable to estimate not only the mass transport (Fig. 5.9) but also unknown parameters (Table 5.1 and Fig. 5.10). With these validations, it is confident that the analytical solution of the diffusional boundary layer will satisfy the model framework. Since the simplicity of the analytical solution in relation to the numerical solution saves the computation efforts, the model framework will then take the analytical solution to simulate the multivalent adsorption from now on.

5.2.2.3 The analytical solutions for the multivalent adsorption

From the expression for the multi-site kinetic model, Eq. (5.10), the power terms $\left(\frac{1-(n+1)\theta_{P,S}}{1-n\theta_{P,S}}\right)^{n-1}$ equals to one if n is much bigger than one. In fact, from Table 5.1 the number of bonds n, as illustrated in Fig. 5.3, is estimated to be some hundreds of bonds for the influenza virus particles. For the human IgG-coated nanoparticles n will have even a large order of magnitude of thousands, which will be depicted later). Thus, it can be concluded that $n \gg 1$. With this conclusion, the multi-site kinetic model can be reduced again by cancelling the power terms of n

$$r^* = \frac{1 - n\theta_{P,S}}{\frac{1}{Da} + \frac{\delta_D^*}{3}\left(1 - n\theta_{P,S}\right)} \tag{5.38}$$

Eq. (5.38) displays an explicit relationship between the adsorption rate $r^*(X,\tau)$ and the dimensionless amount $\theta_{P,S}(X,\tau)$, namely $r^*\left(\theta_{P,S}\right)$. Furthermore, based on this explicit expression, the concentration of adsorbed bionanoparticles at the receptor surface, $\theta_{P,S}$ in ordinary differential equation, Eq. (5.27), can be derived to haven an implicit analytical expression, $\theta_{P,S}(\tau)$

$$1 - n\theta_{P,S} = e^{-nDa\tau} e^{nDa\frac{\delta_D^*}{3}\theta_{P,S}} \tag{5.39}$$

When the amount of BioNPs adsorbed at the receptor surface is relatively small, i. e., $\theta_{P,S} \approx 0$, the exponential term $e^{nDa\frac{\delta_D^*}{3}\theta_{P,S}}$ in Eq. (5.39) can be further deduced using Taylor series expansion at $\theta_{P,S} = 0$. Subsequently, in the vicinity of the initial adsorption, there is an approximate explicit equation for adsorbed amount

$$\theta_{P,S} = \frac{1 - e^{-nDa\tau}}{n\left(1 + Da\frac{\delta_D^*}{3}e^{-nDa\tau}\right)} \tag{5.40}$$

Besides, putting Eq. (5.40) into Eq. (5.34) together with Eq. (5.37) the output quantity sounds

$$\Theta = \frac{l}{nl_p}\left(1 - e^{-nDa\tau}\right) \int_{0.05}^{0.95} \frac{1}{1 + Da\frac{e^{-nDa\tau}}{3}\sqrt[3]{5\left(\frac{l}{h}\right)^2\frac{1}{Pe}}X^{1/3}}\,dX \tag{5.41}$$

The model reductions for the analytical solutions of the multivalent adsorption, Eq. (5.38) and Eq. (5.40), are based on the practical information under experimental conditions. Therefore, the analytical solutions for multivalent adsorption can be applied to predict the binding behavior reasonably, especially when the number of bonds $n \gg 1$.

Although these analytical solutions will only serve the prediction study, it is still questioned if there would be a great deviation between simulations before and after the model reductions. In order to answer this question, Fig. 5.11 illustrates simulated adsorption curves (dash) using the analytical solution, Eq. (5.40), compared with the curves simulated before reductions (solid) from Fig. 5.10.

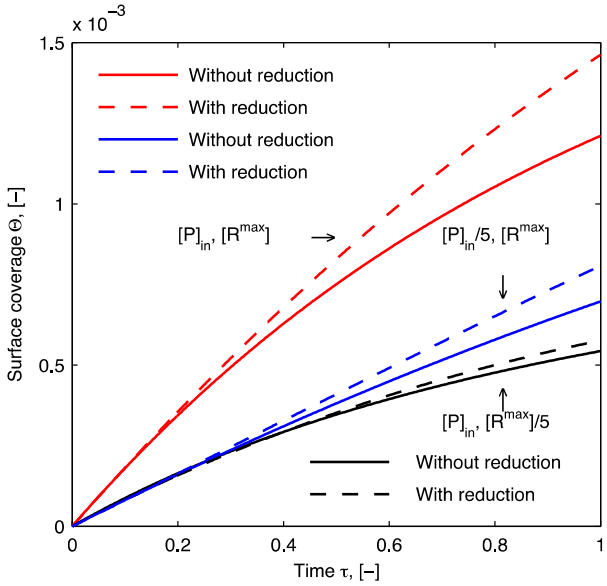

Figure 5.11: Comparison of simulation curves by the reduced equation, Eq. (5.41), with curves by the exact equation without reduction, Eq. (5.34)

The curve comparison in Fig. 5.11 elucidates that the deviation of the adsorption curves simulated by analytical solution, Eq. (5.40), from curves by the non-reduced Eq. (5.34) has the same style. Besides, all the deviations are not too strange within the here considered experimental conditions. It tells that with the analytical solutions adsorption behavior among experimental conditions, e. g. different inlet concentrations or surface capacities, is able to be differentiated from each other and then to be compared further. Furthermore, the analytical solutions provide a quick approach to generally compare the relative quantity among different adsorption experiments. All of these demonstrate the suitability of the reduced model equations, Eq. (5.38) and Eq. (5.40) to predict certain adsorption behavior.

The classical distribution of adsorption rate with particle concentration at the surface, $r^*(\theta_{P,S})$, can be predicted by Eq. (5.38). As one example, Fig. 5.12 (a) displays the simulated rate curves at four different local positions under the experimental condition detected in Fig. 3.6 (d) from Section 3.3.1. Generally speaking, adsorption rate, r^*, at each position decreases with the increase of its respective concentration, $\theta_{P,S}$ and this decrease becomes faster as the BioNPs kept adsorbing to the surface. However, by looking at different X positions, the decreasing profile is spatially dependent. Starting from the inlet, the local decrease of adsorption rate r^* with $\theta_{P,S}$ becomes gradually smaller in the flow direction. For example, r^* decreases more quickly at the inlet ($X = 0$) than at the

outlet ($X = 1$). Besides, when all local surfaces have the same concentration of bound particles, local adsorption rate decreases from the entrance (X = 0) to the exit (X = 1). And this type of decrease turns slower as the solution flows in the X direction. From this point, it can imply that the adsorption at the local surface near the inlet arrives at the equilibrium quickly. If all the mentioned results from Fig. 5.12 (a) are connected with the profile of the diffusional boundary layer thickness, δ_D^*, in Fig. 5.7, one can realize their local correlation. According to Fig. 5.7, the diffusional boundary layer becomes thicker in the flow direction, i.e., X direction. Therefore, one can conclude that r^* decreases as δ_D^* increases in the flow direction. Moreover, the concentration-related decrease of r^* becomes slower at the position where δ_D^* is thicker. This clarifies an inverse relationship as $r^* \propto \frac{1}{\delta_D^*}$, which can also be clearly seen from Eq. (5.38).

Additionally, Fig. 5.12 (a) also elucidates each local maximum adsorption rate, ${r^*}_{max}(X)$, at $\theta_{P,S} = 0$. According to Eq. (5.38), ${r^*}_{max}(X) = Da/(1 + Da\delta_D^*/3)$. By further combining with the analytical expression of diffusional boundary layer, Eq. (5.37), ${r^*}_{max}(X = 0) = Da$. Physically speaking, it means that all local adsorption rates are maximum at the beginning of an experiment, $\tau = 0$. Moreover, among these space-dependent maximums the global maximum adsorption rate is observed at the entrance point, $X = 0$. The local maximum concentration of adsorbed BioNPs, $\theta_{P,s,max}$, appears at the same position when $r^* = 0$ (see the red point in Fig. 5.12 (a)), and its value can be estimated from the plots of $\theta_{P,S}$ by Eq. (5.40) in Fig. 5.12 (b).

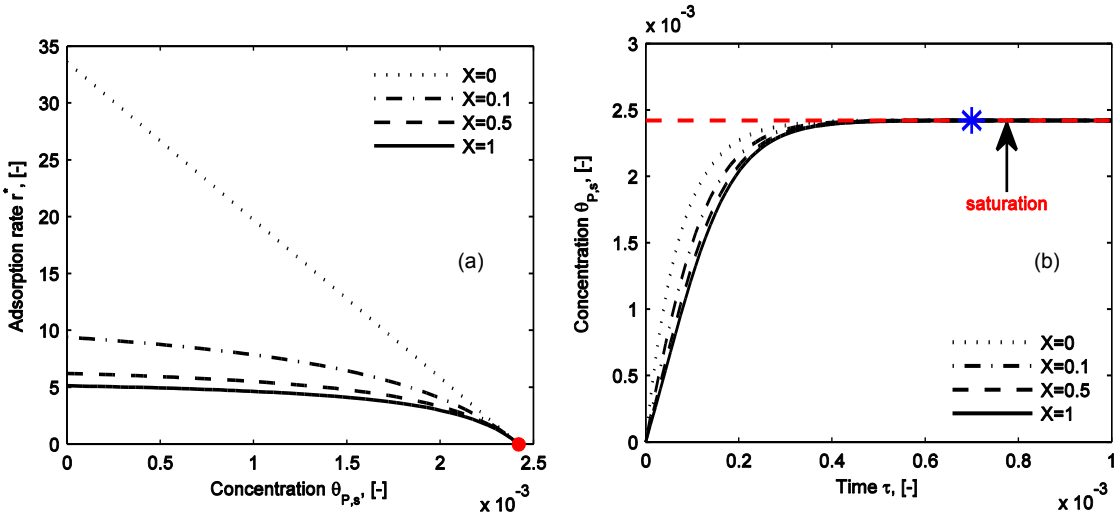

Figure 5.12: Prediction of multivalent interaction using the reduced analytical solutions. (a) Adsorption rate, r^*, versus local concentration of adsorbed BioNPs, $\theta_{P,S}$, plotted by Eq. (5.38) at four different X locations. The parameters used in the simulation are Da = 33.6, n = 413, $[P]_{in,2}$ = 1 x 10^6 particles/µl, $[R^{max,2}]$ = 1.19 x 10^9 receptors/mm^2, D = 3.76 x 10^{-12} m^2/s and the experiment time of 6.5 minutes. (b) Evolution of local concentration $\theta_{P,S}$ in time domain, simulated by Eq. (5.40). The parameters used in the simulation keep constant except for an increase of time to 110 minutes. The asterisk approximates the starting point of the saturation period and the saturation level is marked by the red line.

The distribution of local concentration of BioNPs adsorbed at the receptor surface, $\theta_{P,s}(X,\tau)$ can be predicted by Eq. (5.40). For example, Fig. 5.12 (b) displays the evolution profiles of concentration $\theta_{P,s}$ in time domain at four X positions. The simulations were performed under the same conditions as those for Fig. 5.12 (a) except for a prolonged experimental time. The curves elucidate that $\theta_{P,s}$ keeps increasing over time until it reaches a saturation level (see the red dash line in Fig. 5.12 (b)). All local concentrations finally arrive at a flat plateau that is named here as the saturation because the receptor surface can be fully occupied by the adsorbed particles after a certain adsorption time. This certain time can be indicated by the intersection between the simulated $\theta_{P,s}$ curve and the saturation line, as illustrated by the blue asterisk. One advantage to know the saturation is to predict the adsorption equilibrium, which is very helpful for the slow adsorption resulting in a difficult experimental determination of equilibrium. Thus, with the help of the saturation information, the time to reach equilibrium can be estimated by the saturation time (see the blue asterisk), and the equilibrium concentration by the saturation concentration, i. e., the maximum concentration $\theta_{P,s,max}$ (see the red dash line). For instance, the here considered example of influenza virus adsorption is revealed to have a saturation time of about 4400 s. It tells that the equilibrium time should be no shorter than this time. But in Section 3.3.1 the detection time was only about 390 s. Thus, there was a big difference about time. This time difference demonstrates again our model assumptions for developing multi-site kinetic model in Section 5.1 that the here considered multivalent interaction was far away from reaching the equilibrium status. Additionally, by comparing the values in Fig. 5.12 (b), it is found that $\theta_{P,s,max}$ equals to $1/n$, which can also be seen from Eq. (5.40).

These results from Fig. 5.12 (b) can help to analyze SPR experimental data more flexibly in alternative ways. For example, with the experimentally determined value for $\theta_{P,s,max}$, the number of bonds could be roughly approximated as $1/\,\theta_{P,s,max}$. Furthermore, they can also help to optimize the experimental design. For example, the receptor amount necessary for equilibrium can be generally acquired by multiplying n with the total amount within the probing area, Θ in Eq. (5.41). Also, with the approximated equilibrium time based on the model estimates, the injection volume of the BioNP solution could be calculate under a given flow rate in order to reach the equilibrium.

5.3 Parameter estimation

In total there are four dimensionless parameters (Pe, (l/h), Da, and n) in the model framework. Among them, the kinetics-related unknown parameters (Da and n in Fig. 5.3) are estimated based on model-simulated curve fitted to adsorption experimental data (see Eqs. (5.34), (5.35) and (5.36)), while the transport-related parameter, Pe, and the geometrical parameter, (l/h), are known from the experimental conditions and flow cell geometry. All the following experimental data are taken from Chapter 3. The parameter estimation of Da and n is implemented by least squares fitting based on the Gauß-Newton method. The calculation details of the equations are given in the Supplementary Information A.

5.3.1 Adsorption of influenza virus particles

As examples, the adsorption experimental data in Fig. 3.7 (d), (e), and (f) are chosen to display the comparison between the simulated curves using estimated parameters and the experimental data in Fig. 5.13. The results demonstrate that the simulated curves fit to the experimental data very well, which is also true for all the other experimental data set in Section 3.3.1. In order to avoid the redundancy, only the selected examples are discussed here. Obviously, the proposed multi-site kinetic model can adequately describe the adsorption kinetics of influenza virus particles at the EEL-immobilized surface. Besides, the results display that, when inlet concentration increased from $[P]_{in,2}$, $[P]_{in,4}$, to $[P]_{in,5}$ with surface capacity kept constant as $R^{max,2}$, the magnitude of the adsorption curves as well as the curvature increases from Fig. 5.13 (d), (e) to (f). Furthermore, by comparing the concentration increase with the adsorbed amount increase (see values in Table 3.1 and Fig. 5.13), one can see that the adsorption curve appears almost the same from $[P]_{in,2}$ to $[P]_{in,4}$ but bends up quickly from $[P]_{in,4}$ to $[P]_{in,5}$. It seems that the adsorption amount has a nonlinear relationship with the inlet concentration. This reflects clearly that the adsorbed particle amount grew at the EEL surface because of the increase of the inlet concentration. Again, as already discussed in Section 3.3.1, at each inlet concentration the repeated adsorption of influenza A virus particles appears to bend down due to the partial surface regeneration.

Accordingly, the finally optimized parameters used to plot curves in Fig. 5.13 are summarized in Table 5.2. Combining the curves in Fig. 5.13 with the parameters in Table 5.2, it is interesting to see that the adsorption rate constant, Da, has a close relationship with the slope of the adsorption curve while the number of bonds, n, with the curvature. For example, at the given inlet concentration $[P]_{in,5}$, the adsorption curve went down from the first run to the fourth run, which means that the slop decreased and the curvature increased. Accordingly, Da decreased and n increased. Moreover, although the adsorption amount increased with the increase of inlet concentration from $[P]_{in,2}$, $[P]_{in,4}$, to $[P]_{in,5}$ (see Fig. 5.13 (d), (e), to (f)), the adsorption rate constant decreased (see k_a values in Table 5.2). The number of bonds n decreased as well. It implies that the SPR detected amount increase does not necessarily mean the increase of adsorption rate and one has to consider the effect of the number of bonds, i.e., the multivalence. The decrease of the number of bonds is because the number of receptors at the surface is constant. When more virus particles are bound to the receptor surface as indicated in Fig. 5.13, each particle obtains finally less number of receptors, i.e., n decreases.

It has been pointed out before that mass transport plays a role in the evaluation of adsorption kinetics from SPR detected data. In Section 5.2, it has elucidated that the transport influence can be finally deduced in the form of the diffusional boundary layer δ_D^*. Here, by combining δ_D^* in Fig. 5.8 and k_a in Table 5.2, it reveals a correlation that the thickness of the diffusional boundary layer connects closely to the value of the adsorption rate constant in a way that δ_{D} decreases if Da decreases.

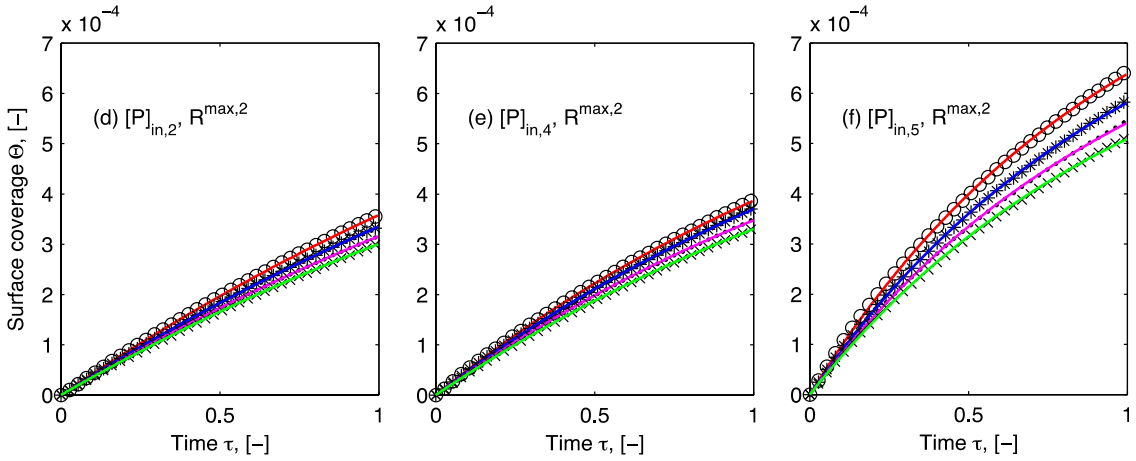

Figure 5.13: Comparison of the simulated curves with the experimental data. Each experiment for each inlet concentration was repeated four times: "o" is the first run, "*" is the second, "•" is the third, and "x" is the fourth. The experimental data are taken from Figure 3.7 (d), (e) and (f). The estimated parameters are listed in Table 5.2

Table 5.2. Estimated parameters for the adsorption of influenza virus particles.

Experimental runs		1st	2nd	3rd	4th
n, [-] [a]	$[P]_{in,2}$	425	413	427	459
	$[P]_{in,4}$	391	388	402	411
	$[P]_{in,5}$	314	330	349	368
k_a, [M^{-1} s^{-1}] [b] X 10^6	$[P]_{in,2}$	3.87	3.20	2.81	2.59
	$[P]_{in,4}$	1.35	1.23	1.12	1.03
	$[P]_{in,5}$	0.95	0.82	0.74	0.68

[a] The number of bonds as illustrated in Fig. 5.3.

[b] Adsorption rate constant calculated based on Damköhler number, $Da = 2h[R^{max}]k_a/D$.

The avidity is considered in the multi-site kinetic adsorption model as n quantifies the number of active adsorbing sites in Section 5.1. The parameter values in Table 5.2 display that influenza A virus particles to the EEL-immobilized surface have the avidity in the order of magnitude as 10^6 M^{-1} s^{-1}, and thus the affinity of a single binding site can be estimated as 10^4 M^{-1} s^{-1}. What is more, the effective binding ratio of all ligands on top of a single virus particle can be estimated with the help of the parameter n as long as the total ligand number of a single particle is known. According to Textbook of Influenza (Nicholson et al. 1998), the maximum glycosylation sites per viron can be assumed as 8000. One glycosylation site is further assumed to have 4 terminal galactose residues on average. Then, there are 32000 galactose residues per viron. However, roughly 30% of this total residue amount belongs to terminal α-galactose (Schwarzer et al. 2008, Schwarzer et al. 2009, Hennig 2013). Finally, the total ligand number of single virus particles is assumed to be about 9600. From Table 5.2, the average binding ratio of effective ligands to the total ligands is about 4% as the parameter n is revealed here in a range from about 300 to 460 ($n \gg 1$).

5.3.2 Adsorption of synthetic bionanoparticles

In this section the model framework is applied to analyze the synthesized multivalent adsorption where the human IgG-coated nanoparticles interacted with the Protein A-immobilized surface. The experimental data were taken from Section 3.3.2. The Damköhler number Da and the number of bonds n will be estimated again to illustrate the influence of the synthetic methods on the adsorption kinetics.

Thanks to the flexible advantage of the synthetic approach, the presenting way of the ligands for their interactions with the receptor surface can be either free without any scaffold (free human IgGs) or assembled by the scaffold (human IgG-coated BioNPs). Accordingly, the model framework can be used to estimate not only the multi-site adsorption of ligand-coasted BioNPs but also the single-site adsorption of free ligands. Fig. 5.14 displays typical examples for these synthetic adsorptions. Fig. 5.14 (A) illustrates the single-site adsorption of free human IgGs at the Protein A surface and Fig. 5.14 (B) shows the multi-site adsorption of human IgG-coated BioNPs at the same surface. With the intention of revealing the differences of the adsorption kinetics between free ligands and assembled ones, the adsorption experiments were performed under the same experimental conditions for both cases. Moreover, in order to achieve a more valid comparison, one experimental condition is that the total amount of free ligands used in the detection in Fig. 5.14 (A) is the same as the amount of attached ligands in Fig. 5.14 (B). According to the experimental data, Fig. 5.14 (A) illustrates that as the injection starting the adsorption of free ligands jumps quickly to the relatively stable status where it seems to arrive at the equilibrium. On the contrary, Fig. 5.14 (B) elucidates that the adsorption of BioNPs appears to be a relatively slow increasing curve, which indicates that the adsorption still stays in the initial adsorption period and is far away from the equilibrium. Furthermore, one can see that the simulation curves fit to experimental data well. It tells that the model framework with either multi-site or single-site kinetic model is appropriate for estimating parameters of the synthetic adsorptions. The adsorption kinetics of free ligands at the receptor surface appears different from that of assembled ligands because the degree of the geometrical freedom is changed. Thus, entropy and enthalpy between the free ligands and the assembled ones should be different.

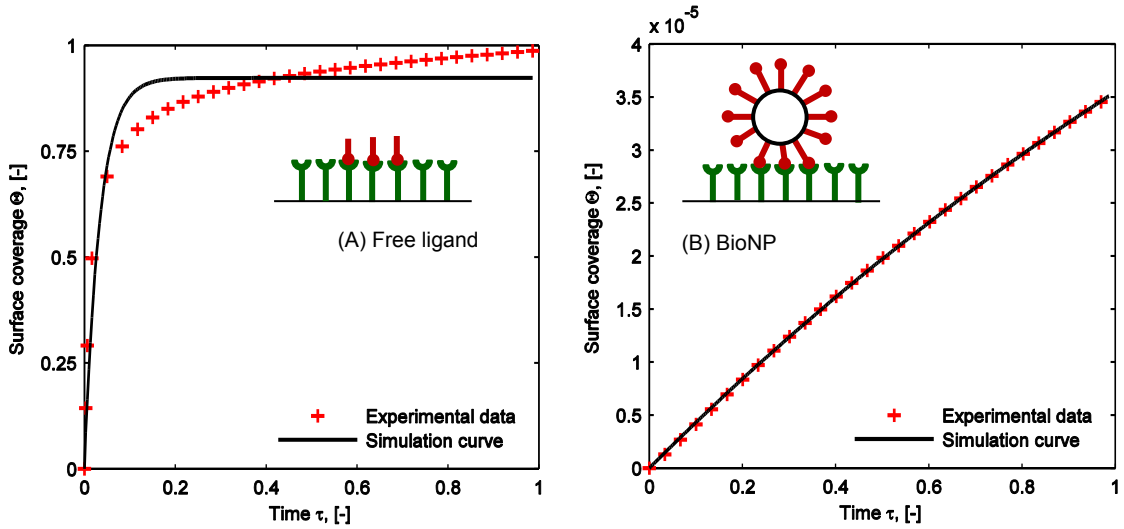

Figure 5.14: Comparison of the simulation curves with the experimental data. (A) Adsorption of free ligands (human IgGs) at the receptor surface. The single-site adsorption kinetic model, Eq. (5.11), was used to estimate adsorption rate constant: k_a = 6.28 X 10^4 M^{-1} S^{-1} by setting n =1. (B) Adsorption of synthetic bionanoparticles (human IgG coated nanoparticles) at the receptor surface. The multi-site model, Eq. (5.10), was used to estimate parameters: k_a = 3.72 X 10^4 M^{-1} S^{-1} and n = 6275. The other parameters used in both simulations were $[R^{max}]$ = 1.56 x 10^{10} receptors / mm^2, $[P]_{in,Y}$= 9.15 x 10^{11} particles / µl, D_Y = 0.389 x 10^{-12} m^2 / s as the diameter of 15 nm, $[P]_{in,BioNP}$ = 3 x 10^6 particles / µl, and D_{BioNP} = 3.42 10^{-12} m^2 / s as the diameter of 143 nm. Y denotes free human IgG.

During the development of the multi-site kinetic model in Section 5.1, the desorption was assumed to be negligible since the adsorption is still close to the initial adsorption and far away from the equilibrium. However, Fig. 5.14 (A) illustrates that in the case of the free human IgGs the adsorption almost reaches the equilibrium state within the experimental time. It implies that the desorption relative to the adsorption will also play an important role in the interaction of free ligands. Under such circumstance, the desorption rate should be included in the adsorption kinetic expression. It has been clarified that, when the number of bonds equals to one, the multi-site model (Eq. (5.10)) is deduced to the single-site model (Eq. (5.11)), which is Langmuir-type adsorption kinetic model and has been applied to investigate the adsorption kinetics of human IgG at Protein A surface (Hahn et al. 2003, Saha et al. 2003). Based on this single-site model in the Eq. (5.11), the desorption term can be added by introducing the desorption rate constant, k_d

$$r^* = \frac{1 - \left(1 + \frac{k_d}{k_a[P]_{in}}\right)\theta_{P,s}}{\frac{1}{Da} + \frac{\delta_D^*}{3}\left(1 - \theta_{P,s}\right)} \tag{5.42}$$

The parameter Da and n for the adsorption of the free human IgGs are then estimated with the help of Eq. (5.24). From Fig. 5.14 (A), one may argue that there is a slight derivation of the simulation curve from the experimental data. But this derivation is acceptable, which may result from the nonspecific binding among proteins themselves.

The adsorption rate constant, k_a, of free ligand in Fig. 5.14 (A) was estimated as 6.28 X 10^4 M^{-1} S^{-1} while that of BioNP in Fig. 5.14 (B) was 3.72 X 10^4 M^{-1} S^{-1}. By comparing these two values of k_a, it reveals that at the same surface with Protein A immobilized the free human IgGs adsorb almost two-fold faster than the human IgG-coated BioNPs. Thus, it manifests an advantage by using the model framework that the adsorption kinetics of the synthesized bionanoparticles can be compared with that of the corresponding free ligands not only qualitatively but also quantitatively, i. e., by comparing the values of the characteristic parameters, namely the adsorption rate constant, k_a.

For the adsorption of influenza A virus particles, an effective adsorption ratio of the attached ligands has been revealed in the last section. In addition to the effective ligand adsorption ratio, an efficiency of the surface receptors would be also revealed with respect to the estimated parameter, n (the number of bonds formed between a single bionanoparticle and the receptor surface). The receptor efficiency is defined here by calculating the coverage ratio of the receptors occupied by binding BioNPs. First, the total ligands occupying the surface receptors can be summed up via multiplying the final number of adsorbed BioNPs by the number of bonds. Then, the receptor coverage ratio is calculated by dividing this number of total ligands by the surface receptor capacity, which equals essentially to multiply Eq. (5.35) by the parameter, n. For example, in case of the multivalent adsorption in Fig. 5.14 (B) the number of bonds was estimated as about 6000. Consequently, the receptor efficiency is about 24%, which indicates that there are still a lot of unused receptors at the surface. The required values in the calculation are provided in the caption of Fig. 5.14. It helps to evaluate the multivalent interaction with respect to the receptor usage, which may be advantageous to design the functionalized interaction more economically.

As the experiments described in Section 3.3.2, for the synthesized multivalent interaction, the influence of the receptor density on the adsorption kinetics was detected. In addition to the experimental investigations, in this section this receptor influence can be further studied from the perspective of the model simulation based on the multi-site kinetic model. Fig. 5.15 displays the model simulated results for the adsorption of BioNP1 at two receptor surfaces, $R^{max,a}$ and $R^{max,b}$ together with the experimental data, which were taken from Fig. 3.11. The results demonstrate that the simulated curves fit well to the experimental curves. One may notice that the position of the adsorption curves in Fig. 5.15 after the model analysis using the dimensionless amount is different from that of the SPR detected experimental curves in Fig. 3.11. It is interesting that, with the receptor density increasing, ($R^{max,b} > R^{max,a}$) although the dimensional amount of adsorbed BioNPs increased (see Fig. 3.11), the adsorption rate of particles actually decreased (see Fig. 5.15). The dimensional amount of BioNPs at the receptor surface equals directly to the SPR signal, which grows with the receptor density increase. However, if the dimensional amount is normalized according to the surface capacity, i.e., the maximum receptor density, a more precise picture is that the adsorption rate does not necessarily goes higher with a higher receptor density. The existed number of bonds has to be considered more specifically. In the here presented work this specific consideration can be realized by using the R^{max} value for normalization (see Eq. (5.35)).

For the multivalent adsorption, the number of bonds should play a role in the SPR signal and this has not been considered before. As illustrated in Fig. 5.15, from $R^{max,a}$ to $R^{max,b}$, although the receptor capacity was doubled, the normalized adsorption rate decreased. It indicates that the increase of SPR detected adsorption amount may reflect actually a decrease of the adsorption rate, especially when the increase of the multivalence, i.e., the number of bonds, at a higher receptor density may hinder the adsorption. It is predicted that there is a maximum value for the number of bonds due to geometrical constraints for the contact between one particle and the surface. Below this maximum value, the number of bonds will keep increasing with the increase of the receptor density when the ligand density of BioNP is constant. However, the increase in building bonds can make the spatial approach of BioNP to the surface receptors more sophisticated, especially for the structural (pre)organization. Besides, more bonds may increase the enthalpy. And the increase of receptor density may reduce the entropy because under such circumstance the attachments of the receptors to the limited 2D static surface will become more crowed and thus reduce the degree of freedoms of the attached receptors. Consequently, the entire free energy of a single bionanoparticle required for its attachment to the cluster of receptors, i.e., forming the bonds, will be higher, which finally results in the lower adsorption rate at the higher receptor density as observed in Fig. 5.15. On the contrary to this observation, previous studies about the number of bonds in a range of tens show that the adsorption rate grow with the increase of the receptor density. In accordance with the aforementioned discussions, it is speculated that the number of bonds is bigger for BioNPs at surface $R^{max,b}$ relative to surface $R^{max,a}$. Fig. 5.15 explains that the influence of the receptor density on the adsorption rate is complex and here appears to be a negative contribution.

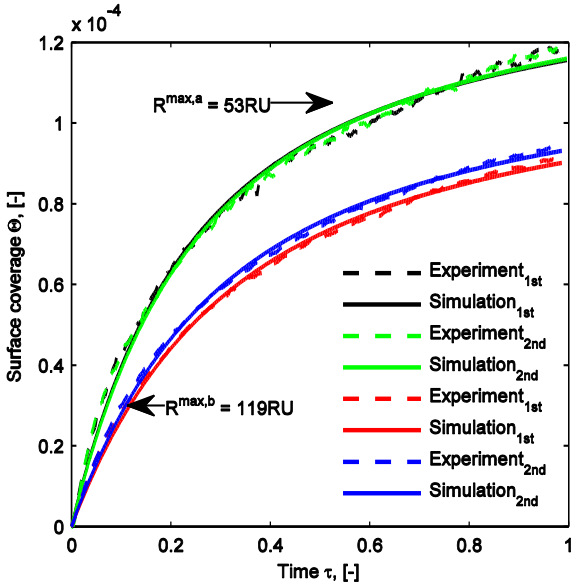

Figure 5.15: Adsorption of BioNP1 at two receptor surfaces with different capacities, $R_{max,a}$ and $R_{max,b}$. The experimental data were taken from Figure 3.11.

In order to enlarge the understanding horizon about the receptor density influence on the adsorption kinetics, the model-simulated results under the condition of higher receptor density ($R^{max,c}$ to $R^{max,d}$) are displayed in Fig. 5.16 in addition to the receptor density in the relative low range ($R^{max,a}$ to $R^{max,b}$) in Fig. 5.15. Due to the limited material amount of BioNP1 solutions, BioNP4 was used in Fig. 5.16 because characteristics of BioNP4 are essentially the same as those of BioNP1 as displayed in Table 2.2. Like in Fig. 5.15, all simulated curves based on the multi-site kinetic model fit to the experimental data very well. In contrast to the decrease of adsorption rate under the changing condition of receptor density in the low range in Fig. 5.15, the adsorption rate in Fig. 5.16 increases as the receptor density increases in the high range ($R^{max,d} > R^{max,c}$). This increase again should be related to the effects of the bonds. As mentioned in Fig. 5.15, there should be a maximum value for the number of bonds. For the adsorption at the high receptor density in Fig. 5.16, the number of bonds is possible to be close to or even reach the maximum value. This maximum can be high enough to neglect any relatively small changes of bonds. Thus, the difference of the number of bonds between two receptor densities, $R^{max,c}$ and $R^{max,d}$, would play a tiny role in the adsorption rate. In such case, one BioNP can be assumed as one entity without regard to the bonds inside, i.e., the free energy of a BioNP binding to a group of receptors would be almost same at both surfaces. The multivalent adsorption at higher receptor density would be analogous to the monovalent adsorption. So, the adsorption rate grows when the receptor density increases (Fig. 5.16).

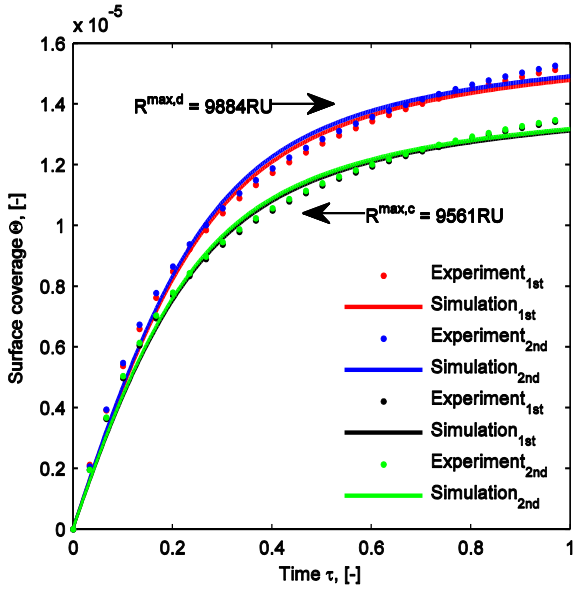

Figure 5.16: Adsorption of BioNP4 at two receptor surfaces with different capacities, $R_{max,c}$ and $R_{max,d}$. The experimental data were taken from Figure 3.12.

Fig. 5.15 illustrates the case when the number of bonds is far below the maximum value whereas Fig. 5.16 belongs to the case when the number of bonds is close to the maximum value. By comparing two cases, it can be summarized that saturation should exist when bonds between each BioNP and the corresponding surface receptors keeps

increaseing. This saturation status can change the impact on the adsorption rate by increasing the receptor density from negative (Fig. 5.15) to positive (Fig. 5.16). What is more, by comparing the dimensionless amount of the adsorbed BioNPs at all surfaces, the surface coverage at the high range of receptor density (Fig. 5.16) was smaller than at the low range (Fig. 5.15).

So far, the influence of the receptor density on the adsorption kinetics has been investigated and from now on the influence of the ligand density with regard to single BioNP on the adsorption kinetics will be studied. The experimental investigation has been described in Section 3.3.2 and presented in Fig. 3.13. Based on the experimental data, Fig. 5.17 displays the model simulations of the adsorption of BioNPs with three different ligand densities (BioNP1, BioNP2 and BioNP3, see the number of human IgGs in Table 2.2) at the same receptor surface ($R^{max,b}$). In the model analysis of the receptor density, it has been clarified that after normalizing the SPR signals with respect to each receptor density the position of adsorption curves is completely different from the experimental appearance. Likewise, after normalizing the SPR signals by each corresponding ligand density, the adsorption curves are different from the experimental situation (Fig. 3.13). To retrieve the model formulation, the explanation follows again in Eq. (5.35) where there is an important term, the molecular weight of a single particle, MW_{BioNP}, which reflects the ligand density. When the ligand density is higher, the molecular weight is higher as displayed in Table 2.2. Therefore, after the normalization of the SPR detected experimental curves in Fig. 3.13 based on Eq. (5.35), the final adsorption curves plotted in Fig. 5.17 can be applicable in order to compare adsorption rate by including the influence of different molecular weight of each particle, i.e., the ligand density.

The differences of adsorption rate between BioNP1 and BioNP2 (or BioNP3) can be described as follows: BioNP1 adsorbs first slower than BioNP2 and BioNP3 at the beginning of the experiments, and then gradually faster than BioNP3, and finally also faster than BioNP2. The reasons are that at the beginning of the experiments there is no limit to the binding from the receptor side because there are enough receptors available to BioNPs. In this case, the higher ligand density will increase the contacting possibility of each particle to the surface receptors and thus increase the adsorption rate. For example, from Fig. 5.17, within a dimensionless time of about 0.3 the adsorption rate of BioNP2 or BioNP3 is always higher than that of BioNP1. However, as the surface receptors are kept occupied by the adsorbed BioNPs, the receptor density will start to influence the adsorption in addition to the ligand density. In the here considered case, BioNP2 and BioNP3 have the higher ligand density, and it is thus assumed that for both cases each particle occupies more receptors than BioNP1. As the total amount of receptors is constant, the decrease of the available receptors in each of these two cases is accordingly accelerated, and thus the adsorption rate of either BioNP2 or BioNP3 gradually becomes slower than that of BioNP1 (see curve slopes in Fig. 5.17). Besides, this is also reflected in the final amount of BioNPs at the receptor surface: the amount of either BioNP2 or BioNP3 is smaller than that of BioNP1.

Another comparison of adsorption rate between BioNP2 and BioNP3 from Fig. 5.17 is as follows: BioNP3 always adsorbs slower than BioNP2 in the entire experimental time. From Table 2.2, one can see that the coating layer structure of BioNP2 and BioNP3 is different from that of BioNP1. Therefore, the adsorption differences caused by the

increase of ligand density from BioNP2 to BioNP3 are dissimilar to those from BioNP1 to BioNP2 or BioNP3. From the point of the synthetic strategy for the multivalent interaction, it seems that it does not always benefit the adsorption by attaching more ligands to a single particle. As example used here, when the coating layer of ligands on top of one particle surface is beyond one layer (BioNP2 and BioNP3), the further attachment of more ligands to BioNP will decrease its adsorption rate. Since the grouping structures among human IgGs stretching over the particle surface are more complex in case of the non mono-layer, the reasons could be speculatively related to: 1) the arrangement of the ligands, 2) the approaching directions of the ligands to the receptors, or 3) even the steric hindrance among the ligands.(Perumal et al. 2011, Chen et al. 2014)

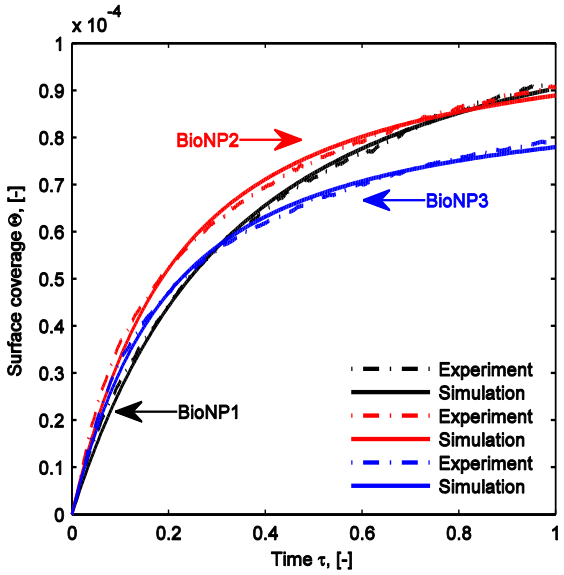

Figure 5.17: Adsorption of BioNP1, BioNP2 and BioNP3 at the receptor surface with the capacity of $R^{max,b}$. The experimental data were taken from Figure 3.13.

The comparison of adsorption curves in Fig.s (5.15), (5.16), and (5.17) has demonstrated that the multi-site kinetic model in the model framework is able to describe the synthetic multivalent interaction properly. Additionally, resulting from the fitting studies, two parameters, adsorption rate constant k_a and the number of bonds n, were estimated. Fig. 5.18 displays the results for these two parameters with the intention of further elucidating the adsorption kinetics. Each result point in Fig. 5.18 represents the average between the repeated experiments under each condition illustrated in Fig.s (5.15), (5.16), and (5.17). The parameter estimation has been performed for each experimental run separately. It is observed that the estimated parameters have very small changes among the repeated experiments. From the perspective of percentage, the change of k_a is less than 4% and the change of n is about 1%.

Fig. 5.18 (A1) elucidates the influence of the receptor density on the multivalence in terms of the number of bonds, n. In case of the synthesized multivalent interaction, the number of bonds can be calculated via the number of human IgGs bound to the receptor

surface per BioNP, which is the same as the case of influenza A virus particles in the last section. According to the work of Deisenhofer, it is assumed about 30 residuals from the Fc fragment involved in the adsorption of one human IgG to one Protein A.(Deisenhofer 1981) Based on this value and the estimated values for n, the numbers of human IgGs of one single BioNP bound to the receptors are finally calculated. When the receptor density increase (from $R^{max,a}$, $R^{max,b}$, $R^{max,c}$, to $R^{max,d}$), the number of bonds, n, increases, which demonstrates the previous predictions. For instance, n at $R^{max,b}$ (232) is higher than n at $R^{max,a}$ (193), which has been predicted from Fig. 5.15. Besides, if the receptor density increases strongly, the number of bonds may increase accordingly significantly. For example, as receptor density increasing from $R^{max,b}$ to $R^{max,c}$ (from 119 RU to 9561 RU in Section 3.2.2), an increase in one order of magnitude for the number of bonds appears from 232 to 1940 in Fig. 5.18 (A1). However, one may argue that the small increase of receptor density from $R^{max,c}$ to $R^{max,d}$ (from 9561 RU to 9884 RU in Section 3.2.2) results in the decrease of n (from 1940 to 1733). These two values of n are still close to each other and in the same order of magnitude. As receptor densities of $R^{max,c}$ to $R^{max,d}$ are relatively high and are not recommended normally for detecting the adsorption kinetics, the experimental data might contain certain errors. Since the sensitivity of the parameters depends highly on the experimental data, it would be possible that the number of bonds changes in the high range of receptor density differently from in the low range.

An effective adsorption ratio of ligands has been proposed before in the last section for the adsorption of the influenza virus particles and here can be applied again. Based on the known number of attached human IgGs per BioNP after the coating step in Chapter 2 (see Table 2.2), the effective adsorption ratio can be calculated by dividing the adsorbed human IgG number, i.e., the estimated parameter n, by this attachment number. Therefore, the effective adsorption ratios of BioNP1 ligands at four receptor densities are about 21% for $R^{max,a}$, 25% for $R^{max,b}$, and more than 100% for $R^{max,c}$ and $R^{max,d}$, respectively. Like the predictions from Fig. 5.16, the ratio values at $R^{max,c}$ and $R^{max,d}$ indicate again that the number of bonds at these two high receptor densities may already reach the maximum value of bonds. Moreover, the over-100% value might result from the other type of adsorption that is the bound BioNPs will build a more complex geometrical structure at the receptor surface having higher receptor density. In these circumstances, the surface structure would deviate from the monolayer adsorption assumption and appear totally disordered due to the crowed receptors. Some BioNPs may group together as clusters and some may stay on top of each other to form particle layers at $R^{max,c}$ and $R^{max,d}$.

Fig. 5.18 (A2) illustrates the number of bonds, n, under variation of ligand density. The numbers demonstrate that n increases with the increasing of ligand density exemplified here from BioNP1, BioNP2, to BioNP3. In the last discussion of the receptor density in Fig. 5.18 (A1), it is mentioned that there is the maximum value of the number of bonds when receptor density increases. However, Fig. 5.18 (A2) does not display a maximum value when ligand density increases. From the increasing style of the points, it seems that the increase of bonds with ligand density increasing is almost in a linear way. Conversely, there is an alternative picture when the effective adsorption ratio of human IgGs is considered. In fact, the effective adsorption ratio of ligands decreases from 25% (BioNP1)

to 11% (BioNP2) down to 9% (BioNP3). This decrease indicates another synthetic strategy that the aim to increase the bonds possibly results in the waste of the ligands. The reasons for the decreasing ratio may lie in the disorder of ligands in the coating step of the synthesis of BioNPs. As ligand density increasing, more and more ligands (human IgG) crowds at the limited space of one particle surface, which strengthens the disorder of ligand arrangement from BioNP1, BioNP2, to BioNP3.

Furthermore, by comparing the effective adsorption ratio, the effective adsorption ratio of human IgGs decreases gradually and slowly when the ligand density increases. Besides, one can find that the effective ratios of BioNP2 (11%) and BioNP3 (9%) are quite close. It implies that there may be an asymptotic value for the ratio. Given the grouping of receptors (Chittasupho 2012), one can imagine that the number of bonds will grow continuously with more ligand density of BioNP. However, the particle will become bigger and bigger, and the effective adsorption ratio will be reduced until it reaches the asymptotic value in a certain ligand density and will then stay constant.

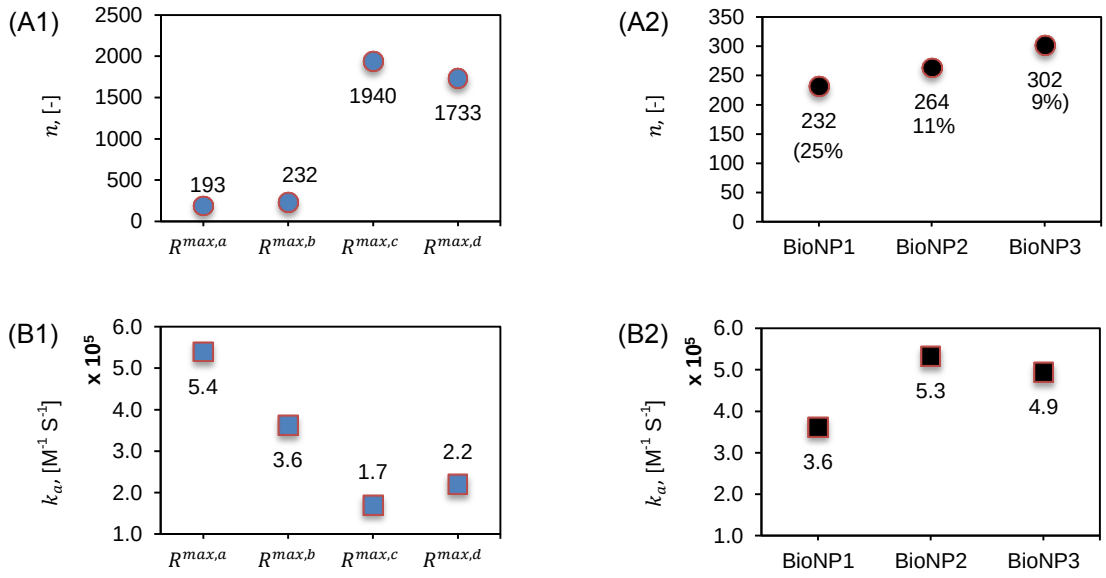

Figure 5.18: Comparison of the estimated parameters, adsorption rate constant, k_a, and the number of bonds, n. The corresponding adsorption curves have been illustrated in Figure 5.15, Figure 5.16 and Figure 5.17. (A1) and (B1) were plotted by varying the receptor density ($R^{max,a}$ = 53.4 RU, $R^{max,b}$ = 119.7 RU, $R^{max,c}$ = 9561 RU, and $R^{max,d}$ = 9884 RU). (A2) and (B2) were plotted with varying the ligand density (BioNP1, BioNP2, and BioNP3) at $R^{max,b}$. In Figure A2, the percentages are the effective adsorption of ratio of ligands on one single BioNP.

Previously, the influence of the receptor density on the adsorption rates under the condition of the constant ligand density is revealed in such a way that the increase of the receptor density first decreases the adsorption rate in the low range of receptor density (Fig. 5.15) and then increases it again in the relatively high range (Fig. 5.16) due to the effect of the multivalence as reflected by the number of bonds displayed in Fig. 5.18 (A1). In addition to the qualitative comparison of the adsorption curves, this influence can be

quantitatively observed further in terms of the adsorption rate constant, k_a, as plotted in Fig. 5.18 (B1). In the same way, one can see that k_a first decreases from $R^{max,a}$ to $R^{max,b}$ and then increases from $R^{max,c}$ to $R^{max,d}$. Moreover, from the values, the quantitative change of k_a is bigger between $R^{max,a}$ to $R^{max,b}$ than that from $R^{max,c}$ to $R^{max,d}$, which is in accordance to the different y-axis distance between the curves in Fig. 5.15 and Fig. 5.16. The highest value of k_a is at $R^{max,a}$. It indicates that, if it is aimed for a high adsorption rate constant, k_a, it is better to perform the multivalent adsorption under the circumstances of low receptor density. From the perspective of changing style, it seems that k_a varies fast in the low range of receptor density (from 5.4 at $R^{max,a}$ to 3.6 at $R^{max,b}$) but slow in the high range (from 1.7 at $R^{max,c}$ to 2.2 at $R^{max,d}$). It has been already argued in the discussion of Fig. 5.18 (A1) that the number of bonds will arrive at its maximum value by increasing the receptor density, R^{max}. Based on this maximum, it can elucidate that the sensitivity of the adsorption system becomes apparently higher at low receptor density when the number of bonds is still far away from the maximum number. This sensitivity suggests that for the experimental design the adjustment of the receptor side should be carefully considered in order to manipulate the adsorption rate. The smallest value of k_a is at $R^{max,c}$ in Fig. 5.18 (B1). By combining this value with the data of the number of bonds in Fig. 5.18 (A1), it is argued that the adsorption rate constant k_a is minimum at a point of the adsorption system where the multivalence of each BioNP is at its maximum number of bonds.

The influence of ligand density on the adsorption rate constant, k_a, is illustrated in Fig. 5.18 (B2). Generally speaking, k_a is low when BioNP ligand is presented in the monolayer coating (BioNP1) compared to the non-monolayer (BioNP2 and BioNP3), which is similar to the discussion of adsorption curves in Fig. 5.17. Besides, there is one similarity of k_a variation by changing either ligand density or receptor density by comparing sub-figure B1 and sub-figure B2. In both sub-figures, there is the same k_a of BioNP1 at $R^{max,b}$, which is 3.6. From figure B2, the ligand density of BioNP1 is increased by double to BioNP2 from about 1000 to 2000 (see Table 2.2) and it results in 5.3 for k_a. From figure B1, the receptor density is decreased in half to $R^{max,a}$ from about 120 to 53 (see Section 3.2.2) and it results in 5.4 for k_a. These two results appear surprisingly nearly identical. The values imply that, with the increasing of ligand density, the adsorption rate constant first increases (from BioNP1 to BioNP2) and then decrease (from BioNP2 to BioNP3). Therefore, it suggests to the coating performance that there may be a critical value of ligand density that will switch its influence on the adsorption rate. As a short conclusion based on the developing trend of k_a, by increasing the ligand density at the same receptor surface, the adsorption rate would first keep increasing until the ligand density arrives at the critical value and then be weakened. It is speculated that the main reason may be that the orientation of ligands in space becomes more complex.

5.4 Evaluation of multivalent interaction

In Section 5.3, the parameter estimation for the adsorption of two types of BioNPs has elucidated the important influence of the formed bonds, i.e., the multivalence, between a single bound BioNP and the surface receptors on the adsorption kinetics. With the help of

the model simulation, this influence can be further investigated systematically with the intention of providing more useful information for an efficient design of the multivalent interacting system. So far, the researchers have considered the contrast in the avidity due to different valences from the side of BioNP ligand as one criterion for evaluating the influence of multivalence, such as evaluating the selectivity in the targeting process. However, this evaluation requires the experimental data and cannot be applied to the pure simulation works here. Instead, another important contrast in the amount of adsorbed BioNPs at the receptor surface, Θ, caused by different number of bonds, n, is used. This contrast is still seldom quantitatively investigated. It may also help to achieve a qualitative measurement of the ligand density attached to one particle surface for generally comparing different coating performances. For a demonstration, Fig. 5.19 displays a series of adsorption curves simulated by changing the number of bonds, n, under the same set of all the other parameters. If the set of parameters used in the simulation is adjusted to different experimental conditions, the same pattern of results is observed as those in Fig. 5.19 with the same variation of n. All of the following results and discussions from Fig. 5.19 are not only meaningful for the here considered example but also applicable in a wide range.

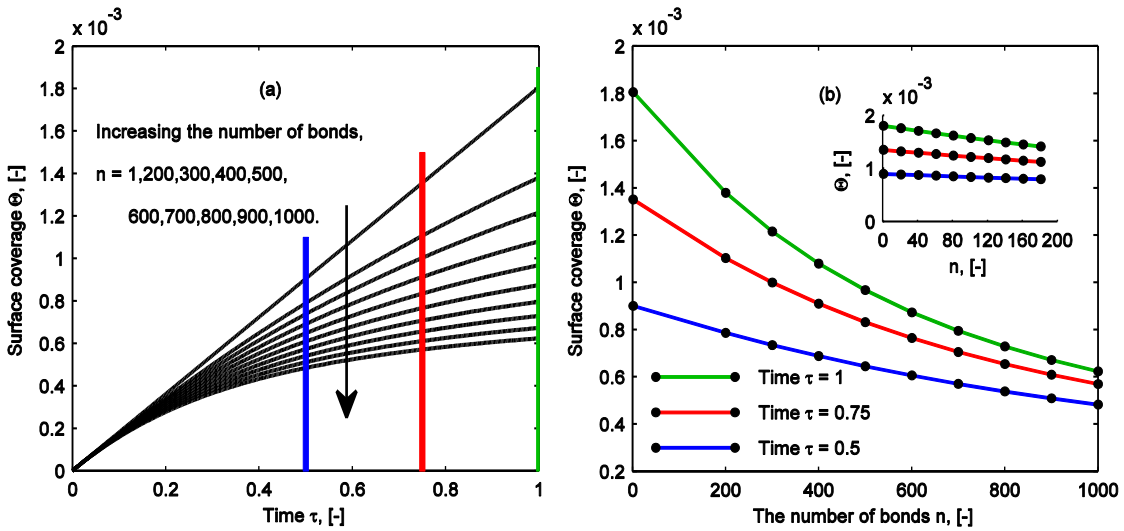

Figure 5.19: Profile variation of adsorption under the influence of the number of bonds, n. (a) Variation of the adsorption rate by increasing n. (b) Variation of surface coverage, Θ, as a function of n at certain time point τ taken from Figure 5.19a. The parameters used in the simulation were Da = 8, $[P]_{in}$ = 5 x 10^6 particles/µl, $[R^{max}]$ = 1.19 x 10^9 receptors/mm^2, D = 3.7 x 10^{-12} m^2/s as the diameter of 130 nm and the time was 6.5 minutes.

Fig. 5.19 (a) illustrates that the adsorption curves bend down accordingly with the increase of the number of bonds, n. Mathematically speaking, it implies that the number of bonds has a relationship with the curvature of the adsorption curves, which has been mentioned in the section of parameter estimation. It indicates that the bigger curvature corresponds to the higher number of bonds. Based on this indication, it seems that one can briefly assess the BioNP performance after the coating. Because the density of ligands attached to the particle surface can be qualitatively revealed. If the receptor

surface is kept constant, the higher number of bonds results from the increase of ligand density. Connected by the mentioned relationship between the number of bonds and curvature, e. g., the simulation results in Fig. 5.19 (a), it is clear that the appeared higher curvature of adsorption means the higher ligand density of the detected type of coated BioNP. In such a way, the experimentalist can briefly differentiate which coating strategy would produce a high ligand density.

In order to further clarify the direct correlation between the surface coverage, Θ, and the number of bonds, n, Fig. 5.19 (b) illustrates the changing profile of Θ with the independent variable of n at three time points τ selected from Fig. 5.19 (a) (depicted in color lines). The parameters used in the simulation are given according to the SPR experimental conditions described in Chapter 3. The simulation demonstrates that Θ decreases with the increase of n. This decrease appears stronger as the time increases, which corresponds to the bending-down trend in Fig. 5.19 (b). For example, as the adsorption time increases, shown for $\tau = 0.5$, $\tau = 0.75$ to $\tau = 1$, the decreasing value of the surface coverage Θ becomes bigger even with the same increasing value of the number of bonds. The reason for the decrease is that the surface receptor capacity $[R^{max}]$ is constant for all the simulations. When the allocated receptor amount for each individual BioNP increases (i.e., the number of bonds increases), the amount of particles bound at the surface naturally reduces. Furthermore, the curve slope in Fig. 5.19 (b) reflects the bending-down rate of the adsorption curves with the increase of the number of bonds in Fig. 5.19 (a). Thus, one can see that the bending rate of the adsorption amount curve becomes larger as the number of bonds goes smaller. Particularly, the profile is zoomed in in the low range from 1 to 200 bonds as displayed in the inset of Fig. 5.19 (b), and thereby a quasi-linear decrease of the adsorbed amount along with the increase of the number of bonds is observed. It seems that as long as the relative decrease of the adsorption amount at a certain receptor surface is detectable, the number of bonds can be predicted according to the revealed linear relationship (see the inset in Fig. 5.19 (b)). All the results may be more useful for experimental design methods targeting in the low multivalence situation between two interacting partners.

5.5 Summary

In this chapter, a multi-site adsorption kinetic model was developed to describe the multivalent adsorptions, ref. Eq. (5.8). Based on the developed kinetic model, a model framework was established to account for the transport influence on the adsorption kinetics. Momentum transport and mass transport were modeled with the help of the classical boundary layer theory. The mask of mass transport, i.e., convection and diffusion, to the adsorption kinetics is common to detect the big particle using SPR system and has to be considered for identifying the real adsorption kinetics. The derivation results elucidate that the velocity field distribution in the here applied SPR channel is already in the fully developed region and therefore a steady velocity profile is obtained in Eq. (5.15). Conversely, the concentration field distribution is still under the developing region where a diffusional boundary layer is formed, ref. Eq. (5.25).

By further applying the model framework to the SPR experimental data from Chapter 3, the multi-site kinetic model is demonstrated to be valid to describe the multivalent interactions of ligand-coated BioNPs, not only the natural particles but also the synthetic ones. Using the analysis of the order of magnitude based on the simulation results, an analytical approximation (Eq. (5.37)) to the diffusional boundary layer was further deduced and also verified to be proper to describe the diffusion effect of BioNPs from the mobile phase to the receptor surface. Based on this analytical approximation of diffusional boundary layer, the model framework including the multi-site kinetic model is able to estimate two unknown parameters, the number of bonds, n, and Damköhler number, Da, from the SPR experimental data. By controlling the parameter n, the model framework is versatile enough to estimate the parameters of not only the multi-site adsorption ($n > 1$) but also the mono-site adsorption ($n = 1$), which benefits a further comparison between them in terms of adsorption rate constants. What is more, the parameter estimations reveal that the number of bonds is much bigger than one, i.e., $n \gg 1$. Given this important information, the analytical solutions to the adsorption rate, Eq. (5.38), and further to the concentration of bound BioNPs at the receptor surface, Eq. (5.40), can be derived by reducing model equations inside the model framework. They are advantageous to predict the multivalent interacting behavior that is difficult to be monitored experimentally.

The parameter estimation also demonstrates that the multivalent adsorption can be evaluated in a quantitative modeling approach. The results reveal that the adsorption rate constant is minimum as the number of bonds is maximum. Therefore, a higher adsorption rate may be obtained when the bonds between BioNP ligands and surface receptors are less, which may correspond to the relatively low density of surface receptor. The controllable sensitivity of the adsorption rate through the variation of the receptor density was displayed to be different. This provides a possibility to achieve the specific binding selectivity by designing the receptor surface in a selective cocktail approach. The results also demonstrate that, when the ligand density at BioNP surface increases, the adsorption becomes faster in the beginning of the adsorption and then reaches the surface saturation quickly due to the higher number of bonds. With respect to the synthesis optimization in view of ligand density, one has to consider two contradicting issues, process time and material consumption. Apparently, a faster adsorption rate is achievable if more ligand material is used to coat particle with the intention of a bigger ligand density. However, such a method wastes the ligand material, which is disclosed through the evaluation of the efficient adsorption ratio of ligands on a single BioNP. The new way of examining the number of bonds quantitatively in details discovers three important terms: i) a critical density of ligand attached to the surface of one single BioNP in the coating step, ii) a most efficient number of bonds for the BioNP desorptions to resist density changes, and iii) an asymptotic value for the efficient adsorption ratio of ligands on a single BioNP.

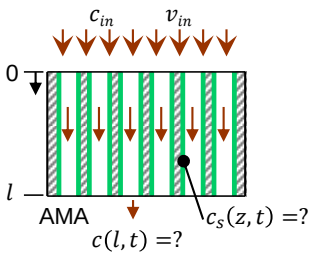

Chapter 6

Development of the adsorption process model

The model to describe the adsorption process occurring within the affinity membrane adsorber (AMA) will be developed through this chapter. Fig. 6.1 illustrates the schematic diagram of the AMA that is used for the model simulation. The feed solution of the particles flows through the AMA while the particles adsorb and desorb from the membrane surface.

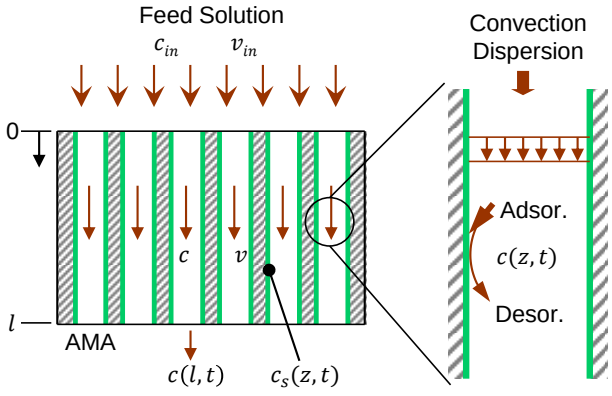

Figure 6.1: Schematic diagram of an affinity membrane adsorber.

In the following, the kinetic model for the adsorption process in the AMA is first developed based on the multi-site kinetic model developed in Chapter 5. Additionally, the mass balances for the particles in the mobile phase and in the solid phase are developed

as well. In order to understand the concentration distribution of the solution injected at the inlet of the AMA, a dispersion model is proposed. It is also important to describe the dispersion effects on the breakthrough of the particle solutions through the AMA. After the development of model equations, the adsorption process model and the dispersion model are both validated by fitting the simulated curves to their corresponding experimental data that are taken in Chapter 4. Simultaneously, the unknown parameters, including the volumetric parameters in the dispersion model and the kinetic parameters in the adsorption process model, are estimated. Finally, the adsorption process of the AMA is simulated with regard to the column dynamics and the adsorption isotherm, and furthermore the optimal design is discussed in terms of process time and material consumption.

6.1 Adsorption process model of an affinity membrane adsorber

During the development of the model equations, the following assumptions are introduced.

- A laminar flow due to the relatively low flow rate
- The negligible concentration gradient in the radial direction
- A cylinder with straight channels representing all constitutive pores inside AMA (see Fig. 6.1)
- A constant interstitial flow velocity
- A plug flow with convection and axial dispersion
- Particle adsorption and desorption at the membrane surface of the pore wall

In the mobile phase, the mass balance of BioNPs is

$$\varepsilon \frac{\partial c}{\partial t} = -\varepsilon v \frac{\partial c}{\partial z} + \varepsilon D \frac{\partial^2 c}{\partial z^2} - (1-\varepsilon) r \tag{6.1}$$

where c is the concentration of bionanoparticles in the mobile phase, mg/ml; ε is the void porosity and has a value of 0.8 according to Chapter 4; t is time, s, and z is the axial distance from the inlet surface, cm; v is the constant interstitial velocity, about 0.004 cm/s according to Chapter 4; D is the diffusivity of BioNP4, which was provided in Chapter 2; r is the adsorption rate of BioNP4 to the receptor surface of AMA.

In the solid phase, the mass balance of adsorbed BioNPs is

$$\frac{\partial c_s}{\partial t} = r \tag{6.2}$$

where c_s is the concentration of adsorbed BioNP4 in the solid phase, mg/ml.

The adsorption rate expression is

$$r = k_a c \cdot c_{R_n} - k_d c_s \tag{6.3}$$

where c_{R_n} is the concentration of the cluster of receptors bound to one single BioNP4, mg/ml; k_a is the adsorption kinetic rate constant, ml/(mg • s), and k_d is the desorption kinetic rate constant, s^{-1}.

In Chapter 5 the multi-site kinetic model was developed to describe the multivalent adsorption between BioNPs and receptors immobilized on the micro-scale surface. Based on that, the concentration of the cluster of receptors can be expressed as

$$c_{R_n} = c_{R_n}^{max} - nc_s \tag{6.4}$$

where $c_{R_n}^{max}$ is the maximum capacity of the available receptor clusters for adsorbing BioNPs, about 0.1 mg/ml calculated based on the experimental data in Chapter 4. n is the number of bonds formed between one single particle and surface receptors, which has been illustrated in Fig. 5.3 in Chapter 5.

The adsorption isotherm under the condition of equilibrium, i.e., $r = 0$, can be then derived as

$$c_{s_equilibrium} = \frac{c_{in} c_{R_n}^{max}}{nc_{in} + K_d} \tag{6.5}$$

where K_d is the desorption equilibrium constant, $K_d = k_d/k_a$.

Danckwerts' boundary condition was taken as the inlet boundary condition

$$\varepsilon v c(z = 0, t) - \varepsilon D \frac{\partial c(z = 0, t)}{\partial z} = v_{in} c_{in} \tag{6.6}$$

where v_{in} is the inlet velocity and equals to $\varepsilon \cdot v$; c_{in} is the inlet concentration of the particle solution and will be solved using the dispersion model based on the concentration of the feed solution in the next section.

The outlet boundary condition was assumed as the open vessel condition

$$\frac{\partial c(z = l, t)}{\partial z} = 0 \tag{6.7}$$

Initial conditions of the particle concentration both in the mobile phase and in the solid phase are

$$c(z, t = 0) = 0 \tag{6.8}$$

$$c_s(z, t = 0) = 0 \tag{6.9}$$

After putting Eq. (6.3) and Eq. (6.4) in Eq. (6.2), the dimensionless set of mass balances, Eq. (6.1) and Eq. (6.2), yields

$$\frac{\partial\theta}{\partial\tau} = -\frac{\partial\theta}{\partial\zeta} + \frac{1}{Pe}\frac{\partial^2\theta}{\partial\zeta^2} - m\frac{\partial\theta_s}{\partial\tau} \tag{6.10}$$

$$\frac{\partial\theta_s}{\partial\tau} = Da\theta(1 - n\theta_s) - b\theta_s \tag{6.11}$$

Boundary conditions

$$\theta(\zeta = 0, \tau) - \frac{1}{Pe}\frac{\partial\theta(\zeta = 0, \tau)}{\partial\zeta} = \varepsilon \tag{6.12}$$

$$\frac{\partial\theta(\zeta = 1, \tau)}{\partial\zeta} = 0 \tag{6.13}$$

Initial conditions

$$\theta(\zeta, \tau = 0) = 0 \tag{6.14}$$

$$\theta_s(\zeta, \tau = 0) = 0 \tag{6.15}$$

The dimensionless equations will be applied later to the estimation of parameters. The dimensionless parameters are defined as follows:

Table 6.1: Dimensionless parameters.

$\tau = \frac{t}{l/v}$	Dimensionless time variable
$\zeta = z/l$	Dimensionless spatial variable
$\theta = c/c_{feed}$	Dimensionless particle concentration in the mobile phase
$\theta_s = c_s/c_{R_n}^{max}$	Dimensionless particle concentration in the solid phase
$Pe = lv/D$	Axial Péclet number
$m = \frac{(1-\varepsilon)c_{R_n}^{max}}{\varepsilon c_{feed}}$	Ratio of maximum receptor capacity to feed particle concentration
$Da = \frac{k_a}{v/(lc_{feed})}$	Damköhler number
$b = \frac{l/v}{1/k_d}$	Ratio of convective time scale to desorption time scale

To simulate the particle concentration distribution in space, the partial differential equation, Eq. (6.10), was transformed into the discrete differential equations by combining

Eq. (6.12) and Eq. (6.13). The discretization in the spatial domain ($\zeta \in [0,1]$) was based on finite volume method.

$$\frac{d\theta_1}{d\tau} = \frac{\varepsilon - \theta_1}{\Delta\zeta} + \frac{1}{Pe}\frac{\theta_2 - \theta_1}{\Delta\zeta^2} - m\frac{d\theta_{s,1}}{d\tau} \tag{6.16}$$

$$\frac{d\theta_i}{d\tau} = -\frac{\theta_i - \theta_{i-1}}{\Delta\zeta} + \frac{1}{Pe}\left(\frac{\theta_{i+1} - \theta_i}{\Delta\zeta^2} - \frac{\theta_i - \theta_{i-1}}{\Delta\zeta^2}\right) - m\frac{d\theta_{s,i}}{d\tau} \tag{6.17}$$

$$\frac{d\theta_I}{d\tau} = -\frac{\theta_I - \theta_{I-1}}{\Delta\zeta} - \frac{1}{Pe}\frac{\theta_I - \theta_{I-1}}{\Delta\zeta^2} - m\frac{d\theta_{s,I}}{d\tau} \tag{6.18}$$

where i is the spatial volume element, which is an integer with $2 \leq i \leq I-1$; I is the total number of the volume elements and is 100 here.

Accordingly,

$$\frac{d\theta_{s,j}}{d\tau} = Da\theta_j\left(1 - n\theta_{s,j}\right) - b\theta_{s,j} \tag{6.19}$$

where j corresponds to each volume element, $1 \leq j \leq I$.

The implementation of the discrete differential equations was performed using the ode15s solver in MATLAB 7.12.0 (R2011a).

6.2 System dispersion model of the LC system

The breakthrough curves are influenced by the adsorption occurring in the AMA and by the dispersion happening before the AMA. In order to account for the dispersion effects, a model has been developed. The importance of developing the appropriate model to describe the dispersion effects has been demonstrated by experimental detections in Chapter 4. There are two major effects of the dispersion. One is the broadening of the pulse response that can be described via the CSTR model (an ideal continuously stirred tank reactor). The other is the time delay of the pulse response that can be described via the PFR model (an ideal plug flow reactor). Therefore, a combination of CSTR with PFR in series was proposed to compose the system dispersion model as illustrated in Fig. 6.2. Based on that, the profiles of the particle concentrations in the experimental system before entering the AMA can be obtained by solving the mass balances of two reactors in Fig. 6.2.

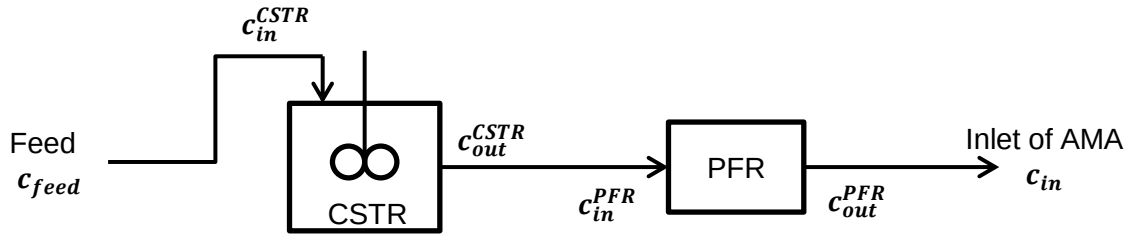

Figure 6.2: System dispersion model.

Mass balance for the CSTR model is

$$\frac{dc_{out}^{CSTR}}{dt} = \frac{Q}{V_{CSTR}}\left(c_{in}^{CSTR} - c_{out}^{CSTR}\right) \tag{6.20}$$

where c_{in}^{CSTR} is the inlet concentration of CSTR model, $c_{feed} = c_{in}^{CSTR}$; Q is the volumetric flow rate, 1ml/min.

With an initial condition for the outlet concentration of CSTR, c_{out}^{CSTR}

$$c_{out}^{CSTR}(t = 0) = 0 \tag{6.21}$$

Mass balance for the PFR model is

$$c_{out}^{PFR}(t) = \begin{cases} 0, \ t < V_{PFR}/Q \\ c_{in}^{PFR}, \ t \geq V_{PFR}/Q \end{cases} \tag{6.22}$$

where $c_{out}^{PFR}(t)$ is the outlet concentration of PFR model, which equals to the inlet concentration of AMA $c_{in} = c_{out}^{CSTR}$; c_{in}^{PFR} is the inlet concentration of PFR model, $c_{in}^{PFR} = c_{out}^{CSTR}$.

Finally, the inlet concentration for the affinity membrane adsorber can be analytically solved

$$c_{in}(t) = \begin{cases} 0, \ t < V_{PFR}/Q \\ c_{feed}\left(1 - e^{-\frac{t - V_{PFR}/Q}{V_{CSTR}/Q}}\right), \ t \geq V_{PFR}/Q \end{cases} \tag{6.23}$$

where c_{feed} is the concentration of feed solution and is about 2 x 10^{-6} mg/ml according to the experimental results of BioNP4 in Chapter 2.

To connect to the dimensionless forms of mass balances in the adsorption process of AMA in the last section, the inlet concentration was expressed in the following dimensionless form

$$\theta_{in}(\tau) = \begin{cases} 0, & \tau < \tau_{PFR} \\ 1 - e^{-\frac{\tau - \tau_{PFR}}{\tau_{CSTR}}}, & \tau \geq \tau_{PFR} \end{cases} \quad (6.24)$$

where the dimensionless time τ is listed in Table 5.1; τ_{PFR} represents a time delay, $\tau_{PFR} = \frac{V_{PFR}/Q}{l/v}$; τ_{CSTR} represents a time resulted from the system mixing effect, $\tau_{CSTR} = \frac{V_{CSTR}/Q}{l/v}$. Importantly, for the simulation, $\theta_{in}(\tau) = c_{in}/c_{feed}$ equals to θ_1 in Eq. (6.16).

To solve the inlet concentration, $c_{in}(t)$ or $\theta_{in}(\tau)$, two volumetric parameters, V_{CSTR} and V_{PFR}, need to be estimated first. For that purpose, a system volume, V_{system}, was considered here to represent the total volume of the fluidic flow in the experimental system. In reality, it is composed of the void volume of AMA and the external volume of the LC device. Here, from the model point of view, V_{system} can be expressed as

$$V_{system} = V_{CSTR} + V_{PFR} + V_{AMA} \quad (6.25)$$

where the volume of AMA, V_{AMA}, can be omitted when the experimental data was obtained without the connection of AMA.

Furthermore, the value of V_{system} can be approximated based on the mean residence time, $t_{residence}$ (see Eq. (4.1) and Table 4.1 in Chapter 4), and the flow rate, Q

$$V_{system} = Q t_{residence} \quad (6.26)$$

With the help of V_{system}, it is possible to estimate only either V_{CSTR} or V_{PFR} based on the fitting of simulated curves to experimental data.

6.3 Parameter estimation

6.3.1 Volumetric parameters in the dispersion model

Experimental data in Fig. 4.5 was taken as an example to estimate two volumetric parameters, V_{CSTR} and V_{PFR}. Fig. 6.3 illustrates the comparison between the simulation curve and experimental data. The curve was simulated on the basis of the estimated parameters. The experimental data were measured under the condition that naked NPs without the ligand-coating layer were injected through the receptor immobilized AMA. Thus, the volume of AMA was included in the calculation of the system volume. In addition, there is no multivalent interaction and, thus, the adsorption term, $m\frac{\partial \theta_s}{\partial \tau}$, in Eq. (6.10) can be neglected. Furthermore, the axial Péclet number was about 5 x 10^4, and, thus, the diffusional term, $\frac{1}{Pe}\frac{\partial^2 \theta}{\partial \zeta^2}$, in Eq. (6.10) can be also cancelled due to the coefficient $\frac{1}{Pe} \ll 1$. Finally, the mass balance in Eq. (6.10) was reduced as

$$\frac{\partial \theta}{\partial \tau} = -\frac{\partial \theta}{\partial \zeta} \tag{6.27}$$

Eq. (6.27) elucidates that the flow behavior of particles through AMA was influenced mainly by the convection. As a short summary, Eq. (6.27) together with Eq. (6.24) were used to simulate the particle concentration profile at the outlet of AMA, as the example of simulation curve shown in Fig. 6.3. The experimental noise before the breakthrough point, as illustrated in Fig. 4.5, was taken out by setting the signal as zero in order to support the parameter estimation. The estimated parameters for the volumes as displayed in Eq. (6.25) were listed in Table 6.2. The results in Figure 6.3 demonstrate that the proposed dispersion model as illustrated in Fig. 6.2 is suitable for describing the dispersion effects of the experimental system.

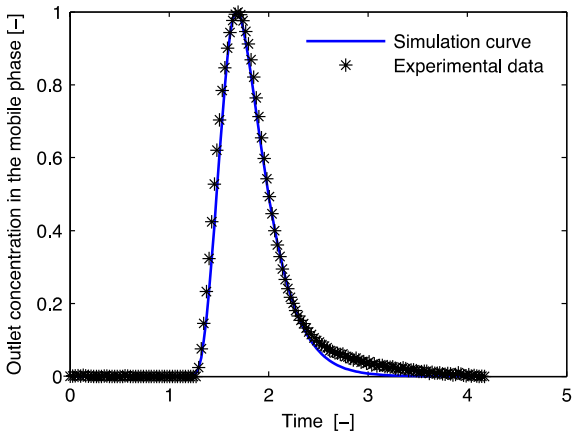

Figure 6.3: Comparison of simulated curve with experimental data. The simulation curve was plotted based on Eq. (6.24) and Eq. (6.27) using the estimated volumetric parameters in Table 6.2. The experimental data was taken from Figure 4.5 in Chapter 4.

By comparing the volume of AMA with the other volumes, it confirms the previous prediction (see section 4.3.1) in which the volume resulted from the flow non-idealities is comparable to the volume of the applied adsorber in the lab scale.

Table 6.2: Volumetric parameters in the dispersion model.

Volumetric parameters	V_{system}	V_{AMA}	V_{CSTR}	V_{PFR}
Value, ml	3.6	2	0.6	1

6.3.2 Kinetic parameters in the adsorption process model

After the validation of the dispersion model, the kinetic parameters in the process model for the multivalent interaction between BioNP4 and AMA can be estimated. The

experimental example was taken from Fig. 4.8 in Chapter 4. Figure 6.4 displays an acceptable fitting result of the simulation curve to the experimental data. The curve was simulated using the estimated parameters in Table 6.3. The experimental noise in Fig. 4.8 before the breakthrough point was neglected here by setting the signals as zero in Fig. 6.4. The purpose was to support the parameter estimation. Fig. 6.4 demonstrates that the derived multi-site kinetic model, Eq. (6.11), is appropriate to describe the adsorption behavior of biological nanoparticles through the affinity membrane adsorber.

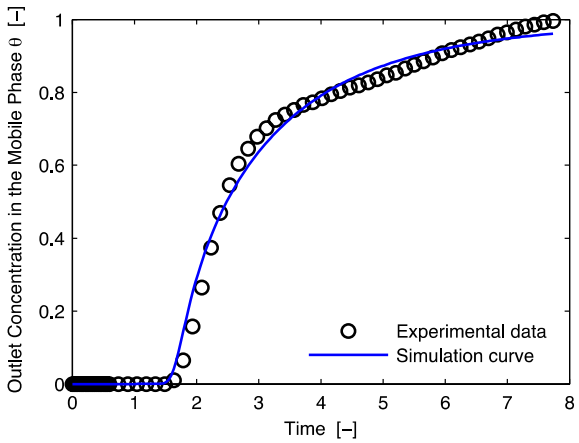

Figure 6.4: Comparison of simulation curve with experimental data. The simulation curve was plotted based on Eq. (6.10) with the help of the inlet concentration function, Eq. (6.24), using the estimated parameters in Table 6.3. The experimental data was taken from Figure 4.8 in Chapter 4.

Table 6.3 displays the estimated results of the kinetic parameters in the process model. The number of bonds, n, is about 71, which sounds reasonable according to the ligand numbers per BioNP4, 933, in Table 2.2 in Chapter 2. It is interesting to compare it with the estimated result (more than 200) based on the micro-scale surface in Chapter 5. It seems that the particle has less bonds formed with receptors in the adsorber unit in the LC system than on a micro-scale surface in the SPR system. Besides, the desorption equilibrium constant, $K_d = k_d/k_a$, can be calculated as about 1.7x10^{-3} mg/ml.

Table 6.3: Estimated kinetic parameters of the multivalent interaction.

Kinetic parameters	k_a, ml•mg^{-1}•s^{-1}	k_d, s^{-1}	n, -
Values	18.67	0.032	71

6.4 Simulation of the adsorption process of AMA

The dispersion model and the adsorption process model have been both validated by fitting the simulation curves to the corresponding experimental data. After their validation, they can be used to simulate the adsorption process of AMA, which provides more theoretical knowledge in addition to the experimental data. In particular, the adsorber

dynamics and the adsorption isotherm at the equilibrium are the two focuses here. The biggest advantage of the proposed multi-site kinetic model is that the adsorption behavior can be compared under the influence of the bond number in addition to the receptor capacity. The purpose of this section is to provide useful knowledge for an optimal design of the affinity membrane adsorber.

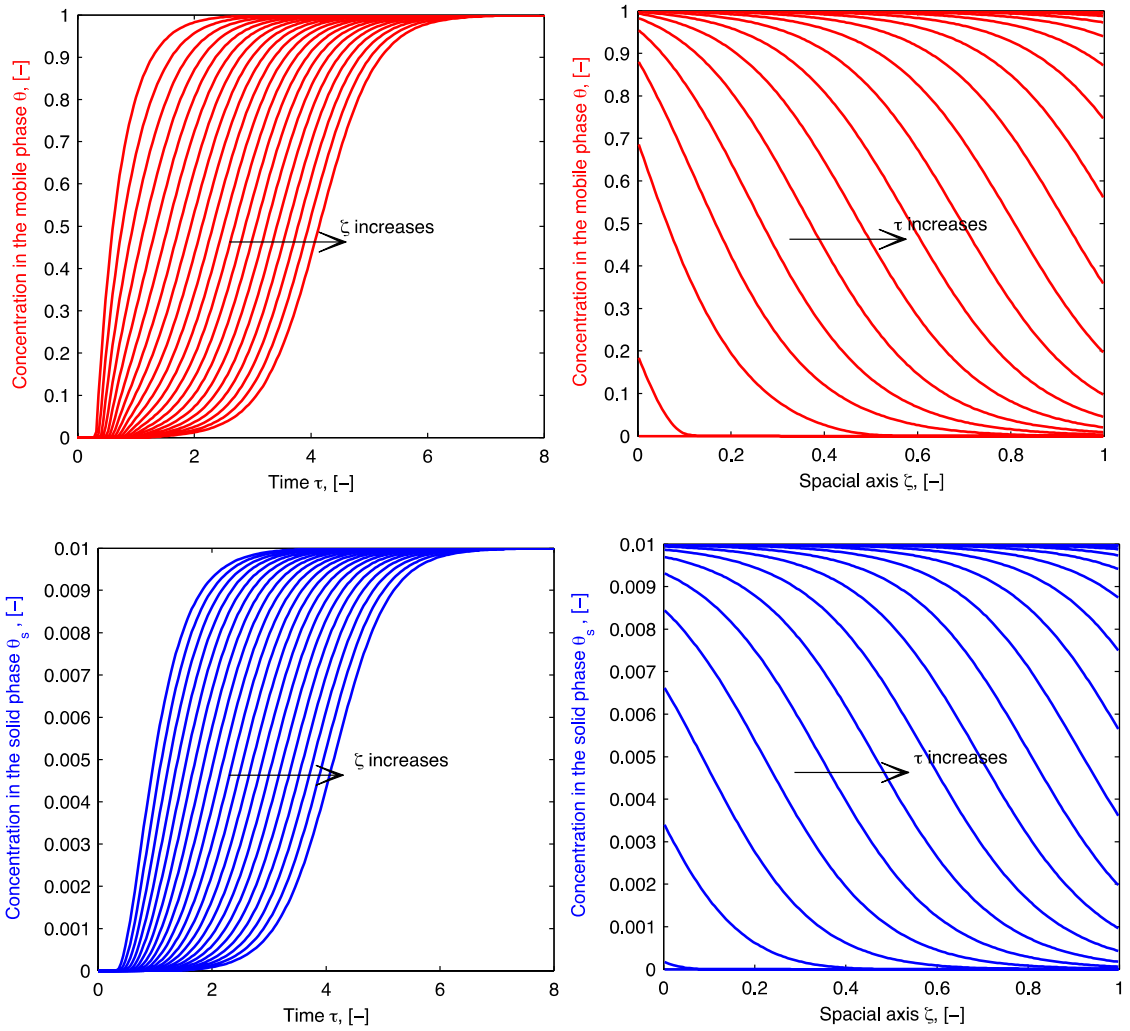

Figure 6.5: Concentration distributions of particles in the mobile phase and in the solid phase. The estimated parameters were taken in Table 6.2 and Table 6.3, and the other experimental related ones were taken in Chapter 4.

Fig. 6.5 illustrates the concentration distributions of particles in space domain as well as in time domain. The concentration distribution of particles in the mobile phase in the time axis shows that the concentration keeps increasing with increasing time at all positions until it reaches the inlet concentration. This increase becomes gradually slow as the flow moves its position in the flow direction. Additionally, the concentration distribution of particles in the mobile phase on the spatial axis shows that at the beginning of the injection (time t = 0) the local concentrations are zero due to no exiting solution, and then

appear a decrease starting from the inlet in the flow direction before they grow as a constant (1 in Fig. 6.5) as time increases. Furthermore, by comparing the shapes of the decreasing profiles in the space axis among all non-zero time points, i.e., the slope of the concentration curve, it appears that, as time increases, the concentration at the positions near the outlet arrives at the feed concentration later than that near the inlet. In contrast with the zero value at the beginning, all the local dimensionless concentrations arrive at 1, which implies that concentrations at all local positions arrive at a steady level that equals to the inlet concentration at the end of the injection. For the concentration distribution of particles in the solid phase, Fig. 6.5 displays that simulation curves both in space domain and in time domain have nearly the same variation as them in the case of the mobile phase. In terms of the dimensionless quantity, the final concentration in the solid phase at the steady state is two orders of magnitude smaller than that in the mobile phase. It is obvious that the local adsorption amounts decrease in the flow direction until they become constant at the adsorption equilibrium. Particularly, the adsorption near the inlet position arrives at the adsorption equilibrium earlier than that near the outlet position.

In addition to the adsorption dynamics of the affinity membrane adsorber (AMA) illustrated in Fig. 6.5, Fig. 6.6 elucidates the isotherm of AMA that was applied to the experimental studies in Chapter 4. The curve was plotted using Eq. (6.5). The shape of the adsorption isotherm demonstrates that the equilibrium concentration of adsorbed particles in the solid phase grows quickly as the inlet concentration increases. For the here applied AMA in the lab scale, the final equilibrium concentration that saturates the receptor capacity of AMA is about 1.4 x 10^{-3} mg/ml when the inlet concentration of the particle solution is no smaller than 1.5 x 10^{-3} mg/ml. It indicates that the model simulation can provide useful information to generally estimate the dynamic binding capacity of AMA.

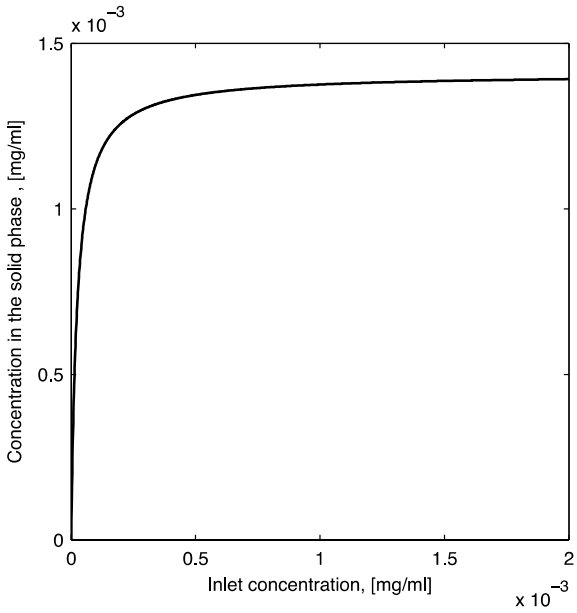

Figure 6.6: Isotherm. The simulation conditions were taken from the applied experimental system in this work.

Two further examples concerning the optimal design of AMA are illustrated in Fig. 6.7. The simulation curves were plotted under the condition of the applied experimental system. Fig. 6.7 (a) shows the influence of the number of bonds, n, on the breakthrough curves of AMA. From the aspect of time, it can save the time when the number of bonds formed between a single biological nanoparticle and membrane receptors is increase. The example here is that time is reduced in half (from 12 minutes to 6 minutes) when n increases from 1 to 800. Here the change of bond number can be caused by the density change of ligands attached to a single particle. The ligand density can be different due to different production batch of the biological particles in the upstream processing, which may serve as an influencing factor from the upstream processing. Therefore, it seems that the number of bonds can be an important parameter that conveys the information of the upstream processing to the downstream processing in the modeling approach. Fig. 6.7 (b) illustrates the influence of the receptor capacity, $c_{R_n}^{max}$, on the breakthrough curves. From the aspect of material amount, when the increase of the adsorbed amount of particles in the AMA is aimed, one can increase the receptor capacity. The curves exemplify that the breakthrough point can be delayed by increasing, $c_{R_n}^{max}$. For the given inlet solution, the delay of the breakthrough points indicates the increase of the adsorbed amount of particles.

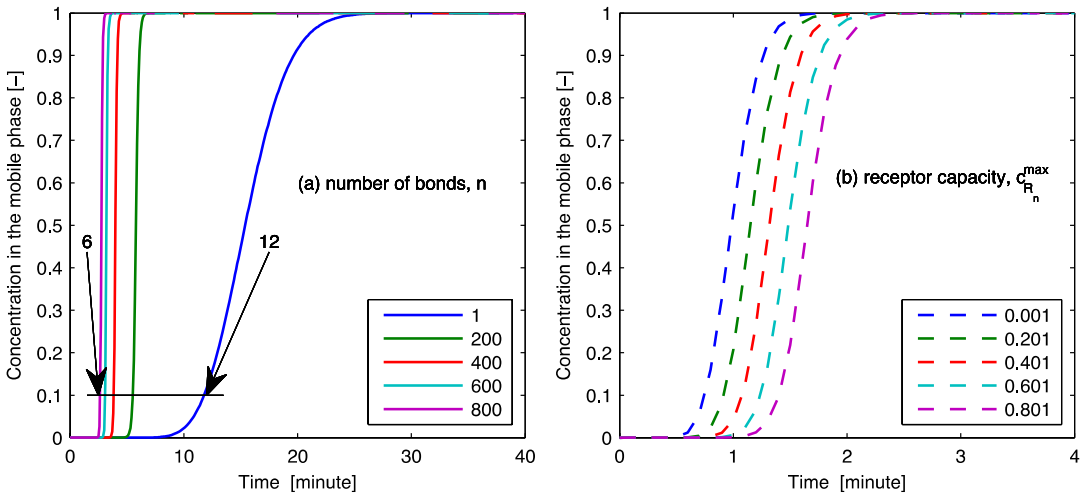

Figure 6.7: Influence of the number of bonds (a) and the receptor capacity (b) on breakthrough curves.

In brief, one can simulate the adsorption dynamics and equilibrium by changing the target parameters under different conditions that are related to the practical processes. Therefore, the adsorption model along with the dispersion model is valuable for designing the affinity membrane adsorber.

6.5 Summary

This chapter clarifies that the adsorption kinetic model in a unit operation (LC system) can be connected to that on a micro-scale surface (SPR system in Chapter 5). The adsorption process model together with the dispersion model was developed and validated to describe the breakthrough of the particles through the AMA. The results also demonstrate that it is a valid approach to quantitatively analyze the experimental data from the man-made biological systems by means of estimating the key parameters from the developed model equations. With this, one can simulate the adsorption breakthrough curves in order to analyze the adsorption process in terms of time and material. If one wants to save the process time by speeding up the breakthrough point, one can increase the number of bonds by increasing the attached-ligand density on a single particle surface or the immobilized-receptor density on the membrane surface. It means that the consumption of the materials (ligand or receptor) will be high. On the other hand, if the capture amount of the targeted particles by an AMA is to be increase rather than saving the process time, one can delay the breakthrough point. In these circumstances, one possible way is to increase the maximum density of the receptors immobilized on the membrane surface. The breakthrough curve appears a parallel delay mode when the receptor capacity increases in series. Moreover, the dynamic binding capacity of an AMA can be approximately calculated with the help of the isotherm.

Chapter 7

Summary, conclusion and outlook

7.1 Summary and conclusion

This thesis clarifies the modeling approaches as well as the experimental methods on how to implement the concept of the multivalent adsorption for the biological technologies. Thus, the challenges lie in the quantitative agreements between experimental data and simulation results. This work is first initiated by a cooperation project between the group of Process Systems Engineering (Prof. Dr.-Ing. Kai Sundmacher) and the group of Bioprocess Engineering (Prof. Dr.-Ing. Udo Reichl) of Max Planck Institute for Dynamics of Complex Technical Systems. Accordingly, the beginning task of this work is to model the capture of influenza virus by the affinity membrane adsorber in order to establish a model framework as a tool for the optimal design of such an adsorber.

In searching of pivotal experimental data used for the model identification, the biomimetic systems are experimentally established with the help of the chemical synthesis reactions. The assembling method is simple with respect to the experimental procedure, efficient with respect to time, and low with respect to cost. Moreover, it is stable enough to be reproducible and repeatable. Chapter 2 clarifies the synthesis method that uses a carbodiimide reaction to coat polystyrene particles with human IgGs. This chapter also indicates that the biological activity can be obtained by performing an oriented conjugation, e.g., manipulating the position of the reacting groups of ligands. In particular, the assembled particle mimics the geometrical structure of the influenza virus particle. Besides, a simple way to vary the coating in terms of the ligand density and the layer number is to change the amount ratio of ligands to the uncoated nanoparticles during conjugation. Here, corresponding to the affinity of human IgGs, the receptor is Protein A. The receptor-membrane surface is varied via changing the immobilized-receptor density, which is intended to mimic some biological targeting situations as well as the membrane surface of the adsorber. The assembled ligand-particle entities are then used for the entire experimental part in this work, including Chapter 3 and Chapter 4. From these two chapters, the striking point is that the synthesized multivalent adsorption can be operational for detecting the adsorption kinetics in the phase level, i.e., the microfluidic channel in the SPR system, and also for measuring the adsorption process in the unit level, i.e., the affinity membrane adsorber in the LC system. The connected experimental data allows the continuous developments of the models from the kinetic details to the process performances.

Concerning the model development of the multivalent adsorption kinetics, the multi-site kinetic model is proposed and identified from experimental data in Chapter 5. Its

advantage is that the number of bonds formed between a single ligand-particle and some receptors on the membrane surface is parameterized into the equations in addition to the adsorption rate constants. By performing parameter estimation, the bond number on average can be quantitatively evaluated under each experimental condition. It opens up a new way to analyze the correlation of the adsorption kinetics with the ligand density and the receptor density. The results in Chapter 5 imply that the adsorption rate can be higher when the number of bonds is smaller that is caused by the relatively lower surface receptor density. Based on the proposed multi-site kinetic model, the adsorption kinetic model of the biological particles through the affinity membrane adsorber is developed in Chapter 6. As related to the surface property of biological particle, the number of bonds can be seen as a type of input from the production in the upstream processing. Hence, by analyzing the influence of this bond number on the capture of biological particles via AMA, it provides a way to evaluate the production effects of the upstream processing on the capture of the downstream processing in a modeling approach. Such a way may imply that the modeling between the downstream processing and the upstream processing can be bridged with the help of parameterizing the key factors. Besides, the modeling studies using SPR device in Chapter 5 give an analytical solution to describe the mass transport in addition to the adsorption kinetics. With respect to designing AMA, its process dynamic model and the isotherm at the adsorption equilibrium are both derived in Chapter 6. The former displays the frontal analysis of the breakthrough curves and the later implies the dynamic binding capacity of AMA. By varying the parameters, the model simulation results show that an optimal design of AMA has to handle the conflict between material consumption and time duration.

In summary, the most important achievement of this work is to realize the concept of the multivalent adsorption for its applications to the biological technologies guided by the methodology of the process systems engineering. Furthermore, it is novel to quantitatively evaluate the multivalence, i.e., the number of bonds, in a more systematic way.

7.2 Outlook

The results in this work are helpful to the applications of the multivalent adsorption to the biological technologies, mainly including the targeting of therapeutic nanoparticles and the separation of the biological particles. In the field of the biological targeting, the designing strategies normally rest on changing the ligand of biological nanoparticle or the receptor on the membrane surface. Thus, the results about the correlation of the adsorption kinetics with the ligand density and the receptor density in this work can contribute to the targeting design of the ligand-particle entity. Particularly, as human IgG is the ligand, it can be valuable for the antibody-modified pharmaceuticals. In the field of the biological separation, affinity chromatography is normally based on bead columns that result in the high mass transfer resistance, especially the diffusion through the beads, for the big biological particles, like influenza virus particles. Thus, in order to break the technology bottleneck, the affinity membrane adsorber with the porous structure has been proposed, which decreases the diffusion resistance that is finally almost negligible. This work shows the possible model methods for optimally designing such an affinity

membrane adsorber. In total, not to repeat the summarized results, the most important contributions of this thesis are:

- With the proposed multi-site kinetic model, the multivalence, or the number of bonds, or the avidity, can be estimated from the experimental data obtained either for the adsorption kinetics or for the adsorption process. It can be analyzed in a wide range of bond number starting from one to several thousands.
- With the selected affinity interaction partners, the multivalent adsorption can be experimentally performed at the molecular level for synthesizing entities, at the phase level for detecting adsorption kinetics, and at the unit level for measuring adsorption process. Beside the technical details, the multivalence can be varied by changing either the ligand density of nanoparticles or the receptor density on the membrane surface.

Certainly, there are still some other investigation aspects beyond this work. With the presented methods in this work, the influence of the structural elements on the adsorption can be measured, such as the geometry of the scaffold, the linker between the ligands and the nanoparticle, the layer number of the coating, the grouping effect of the receptors during the immobilization, the structure of the receptors, etc.. All of these analyses should be useful for the biological targeting. In addition, the scale-up of the affinity membrane adsorber is to be further investigated for the purpose of the industrial application, such as the capture of influenza virus particles. For this point, the model simulations can be based on the models in this work (see Chapter 6). However, the experimental investigations in the scaled-up adsorber should be newly performed again. Here the natural biological particles may be possibly tested. As a basic study, the experimental particles in this work are solved in the purified solution, which helps the model developments. As a further advanced study, the complex mixture of the biological nanoparticle together with the impurities should be investigated. In case of the influenza virus mixture, the influence of the impurities, e.g., the DNA and proteins of the host cells, on the adsorption process should be measured and also parameterized into the adsorption process model. This thesis opens up the possible development of the multivalent adsorption in the biological field.

Supplementary Information.

Derivation of system equations in SPR flow domain

A.1 Flow field equations

A.1.1. Entrance region

First, the assumption of steady laminar flow in Section 5.2.1 was made because of the small Reynolds number. The calculation of Reynolds number was as follows. The feed volume flow rate, Q, is 50 µl/min (see Section 3.3). Average velocity: $\overline{v_x} = \frac{Q}{2wh} = \frac{50\ \mu l/min}{0.5\ mm * 0.02\ mm} \approx 83.33$ mm/s. As a first rough estimation, take ρ and η as them of water at 25 °C: $\rho = 997.0479$ kg/m^3, η_w = 8.94 x 10^{-4} Pa·s. If characteristic length is the hydraulic diameter of the fluid flow in a rectangular duct: $d_H = \frac{4Area}{Perimeter} = \frac{4wh}{2(w+h)} = 2 * \frac{0.5\ mm * 0.02\ mm}{0.52\ mm} \approx 0.0385$ mm, then $Re_d = \frac{\rho v l}{\eta}$ = (997.0479 * 83.33 x 10^{-3} * 0.0385x10^{-3}) / 8.94x10^{-4} ≈ 3.58. If characteristic length is the length of the flow cell 2 mm, then $Re_l =$ (997.0479 * 83.33 x 10^{-3} * 2x10^{-3}) / 8.94x10^{-4} ≈ 185.87. Both Reynolds numbers are low. So, the particle solution can be considered as a laminar flow.

Second, the density of the total mass in the fluid ρ can be assumed constant because the adsorbed amount of BioNPs compared with the total amount of BioNPs during the injection time for the adsorption detection is too small to be neglected. For example, the final RU signal in Fig. 3.6 (f) is about 391.19 RU. As 1 RU ≈ 1607 virons/mm^2, the reduced amount, Δm_{reduce}, due to the adsorption in the probing area is roughly calculated as: 391 RU x 1607 virons/mm^2 x 0.5 mm x 2 mm ≈ 6.3x10^5 virons. But the total amount in the inlet is roughly as: 50 ul/min x 389 s x 5.1x10^9 virons/ml = 1.6*10^9 virons. Comparing Δm_{reduce} with the inlet amount, the reduced amount Δm_{reduce} can be neglected. Thus, the density of total mass $\rho = \text{constant}$, so $\frac{\partial \rho}{\partial t} = 0$. Viscosity $\eta = \text{constant}$, so kinematic viscosity $\frac{\partial v_j}{\partial t} = 0\ (j = x, y)$.

Some additional parameters have to be introduced. The residence time of the particle solution in the flow cell is $t_r = \frac{l}{\overline{v_x}}$ [s]. Here, $\overline{v_x}$ is calculated as 83.33 mm/s. So, $t_r \approx 0.024$ s, which is in an order of magnitude of O(10^{-2}). The adsorption time for the binding surface to reach the equilibrium is t_a [s], which has an approximate order of magnitude of O(10^2) according to RU curves in Section 3.3.

The fluid enters at $x = 0$ with $v_y = 0$ and $v_x = \overline{v_x}$. As the volume flow rate along the x direction should be the same, it is valid that

$$\overline{v_x}h = \int_0^h v_x\, dy$$

Here, because the fluid domain in the flow cell is assumed to be symmetrical along the central surface at $y = h$, the upper half domain from $y = 0$ to $y = h$ is

$$\Rightarrow \overline{v_x}h = \int_0^{\delta} v_e\left(2\left(\frac{y}{\delta}\right) - \left(\frac{y}{\delta}\right)^2\right)dy + \int_{\delta}^{h} v_e dy$$

$$\Rightarrow \overline{v_x}h = v_e\left(\frac{y^2}{\delta} - \frac{y^3}{3\delta^2}\right)\Bigg|_0^{\delta} + v_e(h-\delta)$$

$$\frac{v_e(x)}{\overline{v_x}} = \frac{h}{h - \frac{1}{3}\delta(x)} \tag{A.1}$$

A.1.2. Total mass balance

The total continuity equation is

$$\frac{\partial \rho}{\partial t} = -\frac{\partial}{\partial x}(\rho v_x) - \frac{\partial}{\partial y}(\rho v_y) \tag{A.2}$$

$$\because \rho = \text{constant}, \frac{\partial \rho}{\partial t} = 0 \ \therefore \ \frac{\partial v_x}{\partial x} + \frac{\partial v_y}{\partial y} = 0, \text{ i. e., } \frac{\partial v_k}{\partial z_k} = 0\ (k = x, y) \tag{A.3}$$

A.1.3. Momentum balance

$$\frac{\partial(\rho v_j)}{\partial t} = -\frac{\partial}{\partial z_k}\Big((\rho v_j)v_k + P_{jk}\Big) + \sum_{\alpha} \rho f_{j,\alpha}\ \ (j,k = x,y) \tag{A.4}$$

i) $\frac{\partial(\rho v_j)}{\partial t} = \rho \underbrace{\frac{\partial v_j}{\partial t}}_{\text{steady flow, 0}} = 0$

ii) $\frac{\partial}{\partial z_k}\Big((\rho v_j)v_k\Big) = \rho\left(v_k\frac{\partial v_j}{\partial z_k} + v_j\frac{\partial v_k}{\partial z_k}\right) = \rho v_k\frac{\partial v_j}{\partial z_k}$

iii) $P_{jk} = p\delta_{jk} + \pi_{jk}, \text{where } \delta_{jk} = \begin{cases}1, j = k\\ 0, j \neq k\end{cases}, \pi_{jk} = -\eta\left(\frac{\partial v_j}{\partial z_k} + \frac{\partial v_k}{\partial z_j}\right)$

$$-\frac{\partial P_{jk}}{\partial z_k} = -\frac{\partial}{\partial z_k}(p\delta_{jk} + \pi_{jk}) = -\frac{\partial p\delta_{jk}}{\partial z_k} - \frac{\partial}{\partial z_k}\left(-\eta\left(\frac{\partial v_j}{\partial z_k} + \frac{\partial v_k}{\partial z_j}\right)\right)$$

$$-\frac{\partial}{\partial z_k}\left(-\eta\left(\frac{\partial v_j}{\partial z_k} + \frac{\partial v_k}{\partial z_j}\right)\right) = \underbrace{\eta}_{\text{constant}}\left(\frac{\partial^2 v_j}{\partial {z_k}^2} + \frac{\partial}{\partial z_k}\left(\frac{v_k}{\partial z_j}\right)\right) = \eta\left(\frac{\partial^2 v_j}{\partial {z_k}^2} + \frac{\partial}{\partial z_j}\left(\underbrace{\frac{v_k}{\partial z_k}}_{0}\right)\right)$$

$$\Rightarrow -\frac{\partial P_{jk}}{\partial z_k} = -\frac{\partial p\delta_{jk}}{\partial z_k} + \eta\frac{\partial^2 v_j}{\partial {z_k}^2}$$

Finally, Eq. (A.4) becomes

$$\rho v_k \frac{\partial v_j}{\partial z_k} + \frac{\partial p \delta_{jk}}{\partial z_k} - \eta \frac{\partial^2 v_j}{\partial {z_k}^2} + \sum_\alpha \rho f_{j,\alpha} = 0 \; (j,k = x,y) \tag{A.5}$$

Retrieving Eq. (A.5) along each coordinate, it gives

$$v_x \frac{\partial v_x}{\partial x} + v_y \frac{\partial v_x}{\partial y} + \frac{1}{\rho}\frac{\partial p}{\partial x} - \nu\left(\frac{\partial^2 v_x}{\partial x^2} + \frac{\partial^2 v_x}{\partial y^2}\right) = 0 \tag{A.6}$$

$$v_x \frac{\partial v_y}{\partial x} + v_y \frac{\partial v_y}{\partial y} + \frac{1}{\rho}\frac{\partial p}{\partial y} - \nu\left(\frac{\partial^2 v_y}{\partial x^2} + \frac{\partial^2 v_y}{\partial y^2}\right) - g = 0 \tag{A.7}$$

A.1.4. Analysis based on the orders of magnitude and von Karman Method

An average thickness of the boundary layer $\bar{\delta}$ is presumed as $\bar{\delta} \ll l$ and it allows us to make a number of rough calculations of orders of magnitude. The maximum variation in v_x over the length l is $\overline{v_x}$, so that $\frac{\partial v_x}{\partial x} = \mathrm{O}\left(\frac{\overline{v_x}}{l}\right)$. Here, O means “order of magnitude of”, and the signs of the quantities are not concerned. With Eq. (A.3), $\frac{\partial v_y}{\partial y} = \mathrm{O}\left(\frac{\overline{v_x}}{l}\right)$. Similarly, the maximum variation in v_x over the boundary layer δ is approximated as $\frac{\partial v_x}{\partial y} = \mathrm{O}\left(\frac{\overline{v_x}}{\bar{\delta}}\right)$

$$v_y = \int \frac{\partial v_y}{\partial y} dy = \mathrm{O}\left(\frac{\bar{\delta}}{l}\overline{v_x}\right) \overset{\bar{\delta} \ll l}{\Longrightarrow} v_y \ll v_x$$

So, the terms in Eq. (A.6) may be estimated as

$$v_x \frac{\partial v_x}{\partial x} = \mathrm{O}\left(\frac{\overline{v_x}^2}{l}\right);$$

$$v_y \frac{\partial v_x}{\partial y} = \mathrm{O}\left(\frac{\bar{\delta}}{l}\overline{v_x}\right)\mathrm{O}\left(\frac{\overline{v_x}}{\bar{\delta}}\right) = \mathrm{O}\left(\frac{\overline{v_x}^2}{l}\right);$$

$$\frac{\partial^2 v_x}{\partial x^2} = \mathrm{O}\left(\frac{\overline{v_x}}{l^2}\right);$$

$\frac{\partial^2 v_x}{\partial y^2} = \mathrm{O}\left(\frac{\overline{v_x}}{\bar{\delta}^2}\right) \overset{\bar{\delta} \ll l}{\Longrightarrow} \frac{\partial^2 v_x}{\partial y^2} \gg \frac{\partial^2 v_x}{\partial x^2}$, so the latter can be safely neglected.

In the boundary layer it is expected that the terms of Eq. (A.6) should be the same order of magnitude, and therefore

$\frac{\overline{v_x}^2}{l} = \mathrm{O}\left(\nu\frac{\overline{v_x}}{\bar{\delta}^2}\right)$ or $\frac{\bar{\delta}}{l} = \mathrm{O}\left(\sqrt{\frac{\nu}{\overline{v_x} l}}\right) = \mathrm{O}\left(\sqrt{\frac{1}{\mathrm{Re}_l}}\right) \overset{Re_l = 185.87}{\Longrightarrow} \frac{\bar{\delta}}{l}$ has an order of magnitude, -2.

Similarly, it can be shown the terms in Eq. (A.7) as

$$v_x \frac{\partial v_y}{\partial x} = \mathrm{O}\left(\overline{v_x}\frac{\frac{\bar{\delta}}{l}\overline{v_x}}{l}\right) = \mathrm{O}\left(\overline{v_x}^2\frac{\bar{\delta}}{l^2}\right)$$

$$v_y \frac{\partial v_y}{\partial y} = \mathrm{O}\left(\frac{\bar{\delta}}{l}\overline{v_x}\frac{\bar{\delta}}{l}\frac{\overline{v_x}}{\bar{\delta}}\right) = \mathrm{O}\left(\overline{v_x}^2\frac{\bar{\delta}}{l^2}\right)$$

$$\frac{\partial^2 v_y}{\partial x^2} = \mathrm{O}\left(\frac{\bar{\delta}}{l}\frac{\overline{v_x}}{l^2}\right)$$

$\frac{\partial^2 v_y}{\partial y^2} = \mathrm{O}\left(\frac{\bar{\delta}}{l}\frac{\overline{v_x}}{\bar{\delta}^2}\right) \overset{\bar{\delta}\ll l}{\Longrightarrow} \frac{\partial^2 v_x}{\partial y^2} \gg \frac{\partial^2 v_x}{\partial x^2}$. So, the latter can be safely neglected.

$$\nu\frac{\partial^2 v_y}{\partial y^2} = \mathrm{O}\left(\nu\frac{\bar{\delta}}{l}\frac{\overline{v_x}}{\bar{\delta}^2}\right) \overset{\frac{\overline{v_x}^2}{l}=\mathrm{O}\left(\nu\frac{\overline{v_x}}{\bar{\delta}^2}\right)}{\Longrightarrow} \nu\frac{\partial^2 v_y}{\partial y^2} = \mathrm{O}\left(\overline{v_x}^2\frac{\bar{\delta}}{l^2}\right)$$

$$\mathrm{O}(\text{Eq. (A.6)}) = \mathrm{O}\left(\frac{\overline{v_x}^2}{l}\right), \mathrm{O}(\text{Eq. (A.7)}) = \mathrm{O}\left(\frac{\overline{v_x}^2}{l}\frac{\bar{\delta}}{l}\right) \Longrightarrow \frac{\partial p}{\partial y} \ll \frac{\partial p}{\partial x}$$

This means that the y-component of the momentum transport is not needed and that the modified pressure can be treated as a function of x alone.

As a result of these order-of-magnitude arguments, we get the Prandtl boundary layer equations:

$$\frac{\partial v_x}{\partial x} + \frac{\partial v_y}{\partial y} = 0 \tag{A.8}$$

$$v_x\frac{\partial v_x}{\partial x} + v_y\frac{\partial v_x}{\partial y} + \frac{1}{\rho}\frac{dp}{dx} - \nu\frac{\partial^2 v_x}{\partial y^2} = 0 \tag{A.9}$$

The function $p(x)$ is related to $v_e(x)$ according to the potential-flow equation of motion, $\frac{1}{2}\rho {v_e}^2 + p =$ constant. Therefore, $\frac{dp}{dx} = -\rho v_e\frac{dv_e}{dx}$. Thus Eq. (A.9) can be rewritten as

$$v_x\frac{\partial v_x}{\partial x} + v_y\frac{\partial v_x}{\partial y} - v_e\frac{dv_e}{dx} - \nu\frac{\partial^2 v_x}{\partial y^2} = 0 \tag{A.10}$$

With Eq. (A.3), v_y can be solved by using the boundary condition that $v_y = 0$ *at* $y = 0$

$$v_y = -\int_0^y \frac{\partial v_x}{\partial x}dy \tag{A.11}$$

Combining Eqs. (A.10) and (A.11) to give

$$v_x\frac{\partial v_x}{\partial x} - \left(\int_0^y \frac{\partial v_x}{\partial x}dy\right)\frac{\partial v_x}{\partial y} - v_e\frac{dv_e}{dx} - \nu\frac{\partial^2 v_x}{\partial y^2} = 0 \tag{A.12}$$

Now integrate Eq. (A.12) from $y = 0$ to $y = h$ because of the symmetrical geometry of the flow cell,

$$\int_0^h v_x\frac{\partial v_x}{\partial x}dy - \int_0^h\left(\int_0^y \frac{\partial v_x}{\partial x}dy\right)\frac{\partial v_x}{\partial y}dy - \int_0^h v_e\frac{dv_e}{dx}dy - \int_0^h \nu\frac{\partial^2 v_x}{\partial y^2}dy = 0 \tag{A.13}$$

For the second term in Eq. (A.13),

$$\int_0^h \left(\int_0^y \frac{\partial v_x}{\partial x} dy \right) \frac{\partial v_x}{\partial y} dy$$

According to the rule of integration by parts, $\int UP' dy = UP - \int U'P dy$.

Setting $U(y) = \int_0^y \frac{\partial v_x}{\partial x} dy, P'(y) = \frac{\partial v_x}{\partial y}$, then $U'(y) = \frac{\partial v_x}{\partial x}$ and $P = \int P'(y) dy = v_x$.

Therefore,

$$\begin{aligned} \int_0^h \left(\int_0^y \frac{\partial v_x}{\partial x} dy \right) \frac{\partial v_x}{\partial y} dy &= \left(v_x|_{y=h} \right) \left(\int_0^h \frac{\partial v_x}{\partial x} dy \right) - \int_0^h \frac{\partial v_x}{\partial x} v_x dy \\ &= v_e \int_0^h \frac{\partial v_x}{\partial x} dy - \int_0^h v_x \frac{\partial v_x}{\partial x} dy = \int_0^h v_e \frac{\partial v_x}{\partial x} dy - \int_0^h v_x \frac{\partial v_x}{\partial x} dy \end{aligned} \quad \text{(A.14)}$$

For the fourth term in the Eq. (A.13),

$$\int_0^h \nu \frac{\partial^2 v_x}{\partial y^2} dy = \nu \frac{\partial v_x}{\partial y}\Big|_0^h = \underbrace{\nu \frac{\partial v_x}{\partial y}\Big|_{y=h}}_{\text{symmetry},0} - \nu \frac{\partial v_x}{\partial y}\Big|_{y=0} = -\nu \frac{\partial v_x}{\partial y}\Big|_{y=0} \quad \text{(A.15)}$$

Substituting terms by Eqs. (A.14) and (A.15) into Eq. (A.13) to give

$$\int_0^h v_x \frac{\partial v_x}{\partial x} dy - \int_0^h v_e \frac{\partial v_x}{\partial x} dy + \int_0^h v_x \frac{\partial v_x}{\partial x} dy - \int_0^h v_e \frac{dv_e}{dx} dy + \nu \frac{\partial v_x}{\partial y}\Big|_{y=0} = 0 \quad \text{(A.16)}$$

Reformulating Eq. (A.16),

$$\begin{aligned} \nu \frac{\partial v_x}{\partial y}\Big|_{y=0} &= \int_0^h \left(\left(v_e \frac{\partial v_x}{\partial x} + v_x \frac{dv_e}{dx} \right) - v_x \frac{dv_e}{dx} - 2 v_x \frac{\partial v_x}{\partial x} + v_e \frac{dv_e}{dx} \right) dy \\ &= \int_0^h \left(\frac{\partial v_e v_x}{\partial x} - v_x \frac{dv_e}{dx} - \frac{\partial {v_x}^2}{\partial x} + v_e \frac{dv_e}{dx} \right) dy \\ &= \int_0^h \left(\frac{\partial}{\partial x} (v_e v_x - {v_x}^2) + (v_e - v_x) \frac{dv_e}{dx} \right) dy \\ &= \frac{d}{dx} \int_0^h (v_e v_x - {v_x}^2)\, dy + \frac{dv_e}{dx} \int_o^h (v_e - v_x)\, dy \end{aligned}$$

Finally, we get the momentum balance for the single dependent variable v_x based on the von Kármán method,

$$\nu \frac{\partial v_x}{\partial y}\Big|_{y=0} = \frac{d}{dx} \int_0^h v_x (v_e - v_x)\, dy + \frac{dv_e}{dx} \int_o^h (v_e - v_x)\, dy \quad \text{(A.17)}$$

According to the assumed velocity profiles (ref. Eqs. (5.12) and (5.13)), the terms in the Eq. (A.17) become

$$\nu \frac{\partial v_x}{\partial y}\Big|_{y=0} = \nu v_e \left(2 \frac{1}{\delta} - 2 \frac{y}{\delta^2} \right)\Big|_{y=0} = 2 \nu v_e \frac{1}{\delta} \quad \text{(A.18)}$$

$$\frac{d}{dx}\int_0^h v_x(v_e - v_x)\,dy$$

$$= \frac{d}{dx}\int_0^\delta v_x(v_e - v_x)\,dy + \frac{d}{dx}\int_\delta^h v_e(v_e - v_e)\,dy$$

$$= \frac{d}{dx}\int_0^\delta v_x(v_e - v_x)\,dy$$

$$= \frac{d}{dx}\int_0^\delta v_e\left(2\left(\frac{y}{\delta}\right) - \left(\frac{y}{\delta}\right)^2\right)\left(v_e - v_e\left(2\left(\frac{y}{\delta}\right) - \left(\frac{y}{\delta}\right)^2\right)\right)dy$$

$$= \frac{d}{dx}\int_0^\delta {v_e}^2\left(2\left(\frac{y}{\delta}\right) - \left(\frac{y}{\delta}\right)^2\right)\left(1 - 2\left(\frac{y}{\delta}\right) + \left(\frac{y}{\delta}\right)^2\right)dy$$

$$= \frac{d}{dx}\int_0^\delta {v_e}^2\left(2\left(\frac{y}{\delta}\right) - \left(\frac{y}{\delta}\right)^2 - 4\left(\frac{y}{\delta}\right)^2 + 2\left(\frac{y}{\delta}\right)^3 + 2\left(\frac{y}{\delta}\right)^3 - \left(\frac{y}{\delta}\right)^4\right)dy$$

$$= \frac{d}{dx}\left({v_e}^2\int_0^\delta \left(2\left(\frac{y}{\delta}\right) - 5\left(\frac{y}{\delta}\right)^2 + 4\left(\frac{y}{\delta}\right)^3 - \left(\frac{y}{\delta}\right)^4\right)dy\right)$$

$$= \frac{d}{dx}\left[{v_e}^2\left(\left(\frac{y^2}{\delta} - \frac{5}{3}\frac{y^3}{\delta^2} + \frac{y^4}{\delta^3} - \frac{1}{5}\frac{y^5}{\delta^4}\right)\Big|_0^\delta\right)\right]$$

$$= \frac{d}{dx}\left[{v_e}^2\left(\frac{\delta^2}{\delta} - \frac{5}{3}\frac{\delta^3}{\delta^2} + \frac{\delta^4}{\delta^3} - \frac{1}{5}\frac{\delta^5}{\delta^4}\right)\right]$$

$$= \frac{d}{dx}\left[{v_e}^2\left(\delta - \frac{5}{3}\delta + \delta - \frac{1}{5}\delta\right)\right]$$

$$= \frac{d}{dx}\left[{v_e}^2\delta\left(-\frac{2}{3} + \frac{4}{5}\right)\right]$$

$$= \frac{2}{15}\frac{d}{dx}({v_e}^2\delta)$$

$$\frac{d}{dx}\int_0^h v_x(v_e - v_x)\,dy = \frac{2}{15}{v_e}^2\frac{d\delta}{dx} + \frac{4}{15}\delta v_e\frac{dv_e}{dx} \qquad \text{(A.19)}$$

$$\frac{dv_e}{dx}\int_o^h (v_e - v_x)\,dy = \frac{dv_e}{dx}\int_o^\delta \left(v_e - v_e\left(2\left(\frac{y}{\delta}\right) - \left(\frac{y}{\delta}\right)^2\right)\right)dy$$

$$= \frac{dv_e}{dx}\int_o^\delta v_e\left(1 - 2\left(\frac{y}{\delta}\right) + \left(\frac{y}{\delta}\right)^2\right)dy$$

$$= \frac{dv_e}{dx}v_e\left(y - \frac{y^2}{\delta} + \frac{1}{3}\frac{y^3}{\delta^2}\right)\Big|_0^\delta$$

$$= \frac{dv_e}{dx}v_e\left(\delta - \frac{\delta^2}{\delta} + \frac{1}{3}\frac{\delta^3}{\delta^2}\right)$$

$$= \frac{dv_e}{dx} v_e \left(\delta - \delta + \frac{1}{3}\delta\right)$$

$$\frac{dv_e}{dx}\int_o^h (v_e - v_x)\, dy = \frac{1}{3}\delta v_e \frac{dv_e}{dx} \tag{A.20}$$

Finally, from Eqs. (A.17~A.20) it gives as

$$2\nu v_e \frac{1}{\delta} = \frac{2}{15} {v_e}^2 \frac{d\delta}{dx} + \frac{4}{15}\delta v_e \frac{dv_e}{dx} + \frac{1}{3}\delta v_e \frac{dv_e}{dx}$$

$$30\nu = 2v_e\delta \frac{d\delta}{dx} + 9\delta^2 \frac{dv_e}{dx} \tag{A.21}$$

According to Eq. (A.1), we get

$$v_e(x) = \frac{h\overline{v_x}}{h - \frac{1}{3}\delta(x)} \tag{A.22}$$

$$\frac{dv_e}{dx} = \frac{h\overline{v_x}}{3\left(h - \frac{1}{3}\delta\right)^2}\frac{d\delta}{dx} \tag{A.23}$$

With Eqs. (A.21-A.23),

$$30\nu = 2\frac{h\overline{v_x}}{h - \frac{1}{3}\delta}\delta\frac{d\delta}{dx} + 9\delta^2 \frac{h\overline{v_x}}{3\left(h - \frac{1}{3}\delta\right)^2}\frac{d\delta}{dx}$$

$$\Rightarrow 30\nu = \left(2\frac{h\overline{v_x}}{h - \frac{1}{3}\delta}\delta + 9\delta^2 \frac{h\overline{v_x}}{3\left(h - \frac{1}{3}\delta\right)^2}\right)\frac{d\delta}{dx}$$

$$\Rightarrow 30\nu = \frac{2h\overline{v_x}\delta\left(h - \frac{1}{3}\delta\right) + 3\delta^2 h\overline{v_x}}{\left(h - \frac{1}{3}\delta\right)^2}\frac{d\delta}{dx}$$

$$\Rightarrow 30\nu = \frac{18h^2\overline{v_x}\delta - 6h\overline{v_x}\delta^2 + 27\delta^2 h\overline{v_x}}{(3h - \delta)^2}\frac{d\delta}{dx}$$

$$10\frac{\nu}{h\overline{v_x}} = \frac{6h\delta + 7\delta^2}{(3h - \delta)^2}\frac{d\delta}{dx} \tag{A.24}$$

Let $\delta^* = \frac{\delta}{h}$, then $\frac{d\delta}{dx} = h\frac{d\delta^*}{dx}$. Substituting the terms into the Eq. (A. 24) to give

$$\frac{6\delta^* + 7{\delta^*}^2}{(3 - \delta^*)^2}\frac{d\delta^*}{dx} = 10\frac{\nu}{h^2\overline{v_x}} \tag{A.25}$$

Integrating Eq. (A.25) from $\delta^* = 0$ at $x = 0$,

$$\int_0^{\delta^*} \frac{6\delta^* + 7{\delta^*}^2}{(3 - \delta^*)^2} d\delta^* = \int_0^x 10\frac{\nu}{h^2\overline{v_x}} dx$$

$$\Rightarrow \int_0^{\delta^*} \frac{81-48(3-\delta^*)+7(3-\delta^*)^2}{(3-\delta^*)^2} d\delta^* = 10\frac{vx}{h^2\overline{v_x}}$$

$$\Rightarrow \int_0^{\delta^*} \left(\frac{81}{(3-\delta^*)^2} - \frac{48}{3-\delta^*} + 7\right) d\delta^* = 10\frac{vx}{h^2\overline{v_x}}$$

$$\Rightarrow \left(\frac{81}{3-\delta^*} + 48ln(3-\delta^*) + 7\delta^*\right)\Big|_0^{\delta^*} = 10\frac{vx}{h^2\overline{v_x}}$$

$$\Rightarrow \left(\frac{81}{3-\delta^*} + 48ln(3-\delta^*) + 7\delta^*\right) - \left(\frac{81}{3} + 48ln3\right) = 10\frac{vx}{h^2\overline{v_x}}$$

$$\Rightarrow 81\left(\frac{1}{3-\delta^*} - \frac{1}{3}\right) + 48(ln(3-\delta^*) - ln3) + 7\delta^* = 10\frac{vx}{h^2\overline{v_x}}$$

$$\frac{27\delta^*}{3-\delta^*} + 48ln\left(1-\frac{\delta^*}{3}\right) + 7\delta^* = \frac{10\nu}{h^2\overline{v_x}}x \tag{A.26}$$

With the Eq. (A.26), we can calculate the entrance length l_e shown in Fig. 5.5, where l_e is that value of x for which $\delta = h, i.e., \delta^* = 1$.

$$\frac{27}{3-1} + 48ln\left(1-\frac{1}{3}\right) + 7 = \frac{10\nu}{h^2\overline{v_x}}l_e$$

$$\Rightarrow l_e = \left(\frac{27}{2} + 48ln\frac{2}{3} + 7\right)\frac{h^2\overline{v_x}}{10\nu}$$

$$l_e \approx \frac{0.104h^2\overline{v_x}}{\nu} \tag{A.27}$$

where, $h = 0.01$ mm, $\overline{v_x} = 83.33$ mm/s, and $\nu = 0.897$ mm^2/s. So, $l_e = 9.66 * 10^{-4}$ mm.

A.1.5. Velocity profile

As the plausible assumption of fully developed flow, $\frac{\partial v_x}{\partial x} = 0$. With Eq. (A.3), $\frac{\partial v_y}{\partial y} = 0$, which means that v_y = constant. According to the boundary condition that $v_y = 0$ *at* $y = 0$, $v_y = 0$ at any position. We now look back into Eq. (A.9), by these simplifications,

$$\text{Eq. (A. 9)} \Longrightarrow v_x \underbrace{\frac{\partial v_x}{\partial x}}_{0} + \underbrace{v_y}_{0}\frac{\partial v_x}{\partial y} + \frac{1}{\rho}\frac{dp}{dx} - \nu\frac{\partial^2 v_x}{\partial y^2} = 0$$

Finally,

$$\frac{\partial^2 v_x}{\partial y^2} = \frac{1}{\eta}\frac{dp}{dx} \tag{A.28}$$

$$\frac{\partial v_x}{\partial x} = 0 \Rightarrow v_x = v_x(y) \Rightarrow \frac{\partial^2 v_x}{\partial y^2} = \frac{d^2 v_x}{dy^2} \tag{A.29}$$

Integrate Eq. (A.28) in the y direction, as $\frac{dp}{dx}$ is a term mentioned before with no relation of y, hence,

$$v_x = \frac{1}{2\eta}\left(\frac{dp}{dx}\right)y^2 + c_1 y + c_2 \tag{A.30}$$

B. C. : Continuity of velocity along the static wall⇒ $y = 0$ and $2h, v_x = 0$;

Symmetry about the central surface⇒ $y = h, \frac{dv_x}{dy} = 0$;

Finally, $c_1 = -\frac{h}{\eta}\frac{dp}{dx}$, $c_2 = 0$.

$$v_x = -\frac{h^2}{2\eta}\frac{dp}{dx}\left(2\left(\frac{y}{h}\right) - \left(\frac{y}{h}\right)^2\right) \tag{A.31}$$

$$Q = 2\int_0^h v_x(y)wdy = 2\int_0^h -\frac{h^2}{2\eta}\left(\frac{dp}{dx}\right)\left(2\left(\frac{y}{h}\right) - \left(\frac{y}{h}\right)^2\right)wdy = \left(-\frac{wh^2}{\eta}\frac{dp}{dx}\right)\left(\frac{y^2}{h} - \frac{y^3}{3h^2}\right)\Bigg|_0^h$$

$$\Rightarrow -\frac{h^2}{2\eta}\left(\frac{dp}{dx}\right) = \frac{3Q}{4wh} = \frac{3}{2}\overline{v_x}$$

$$v_x(y) = \frac{3}{2}\overline{v_x}\left(2\left(\frac{y}{h}\right) - \left(\frac{y}{h}\right)^2\right) \tag{A.32}$$

By comparing Eq. (A.32) with the assumed velocity profile (Eqs. (5.12-5.14)), it seems that the guess of velocity distribution in the entrance region may be safely reasonable.

A.2 Models for the species of virus

A.2.1. Mass balance of the virus in the fluid flow

$$\frac{\partial[P]}{\partial t} = -\frac{\partial}{\partial z_k}\left([P]v_k + j_{k,P}\right) \tag{A.33}$$

$$\Rightarrow \frac{\partial[P]}{\partial t} = -\left([P]\underbrace{\frac{\partial v_k}{\partial z_k}}_{0} + v_k\frac{\partial[P]}{\partial z_k}\right) - \frac{\partial j_{k,P}}{\partial z_k}$$

$$\Rightarrow \frac{\partial[P]}{\partial t} = -v_k\frac{\partial[P]}{\partial z_k} - \frac{\partial j_{k,P}}{\partial z_k}$$

$$\Rightarrow \frac{\partial[P]}{\partial t} = -\left(v_x\frac{\partial[P]}{\partial x} + \underbrace{v_y}_{0}\frac{\partial[P]}{\partial y}\right) - \left(\frac{\partial j_{x,P}}{\partial x} + \frac{\partial j_{y,P}}{\partial y}\right)$$

$$\frac{\partial[P]}{\partial t} = -v_x\frac{\partial[P]}{\partial x} - \frac{\partial j_{x,P}}{\partial x} - \frac{\partial j_{y,P}}{\partial y} \tag{A.34}$$

The particle solution is highly diluted, and the Fick's law is used to formulate the diffusion flux of particle solution in the channel. Thus,

$$j_{x,P} = -D\frac{\partial[P]}{\partial x};\ j_{y,P} = -D\frac{\partial[P]}{\partial y} \tag{A.35}$$

The order of magnitude of D is O(10^{-12}) as calculated in Chapter 2.

With Eqs. (A.34-A.35),

$$\frac{\partial[P]}{\partial t} = -v_x(y)\frac{\partial[P]}{\partial x} + D\left(\frac{\partial^2[P]}{\partial x^2} + \frac{\partial^2[P]}{\partial y^2}\right) \quad \text{(A.36)}$$

A.2.2. Dimensionless Formulation

Eq. (A.36) is manipulated by the dimensionless operations. The dimensionless terms are defined as may be cancelled? Due to the repetition?

$\theta_{P,l} = \frac{[P]}{[P_{in}]}$, the percentage of particle concentration in the liquid phase;

$\tau = \frac{t}{t_{\mathrm{r}}} = \frac{t}{l/\overline{v_x}}$, the dimensionless time of the fluid flowing through the flow cell;

$v_x^* = \frac{v_x}{\overline{v_x}}$, the dimensionless velocity of the particles in the fluid;

$Pe = \frac{l\overline{v_x}}{D}$, Peclet number;

$\theta_{P,s} = \frac{[PR_n]}{[R^{max}]}$, the percentage of particle concentration on the surface;

$\tau_a = \frac{t}{t_{\mathrm{a}}} = \tau\frac{t_r}{t_a}$, the dimensionless time of the adsorption to reach equilibrium on the surface;

$X = \frac{x}{l}$, the dimensionless x coordinate;

$Y = \frac{y}{H}$,where $H = 2h$, the dimensionless y coordinate;

The mass balance of particles in the liquid phase, Eq. (A.36) is

$$\frac{\partial[P]}{\partial t} = -v_x(y)\frac{\partial[P]}{\partial x} + D\left(\frac{\partial^2[P]}{\partial x^2} + \frac{\partial^2[P]}{\partial y^2}\right)$$

$$\text{Accumulation: } \frac{\partial\theta_{P,l}}{\partial\tau} = \frac{\partial([P]/[P_{in}])}{\partial\left(\frac{t}{l/\overline{v_x}}\right)} = \frac{l}{[P_{in}]\overline{v_x}}\frac{\partial[P]}{\partial t}$$

$$\text{Convection: } \left(\frac{l}{[P_{in}]\overline{v_x}}\right)\left(-v_x(y)\frac{\partial[P]}{\partial x}\right) = -\frac{v_x(y)}{\overline{v_x}}\frac{\partial([P]/[P_{in}])}{\partial\left(\frac{x}{l}\right)} = -\frac{v_x(y)}{\overline{v_x}}\frac{\partial\theta_{P,l}}{\partial X}$$

$$\text{Diffusion: } \left(\frac{l}{[P_{in}]\overline{v_x}}\right)D\left(\frac{\partial^2[P]}{\partial x^2} + \frac{\partial^2[P]}{\partial y^2}\right)$$

$$= \left(\frac{l}{\overline{v_x}}\right)D\left(\frac{1}{l}\frac{\partial}{\partial x}\left(\frac{\partial\left(\frac{[P]}{[P_{in}]}\right)}{\partial\left(\frac{x}{l}\right)}\right) + \frac{1}{H}\frac{\partial}{\partial y}\left(\frac{\partial\left(\frac{[P]}{[P_{in}]}\right)}{\partial\left(\frac{y}{H}\right)}\right)\right)$$

$$= \left(\frac{l}{\overline{v_x}}\right)D\left(\frac{1}{l^2}\frac{\partial}{\partial\left(\frac{x}{l}\right)}\left(\frac{\partial\theta_{P,l}}{\partial X}\right) + \frac{1}{H^2}\frac{\partial}{\partial\left(\frac{y}{H}\right)}\left(\frac{\partial\theta_{P,l}}{\partial Y}\right)\right)$$

$$= \left(\frac{l}{\overline{v_x}}\right) D \left(\frac{1}{l^2}\frac{\partial}{\partial X}\left(\frac{\partial \theta_{P,l}}{\partial X}\right) + \frac{1}{H^2}\frac{\partial}{\partial Y}\left(\frac{\partial \theta_{P,l}}{\partial Y}\right)\right)$$

$$= \left(\frac{l}{\overline{v_x}}\right) D \left(\frac{1}{l^2}\frac{\partial}{\partial X}\left(\frac{\partial \theta_{P,l}}{\partial X}\right) + \frac{1}{H^2}\frac{\partial}{\partial Y}\left(\frac{\partial \theta_{P,l}}{\partial Y}\right)\right)$$

$$= \frac{D}{l\overline{v_x}}\left(\frac{\partial^2 \theta_{P,l}}{\partial X^2} + \left(\frac{l}{H}\right)^2 \frac{\partial^2 \theta_{P,l}}{\partial Y^2}\right)$$

Therefore, the dimensionless form of Eq. (A.36) is

$$\frac{\partial \theta_{P,l}}{\partial \tau} = -\frac{v_x}{\overline{v_x}}\frac{\partial \theta_{P,l}}{\partial X} + \frac{1}{Pe}\left(\frac{\partial^2 \theta_{P,l}}{\partial X^2} + \left(\frac{l}{H}\right)^2 \frac{\partial^2 \theta_{P,l}}{\partial Y^2}\right) \tag{A.37}$$

All of the dimensionless terms should have an order of magnitude of 1

$$\frac{\partial^2 \theta_{P,l}}{\partial X^2} = \mathrm{O}(1);\ \frac{\partial^2 \theta_{P,l}}{\partial Y^2} = \mathrm{O}(1)$$

$$\frac{l}{H} = 48 \gg \mathrm{O}(1) \Longrightarrow \left(\frac{l}{H}\right)^2 \frac{\partial^2 \theta_{P,l}}{\partial Y^2} \gg \mathrm{O}(1) \Longrightarrow \left(\frac{l}{H}\right)^2 \frac{\partial^2 \theta_{P,l}}{\partial Y^2} \gg \frac{\partial^2 \theta_{P,l}}{\partial X^2}$$

Therefore, the term of $\frac{\partial^2 \theta_{P,l}}{\partial X^2}$ may be safely neglected. Finally,

$$\frac{\partial \theta_{P,l}}{\partial \tau} = -v_x^* \frac{\partial \theta_{P,l}}{\partial X} + \frac{1}{Pe}\left(\frac{l}{H}\right)^2 \frac{\partial^2 \theta_{P,l}}{\partial Y^2} \tag{A.38}$$

$$Pe = \frac{l\overline{v_x}}{D} = \mathrm{O}\left(\frac{2\mathrm{x}10^{-3} \cdot 83.3\mathrm{x}10^{-3}}{10^{-12}}\right) = \mathrm{O}(1.67\ \mathrm{x}\ 10^8)$$

$$\Longrightarrow \frac{1}{Pe}\left(\frac{l}{H}\right)^2 = \mathrm{O}\left(\frac{1}{1.67\ \mathrm{x}\ 10^8}\left(\frac{2}{0.02}\right)^2\right) = \mathrm{O}(6\ \mathrm{x}\ 10^{-5})$$

$$v_x^* \frac{\partial \theta_{P,l}}{\partial X} = \mathrm{O}(1)$$

Comparing these numbers, the coefficient of the diffusion term has an approximate order of magnitude of 10^{-5}, which means the diffusion term may be small enough to be neglected totally, and the mass transportation is dominated by the convection. Hence, we may reduce Eq. (A.38) again,

$$\frac{\partial \theta_{P,l}}{\partial \tau} + v_x^* \frac{\partial \theta_{P,l}}{\partial X} = 0 \tag{A.39}$$

Equation (A.39) is the Eulerian approach and can be transformed into the substantial derivative by the Lagrangian approach based on the relation $\frac{D}{Dt} = \frac{\partial}{\partial t} + v_x \frac{\partial}{\partial x}$, therefore

$$\frac{D\theta_{P,l}}{D\tau} = 0 \tag{A.40}$$

This means that the particle concentration in the bulk of the fluid inside the flow cell almost remains the same as the inlet concentration. However, the particle is indeed adsorbed on the surface at $y = 0$ and there should be changes of particle concentration in

the neighborhood of the surface at $y = 0$. Hence, we need to analyze the system equations inside a diffusional boundary layer in the vicinity of the surface at $y = 0$ where the adsorption behavior happens.

A.2.3. Diffusional boundary layer

The thickness of the diffusive boundary layer is $\delta_D = \delta_D(x)$. The dimensionless Schmidt number $\mathrm{S_c} = \frac{\nu}{D} = \mathrm{O}(10^6)$. In fluids with constant density and viscosity and large Schmidt number, the diffusional boundary layer should lie within the velocity boundary layer, i.e., $\delta_D(x) \ll \delta(x)$. By analogy to Eq. (A.38), the dimensionless form of the equation of change for the particle species in the fluid becomes

$$\frac{\partial \theta_{P,l}}{\partial \tau} = -v_x^* \frac{\partial \theta_{P,l}}{\partial X} + \frac{1}{Pe}\left(\frac{l}{\delta_D}\right)^2 \frac{\partial^2 \theta_{P,l}}{\partial {Y_D}^2} \tag{A.41}$$

where, $Y_D = y/\delta_D$.

We analyze the behavior of the fluid within the diffusional boundary layer in the time range of the adsorption, t_a. Hence, the dimensionless time should be the dimensional time divided by the adsorption time, and Eq. (A.41) is reformulated as

$$\left(\frac{t_r}{t_a}\right)\frac{\partial \theta_{P,l}}{\partial \tau_a} = -v_x^* \frac{\partial \theta_{P,l}}{\partial X} + \frac{1}{Pe}\left(\frac{l}{\delta_D}\right)^2 \frac{\partial^2 \theta_{P,l}}{\partial {Y_D}^2} \tag{A.42}$$

As mentioned before,

$$t_r = \mathrm{O}(10^{-2})\ \mathrm{s}, t_a = \mathrm{O}(10^2)\ \mathrm{s} \Rightarrow \frac{t_r}{t_a} = \mathrm{O}(10^{-4})$$

If the order of magnitude of δ_D would lie in the range of micrometer, it would be just a preliminary guess that $\delta_D \approx \mathrm{O}(10^{-6})$. Then,

$$\frac{1}{Pe}\left(\frac{l}{\delta_D}\right)^2 \approx \mathrm{O}\left(10^{-8}\left(\frac{10^{-3}}{10^{-6}}\right)^2\right) = \mathrm{O}(0.01)$$

Therefore, comparing their orders of magnitude of all terms in the Eq. (A.42), the accumulation term may be neglected. Finally, we get the equation of the species mass balance of particle in the diffusional boundary layer

$$-v_x^* \frac{\partial \theta_{P,l}}{\partial X} + \frac{1}{Pe}\left(\frac{l}{\delta_D}\right)^2 \frac{\partial^2 \theta_{P,l}}{\partial {Y_D}^2} = 0 \tag{A.43}$$

Returning Eq. (A.43) to the dimensional form

$$-v_x(y)\frac{\partial [P]}{\partial x} + D\frac{\partial^2 [P]}{\partial y^2} = 0 \tag{A.44}$$

$$\Rightarrow v_x(y)\frac{\partial [P]}{\partial x} = D\frac{\partial^2 [P]}{\partial y^2}$$

$$\Rightarrow \int_0^h v_x(y)\frac{\partial [P]}{\partial x}dy = \int_0^h D\frac{\partial^2 [P]}{\partial y^2}dy$$

$$\Longrightarrow \int_0^h v_x(y)\frac{\partial[P]}{\partial x}dy = D\underbrace{\left(\frac{\partial[P]}{\partial y}\right)\Big|_{y=h}}_{0,symmetry} - D\left(\frac{\partial[P]}{\partial y}\right)\Big|_{y=0}$$

$$\Longrightarrow \int_0^h v_x(y)\frac{\partial[P]}{\partial x}dy = -D\left(\frac{\partial[P]}{\partial y}\right)\Big|_{y=0}$$

$$\frac{d}{dx}\int_0^h v_x(y)[P]dy = -D\left(\frac{\partial[P]}{\partial y}\right)\Big|_{y=0} \tag{A.45}$$

There is another method to get Eq. (A.45) based on the expansion of functions in Taylor series.

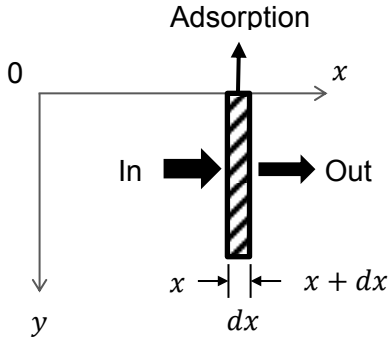

Figure A.1: Fluid element.

In Fig. A.1, the fluid flows in the element of the fluid at x, and flows out at $x + dx$, and the adsorption takes place at $y = 0$. The element is thin enough $(dx)^n \approx 0\ (n \geq 2)$ and we expand the function $[P](t, x + dx, y)$ in a Taylor series about the point x

$$[P](t, x + dx, y) = [P](t, x, y) + \frac{1}{1!}\left(\frac{\partial[P]}{\partial x}\right)dx + \frac{1}{2!}\left(\frac{\partial^2[P]}{\partial x^2}\right)(dx)^2 + \cdots \tag{A.46}$$

As an approximation, it is plausible to take only the first and the second terms in the right side of Eq. (A.46), and therefore,

$$[P](t, x + dx, y) \approx [P](t, x, y) + \left(\frac{\partial[P]}{\partial x}\right)dx \tag{A.47}$$

The balance of the species inside this tiny element is

$$Flow\ in - Flow\ out - Adsorption = 0$$

$$\int_0^h \big(v_x(y)[P](t, x, y) - v_x(y)[P](t, x + dx, y)\big)dy - rdx = 0 \tag{A.48}$$

Next, we will introduce the boundary condition $-\left(-D\left(\frac{\partial[P]}{\partial y}\right)\Big|_{y=0}\right)=r$. The reason for the term in the left side is that the diffusion flux is opposite to the y direction.

$$\Longrightarrow \int_0^h v_x(y)\big([P](t,x,y)-[P](t,x+dx,y)\big)dy-\left(D\left(\frac{\partial[P]}{\partial y}\right)\Big|_{y=0}\right)dx=0$$

$$\Longrightarrow \int_0^h v_x(y)\left(-\left(\frac{\partial[P]}{\partial x}\right)dx\right)dy=\left(D\left(\frac{\partial[P]}{\partial y}\right)\Big|_{y=0}\right)dx$$

$$\Longrightarrow \int_0^h v_x(y)\left(\frac{\partial[P]}{\partial x}\right)dy=-D\left(\frac{\partial[P]}{\partial y}\right)\Big|_{y=0}$$

$$\frac{d}{dx}\int_0^h v_x(y)[P]dy=-D\left(\frac{\partial[P]}{\partial y}\right)\Big|_{y=0} \tag{A.49}$$

The function $[P](t,x,y)$ in the diffusional boundary layer may be plausibly formed by a polynomial profile assumption of the third order,

$$[P](t,x,y)=a+by+cy^2+dy^3\ \big(0\le y\le \delta_D(x)\big) \tag{A.50}$$

where, a,b,c, and d are functions of x and t.

$$[P](t,x,y)=[P]_{in}\ \big(y\ge \delta_D(x)\big) \tag{A.51}$$

Therefore, the derivations of the velocity in the diffusional boundary layer are

$$\frac{\partial[P]}{\partial y}=b+2cy+y^2 3d \tag{A.52}$$

$$\frac{\partial^2[P]}{\partial y^2}=2c+y6d \tag{A.53}$$

There are four boundary conditions,

B. C. 1: $y=\delta_D(x),\frac{\partial[P]}{\partial y}\Big|_{y=\delta_D}=0$ (A.54)

B. C. 2: $y=\delta_D(x),\ [P](t,x,y=\delta_D)=[P]_{in}$ (A.55)

B. C. 3: $y=0, D\frac{\partial[P]}{\partial y}\Big|_{y=0}=r$ (A.56)

B. C. 4: $y=0, D\frac{\partial^2[P]}{\partial y^2}\Big|_{y=0}=0$ (A.57)

The reasons of the fourth boundary condition are

$$\begin{cases}\text{Eq. (A.45)}\ \Longrightarrow \left(-v_x(y)\dfrac{\partial[P]}{\partial x}+D\dfrac{\partial^2[P]}{\partial y^2}\right)\Big|_{y=0}=0\\ \text{No slip condition}\ \Longrightarrow v_x(y)=0\end{cases}$$

$$\Longrightarrow\ D\frac{\partial^2[P]}{\partial y^2}\Big|_{y=0}=0$$

Inserting the boundary conditions, Eqs. (A.54 ~ A.57) into Eqs. (A.52) and (A.53),

$$b + 2c\delta_D + 3d{\delta_D}^2 = 0 \tag{A.58}$$

$$a + b\delta_D + c{\delta_D}^2 + d{\delta_D}^3 = [P]_{in} \tag{A.59}$$

$$D(b + 2c0 + 3d0) = r \tag{A.60}$$

$$D(2c + 6d0) = 0 \tag{A.61}$$

Hence, we get

$$a = [P]_{in} - \frac{2r}{3D}\delta_D \tag{A.62}$$

$$b = \frac{r}{D} \tag{A.63}$$

$$c = 0 \tag{A.64}$$

$$d = -\frac{r}{3D\delta_D^2} \tag{A.65}$$

Therefore,

$$[P](t,x,y) = [P]_{in} - \frac{2r}{3D}\delta_D + \frac{r}{D}y - \frac{r}{3D\delta_D^2}y^3 \left(0 \le y \le \delta_D(x)\right) \tag{A.66}$$

$$\frac{\partial [P]}{\partial y} = \frac{r}{D} - \frac{r}{D\delta_D^2}y^2\left(0 \le y \le \delta_D(x)\right) \tag{A.67}$$

The left term in Eq. (A.45) is

$$\frac{d}{dx}\int_0^h v_x(y)[P]dy = \frac{d}{dx}\left(\int_0^{\delta_D} v_x(y)[P]dy + \int_{\delta_D}^h v_x(y)[P]dy\right)$$
$$= \frac{d}{dx}\left(\int_0^{\delta_D} v_x(y)[P]dy + \int_{\delta_D}^h v_x(y)[P]_{in}dy\right)$$

Multiplying the concentration function in the boundary layer, Eq. (A.66), by the equation of the velocity, Eq. (A.32), when $0 \le y \le \delta_D(x)$

$$v_x(y)[P] = \frac{3}{2}\overline{v_x}\left(2\left(\frac{y}{h}\right) - \left(\frac{y}{h}\right)^2\right)\left([P]_{in} - \frac{2r}{3D}\delta_D + \frac{r}{D}y - \frac{r}{3D\delta_D^2}y^3\right)$$

$$= [P]_{in}\frac{3}{2}\overline{v_x}\left(2\left(\frac{y}{h}\right) - \left(\frac{y}{h}\right)^2\right) - \frac{r}{D}\delta_D\overline{v_x}\left(2\left(\frac{y}{h}\right) - \left(\frac{y}{h}\right)^2\right) + \frac{r}{D}\frac{y}{h}h\frac{3}{2}\overline{v_x}\left(2\left(\frac{y}{h}\right) - \left(\frac{y}{h}\right)^2\right)$$
$$- \frac{r}{D\delta_D^2}h^3\left(\frac{y}{h}\right)^3\frac{1}{2}\overline{v_x}\left(2\left(\frac{y}{h}\right) - \left(\frac{y}{h}\right)^2\right)$$

$$= 3\overline{v_x}[P]_{in}\left(\frac{y}{h}\right) - \frac{3}{2}\overline{v_x}[P]_{in}\left(\frac{y}{h}\right)^2 - 2\overline{v_x}\frac{r}{D}\delta_D\left(\frac{y}{h}\right) + \overline{v_x}\frac{r}{D}\delta_D\left(\frac{y}{h}\right)^2 + 3h\overline{v_x}\frac{r}{D}\left(\frac{y}{h}\right)^2 - \frac{3}{2}h\overline{v_x}\frac{r}{D}\left(\frac{y}{h}\right)^3$$
$$- \overline{v_x}\frac{rh^3}{D\delta_D^2}\left(\frac{y}{h}\right)^4 + \frac{1}{2}\overline{v_x}\frac{rh^3}{D\delta_D^2}\left(\frac{y}{h}\right)^5$$

$$= \left(3\overline{v_x}[P]_{in} - 2\overline{v_x}\frac{r}{D}\delta_D\right)\left(\frac{y}{h}\right) + \left(-\frac{3}{2}\overline{v_x}[P]_{in} + \overline{v_x}\frac{r}{D}\delta_D + 3h\overline{v_x}\frac{r}{D}\right)\left(\frac{y}{h}\right)^2 - \frac{3}{2}h\overline{v_x}\frac{r}{D}\left(\frac{y}{h}\right)^3 - \overline{v_x}\frac{rh^3}{D\delta_D^2}\left(\frac{y}{h}\right)^4 + \frac{1}{2}\overline{v_x}\frac{rh^3}{D\delta_D^2}\left(\frac{y}{h}\right)^5$$

Multiplying the concentration profile outside the boundary layer, Eq. (A.51), by the velocity, Eq. (A.32), when $y \geq \delta_D(x)$

$$v_x(y)[P] = \frac{3}{2}\overline{v_x}\left(2\left(\frac{y}{h}\right) - \left(\frac{y}{h}\right)^2\right)[P]_{in}$$

$$\Longrightarrow \int_0^h v_x(y)[P]dy$$

$$= \int_0^{\delta_D}\left[\left(3\overline{v_x}[P]_{in} - 2\overline{v_x}\frac{r}{D}\delta_D\right)\left(\frac{y}{h}\right) + \left(-\frac{3}{2}\overline{v_x}[P]_{in} + \overline{v_x}\frac{r}{D}\delta_D + 3h\overline{v_x}\frac{r}{D}\right)\left(\frac{y}{h}\right)^2 - \frac{3}{2}h\overline{v_x}\frac{r}{D}\left(\frac{y}{h}\right)^3 - \overline{v_x}\frac{rh^3}{D\delta_D^2}\left(\frac{y}{h}\right)^4 + \frac{1}{2}\overline{v_x}\frac{rh^3}{D\delta_D^2}\left(\frac{y}{h}\right)^5\right]dy + \int_{\delta_D}^h \frac{3}{2}\overline{v_x}\left(2\left(\frac{y}{h}\right) - \left(\frac{y}{h}\right)^2\right)[P]_{in}dy$$

$$= \left(3\overline{v_x}[P]_{in} - 2\overline{v_x}\frac{r}{D}\delta_D\right)\frac{h}{2}\left(\frac{\delta_D}{h}\right)^2 + \left(-\frac{3}{2}\overline{v_x}[P]_{in} + \overline{v_x}\frac{r}{D}\delta_D + 3h\overline{v_x}\frac{r}{D}\right)\frac{h}{3}\left(\frac{\delta_D}{h}\right)^3 - \frac{3}{2}h\overline{v_x}\frac{r}{D}\frac{h}{4}\left(\frac{\delta_D}{h}\right)^4 - \overline{v_x}\frac{rh^3}{D\delta_D^2}\frac{h}{5}\left(\frac{\delta_D}{h}\right)^5 + \frac{1}{2}\overline{v_x}\frac{rh^3}{D\delta_D^2}\frac{h}{6}\left(\frac{\delta_D}{h}\right)^6 + \frac{3}{2}\overline{v_x}[P]_{in}\left(h\left(\frac{y}{h}\right)^2 - \frac{h}{3}\left(\frac{y}{h}\right)^3\right)\Bigg|_{\delta_D}^h$$

$$= \left(3\overline{v_x}[P]_{in} - 2\overline{v_x}\frac{r}{D}\delta_D\right)\frac{h}{2}\left(\frac{\delta_D}{h}\right)^2 + \left(-\frac{3}{2}\overline{v_x}[P]_{in} + \overline{v_x}\frac{r}{D}\delta_D + 3h\overline{v_x}\frac{r}{D}\right)\frac{h}{3}\left(\frac{\delta_D}{h}\right)^3 - \frac{3}{2}h\overline{v_x}\frac{r}{D}\frac{h}{4}\left(\frac{\delta_D}{h}\right)^4 - \overline{v_x}\frac{rh^3}{D\delta_D^2}\frac{h}{5}\left(\frac{\delta_D}{h}\right)^5 + \frac{1}{2}\overline{v_x}\frac{rh^3}{D\delta_D^2}\frac{h}{6}\left(\frac{\delta_D}{h}\right)^6 + \frac{3}{2}\overline{v_x}[P]_{in}\left(\frac{2h}{3} - h\left(\frac{\delta_D}{h}\right)^2 + \frac{h}{3}\left(\frac{\delta_D}{h}\right)^3\right)$$

$$= \left(3\overline{v_x}[P]_{in} - 2\overline{v_x}\frac{r}{D}\delta_D - 3\overline{v_x}[P]_{in}\right)\frac{h}{2}\left(\frac{\delta_D}{h}\right)^2 + \left(-\frac{3}{2}\overline{v_x}[P]_{in} + \overline{v_x}\frac{r}{D}\delta_D + \frac{3}{2}\overline{v_x}[P]_{in} + 3h\overline{v_x}\frac{r}{D}\right)\frac{h}{3}\left(\frac{\delta_D}{h}\right)^3 - \frac{3}{2}h\overline{v_x}\frac{r}{D}\frac{h}{4}\left(\frac{\delta_D}{h}\right)^4 - \overline{v_x}\frac{rh^3}{D\delta_D^2}\frac{h}{5}\left(\frac{\delta_D}{h}\right)^5 + \frac{1}{2}\overline{v_x}\frac{rh^3}{D\delta_D^2}\frac{h}{6}\left(\frac{\delta_D}{h}\right)^6 + h\overline{v_x}[P]_{in}$$

$$= \left(-2\overline{v_x}\frac{r}{D}\delta_D\right)\frac{h}{2}\left(\frac{\delta_D}{h}\right)^2 + \left(\overline{v_x}\frac{r}{D}\delta_D + 3h\overline{v_x}\frac{r}{D}\right)\frac{h}{3}\left(\frac{\delta_D}{h}\right)^3 - \frac{3}{2}h\overline{v_x}\frac{r}{D}\frac{h}{4}\left(\frac{\delta_D}{h}\right)^4 - \overline{v_x}\frac{rh^3}{D\delta_D^2}\frac{h}{5}\left(\frac{\delta_D}{h}\right)^5 + \frac{1}{2}\overline{v_x}\frac{rh^3}{D\delta_D^2}\frac{h}{6}\left(\frac{\delta_D}{h}\right)^6 + h\overline{v_x}[P]_{in}$$

$$= -h^2\overline{v_x}\frac{r}{D}\left(\frac{\delta_D}{h}\right)^3 + \left(\frac{h^2}{3}\overline{v_x}\frac{r}{D}\frac{\delta_D}{h} + h^2\overline{v_x}\frac{r}{D}\right)\left(\frac{\delta_D}{h}\right)^3 - \frac{3}{8}h^2\overline{v_x}\frac{r}{D}\left(\frac{\delta_D}{h}\right)^4 - \frac{1}{5}h^2\overline{v_x}\frac{r}{D}\left(\frac{\delta_D}{h}\right)^3 + \frac{1}{12}h^2\overline{v_x}\frac{r}{D}\left(\frac{\delta_D}{h}\right)^4 + \overline{v_x}[P]_{in}h$$

$$= \frac{h^2}{3}\overline{v_x}\frac{r}{D}\left(\frac{\delta_D}{h}\right)^4 - \frac{3}{8}h^2\overline{v_x}\frac{r}{D}\left(\frac{\delta_D}{h}\right)^4 - \frac{1}{5}h^2\overline{v_x}\frac{r}{D}\left(\frac{\delta_D}{h}\right)^3 + \frac{1}{12}h^2\overline{v_x}\frac{r}{D}\left(\frac{\delta_D}{h}\right)^4 + \overline{v_x}[P]_{in}h$$

$$= \frac{1}{24}h^2\overline{v_x}\frac{r}{D}\left(\frac{\delta_D}{h}\right)^4 - \frac{1}{5}h^2\overline{v_x}\frac{r}{D}\left(\frac{\delta_D}{h}\right)^3 + \overline{v_x}[P]_{in}h$$

Finally,

$$\int_0^h v_x(y)[P]dy = -\frac{1}{5}h^2\overline{v_x}\frac{r}{D}\left(\frac{\delta_D}{h}\right)^3 + \frac{1}{24}h^2\overline{v_x}\frac{r}{D}\left(\frac{\delta_D}{h}\right)^4 + \overline{v_x}[P]_{in}h$$

$$\frac{d}{dx}\int_0^h v_x(y)[P]dy = \left(-\frac{3}{5}h\overline{v_x}\frac{r}{D}\left(\frac{\delta_D}{h}\right)^2 + \frac{1}{6}h\overline{v_x}\frac{r}{D}\left(\frac{\delta_D}{h}\right)^3\right)\frac{d\delta_D}{dx} + \left(-\frac{1}{5D}h^2\overline{v_x}\left(\frac{\delta_D}{h}\right)^3 + \frac{1}{24D}h^2\overline{v_x}\left(\frac{\delta_D}{h}\right)^4\right)\frac{\partial r}{\partial x} \quad \text{(A.68)}$$

The term on the right side of Eq. (A.45) can be combined with Eq. (A.67),

$$-D\left(\frac{\partial[P]}{\partial y}\right)\Big|_{y=0} = -D\left(\frac{r}{D} - \frac{r}{D\delta_D^2}0^2\right) = -r \quad \text{(A.69)}$$

Finally, from Eqs. (A.45), (A.68) and (A.69),

$$\left(-\frac{3}{5}h\overline{v_x}\frac{r}{D}\left(\frac{\delta_D}{h}\right)^2 + \frac{1}{6}h\overline{v_x}\frac{r}{D}\left(\frac{\delta_D}{h}\right)^3\right)\frac{d\delta_D}{dx} + \left(-\frac{1}{5D}h^2\overline{v_x}\left(\frac{\delta_D}{h}\right)^3 + \frac{1}{24D}h^2\overline{v_x}\left(\frac{\delta_D}{h}\right)^4\right)\frac{\partial r}{\partial x} = -r \quad \text{(A.70)}$$

As analogy to the analysis of the thickness of the velocity boundary layer δ^*, let $\delta_D^* = \frac{\delta_D}{h}$, then,

$$\left(-\frac{3}{5}h\overline{v_x}\frac{r}{D}(\delta_D^*)^2 + \frac{1}{6}h\overline{v_x}\frac{r}{D}(\delta_D^*)^3\right)\frac{d\delta_D^*}{dx} + \left(-\frac{1}{5D}h\overline{v_x}(\delta_D^*)^3 + \frac{1}{24D}h\overline{v_x}(\delta_D^*)^4\right)\frac{\partial r}{\partial x} = -\frac{r}{h} \quad \text{(A.71)}$$

It is preliminary assumed that $\delta_D \ll h \Longrightarrow \delta_D^* \ll 1$ that we may neglect the terms $(\delta_D^*)^4$ because it would be approximately zero. Therefore, we can reduce Eq. (A.71) again into

$$\left(-\frac{3}{5}h\overline{v_x}\frac{r}{D}(\delta_D^*)^2+\frac{1}{6}h\overline{v_x}\frac{r}{D}(\delta_D^*)^3\right)\frac{d\delta_D^*}{dx}+\left(-\frac{1}{5D}h\overline{v_x}(\delta_D^*)^3\right)\frac{\partial r}{\partial x}=-\frac{r}{h} \tag{A.72}$$

Finally, we get one non-linear ODE for δ_D^*

$$(18(\delta_D^*)^2-5(\delta_D^*)^3)r\frac{d\delta_D^*}{dx}+6(\delta_D^*)^3\frac{\partial r}{\partial x}=\frac{30D}{h^2\overline{v_x}}r \tag{A.73}$$

$$\left(18\delta_D^2-\frac{5}{h}\delta_D^3\right)r\frac{d\delta_D}{dx}+6\delta_D^3\frac{\partial r}{\partial x}=\frac{30hD}{\overline{v_x}}r \tag{A.74}$$

Term r can't be put as the denominator because the initial condition of r in MATLAT is zero.

A.2.4. Mass balance of the particles on the surface

It is assumed that the particles on the surface only have the adsorbing behavior and their surface diffusion can be neglected. The concentration of the particles on the surface, $[PL_n]$, has a function $[PR_n]=[PR_n](t,x)$.

$$\underbrace{\frac{\partial[PR_n]}{\partial t}}_{accumulation}=\underbrace{\sigma}_{source\ due\ to\ adsorption} \tag{A.75}$$

The source term σ in Eq. (A.75) equals to

$$\sigma=r \tag{A.76}$$

A.2.5. Summary of Equations and Dimensionless formulation

It is assumed that the adsorption takes place homogenously on the surface of the flow cell, and therefore, $[PR_n]=[PR_n](t)\Longrightarrow\frac{d[PR_n]}{dt}=r.$

Finally, three equations coupling together by the adsorption term r are as follows

$$[P](t,x,y)=\begin{cases}[P]_{in}-\dfrac{2r}{3D}\delta_D+\dfrac{r}{D}y-\dfrac{r}{3D\delta_D^2}y^3, (0\le y\le\delta_D)\\ [P]_{in}, \qquad\qquad (\delta_D\le y\le 2h)\end{cases} \tag{A.77}$$

$$\frac{\partial[PR_n]}{\partial t}=r \tag{A.78}$$

$$\left(18\delta_D^2-\frac{5}{h}\delta_D^3\right)r\frac{d\delta_D}{dx}+6\delta_D^3\frac{\partial r}{\partial x}=\frac{30hD}{\overline{v_x}}r \tag{A.79}$$

There are three independent variables, t,x,y, four dependent variables, $[P],[PR_n],\delta_D,r$ and six parameters, $[P]_{in},D,h,k_a,[R^{max}],\overline{v_x}$. So far, all these parameters can be seen as constant.

As mentioned before: $X=\frac{x}{l},Y=\frac{y}{H}=\frac{y}{2h},\theta_{P,l}=\frac{[P]}{[P]_{in}},\theta_{P,s}=\frac{[PR_n]}{[R^{max}]}$ and $\delta_D^*=\frac{\delta_D}{h}$. For dimensionless time and adsorption terms, new definitions are made in the following steps.

$$\text{Eq. (A.77)} \Longrightarrow \theta_{P,l} = 1 + \left(\frac{2h}{D[P]_{in}} Y - \frac{(2h)^3}{3D[P]_{in} h^2 \frac{\delta_D^2}{h^2}} Y^3 - \frac{2h\frac{\delta_D}{h}}{3D[P]_{in}} \right) r, \left(0 \le Y \le \frac{\delta_D}{2h} \right)$$

$$\Longrightarrow \theta_{P,l} = 1 + \left(Y - \frac{4}{3{\delta_D^*}^2} Y^3 - \frac{\delta_D^*}{3} \right) \frac{2h}{D[P]_{in}} r, \left(0 \le Y \le \frac{\delta_D^*}{2} \right)$$

$$\text{Eq. (A.77)} \Longrightarrow \theta_{P,l} = 1 \left(\frac{\delta_D^*}{2} \le Y \le 1 \right)$$

Analysis of units of the term $\frac{2h}{D[P]_{in}} r : \left[\frac{mm}{\frac{mm^2}{s} * \frac{\#}{\mu l}} * \frac{\#}{mm^2 \cdot s} \right] = [1]$. Hence, the dimensionless adsorption term may be defined as $r^* = \frac{2h}{D[P]_{in}} r$. Finally,

$$\theta_{P,l} = 1 + \left(Y - \frac{4}{3(\delta_D^*)^2} Y^3 - \frac{\delta_D^*}{3} \right) R, \left(0 \le Y \le \frac{1}{2}\delta_D^* \right)$$

$$\text{Eq. (A.78)} \Longrightarrow \frac{d\theta_{P,S}}{dt} = \frac{1}{[R^{max}]} \frac{D[P]_{in}}{2h} r^* \Longrightarrow \frac{d\theta_{P,S}}{dt} = \frac{D[P]_{in}}{2h[R^{max}]} r^* \Longrightarrow \frac{d\theta_{P,S}}{d\frac{t}{\left(\frac{2h[R^{max}]}{D[P]_{in}}\right)}} = r^*$$

Units of the term, $\frac{t}{\frac{2h[R^{max}]}{D[P]_{in}}}$, are $\left[\frac{s}{\left(\frac{mm * \frac{\#}{mm^2}}{\frac{mm^2}{s} * \frac{\#}{mm^3}} \right)} \right] = [1]$. Hence, the dimensionless time may be defined here as $\tau = \frac{t}{\frac{2h[R^{max}]}{D[P]_{in}}}$.

$$\text{Eq. (A.73)} \Longrightarrow r^*(18(\delta_D^*)^2 - 5(\delta_D^*)^3) \frac{d\delta_D^*}{dX} + 6(\delta_D^*)^3 \frac{\partial r^*}{\partial X} = C_1 r^*$$

where, $C_1 = \frac{30lD}{h^2 \overline{v_x}} = 30 \left(\frac{l}{h}\right)^2 \frac{D}{l\overline{v_x}} = 30 \left(\frac{l}{h}\right)^2 \frac{1}{Pe} \left[= 30 \left(\frac{2}{0.01}\right)^2 \frac{1}{Pe} = \frac{1.2 \times 10^6}{Pe} \right]$

Finally, the dimensionless set is

$$\theta_{P,l} = \begin{cases} 1 + \left(Y - \frac{4}{3(\delta_D^*)^2} Y^3 - \frac{\delta_D^*}{3} \right) r^*, \left(0 \le Y \le \frac{\delta_D^*}{2} \right) \\ 1, \qquad \left(\frac{\delta_D^*}{2} \le Y \le 1 \right) \end{cases} \tag{A.80}$$

$$\frac{d\theta_{P,S}}{d\tau} = r^* \tag{A.81}$$

$$(18(\delta_D^*)^2 - 5(\delta_D^*)^3) r^* \frac{d\delta_D^*}{dX} + 6(\delta_D^*)^3 \frac{\partial r^*}{\partial X} = 30 \left(\frac{l}{h}\right)^2 \frac{r^*}{Pe} \tag{A.82}$$

In comparison with the dimensional set Eqs. (A.77~A.79), the dimensionless set Eqs. (A.80~A.82) has more concise forms with only one parameter, Pe.

$$\frac{\partial R}{\partial X} = \frac{\partial R}{\partial \delta_D^*}\frac{d\delta_D^*}{dX} \tag{A.83}$$

$$\left(18(\delta_D^*)^2 R - 5(\delta_D^*)^3 R + 6(\delta_D^*)^3 \frac{\partial R}{\partial \delta_D^*}\right)\frac{d\delta_D^*}{dX} = 30\left(\frac{l}{h}\right)^2 \frac{R}{Pe} \tag{A.84}$$

A.2.6. Discretization

The first derivatives $\frac{d\delta_D^*}{dX}$ in Eq. (A.84) can be approximated by means of the equidistant local discretization, as illustrated in Fig. A.2.

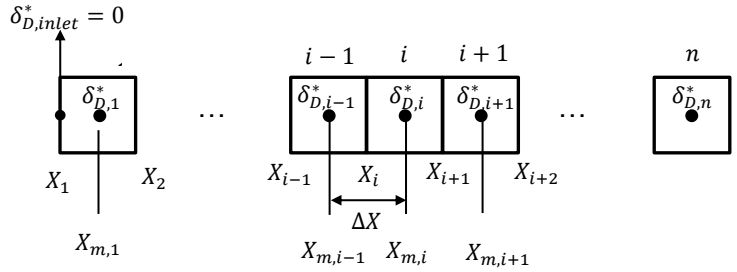

Figure A.2: Spatial discretization of the domain.

As the inlet boundary condition $\delta^*_{D,inlet} = 0$, using the backward difference, the discretized equation of the first control volume is

$$\left.\frac{\partial \delta_D^*}{\partial X}\right|_{X_{M,1}} = \frac{\delta^*_{D,1} - \delta^*_{D,inlet}}{\frac{\Delta X}{2}} = 2\frac{\delta^*_{D,1}}{\Delta X} \tag{A.85}$$

Combining Eq. (A.84) with Eq. (A.85), it gives

$$\left(18\left(\delta^*_{D,1}\right)^2 r_1^* - 5\left(\delta^*_{D,1}\right)^3 r_1^* + 6\left(\delta^*_{D,1}\right)^3 \left.\frac{\partial r^*}{\partial \delta_D^*}\right|_{X_{M,1}}\right)\frac{\delta^*_{D,1}}{\Delta X} = 15\left(\frac{l}{h}\right)^2 \frac{r_1^*}{Pe} \tag{A.86}$$

For the i-element from 2 to n, it is derived

$$\left.\frac{d\delta_D^*}{dX}\right|_{X_{M,i}} = \frac{\delta^*_{D,i} - \delta^*_{D,i-1}}{\Delta X} \tag{A.87}$$

Combining Eq. (A.84) with Eq. (A.87), it gives

$$\left(18\left(\delta^*_{D,i}\right)^2 r_i^* - 5\left(\delta^*_{D,i}\right)^3 r_i^* + 6\left(\delta^*_{D,i}\right)^3 \left.\frac{\partial r^*}{\partial \delta_D^*}\right|_{X_{M,i}}\right)\frac{\delta^*_{D,i} - \delta^*_{D,i-1}}{\Delta X} = 30\left(\frac{l}{h}\right)^2 \frac{r_i^*}{Pe} \tag{A.88}$$

Eq. (A.81) can be discretized as

$$\frac{d\theta_{P,s,i}}{d\tau} = r_i^* \tag{A.89}$$

Eqs. (A.86), (A.88) and (A.89) are the general discretized-AEs for Eqs. (A.81) and (A.82). It can be seen that the adsorption rate r^* becomes the key point to get the numerical solutions.

A.2.7. Output Function

As shown in Fig. 5.4, the BIAcore device monitors the probing area with a width of 0.2 mm and a length of 1.8 mm. With $\theta_{P,S}(t,x) = \frac{[PR_n]}{[R^{max}]}$, we define

$$\Theta(t) = w_p \int_{\frac{l-l_p}{2}}^{\frac{l+l_p}{2}} \theta_{\mathrm{P,S}}(t,x)\, dx \tag{A.90}$$

Put this integral into discretization form as

$$\Theta = \frac{\sum_i \left([PL_n]_i * \Delta x * w_p\right)}{[L^{max}] * l_p * w_p} \tag{A.91}$$

where, the ith volume is within the probing area.

Now, we need to find out which elements of volume are within the probing area. The number of discretization of the whole flow cell is $\mathrm{n} = 100$, so $\Delta\mathrm{X} = \frac{1}{\mathrm{n}} = 0.01$. As the $\frac{\mathrm{l_p}}{\mathrm{l}} = \frac{1.8}{2} = 0.9$, $\frac{1-\frac{\mathrm{l_p}}{\mathrm{l}}}{2} = 0.05$, therefore $\frac{\frac{1-\frac{\mathrm{l_p}}{\mathrm{l}}}{2}}{\Delta\mathrm{X}} = 5$. It means that the first 5 elements and the last 5 elements are out of probing area. Hence, the volumes to count are from the 6th to the 95th.We can reformulate Eq. (A.91) as

$$\Theta = \frac{l}{l_p} \sum_{i=6}^{95} \theta_{P,S,i}\, \Delta X \tag{A.92}$$

The experimental data has a unit of Response Unit [RU], and we need to transfer this unit into the simulation unit as [numbers/mm^2]. As already known, 1 RU = 1 pg/mm^2 (handbook 2008), MW_virus = 374739211.3 Da (Fields et al. 2001), MW_EEL = 1.4 x 10^5 Da. Finally, we can transform the RU signals into the simulation unit as $1\ [\mathrm{RU}] = \frac{1e-12}{\mathrm{MW}} *$ Avogadro's No.. Therefore, for the virus, 1 RU ≈ 1607 virons/mm^2; for the EEL, 1 RU ≈ 4.3 x 10^6 molecules/mm^2.

A.3 Kinetic models of the adsorptionLangmuir kinetic model

According to the adsorption rate expression, Eq.(5.9)

$$r = k_a[P](t,x,y=0)([R^{max}] - [PR]) \tag{A.93}$$

The particle concentration in the diffusional boundary layer, Eq. (A.66), gives

$$[P](t,x,y=0) = [P]_{in} - \frac{2r}{3D}\delta_D \tag{A.94}$$

$$r = k_a\left([P]_{in} - \frac{2r}{3D}\delta_D\right)([R^{max}] - [PR]) \tag{A.95}$$

$$\text{Eq. } (A.95) \Longrightarrow r = \frac{k_a[P]_{in}([R^{max}] - [PR])}{1 + \frac{2\delta_D}{3D}k_a([R^{max}] - [PR])} \Longrightarrow r = \frac{k_a[P]_{in}(1-\theta_{P,s})}{\frac{1}{[R^{max}]} + \frac{2h\delta_D^*}{3D}k_a(1-\theta_{P,s})}$$

$$\Longrightarrow r^* = \frac{2h}{D[P]_{in}} * \frac{k_a[P]_{in}(1-\theta_{P,s})}{\frac{1}{[R^{max}]} + \frac{2h\delta_D^*}{3D}k_a(1-\theta_{P,s})} = \frac{1-\theta_{P,s}}{\frac{D}{2h[R^{max}]k_a} + \frac{\delta_D^*}{3}(1-\theta_{P,s})}$$

$$\Longrightarrow r^* = \frac{1-\theta_{P,s}}{C_2 + \frac{\delta_D^*}{3}(1-\theta_{P,s})}$$

where $C_2 = \frac{D}{2h[R^{max}]k_a} = \frac{1}{Da}$, the reciprocal of the second Damköhler number. It describes the effect of the surface adsorption kinetics on the overall diffusion-adsorption process.

$$r^* = \frac{1-\theta_{P,s}}{\frac{1}{Da} + \frac{1}{3}(1-\theta_{P,s})\delta_D^*} \tag{A.96}$$

Therefore, we can replace the terms r^* in Eqs. (A.86), (A.88), and (A.89) with the following expressions

$$\frac{\partial r^*}{\partial \delta_D^*} = -\frac{(1-\theta_{P,s})^2}{3\left(\frac{1}{Da} + \frac{1}{3}(1-\theta_{P,s})\delta_D^*\right)^2} = -\frac{r^{*2}}{3} \tag{A.97}$$

$$\text{Eq. (A. 97)} \Longrightarrow \left.\frac{\partial r^*}{\partial \delta_D^*}\right|_{X_{M,i}} = -\frac{1}{3}(R_i)^2 \tag{A.98}$$

$$\text{Eq. (A. 96)} \Longrightarrow r_i^* = \frac{1-\theta_{P,s,i}}{\frac{1}{Da} + \frac{1}{3}(1-\theta_{P,s,i})\delta_{D,i}^*} \tag{A.99}$$

Combining Eq. (A.86) with Eq. (A.98) gives

$$\Longrightarrow \left(18(\delta_{D,1}^*)^2 R_1 - 5(\delta_{D,1}^*)^3 R_1 - 2(\delta_{D,1}^*)^3 (R_1)^2\right)\frac{\delta_{D,1}^*}{\Delta X} = 15\left(\frac{l}{h}\right)^2 \frac{R_1}{Pe}$$

$$0 = 15\left(\frac{l}{h}\right)^2 \frac{R_1}{Pe} - \left(18(\delta_{D,1}^*)^2 R_1 - 5(\delta_{D,1}^*)^3 R_1 - 2(\delta_{D,1}^*)^3 (R_1)^2\right)\frac{\delta_{D,1}^*}{\Delta X} \tag{A.100}$$

Combining Eq. (A.88) with Eq. (A.98) gives

$$\Longrightarrow \left(18(\delta_{D,i}^*)^2 R_i - 5(\delta_{D,i}^*)^3 R_i - 2(\delta_{D,i}^*)^3 (R_i)^2\right)\frac{\delta_{D,i}^* - \delta_{D,i-1}^*}{\Delta X} = 30\left(\frac{l}{h}\right)^2 \frac{R_i}{Pe}$$

$$0 = 30\left(\frac{l}{h}\right)^2 \frac{R_i}{Pe} - \left(18(\delta_{D,i}^*)^2 R_i - 5(\delta_{D,i}^*)^3 R_i - 2(\delta_{D,i}^*)^3 (R_i)^2\right)\frac{\delta_{D,i}^* - \delta_{D,i-1}^*}{\Delta X} \tag{A.101}$$

Eq. (A.100) and Eq. (A.101) together with Eq. (A.96) and Eq. (A.89) can be directly implemented into MATLAB by employing the DAE solver, ode15s.

A.3.2. The multi-site kinetic model

$$\overset{\text{Eq.(5.8)}}{\Longrightarrow} r^* = \left(\frac{2h}{D}k_a - k_a\frac{2r^*}{3D}\delta_D\right)([R^{max}] - n[PR_n])\left(\frac{[R^{max}] - (n+1)[PR_n]}{[R^{max}] - n[PR_n]}\right)^{n-1}$$

$$\Longrightarrow r^* = \left(\frac{2h}{D}k_a - k_a\frac{2r^*}{3D}\delta_D\right)[R^{max}]\left(1 - n\theta_{P,s}\right)\left(\frac{1-(n+1)\theta_{P,s}}{1-n\theta_{P,s}}\right)^{n-1}$$

$$\Longrightarrow r^* = \left(\frac{2h[R^{max}]}{D}k_a - k_a[R^{max}]\frac{2h}{D}\frac{r^*\delta_D^*}{3}\right)\left(1 - n\theta_{P,s}\right)\left(\frac{1-(n+1)\theta_{P,s}}{1-n\theta_{P,s}}\right)^{n-1}$$

$$\Longrightarrow r^* = \left(Da - Da\frac{r^*\delta_D^*}{3}\right)\left(1 - n\theta_{P,s}\right)\left(\frac{1-(n+1)\theta_{P,s}}{1-n\theta_{P,s}}\right)^{n-1}$$

$$\Longrightarrow \left(1 + \frac{\delta_D^*}{3}Da\left(1 - n\theta_{P,s}\right)\left(\frac{1-(n+1)\theta_{P,s}}{1-n\theta_{P,s}}\right)^{n-1}\right)r^* = Da\left(1 - n\theta_{P,s}\right)\left(\frac{1-(n+1)\theta_{P,s}}{1-n\theta_{P,s}}\right)^{n-1}$$

$$r^* = \frac{\left(1 - n\theta_{P,s}\right)\left(\frac{1-(n+1)\theta_{P,s}}{1-n\theta_{P,s}}\right)^{n-1}}{\frac{1}{Da} + \frac{\delta_D^*}{3}\left(1 - n\theta_{P,s}\right)\left(\frac{1-(n+1)\theta_{P,s}}{1-n\theta_{P,s}}\right)^{n-1}} \tag{A.102}$$

$$\Longrightarrow \frac{\partial r^*}{\partial \delta_D^*} = -\frac{\left(1 - n\theta_{P,s}\right)\left(\frac{1-(n+1)\theta_{P,s}}{1-n\theta_{P,s}}\right)^{n-1}}{\left(\frac{1}{Da} + \frac{\delta_D^*}{3}\left(1 - n\theta_{P,s}\right)\left(\frac{1-(n+1)\theta_{P,s}}{1-n\theta_{P,s}}\right)^{n-1}\right)^2}\frac{1}{3}\left(1 - n\theta_{P,s}\right)\left(\frac{1-(n+1)\theta_{P,s}}{1-n\theta_{P,s}}\right)^{n-1}$$

$$\frac{\partial r^*}{\partial \delta_D^*} = -\frac{r^{*2}}{3} \tag{A.103}$$

Finally, putting Eq. (103) into Eq. (A.86) and Eq. (A.88),

$$\left(18\left(\delta_{D,1}^*\right)^2 R_1 - 5\left(\delta_{D,1}^*\right)^3 R_1 - 2\left(\delta_{D,1}^*\right)^3 {R_1}^2\right)\frac{\delta_{D,1}^*}{\Delta X} = 15\left(\frac{l}{h}\right)^2\frac{R_1}{Pe} \tag{A.104}$$

$$\left(18\left(\delta_{D,i}^*\right)^2 R_i - 5\left(\delta_{D,i}^*\right)^3 R_i - 2\left(\delta_{D,i}^*\right)^3 {R_i}^2\right)\frac{\delta_{D,i}^* - \delta_{D,i-1}^*}{\Delta X} = 30\left(\frac{l}{h}\right)^2\frac{R_i}{Pe} \tag{A.105}$$

Eq. (A.104) and Eq. (A.105) together with Eq. (A.102) and Eq. (A.89) can be solved directly by MATLAB using ode15s solver.

A.4 Non-linear Parameter Estimation

There are two unknown parameters, Damköhler number Da and the number of bonds n, to be estimated from the experimental data based on the Gauss-Newton method of least squares. It is assumed that the measurement error is independently and identically distributed with variance σ^2.

In the least squares method, the sum of squares needs to be minimized

$$S(\beta) = \sum_{j=1}^{J} \left(\Theta_{exp,j} - \Theta_j(\beta)\right)^2 \tag{A.106}$$

where, Θ_{exp} is the experimental data; Θ is the simulated data from the model; β is the vector of parameters $\beta_1 = Da$ and $\beta_2 = n$; J is the total number of points in the time series.

It is defined that $\hat{\beta} = \begin{bmatrix} \widehat{Da} \\ \hat{n} \end{bmatrix}$ are the true values of the parameters and assumed that iterations are in the small neighborhood of $\hat{\beta}$, and then the function of Θ can be linearized by the first order Taylor expansion

$$\Theta_j(\beta) \approx \Theta_j(\hat{\beta}) + \left.\frac{\partial \Theta_j}{\partial \beta}\right|_{\hat{\beta}} (\beta - \hat{\beta}) \tag{A.107}$$

Combining Eqs. (A.106) with Eq. (A.107)

$$S(\beta) = \sum_{j=1}^{J} \left(\Theta_{exp,j} - \Theta_j(\beta)\right)^2 \approx \sum_{i=1}^{J} \left(\Theta_{exp,j} - \Theta_j(\hat{\beta}) + \left.\frac{\partial \Theta_j}{\partial \beta}\right|_{\hat{\beta}} (\beta - \hat{\beta})\right)^2$$

Here, re-define the terms $y_j = \Theta_{exp,j} - \Theta_j(\hat{\beta})$, $x_p = \left.\frac{\partial \Theta_j}{\partial \beta_p}\right|_{\widehat{\beta_p}}$, $(p = 1, 2)$ and $\mathrm{B} = \beta - \hat{\beta}$, finally Eq. (A.106) becomes

$$S(\beta) = \sum_{j=1}^{J} \left(y_j - x_p B\right)^2 \tag{A.108}$$

It becomes a linear least squares problem and from the properties of the linear model, Eq. (A.108) is minimized when B is given by

$$\mathrm{B} = (\mathrm{X}^T X)^{-1} \mathrm{X}^T Y \tag{A.109}$$

where, $X = X(\hat{\beta})$ is the sensitivity matrix; Y is the vector of the measurement error.

Therefore,

$$\beta = \hat{\beta} + \left(\mathrm{X}^T(\hat{\beta}) X(\hat{\beta})\right)^{-1} \mathrm{X}^T(\hat{\beta}) \sum_{j=1}^{J} \left(\Theta_{exp,j} - \Theta_j(\hat{\beta})\right) \tag{A.110}$$

Now, Eq. (A.110) is introduced to the iteration of the estimation

$$\beta^{k+1} = \beta^k + \left(\mathrm{X}^T(\beta^k) X(\beta^k)\right)^{-1} \mathrm{X}^T(\beta^k) \sum_{j=1}^{J} \left(\Theta_{exp,j} - \Theta_j(\beta^k)\right) \tag{A.111}$$

where, k is the number of the iteration step.

In this form of iteration, iteration will stop if β^k has converged

$$\frac{\left|\beta^{k+1} - \beta^k\right|}{|\beta^k| + \delta_1} < \delta \tag{A.112}$$

where, $\delta_1 = 1e-15, \delta = 1e-4$.

In parallel, the sum is checked as well

$$S\left(\beta^{k+1}\right) = \sum_{j=1}^{J} \left(\Theta_{exp,j} - \Theta_j\left(\beta^{k+1}\right)\right)^2 \tag{A.113}$$

The sum should decrease during iteration and reaches a reasonable value. If the final estimator would be $\check{\beta}$, variance σ^2 of the measurement noise can be estimated by

$$\check{\sigma}^2 = \frac{S\left(\check{\beta}\right)}{m-2} \tag{A.114}$$

Then, the covariance of the parameters can be approximated using the following term

$$\check{\sigma}_p{}^2 = \frac{S\left(\check{\beta}\right)}{m-2}\left(\mathrm{X}^T\left(\check{\beta}\right)X\left(\check{\beta}\right)\right)^{-1} \tag{A.115}$$

Therefore, the initial values for β^0 should be very near to the estimator $\check{\beta}$. We satisfy this condition be simulating the model profile almost the same growing as the experimental profile.

We introduce a sensitivity matrix, $x_p = \frac{\partial \Theta_j}{\partial \beta_p}$, by numerical method.

$$x_1 = \frac{\partial \Theta_j\left(t_j\right)}{\partial Da} \approx \frac{\Theta_j\left(Da + dDa, n, t_j\right) - \Theta_j\left(Da, n, t_j\right)}{dDa} \tag{A.116}$$

$$x_2 = \frac{\partial \Theta_j\left(t_j\right)}{\partial n} \approx \frac{\Theta_j\left(Da, n + dn, t_j\right) - \Theta_j\left(Da, n, t_j\right)}{dn} \tag{A.117}$$

For the values of d_Da and d_n, we use small values as $d_Da = 1 \times 10^{-3}$ and $d_n = 1 \times 10^{-4}$.

List of Figures

1.1: Illustration of multivalent interactions between two interacting partners. 5

1.2: Thesis structure and its main contents. 6

2.1: Sketch of bionanoparticle structure. 9

2.2: Synthesis scheme of human IgG coated BioNP via a carbodiimide reaction 11

2.3: Reactions in the first step of synthesis scheme 11

2.4: Reaction in the coating step of synthesis scheme 12

3.1: Sketch of two interacting partners. 17

3.2: Cascade reaction and typical sensorgram of protein immobilization 19

3.3: Determination of surface capacity of immobilized Protein A. 21

3.4: SPR detection principle. 23

3.5: Main experimental stages of the detection by SPR. 24

3.6: Adsorptions and desorptions of influenza viruses at the lectin surface. 26

3.7: Comparison of influenza virus adsorption 28

3.8: Comparison of influenza virus adsorption by changing the time. 29

3.9: Main experimental stages in the detection of nanoparticles by SPR. 30

3.10: Microscopic pictures of human IgG-coated nanoparticles 31

3.11: Comparison of adsorption and desorption of BioNP1 32

3.12: Comparison of adsorption and desorption of BioNP4 33

3.13: Comparison of BioNP1, BioNP2, and BioNP3 34

4.1: Sketch of two interacting partners. 37

4.2: One typical detected chromatogram of BioNPs through AMA..... 39

4.3: Breakthrough of NPs without ligands through the adsorber without receptors..... 40

4.4: Breakthrough of particles in the LC system without adsorber. 41

4.5: Breakthrough of NPs without ligands through AMA with receptors. 42

4.6: Comparison of the breakthrough influenced by inlet concentration and receptors. 44

4.7: Comparison of the breakthrough influenced by the ligands or the AMA. 45

4.8: Breakthrough profiles of BioNPs through AMA. 46

5.1: Highlights in the modeling study of adsorption kinetics. 49

5.2: Modes of binding sequence 51

5.3: Illustration of multi-site binding in a linear lattice model. 52

5.4: Sketch of the fluid domain and elucidation of the input-output system behavior.... 56

5.5: Entrance region of the velocity field in the SPR flow cell. 57

5.6: Comparison of simulated curves with experimental data. 62

5.7: Profiles of the diffusional boundary layer thickness in X-direction 64

5.8: Dynamic profiles of diffusional boundary layer at the outlet 65

5.9: Comparison between the numerical solution and the analytical solution 66

5.10: Comparison of the model simulated curves with the SPR experimental data. 67

5.11: Comparison of curves..... 69

5.12: Prediction of multivalent interaction using the reduced analytical solutions 70

5.13: Comparison of the simulated curves with the experimental data 73

5.14: Comparison of the simulation curves with the experimental data.. 75

5.15: Adsorption of BioNP1 at two receptor surfaces with different capacities..... 77

5.16: Adsorption of BioNP4 at two receptor surfaces with different capacities 78

5.17: Adsorption of BioNP1, BioNP2 and BioNP3 at R_{max}, b..... 80

5.18: Comparison of the estimated parameters 82

5.19: Profile variation of adsorption under the influence of the number of bonds 84

6.1: Schematic diagram of an affinity membrane adsorber. 87

6.2: System dispersion model. 92

6.3: Comparison of simulated curve with experimental data. 94

6.4: Comparison of simulation curve with experimental data. 95

6.5: Concentration distributions of particles in the mobile phase and in the solid phase. . 96

6.6: Isotherm 97

6.7: Influence of the number of bonds and the receptor capacity on breakthrough. 98

A.1: Fluid element. 117

A.2: Spatial discretization of the domain. 124

List of Tables

2.1: Dilution volumes of human IgG solutions. 13

2.2: Characteristics of synthetic bionanoparticles (BioNP). 15

3.1: Amount usage of materials in the carbodiimide reation. 19

3.1: Inlet concentration of influenza virus solutions and receptor surface capacities. 24

4.1. Residence time in average 43

5.1: Estimated parameters using two solutions of the diffusional boundary layer 66

5.2. Estimated parameters for the adsorption of influenza virus particles. 73

6.1: Dimensionless parameters 90

6.2: Volumetric parameters in the dispersion model. 94

6.3: Estimated kinetic parameters of the multivalent interaction. 95

References

Adak, A. K., H. J. Lin and C. C. Lin (2014). "Multivalent glycosylated nanoparticles for studying carbohydrate-protein interactions." Org Biomol Chem 12(30): 5563-5573.

Akhter, S., I. Ahmad, M. Z. Ahmad, F. Ramazani, A. Singh, Z. Rahman, F. J. Ahmad, G. Storm and R. J. Kok (2013). "Nanomedicines as Cancer Therapeutics: Current Status." Current Cancer Drug Targets 13(4): 362-378.

Amar, J. G. (2006). "The Monte Carlo method in science and engineering." Computing in Science & Engineering 8(2): 9-19.

Ammari, H., Y. J. Deng and P. Millien (2016). "Surface Plasmon Resonance of Nanoparticles and Applications in Imaging." Archive for Rational Mechanics and Analysis 220(1): 109-153.

Barua, S., J. W. Yoo, P. Kolhar, A. Wakankar, Y. R. Gokarn and S. Mitragotri (2013). "Particle shape enhances specificity of antibody-displaying nanoparticles." Proceedings of the National Academy of Sciences of the United States of America 110(9): 3270-3275.

Bastian, A. R., A. Nangarlia, L. D. Bailey, A. Holmes, R. V. K. Sundaram, C. Ang, D. R. M. Moreira, K. Freedman, C. Duffy, M. Contarino, C. Abrams, M. Root and I. Chaiken (2015). "Mechanism of Multivalent Nanoparticle Encounter with HIV-1 for Potency Enhancement of Peptide Triazole Virus Inactivation." Journal of Biological Chemistry 290(1): 529-543.

Bird, R. B., W. E. Stewart and E. N. Lightfoot (2002). Transport phenomena. New York, J. Wiley.

Boi, C., S. Dimartino, S. Hofer, J. Horak, S. Williams, G. C. Sarti and W. Lindner (2011). "Influence of different spacer arms on Mimetic Ligand A2P and B14 membranes for human IgG purification." J Chromatogr B Analyt Technol Biomed Life Sci 879(19): 1633-1640.

Boi, C., S. Dimartino and G. C. Sarti (2007). "Modelling and simulation of affinity membrane adsorption." Journal of Chromatography A 1162(1): 24-33.

Bolley, J., E. Guenin, N. Lievre, M. Lecouvey, M. Soussan, Y. Lalatonne and L. Motte (2013). "Carbodiimide versus click chemistry for nanoparticle surface functionalization: a comparative study for the elaboration of multimodal superparamagnetic nanoparticles targeting alphavbeta3 integrins." Langmuir : the ACS journal of surfaces and colloids 29(47): 14639-14647.

Bozza, W. P., K. Yang, J. L. Wang and Z. H. Zhuang (2012). "Developing peptide-based multivalent antagonists of proliferating cell nuclear antigen and a fluorescence-based PCNA binding assay." Analytical Biochemistry 427(1): 69-78.

Cai, H., Z. Y. Sun, M. S. Chen, Y. F. Zhao, H. Kunz and Y. M. Li (2014). "Synthetic multivalent glycopeptide-lipopeptide antitumor vaccines: impact of the cluster effect on the killing of tumor cells." Angew Chem Int Ed Engl 53(6): 1699-1703.

Che, A. F., X. J. Huang and Z. K. Xu (2010). "Protein adsorption on a glycosylated polyacrylonitrile surface: Monitoring with QCM and SPR." Macromolecular Bioscience 10(8): 955-962.

Chen, B., Q. Ye, K. P. Zhou and Y. F. Wang (2016). "Adsorption and separation of HCV particles by novel affinity aptamer-functionalized adsorbents." Journal of Chromatography B-Analytical Technologies in the Biomedical and Life Sciences 1017: 174-181.

Chen, C. C. and E. E. Dormidontova (2005). "Architectural and structural optimization of the protective polymer layer for enhanced targeting." Langmuir 21(12): 5605-5615.

Chen, C. T., C. L. Zhu, Y. Huang, Y. Nie, J. Z. Yang, R. Q. Shen and D. P. Sun (2016). "Regenerated bacterial cellulose microfluidic column for glycoproteins separation." Carbohydrate Polymers 137: 271-276.

Chen, X., O. Ramström and M. Yan (2014). "Glyconanomaterials: Emerging applications in biomedical research." Nano Research 7(10): 1381-1403.

Chenette, H. (2014). "High-productivity membrane adsorbers: polymer surface-modification studies for ion-exchange and affinity bioseparations."

Chittasupho, C. (2012). "Multivalent ligand: design principle for targeted therapeutic delivery approach." Ther Deliv 3(10): 1171-1187.

Choi, S. K., A. Myc, J. E. Silpe, M. Sumit, P. T. Wong, K. McCarthy, A. M. Desai, T. P. Thomas, A. Kotlyar, M. M. B. Holl, B. G. Orr and J. R. Baker (2013). "Dendrimer-Based Multivalent Vancomycin Nanoplatform for Targeting the Drug-Resistant Bacterial Surface." Acs Nano 7(1): 214-228.

Christensen, L. L. H. (1997). "Theoretical analysis of protein concentration determination using biosensor technology under conditions of partial mass transport limitation." Analytical Biochemistry 249(2): 153-164.

Crespo-Biel, O., B. Dordi, P. Maury, M. Péter, D. N. Reinhoudt and J. Huskens (2006). "Patterned, hybrid, multilayer nanostructures based on multivalent supramolecular interactions." Chemistry of Materials 18(10): 2545-2551.

Crespo-Biel, O., B. Dordi, D. N. Reinhoudt and J. Huskens (2005). "Supramolecular layer-by-layer assembly: Alternating adsorptions of guest- and host-functionalized molecules and particles using multivalent supramolecular interactions." Journal of the American Chemical Society 127(20): 7594-7600.

de Mol, N. J. and M. J. E. Fischer (2010). Surface Plasmon Resonance: A General Introduction. Surface Plasmon Resonance: Methods and Protocols. N. J. DeMol and M. J. E. Fischer. Totowa, Humana Press Inc. 627**:** 1-14.

Deisenhofer, J. (1981). "Crystallographic refinement and atomic models of a human Fc fragment and its complex with fragment B of protein A from Staphylococcus aureus at 2.9- and 2.8-.ANG. resolution." Biochemistry 20(9): 2361-2370.

Destouches, D., E. Huet, M. Sader, S. Frechault, G. Carpentier, F. Ayoul, J. P. Briand, S. Menashi and J. Courty (2012). "Multivalent pseudopeptides targeting cell surface nucleoproteins inhibit cancer cell invasion through tissue inhibitor of metalloproteinases 3 (TIMP-3) release." J Biol Chem 287(52): 43685-43693.

Dimartino, S., C. Boi and G. C. Sarti (2011). "A validated model for the simulation of protein purification through affinity membrane chromatography." Journal of Chromatography A 1218(13): 1677-1690.

Dix, A. V., S. M. Moss, K. Phan, T. Hoppe, S. Paoletta, E. Kozma, Z. G. Gao, S. R. Durell, K. A. Jacobson and D. H. Appella (2014). "Programmable nanoscaffolds that control ligand display to a G-protein-coupled receptor in membranes to allow dissection of multivalent effects." J Am Chem Soc 136(35): 12296-12303.

Dorokhin, D., S. H. Hsu, N. Tomczak, D. N. Reinhoudt, J. Huskens, A. H. Velders and G. J. Vancso (2010). "Fabrication and Luminescence of Designer Surface Patterns with beta-Cyclodextrin Functionalized Quantum Dots via Multivalent Supramolecular Coupling." Acs Nano 4(1): 137-142.

Edwards, P. R. and R. J. Leatherbarrow (1997). "Determination of association rate constants by an optical biosensor using initial rate analysis." Analytical Biochemistry 246(1): 1-6.

Effio, C. L. and J. Hubbuch (2014). "Meeting Report VLPNPV: Session 10: Virus-like particle and nano-particle vaccines." Human Vaccines & Immunotherapeutics 10(10): 3080-3082.

Ellis, J. S., H. G. Abdelhady, S. Allen, M. C. Davies, C. J. Roberts, S. J. B. Tendler and P. M. Williams (2004). "Direct atomic force microscopy observations of monovalent ion induced binding of DNA to mica." Journal of Microscopy 215(3): 297-301.

Elshan, N. G., T. Jayasundera, B. L. Anglin, C. S. Weber, R. M. Lynch and E. A. Mash (2015). "Trigonal scaffolds for multivalent targeting of melanocortin receptors." Org Biomol Chem 13(6): 1778-1791.

Fägerstam, L. G., Å. Frostell-Karlsson, R. Karlsson, B. Persson and I. Rönnberg (1992). "Biospecific interaction analysis using surface plasmon resonance detection applied to kinetic, binding site and concentration analysis." Journal of Chromatography A 597(1–2): 397-410.

Fasting, C., C. A. Schalley, M. Weber, O. Seitz, S. Hecht, B. Koksch, J. Dernedde, C. Graf, E. W. Knapp and R. Haag (2012). "Multivalency as a chemical organization and action principle." Angewandte Chemie 51(42): 10472-10498.

Fields, B. N., D. M. Knipe and P. M. Howley, Eds. (2001). Fields Virology, Lippincot Williams & Wilkins Publishcers.

Fisher-Power, L. M., T. Cheng and Z. S. Rastghalam (2016). "Cu and Zn adsorption to a heterogeneous natural sediment: Influence of leached cations and natural organic matter." Chemosphere 144: 1973-1979.

Friedman, A. D., S. E. Claypool and R. Liu (2013). "The Smart Targeting of Nanoparticles." Current Pharmaceutical Design 19(35): 6315-6329.

Garcia-Vallejo, J. J., M. Ambrosini, A. Overbeek, W. E. van Riel, K. Bloem, W. W. Unger, F. Chiodo, J. G. Bolscher, K. Nazmi, H. Kalay and Y. van Kooyk (2013). "Multivalent glycopeptide dendrimers for the targeted delivery of antigens to dendritic cells." Mol Immunol 53(4): 387-397.

Gervais, T. and K. F. Jensen (2006). "Mass transport and surface reactions in microfluidic systems." Chemical Engineering Science 61(4): 1102-1121.

Glaser, R. W. (1993). "Antigen-Antibody Binding and Mass-Transport by Convection and Diffusion to a Surface - a 2-Dimensional Computer-Model of Binding and Dissociation Kinetics." Analytical Biochemistry 213(1): 152-161.

Goldstein, B., D. Coombs, X. Y. He, A. R. Pineda and C. Wofsy (1999). "The influence of transport on the kinetics of binding to surface receptors: application to cells and BIAcore." Journal of Molecular Recognition 12(5): 293-299.

Gu, L., L. E. Ruff, Z. Qin, M. Corr, S. M. Hedrick and M. J. Sailor (2012). "Multivalent porous silicon nanoparticles enhance the immune activation potency of agonistic CD40 antibody." Adv Mater 24(29): 3981-3987.

Gutiérrez Sánchez, C., Q. Su, H. Schönherr, M. Grininger and G. Nöll (2015). "Multi-Ligand-Binding Flavoprotein Dodecin as a Key Element for Reversible Surface Modification in Nano-biotechnology." ACS Nano.

Hage, D. S., J. A. Anguizola, C. Bi, R. Li, R. Matsuda, E. Papastavros, E. Pfaunmiller, J. Vargas and X. W. Zheng (2012). "Pharmaceutical and biomedical applications of affinity chromatography: Recent trends and developments." Journal of Pharmaceutical and Biomedical Analysis 69: 93-105.

Hahn, R., R. Schlegel and A. Jungbauer (2003). "Comparison of protein A affinity sorbents." Journal of Chromatography B-Analytical Technologies in the Biomedical and Life Sciences 790(1-2): 35-51.

Handa, H., S. Gurczynski, M. P. Jackson and G. Mao (2010). "Immobilization and molecular interactions between bacteriophage and lipopolysaccharide bilayers." Langmuir 26(14): 12095-12103.

handbook, B. s. s. (2008). Biacore sensor surface handbook. Uppsala, Sweden, GE Healthcare Bio-Sciences AB.

Hartwell, B. L., L. Antunez, B. P. Sullivan, S. Thati, J. O. Sestak and C. Berkland (2015). "Multivalent nanomaterials: learning from vaccines and progressing to antigen-specific immunotherapies." J Pharm Sci 104(2): 346-361.

Hennig, R. (2013). Magdeburg, Germany, personal communication.

Holden, M. A. and P. S. Cremer (2005). Mlcrofluidic tools for studying the specific binding, adsorption, and displacement of proteins at interfaces. Annual Review of Physical Chemistry. 56: 369-387.

Howard, M., B. J. Zern, A. C. Anselmo, V. V. Shuvaev, S. Mitragotri and V. Muzykantov (2014). "Vascular Targeting of Nanocarriers: Perplexing Aspects of the Seemingly Straightforward Paradigm." ACS Nano 8(5): 4100-4132.

Hussain, M., D. Lockney, R. Q. Wang, N. Gera and B. M. Rao (2013). "Avidity-mediated virus separation using a hyperthermophilic affinity ligand." Biotechnology Progress 29(1): 237-246.

Jin, X. Z., J. Talbot and N. H. L. Wang (1994). "Analysis of Steric Hindrance Effects on Adsorption-Kinetics and Equilibria." Aiche Journal 40(10): 1685-1696.

Johnsson, B., S. Lofas and G. Lindquist (1991). "Immobilization of proteins to a carboxymethyldextran-modified gold surface for biospecific interaction analysis in surface plasmon resonance sensors." Analytical Biochemistry 198(2): 268-277.

Jurasin, D. D., M. Curlin, I. Capjak, T. Crnkovic, M. Lovric, M. Babic, D. Horak, I. V. Vrcek and S. Gajovic (2016). "Surface coating affects behavior of metallic nanoparticles in a biological environment." Beilstein Journal of Nanotechnology 7: 246-261.

Kalbfuss-Zimmermann, B., U. Reichl, E. P. Wen, R. Ellis and N. S. Pujar (2014). Viral Vaccines Purification. Vaccine Development and Manufacturing, John Wiley & Sons, Inc.**:** 97-180.

Kalinin, N. L., L. D. Ward and D. J. Winzor (1995). "Effects of Solute Multivalence on the Evaluation of Binding Constants by Biosensor Technology: Studies with Concanavalin A and Interleukin-6 as Partitioning Proteins." Analytical Biochemistry 228(2): 238-244.

Karlsson, R., A. Michaelsson and L. Mattsson (1991). "Kinetic analysis of monoclonal antibody-antigen interactions with a new biosensor based analytical system." Journal of Immunological Methods: 229-240.

Karlsson, R., H. Roos, L. Fägerstam and B. Persson (1994). "Kinetic and Concentration Analysis Using BIA Technology." Methods 6(2): 99-110.

Ken A. Dill, Sarina Bromberg and D. Stigter (2003). Molecular driving forces: statistical thermodynamics in chemistry and biology. New York and London, Garland Science.

Kochan, J. E., Y. J. Wu and M. R. Etzel (1996). "Purification of bovine immunoglobulin G via protein G affinity membranes." Industrial & Engineering Chemistry Research 35(4): 1150-1155.

Labanda, J., J. Sabate and J. Llorens (2009). "Modeling of the dynamic adsorption of an anionic dye through ion-exchange membrane adsorber." Journal of Membrane Science 340(1-2): 234-240.

Li, M.-H., S. K. Choi, P. R. Leroueil and J. R. Baker (2014). "Evaluating Binding Avidities of Populations of Heterogeneous Multivalent Ligand-Functionalized Nanoparticles." ACS Nano 8(6): 5600-5609.

Li, X. M., W. Cheng, D. D. Li, J. L. Wu, X. J. Ding, Q. Cheng and S. J. Ding (2016). "A novel surface plasmon resonance biosensor for enzyme-free and highly sensitive detection of microRNA based on multi component nucleic acid enzyme (MNAzyme)-mediated catalyzed hairpin assembly." Biosensors & Bioelectronics 80: 98-104.

Liedberg, B., I. Lundström and E. Stenberg (1993). "Principles of biosensing with an extended coupling matrix and surface plasmon resonance." Sensors and Actuators B: Chemical 11(1–3): 63-72.

Lisec, O., P. Hugo and A. Seidl-Morgenstern (2001). "Frontal analysis method to determine competitive adsorption isotherms." Journal of Chromatography A 908(1-2): 19-34.

Liu, J., N. J. Agrawal, A. Calderon, P. S. Ayyaswamy, D. M. Eckmann and R. Radhakrishnan (2011). "Multivalent binding of nanocarrier to endothelial cells under shear flow." Biophys J 101(2): 319-326.

Lo Schiavo, V., P. Robert, L. Limozin and P. Bongrand (2012). "Quantitative modeling assesses the contribution of bond strengthening, rebinding and force sharing to the avidity of biomolecule interactions." PloS one 7(9): e44070.

Lok, B. K., Y. L. Cheng and C. R. Robertson (1983). "Protein Adsorption on Crosslinked Polydimethylsiloxane Using Total Internal-Reflection Fluorescence." Journal of Colloid and Interface Science 91(1): 104-116.

Lok, B. K., Y. L. Cheng and C. R. Robertson (1983). "Protein adsorption on crosslinked polydimethylsiloxane using total internal reflection fluorescence." Journal of Colloid and Interface Science 91(1): 104-116.

Lundstrom, I. (1985). MODELS OF PROTEIN ADSORPTION ON SOLID SURFACES. Surfactants, Adsorption, Surface Spectroscopy and Disperse Systems. Papers presented at the 8th Scandinavian Symposium on Surface Chemistry., Lund, Swed.

Mahon, E., A. Salvati, F. Baldelli Bombelli, I. Lynch and K. A. Dawson (2012). "Designing the nanoparticle-biomolecule interface for "targeting and therapeutic delivery"." J Control Release 161(2): 164-174.

Maiti, S., C. Pezzato, S. Garcia Martin and L. J. Prins (2014). "Multivalent interactions regulate signal transduction in a self-assembled Hg2+ sensor." J Am Chem Soc 136(32): 11288-11291.

Majonis, D., O. Ornatsky, D. Weinrich and M. A. Winnik (2013). "Dual-Purpose Polymer Labels for Fluorescent and Mass Cytometric Affinity Bioassays." Biomacromolecules 14(5): 1503-1513.

Maric, H. M., V. B. Kasaragod, L. Haugaard-Kedstrom, T. J. Hausrat, M. Kneussel, H. Schindelin and K. Stromgaard (2015). "Design and Synthesis of High-Affinity Dimeric Inhibitors Targeting the Interactions between Gephyrin and Inhibitory Neurotransmitter Receptors." Angewandte Chemie-International Edition 54(2): 490-494.

Martín-Molina, A., G. Luque-Caballero, J. Faraudo, M. Quesada-Pérez and J. Maldonado-Valderrama (2014). "Adsorption of DNA onto anionic lipid surfaces." Advances in Colloid and Interface Science 206: 172-185.

Martinez-Veracoechea, F. J. and D. Frenkel (2011). "Designing super selectivity in multivalent nano-particle binding." Proceedings of the National Academy of Sciences of the United States of America 108(27): 10963-10968.

Matthaiou, E. I., J. Barar, R. Sandaltzopoulos, C. Li, G. Coukos and Y. Omidi (2014). "Shikonin-loaded antibody-armed nanoparticles for targeted therapy of ovarian cancer." International journal of nanomedicine 9: 1855-1870.

Mi, L., M. M. Giarmarco, Q. Shao and S. Jiang (2012). "Divalent cation-mediated polysaccharide interactions with zwitterionic surfaces." Biomaterials 33(7): 2001-2006.

Montesinos-Cisneros, R. M., A. Lucero-Acuna, J. Ortega, R. Guzman and A. Tejeda-Mansir (2007). "Breakthrough performance of large proteins on ion-exchange membrane columns." Biotechnology and Applied Biochemistry 48: 117-125.

Morimoto, J., M. Sarkar, S. Kenrick and T. Kodadek (2014). "Dextran as a generally applicable multivalent scaffold for improving immunoglobulin-binding affinities of peptide and peptidomimetic ligands." Bioconjug Chem 25(8): 1479-1491.

Mouline, Z., E. Mahon, E. Gomez, V. Barragan-Montero, J. L. Montero and M. Barboiu (2014). "Entropy-driven lectin-recognition of multivalent glycovesicles." Chemical Communications 50(6): 731-733.

Mullen, D. G., M. Fang, A. Desai, J. R. Baker, B. G. Orr and M. M. B. Holl (2010). "A Quantitative Assessment of Nanoparticle-Ligand Distributions: Implications for Targeted Drug and Imaging Delivery in Dendrimer Conjugates." Acs Nano 4(2): 657-670.

Myszka, D. G. (1997). "Kinetic analysis of macromolecular interactions using surface plasmon resonance biosensors." Current Opinion in Biotechnology 8(1): 50-57.

Myszka, D. G. (1999). "Improving biosensor analysis." Journal of Molecular Recognition 12(5): 279-284.

Myszka, D. G., X. He, M. Dembo, T. A. Morton and B. Goldstein (1998). "Extending the range of rate constants available from BIACORE: Interpreting mass transport-influenced binding data." Biophysical Journal 75(2): 583-594.

Nicholson, K., R. G. Webster and A. J. Hay (1998). Textbook of influenza. Oxford, Blackwell Science.

Nilsson, C. E., S. Abbas, M. Bennemo, A. Larsson, M. D. Hamalainen and A. Frostell-Karlsson (2010). "A novel assay for influenza virus quantification using surface plasmon resonance." Vaccine 28(3): 759-766.

Nishimura, Y., K. Takeda, J. Ishii, C. Ogino and A. Kondo (2013). "An affinity chromatography method used to purify His-tag-displaying bio-nanocapsules." Journal of Virological Methods 189(2): 393-396.

Olariu, C. I., H. H. Yiu and L. Bouffier (2013). Inorganic–Organic Hybrid Nanoparticles for Medical Applications. New Frontiers of Nanoparticles and Nanocomposite Materials, Springer**:** 85-133.

Olubummo, A., M. Schulz, R. Schöps, J. Kressler and W. H. Binder (2014). "Phase changes in mixed lipid/polymer membranes by multivalent nanoparticle recognition." Langmuir 30(1): 259-267.

Opitz, L., S. Lehmann, A. Zimmermann, U. Reichl and M. W. Wolff (2007). "Impact of adsorbents selection on capture efficiency of cell culture derived human influenza viruses." Journal of Biotechnology 131(3): 309-317.

Opitz, L., J. Salaklang, H. Buttner, U. Reichl and M. W. Wolff (2007). "Lectin-affinity chromatography for downstream processing of MDCK cell culture derived human influenza A viruses." Vaccine 25(5): 939-947.

Opitz, L., A. Zimmermann, S. Lehmann, Y. Genzel, H. Lubben, U. Reichl and M. W. Wolff (2008). "Capture of cell culture-derived influenza virus by lectins: Strain independent, but host cell dependent." Journal of Virological Methods 154(1-2): 61-68.

Paran, N., B. Geiger and Y. Shaul (2001). "HBV infection of cell culture: Evidence for multivalent and cooperative attachment." EMBO Journal 20(16): 4443-4453.

Pastré, D., L. Hamon, F. Landousy, I. Sorel, M. O. David, A. Zozime, E. Le Cam and O. Piétrement (2006). "Anionic polyelectrolyte adsorption on mica mediated by multivalent cations: A solution to DNA imaging by atomic force microscopy under high ionic strengths." Langmuir 22(15): 6651-6660.

Patricia, G.-G. (2012). "Simulation of Frontal Protein Affinity Chromatography Using MATLAB." Journal of Chemical Engineering & Process Technology.

Pease, L. F., 3rd, J. T. Elliott, D. H. Tsai, M. R. Zachariah and M. J. Tarlov (2008). "Determination of protein aggregation with differential mobility analysis: application to IgG antibody." Biotechnol Bioeng 101(6): 1214-1222.

Perelson, A. S. (1981). "Receptor Clustering on a Cell-Surface .3. Theory of Receptor Cross-Linking by Multivalent Ligands - Description by Ligand States." Mathematical Biosciences 53(1-2): 1-39.

Perumal, S., A. Hofmann, N. Scholz, E. Ruhl and C. Graf (2011). "Kinetics study of the binding of multivalent ligands on size-selected gold nanoparticles." Langmuir 27(8): 4456-4464.

Phanse, Y., B. R. Carrillo-Conde, A. E. Ramer-Tait, S. Broderick, C. S. Kong, K. Rajan, R. Flick, R. B. Mandell, B. Narasimhan and M. J. Wannemuehler (2014). "A systems approach to designing next generation vaccines: combining alpha-galactose modified antigens with nanoparticle platforms." Scientific reports 4: 3775.

Philippe, A. and G. E. Schaumann (2014). "Interactions of dissolved organic matter with natural and engineered inorganic colloids: A review." Environmental Science and Technology 48(16): 8946-8962.

Rädler, U., J. Mack, N. Persike, G. Jung and R. Tampé (2000). "Design of supported membranes tethered via metal-affinity ligand-receptor pairs." Biophysical Journal 79(6): 3144-3152.

Reščič, J., D. Kovačević, M. Tomšič, A. Jamnik, S. Ahualli and K. Bohinc (2014). "Experimental and theoretical study of the silica particle interactions in the presence of multivalent rod-like ions." Langmuir 30(32): 9717-9725.

Reynolds, M., M. Marradi, A. Imberty, S. Penades and S. Perez (2013). "Influence of ligand presentation density on the molecular recognition of mannose-functionalised glyconanoparticles by bacterial lectin BC2L-A." Glycoconj J 30(8): 747-757.

Saha, K., F. Bender and E. Gizeli (2003). "Comparative study of IgG binding to proteins G and A: Nonequilibrium kinetic and binding constant determination with the acoustic waveguide device." Analytical Chemistry 75(4): 835-842.

Sarfert, F. T. and M. R. Etzel (1997). "Mass transfer limitations in protein separations using ion-exchange membranes." Journal of Chromatography A 764(1): 3-20.

Schuck, P. and H. Zhao (2010). "The role of mass transport limitation and surface heterogeneity in the biophysical characterization of macromolecular binding processes by SPR biosensing." Methods in molecular biology 627: 15-54.

Schwarzer, J., E. Rapp, R. Hennig, Y. Genzel, I. Jordan, V. Sandig and U. Reichl (2009). "Glycan analysis in cell culture-based influenza vaccine production: Influence of host cell line and virus strain on the glycosylation pattern of viral hemagglutinin." Vaccine 27(32): 4325-4336.

Schwarzer, J., E. Rapp and U. Reichl (2008). "N-glycan analysis by CGE-LIF: Profiling influenza A virus hemagglutinin N-glycosylation during vaccine production." Electrophoresis 29(20): 4203-4214.

Shemetov, A. A., I. Nabiev and A. Sukhanova (2012). "Molecular Interaction of Proteins and Peptides with Nanoparticles." ACS Nano 6(6): 4585-4602.

Sheng, W. A., T. Chen, W. H. Tan and Z. H. Fan (2013). "Multivalent DNA Nanospheres for Enhanced Capture of Cancer Cells in Microfluidic Devices." Acs Nano 7(8): 7067-7076.

Shi, J., T. Yang, S. Kataoka, Y. Zhang, A. J. Diaz and P. S. Cremer (2007). "GM1 clustering inhibits cholera toxin binding in supported phospholipid membranes." Journal of the American Chemical Society 129(18): 5954-5961.

Shi, X., W. Zhan, G. Chen, Q. Yu, Q. Liu, H. Du, L. Cao, X. Liu, L. Yuan and H. Chen (2015). "Regulation of Protein Binding Capability of Surfaces via Host-Guest Interactions: Effects of Localized and Average Ligand Density." Langmuir 31(22): 6172-6178.

Shing Yi Suen and M. R. Etzel (1992). "A mathematical analysis of affinity membrane bioseparations." Chemical engineering Science 47(6): 1355-1364.

Shokeen, M., E. D. Pressly, A. Hagooly, A. Zheleznyak, N. Ramos, A. L. Fiamengo, M. J. Welch, C. J. Hawker and C. J. Anderson (2011). "Evaluation of Multivalent, Functional Polymeric Nanoparticles for Imaging Applications." Acs Nano 5(2): 738-747.

Sieben, C., C. Kappel, R. Zhu, A. Wozniak, C. Rankl, P. Hinterdorfer, H. Grubmuller and A. Herrmann (2012). Influenza virus binds its host cell using multiple dynamic interactions. Proceedings of the National Academy of Sciences of the United States of America.

Siess, D. C., S. L. Kozak and D. Kabat (1996). "Exceptional fusogenicity of Chinese hamster ovary cells with murine retroviruses suggests roles for cellular factor(s) and receptor clusters in the membrane fusion process." Journal of Virology 70(6): 3432-3439.

Silpe, J. E., M. Sumit, T. P. Thomas, B. Huang, A. Kotlyar, M. A. van Dongen, M. M. Banaszak Holl, B. G. Orr and S. K. Choi (2013). "Avidity modulation of folate-targeted multivalent dendrimers for evaluating biophysical models of cancer targeting nanoparticles." ACS Chem Biol 8(9): 2063-2071.

Sletten, E. M. and C. R. Bertozzi (2009). "Bioorthogonal Chemistry: Fishing for Selectivity in a Sea of Functionality." Angewandte Chemie-International Edition 48(38): 6974-6998.

Sonato, A., M. Agostini, G. Ruffato, E. Gazzola, D. Liuni, G. Greco, M. Travagliati, M. Cecchini and F. Romanato (2016). "A surface acoustic wave (SAW)-enhanced grating-coupling phase-interrogation surface plasmon resonance (SPR) microfluidic biosensor." Lab on a Chip 16(7): 1224-1233.

Sridhar, P. (1996). "Design of affinity membrane bioseparations." Chemical Engineering & Technology 19(5): 398-404.

Sykora, D., V. Kasicka, I. Miksik, P. Rezanka, K. Zaruba, P. Matejka and V. Kral (2010). "Application of gold nanoparticles in separation sciences." Journal of Separation Science 33(3): 372-387.

Tassa, C., J. L. Duffner, T. A. Lewis, R. Weissleder, S. L. Schreiber, A. N. Koehler and S. Y. Shaw (2010). "Binding affinity and kinetic analysis of targeted small molecule-modified nanoparticles." Bioconjugate Chemistry 21(1): 14-19.

Tavernaro, I., S. Hartmann, L. Sommer, H. Hausmann, C. Rohner, M. Ruehl, A. Hoffmann-Roeder and S. Schlecht (2015). "Synthesis of tumor-associated MUC1-glycopeptides and their multivalent presentation by functionalized gold colloids." Org Biomol Chem 13(1): 81-97.

Tejeda-Mansir, A., R. M. Montesinos, I. Magana-Plaza and R. Guzman (2003). "Breakthrough performance of stacks of dye-cellulosic fabric in affinity chromatography of lysozyme." Bioprocess and Biosystems Engineering 25(4): 235-242.

Troiano, J. M., L. L. Olenick, T. R. Kuech, E. S. Melby, D. Hu, S. E. Lohse, A. C. Mensch, M. Dogangun, A. M. Vartanian, M. D. Torelli, E. Ehimiaghe, S. R. Walter, L. Fu, C. R. Anderton, Z. Zhu, H. Wang, G. Orr, C. J. Murphy, R. J. Hamers, J. A. Pedersen and F. M. Geiger (2015). "Direct probes of 4 nm diameter gold nanoparticles interacting with supported lipid bilayers." Journal of Physical Chemistry C 119(1): 534-546.

Ugozzoli, M., D. Laera, S. Nuti, D. A. G. Skibinski, S. Bufali, C. Sammicheli, S. Tavarini, M. Singh and D. T. O'Hagan (2011). "Flow cytometry: An alternative method for direct quantification of antigens adsorbed to aluminum hydroxide adjuvant." Analytical Biochemistry 418(2): 224-230.

van Dongen, M. A., C. A. Dougherty and M. M. Banaszak Holl (2014). "Multivalent polymers for drug delivery and imaging: the challenges of conjugation." Biomacromolecules 15(9): 3215-3234.

van Dongen, M. A., J. E. Silpe, C. A. Dougherty, A. K. Kanduluru, S. K. Choi, B. G. Orr, P. S. Low and M. M. Banaszak Holl (2014). "Avidity mechanism of dendrimer-folic acid conjugates." Molecular pharmaceutics 11(5): 1696-1706.

Varga, N., I. Sutkeviciute, R. Ribeiro-Viana, A. Berzi, R. Ramdasi, A. Daghetti, G. Vettoretti, A. Amara, M. Clerici, J. Rojo, F. Fieschi and A. Bernardi (2014). "A multivalent inhibitor of the DC-SIGN dependent uptake of HIV-1 and Dengue virus." Biomaterials 35(13): 4175-4184.

Verbelen, C., V. Dupres, D. Raze, C. Bompard, C. Locht and Y. F. Dufrene (2008). "Interaction of the Mycobacterial Heparin-Binding Hemagglutinin with Actin, as Evidenced by Single-Molecule Force Spectroscopy." Journal of Bacteriology 190(23): 7614-7620.

Vicente, T., J. P. B. Mota, C. Peixoto, P. M. Alves and M. J. T. Carrondo (2010). "Analysis of adsorption of a baculovirus bioreaction bulk on an ion-exchange surface by surface plasmon resonance." Journal of Biotechnology 148(4): 171-181.

Vicente, T., J. P. B. Mota, C. Peixoto, P. M. Alves and M. J. T. Carrondo (2010). "Modeling protein binding and elution over a chromatographic surface probed by surface plasmon resonance." Journal of Chromatography A 1217(13): 2032-2041.

Walke, S., G. Srivastava, M. Nikalje, J. Doshi, R. Kumar, S. Ravetkar and P. Doshi (2015). "Fabrication of chitosan microspheres using vanillin/TPP dual crosslinkers for protein antigens encapsulation." Carbohydrate Polymers 128: 188-198.

Walkey, C. D., J. B. Olsen, H. B. Guo, A. Emili and W. C. W. Chan (2012). "Nanoparticle Size and Surface Chemistry Determine Serum Protein Adsorption and Macrophage Uptake." Journal of the American Chemical Society 134(4): 2139-2147.

Wang, S. H. and E. E. Dormidontova (2011). "Nanoparticle targeting using multivalent ligands: computer modeling." Soft Matter 7(9): 4435-4445.

Wang, W., A. Voigt, M. W. Wolff, U. Reichl and K. Sundmacher (2016). "Binding kinetics and multi-bond: Finding correlations by synthesizing interactions between ligand-coated bionanoparticles and receptor surfaces." Analytical Biochemistry.

Wang, W. J., M. W. Wolff, U. Reichl and K. Sundmacher (2014). "Avidity of influenza virus: Model-based identification of adsorption kinetics from surface plasmon resonance experiments." Journal of Chromatography A 1326: 125-129.

Wei, A., J. G. Mehtala and A. K. Patri (2012). "Challenges and opportunities in the advancement of nanomedicines." J Control Release 164(2): 236-246.

Wu, C. W., C. Y. Chiang, C. H. S. Chen, C. S. Chiang, C. T. Wang and L. K. Chau (2016). "Self-referencing fiber optic particle plasmon resonance sensing system for real-time biological monitoring." Talanta 146: 291-298.

Wu, M. and W. R. Algar (2015). "Acceleration of proteolytic activity associated with selection of thiol ligand coatings on quantum dots." ACS Applied Materials and Interfaces 7(4): 2535-2545.

Xie, X., G. Richard and J. C. Hall (2012). Antibody fragment engineering and applications in diagnosis and therapeutics. Antibodies Applications and New Development**:** 225-279.

Xu, L., J. S. Josan, J. Vagner, M. R. Caplan, V. J. Hruby, E. A. Mash, R. M. Lynch, D. L. Morse and R. J. Gillies (2012). "Heterobivalent ligands target cell-surface receptor combinations in vivo." Proc Natl Acad Sci U S A 109(52): 21295-21300.

Xu, S., B. Z. Olenyuk, C. T. Okamoto and S. F. Hamm-Alvarez (2013). "Targeting receptor-mediated endocytotic pathways with nanoparticles: rationale and advances." Adv Drug Deliv Rev 65(1): 121-138.

Yang, H. and M. R. Etzel (2003). "Evaluation of three kinetic equations in models of protein purification using ion-exchange membranes." Industrial & Engineering Chemistry Research 42(4): 890-896.

Yang, L., M. E. Biswas and P. Chen (2003). "Study of binding between protein a and Immunoglobulin G using a surface tension probe." Biophysical Journal 84(1): 509-522.

Ye, X. Y., X. J. Huang and Z. K. Xu (2014). "Polypropylene non-woven meshes with conformal glycosylated layer for lectin affinity adsorption: The effect of side chain length." Colloids and Surfaces B: Biointerfaces 115: 340-348.

Yin, Z. J., S. Dulaney, C. S. Mckay, C. Baniel, K. Kaczanowska, S. Ramadan, M. G. Finn and X. F. Huang (2016). "Chemical Synthesis of GM2 Glycans, Bioconjugation with Bacteriophage Q beta, and the Induction of Anticancer Antibodies." Chembiochem 17(2): 174-180.

Yu, K., A. L. Creagh, C. A. Haynes and J. N. Kizhakkedathu (2013). "Lectin interactions on surface-grafted glycostructures: influence of the spatial distribution of carbohydrates on the binding kinetics and rupture forces." Anal Chem 85(16): 7786-7793.

Zern, B. J., A. M. Chacko, J. Liu, C. F. Greineder, E. R. Blankemeyer, R. Radhakrishnan and V. Muzykantov (2013). "Reduction of Nanoparticle Avidity Enhances the Selectivity of Vascular Targeting and PET Detection of Pulmonary Inflammation." Acs Nano 7(3): 2461-2469.

Zhang, J. and C. R. Mackenzie (2012). "Multivalent display of single-domain antibodies." Methods Mol Biol 911: 445-456.

Zhang, J., W. Sheng and Z. H. Fan (2014). "An ensemble of aptamers and antibodies for multivalent capture of cancer cells." Chem Commun (Camb) 50(51): 6722-6725.

Publications

Peer-reviewed Contributions

[1] Wang, W.; Voigt, A.; Wolff, M. W.; Reichl, U;.Sundmacher, K.. Binding kinetics and multi-bond: Finding correlations by synthesizing interactions between ligand-coated bionanoparticles and receptor surfaces. Analytical Biochemistry 2016, 505: 8-17.

[2] Wang, W.; Voigt, A.; Sundmacher, K.. The interaction of protein-coated bionanoparticles and surface receptors reevaluated: How important is the number of bonds? Under review by Soft Matter (2016).

[3] Wang, W.; Wolff, M. W.; Reichl, U.; Sundmacher, K.. Avidity of influenza virus: Model-based identification of adsorption kinetics from surface plasmon resonance experiments. Journal of Chromatography A 2014, 1326: 125-129.

[4] Wang, W.; Voigt, A.; Wolff, M.; Reichl, U.; Sundmacher, K.. Adsorption in einer Affinitätsmembran: Ein Ansatz mittels synthetischer Biologie.Chemie Ingenieur Technik 2014, 9: 1410.

Presentations & Posters

[1] Wang, W., Voigt, A., Wolff, M., Reichl, U., Sundmacher, K., Optimization of affinity membrane adsorption by evaluating multivalent interaction, ECCE10 + ECAB3 + EPIC5, Nice/France, Sep 27-Oct 1, 2015 - Oral.

[2] Wang, W., Voigt, A., Sundmacher, K., Application of synthetic bionanoparticles to affinity membrane adsorption, Soft Smart Particles: Preparation and Applications, DECHEMA, Frankfurt/Germany, 2014 – Poster.

[3] Voigt, A., Wang, W., Sundmacher, K., Key-Lock Systems for Bioseparations - Molecular Simulation for Kinetic Models, AIChE Annual Meeting, November 16-21, Atlanta/USA, 2014 - Oral.

[4] Wang, W., Voigt, A., Wolff, M., Reichl, U., Sundmacher, K., A Synthetic Biology Approach to Affinity Membrane Adsorption, ProcessNet-Annual Meeting, September 30 - October 2, 2014, Aachen/Germany - Poster.

Curriculum Vitae

Personal Facts

Name:	Wenjing Wang
Date & place of birth:	December 7th, 1983, Shandong, China
Nationality:	Chinese

Education

09/2010 – 04/2016	PhD student in International Max Planck Research School Magdeburg for Advanced Methods in Process and Systems Engineering, Germany
09/2007 - 07/2010	Master of Engineering in Chemical Technology, University of the Chinese Academy of Sciences, China
09/2003 - 06/2007	Bachelor of Engineering in Processing Equipment & Control Engineering, China University of Petroleum, Beijing, China GPA: 3.87 out of 4.0, **Top 1** out of 56 graduates

Experiences

09/2010 - 12/2015	Max Planck Institute for Dynamics of Complex Technical Systems, Magdeburg, Germany Research assistant
09/2007 - 07/2010	Institute of Process Engineering, Chinese Academy of Sciences, China Research assistant
06/2008 - 10/2008	Tianjin Iron & Steel Group Co., Ltd., Bohai Steel, Tianjing, China Intern
07/2006 - 10/2006	SINOPEC Beijing Yanshan Company, Beijing, China Intern